

# ***Modeling and Experimental Investigation of Spent Fuel Disposal in Crystalline Rocks: FY23 Progress Report***

## **Spent Fuel and Waste Disposition**

*Prepared for*  
*US Department of Energy*  
*Spent Fuel and Waste Science Technology*  
*Y. Wang, Y. Xiong, T. Hadgu, C. M. Lopez,*  
*M. M. Mills, A. C. Sanchez, J. N. Kruichak, T. A. Ho*  
*Sandia National Laboratories*  
*H. Viswanathan, N. Conroy, J. Hyman, M. R. Sweeney,*  
*F. Caporuscio*  
*Los Alamos National Laboratory*  
*M. Hu, Y. Guglielmi, C. Chang, C. Doughty, P. Dobson, T.*  
*Sasaki, S. Borglin, W. Dong, J. Rutqvist, F. Soom, T.*  
*Kneafsey, J. Birkholzer, L. Zheng*  
*Lawrence Berkeley National Laboratory*  
*E. Balboni, L. Williams, A. E. Zandanel, M. Zavarin, S. Han*  
*Lawrence Livermore National Laboratory*  
*August 21, 2023*  
*M2SF-23SN010302072 ; SAND2024-022020*

**DISCLAIMER**

This information was prepared as an account of work sponsored by an agency of the U.S. Government. Neither the U.S. Government nor any agency thereof, nor any of their employees, makes any warranty, expressed or implied, or assumes any legal liability or responsibility for the accuracy, completeness, or usefulness, of any information, apparatus, product, or process disclosed, or represents that its use would not infringe privately owned rights. References herein to any specific commercial product, process, or service by trade name, trade mark, manufacturer, or otherwise, does not necessarily constitute or imply its endorsement, recommendation, or favoring by the U.S. Government or any agency thereof. The views and opinions of authors expressed herein do not necessarily state or reflect those of the U.S. Government or any agency thereof.

Sandia National Laboratories is a multi-mission laboratory managed and operated by National Technology and Engineering Solutions of Sandia, LLC., a wholly owned subsidiary of Honeywell International, Inc., for the U.S. Department of Energy's National Nuclear Security Administration under contract DE-NA0003525

**APPENDIX E**  
**NTRD DOCUMENT COVER SHEET<sup>1</sup>**

Name/Title of Deliverable/Milestone/Revision No. Modeling and and Experimental Investigation for Spent Fuel Disposal in Crystalline Rocks: FY23 Report (M2SF-23SN010302072)

Work Package Title and Number SF-23SN01030207

Work Package WBS Number 1.08.01.03.02

Responsible Work Package Manager Yifeng Wang  
(Name/Signature)

Date Submitted

Quality Rigor Level for Deliverable/Milestone <sup>2</sup>	<input type="checkbox"/> QRL-1 <input type="checkbox"/> Nuclear Data	<input type="checkbox"/> QRL-2	<input checked="" type="checkbox"/> QRL-3	<input type="checkbox"/> QRL-4 Lab QA Program <sup>3</sup>
--	---	--------------------------------	---	---

This deliverable was prepared in accordance with Sandia National Laboratory \_\_\_\_\_  
(Participant/National Laboratory Name)

QA program which meets the requirements of  
 DOE Order 414.1     NQA-1     Other

**This Deliverable was subjected to:**

Technical Review

**Technical Review (TR)**

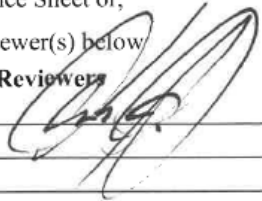
**Review Documentation Provided**

Signed TR Report or,

Signed TR Concurrence Sheet or,

Signature of TR Reviewer(s) below

**Name and Signature of Reviewer(s)**  
Carlos Jove-Colon (SNL)



Peer Review

**Peer Review (PR)**

**Review Documentation Provided**

Signed PR Report or,

Signed PR Concurrence Sheet or,

Signature of PR Reviewer(s) below

**NOTE 1:** Appendix E should be filled out and submitted with the deliverable. Or, if the PICS:NE system permits, completely enter all applicable information in the PICS:NE Deliverable Form. The requirement is to ensure that all applicable information is entered either in the PICS:NE system or by using the NTRD Document Cover Sheet.

- In some cases there may be a milestone where an item is being fabricated, maintenance is being performed on a facility, or a document is being issued through a formal document control process where it specifically calls out a formal review of the document. In these cases, documentation (e.g., inspection report, maintenance request, work planning package documentation or the documented review of the issued document through the document control process) of the completion of the activity, along with the Document Cover Sheet, is sufficient to demonstrate achieving the milestone.

**NOTE 2:** If QRL 1, 2, or 3 is not assigned, then the QRL 4 box must be checked, and the work is understood to be performed using laboratory QA requirements. This includes any deliverable developed in conformance with the respective National Laboratory / Participant, DOE or NNSA-approved QA Program.

**NOTE 3:** If the lab has an NQA-1 program and the work to be conducted requires an NQA-1 program, then the QRL-1 box must be checked in the work Package and on the Appendix E cover sheet and the work must be performed in accordance with the Lab's NQA-1 program. The QRL-4 box should not be checked.

This page left blank intentionally

## EXECUTIVE SUMMARY

**Purpose:** The objective of the crystalline disposal work packages is to advance our understanding of long-term disposal of used fuel in crystalline rocks and to develop necessary experimental and computational capabilities to evaluate various disposal concepts in such media. Specifically, the work packages aim to:

- Assist the geologic disposal safety assessment (GDSA) team to develop a total system performance assessment model for spent fuel disposal in crystalline rocks.
- Provide the GDSA with a necessary set of process models and model feeds to support various GDSA goals.
- Develop a basis for process modeling that enables streamlined integration with system modeling.
- Fully leverage international collaborations for data collection and model development and validation.
- Develop a key set of geologic parameters and criteria for future site screening and characterization.

FY23 work continued to focus on (1) better characterizing and understanding coupled thermal-hydrological-mechanical-chemical (THMC) processes in fracture networks in crystalline rocks and (2) Develop effective engineered barrier systems (EBS), especially buffer materials, for waste isolation.

**FY23 Accomplishments:** Major accomplishments in FY23 are summarized below:

- *Excavation disturbed zone (EDZ) characterization:* The twin-cell triaxial loading system was modified for bentonite sample characterization and bentonite-rock interaction studies. Two sets of experiments were completed on bentonite stacked with a granitic core with a tight and rough fracture embedded under room and elevated temperatures. The fracture permeability was found to be reduced by 5 orders of magnitude. Post-experiment imaging showed a significant intrusion of bentonite particles into the fracture due to clay swelling, causing fracture clogging.
- *Downhole characterization of stress and fractures:* Direct downhole measurements were performed for flow, pressure, and displacement evolution during a water injection cycle in a COSC-1 borehole. The data analyses were performed using both inversion methods and fully coupled hydromechanical forward numerical models. The experimental results highlighted a complex activation sequence of fractures. Adding borehole displacement measurements to a standard hydraulic test allows for determining the three principal stresses orientations and magnitudes.
- *Understanding thermal-hydrological-mechanical couplings in a single fracture (DECOVALEX 2023 Task G):* Using the numerical manifold method model and FLAC3D, numerical simulations were conducted to analyze shearing of intersecting fractures and thermal slip of single fractures. It was found that the intersections of fractures did not fundamentally change the shearing of two intersecting fractures if the intersecting angles satisfy certain conditions. A new simplified discrete fracture network model was developed to simplify modeling of the slip of fracture networks by using major path(s). In addition, numerical simulations were performed for a hydro-mechanical test, in which a cylindrical uniform resin sample with a single vertical fracture was subjected to triaxial external loading and fluid flow. The results obtained allow for constraining a constitutive relationship for modeling the effect of stress on fluid flow and transport in a fracture network.
- *Understanding flow and transport in fracture networks:* Flow and transport simulations were performed for fracture networks with varying degrees of fracture-to-fracture aperture heterogeneity and network density to clarify how changes in these properties could cause the emergence of anomalous flow and transport behavior. If the fracture-to-fracture aperture heterogeneity is increased in sparse networks, velocity fluctuations inhibit high flow rates and therefore solute transport can be delayed. Surprisingly, transport can be slowed even in cases where hydraulic aperture is monotonically increased. As the density of the networks is increased, more connected

pathways allow for particles to bypass these effects. These results reinforce the importance of considering multi-scale effects in fractured systems and can inform flow and transport processes in crystalline rocks.

- *Understanding bentonite erosion, coagulation/flocculation, and clogging in a fractured crystalline rock:* Experiments were designed to investigate bentonite erosion, coagulation, and clogging behavior in a fractured crystalline rock under varying temperature, rock materials, rock fracture aperture properties, and bentonite colloid properties. Much of FY23 work was spent assembling experimental apparatus, developing measurement techniques, and optimizing experimental conditions. Preliminary tests on bentonite colloid flocculation, coagulation and clogging were performed using a microfluidic cell. The results show a significant effect of solution chemistry on bentonite flocculation, coagulation and clogging in microchannels of the cell.
- *Understanding gas migration in low-permeability deformable media (DECOVALEX Task B):* Experimental observations on gas injection into water saturated compacted bentonite have revealed rich distinct dynamic behaviours of such processes. Linear stability analyses showed that such channelling could autonomously emerge from the morphological instability of the interface between the injected gas and the compacted bentonite. The work further showed that channel patterns formed as such would possess a fractal geometry, thus providing a new perspective for upscaling the process from small scale laboratory observations to a field scale.
- *Understanding radionuclide interactions with engineered and natural materials:* Experiments were initiated on radionuclide interactions with hydrothermally altered buffer materials. Recent research performed at LANL and SNL has provided key insights regarding the hydrothermal alteration behavior of bentonite backfill in a disposal environment. The preliminary experimental results indicate a possible impact of material heating on radionuclide uptake by bentonite.
- *Development of new generation buffer materials for high temperature and high pH environments:* The stability of Mg-rich saponite was investigated in alkaline solutions saturated with portlandite at 60°C and 150°C. The results suggest that Mg-rich saponite is stable in alkaline solutions at these temperatures. Thus, saponite can be a strong candidate for buffer materials under harsh conditions. We further showed that saponite could also be an excellent adsorbent for cationic radionuclides, especially trivalent actinides.
- *Application of machine learning in the prediction of thermodynamic properties of complex fluids:* Brønsted-Guggenheim-Scatchard specific interaction theory (SIT) is a model for calculating activity coefficients of aqueous species in moderate to high ionic strength solutions. FY23 work attempted to use deep learning neural networks to correlate the SIT coefficient of a species pair to a basic set of known or easily estimated properties of individual species. It is shown that such correlations did exist and could be extracted using both unsupervised and supervised machine learning. Such correlations were able to provide a reasonable prediction of the SIT coefficients for various species pairs under certain chemical conditions. This work opens a new avenue for modeling thermodynamic properties of complex fluids relevant to nuclear waste disposal.

**Next Stages of This Work:** In the next five years, the disposal research will continue to focus on process model development and model implementation in a GDSA framework for different generic reference cases. At the end of the five years, it is anticipated that a GDSA model developed will contain a sufficiently detailed representation of relevant process models and thus can be used for sensitivity analyses and programmatic prioritization. International collaborations have been, and will continue to be, a significant aspect of the crystalline research area over the next five years. These activities include continued participation in DECOVALEX as well as other international geologic disposal research programs. Collating and analyzing data from international underground research labs will be a continued activity in the crystalline area over the next five years.

## CONTENTS

1.0	GOAL AND OUTLINE	1
2.0	LABORATORY CORE EXPERIMENTS FOR CHARACTERIZATION OF EXCAVATION DISTURBED ZONE	5
2.1	Introduction	5
2.0	Bentonite Characterizations	6
2.2.1	Permeability Evolution	6
2.2.2	Effluent Water Chemistry	10
2.3	Fracture Characterization	11
2.4	Bentonite-Fracture Interactions	12
2.4.1	Permeability Evolutions at 25°C	12
2.4.2	Permeability Evolution at 90°C	13
2.4.3	Effluent Water Chemistry in Stacked Bentonite-Rock System	16
2.5	Bentonite-Flat Fracture Tests	16
2.5.1	Fracture Sample Holder and a Testing System	17
2.5.2	Infiltration Rate Evolution at 25°C	18
2.6	Conclusions	19
3.0	Downhole CHARACTERIZATION OF STRESS AND FRACTURES IN CRYSTALLINE ROCKS	21
3.1	Introduction	21
3.2	Three-Dimensional Displacement Measurements in a Deep Borehole in Scandinavian Caledonides	22
3.3	Deep Borehole Observations and Modeling of Crystalline Rock Hydromechanical Property Evolution During the Development of a Macro-Fracture	26
3.4	New Field Experiments to Study the Crystalline Fault and Fractures Permeability Variations Induced by Weak Aseismic to Seismic Loadings at Relevant Nuclear Repository Depths	35
3.5	Conclusions	41
4.0	GEOMETRIC CHARACTERIZATION OF A SINGLE TRANSMISSIVE FRACTURE	43
4.1	Introduction	43
4.2	Visualizing Aperture Distribution	43

4.3	Conclusion	50
5.0	UNDERSTANDING THERMAL-HYDROLOGICAL-MECHANICAL PROCESSES IN A SINGLE FRACTURE	51
5.1	Introduction	51
5.2	Multiscale Modeling of Shearing of Fractures	53
5.2.1	Fundamentals of NMM	53
5.2.2	Discontinuous Fracture Model in NMM	54
5.2.2.1	Contacts of the Discontinuous Fractures	54
5.2.2.2	Geometric Representation	55
5.2.2.3	NMM Calculation of Shearing Discontinuous Fractures	56
5.2.3	Simplified DFN Model – Proof of Concept	57
5.2.3.1	Shearing of Two Intersecting Fractures	57
5.2.3.2	Simplifying Intersecting Fractures with Major Path(s)	60
5.2.4	Discussion	66
5.3	DECOVALEX-2023 Task G	67
5.3.1	Work scope and team	67
5.3.2	LBNL Work for DECOVALEX 2023 Task G	68
5.3.2.1	Modeling Fractures as Interfaces in FLAC3D	69
5.3.2.2	TM Coupling in FLAC3D	71
5.3.2.3	FLAC3D Modeling of Thermal Slip of Fractures	72
5.3.2.4	Results	77
5.3.2.5	Discussion	87
5.3.3	SNL Work for DECOVALEX 2023 Task G	88
5.3.3.1	Step 1a: Modeling of Surface Deformation of a Solid Body	88
5.3.3.2	Step 2a: Coupled Hydro-Mechanical Modeling	93
5.4	Conclusions	100
6.0	UNDERSTANDING FLOW, TRANSPORT AND CHEMICAL REACTIONS IN FRACTURE NETWORKS	101
6.1	Introduction	101
6.2	Characterizing the Impacts of Multi-Scale Heterogeneity on Solute Transport in Fracture Networks	102
6.2.1	Theoretical Background	102

6.2.2	DFN Simulations	104
6.2.3	Results	105
6.2.3.1	Single Percolation Path	105
6.2.3.2	Multiple Percolation Paths	107
6.2.4	Discussion	110
6.3	Effects of Geometric Features on Reactive Transport and Mineral Precipitation in Fracture networks	111
6.3.1	CrunchFlow for Modeling Reactive Transport	111
6.3.2	<i>Reactive Transport Approach</i>	112
6.3.3	Flow Simulations	113
6.3.4	Simulations of Mixing	113
6.3.5	Discussion	120
6.4	Conclusions	120
7.0	BENTONITE EROSION, COAGULATION/FLOCCULATION, AND CLOGGING IN A FRACTURED CRYSTALLINE ROCK	121
7.1	Introduction	
7.2	Bentonite Erosion Cell	121
7.3	Colloid Concentration Measurement Method Development	122
7.4	Selection of the Titanium Frit	123
7.5	Compacted versus Non-Compacted Bentonite	126
7.6	Bentonite Colloid Flocculation/Coagulation Experiments	128
7.7	Conclusions	136
8.0	GAS CHANNELING AND MIGRATION IN WATER-SATURATED COMPACTED BENTONITE THROUGH INTERFACE INSTABILITY (DECOVALEX 2023 Task B)	137
8.1	Introduction	137
8.2	Compaction, Positive Feedbacks, and Channeling	137
8.3	Hydrological Instability of Gas-Bentonite Interface	138
8.4	Mechanical instability of Gas-Bentonite Interface	139
8.5	Channel Branching	141
8.6	Gas Flow in a Deformable Channel	143
8.7	Discussion	144

8.8	Conclusions	146
9.0	UNDERSTANDING RADIONUCLIDE INTERACTIONS WITH ENGINEERED AND NATURAL MATERIALS	147
9.1	Introduction	147
9.2	Effects of Bentonite Heating on Radionuclide Adsorption	147
9.2.1	Materials and Methods	149
9.2.2	Results	149
9.3	Comprehensive Surface Complexation Reaction Analysis Workflow: Surface Complexation of Se(IV) And Se(VI) on Iron Oxide Phases	151
9.3.1	Development of Radionuclide Surface Complexation Modeling Framework	151
9.3.2	Case Study of Selenium Sorption to Ferrihydrite	153
9.4	Conclusions	157
10.0	SAPONITE AS A NEW ENGINEERED BUFFER MATERIAL FOR HIGH LEVEL NUCLEAR WASTE DISPOSAL: ITS CHEMICAL AND THERMAL STABILITY AND SORPTION CAPABILITY	159
10.1	Introduction	159
10.2	Experimental	160
10.2.1	Materials	160
10.2.2	Procedure	161
10.3	Results and Discussion	164
10.4	Conclusions	174
11.0	USING MACHINE LEARNING TO PREDICT BRØNSTED-GUGGENHEIM-SCATCHARD SPECIFIC ION INTERACTION THEORY (SIT) COEFFICIENTS	175
11.1	Introduction	175
11.2	Methodology	176
11.2.1	Data Selection and Database Preparation	176
11.2.2	Software	178
11.2.3	Machine Learning Methodology	178
11.3	Results and Discussion	179
11.3.1	Unsupervised Machine Learning via K-Means Clustering	179
11.3.2	Supervised Machine Learning via Neural Network	181
11.4	Conclusions	188

---

12.0	SUMMARY	189
13.0	REFERENCES	193
	APPENDIX A. Evaluation of current status	207



## ACRONYMS

ASTM	LLNL Automated Surface Titration Model
CNL	Constant normal load
CNS	Constant normal stiffness
CNSC	Canadian Nuclear Safety Commission
COSC	Collisional Orogeny in the Scandinavian Caledonides Project
CT	Computerized Tomography
DDA	Discontinuous Deformation Analysis
DECOVALEX	DEvelopment of COupled Models and their VALidation Against EXperiments
DFN	Discrete Fracture Network
DOF	Degree of Freedom
DORSA	Downhole Robotic Stress Analyzer
EBS	Engineered Barrier System
EDZ	Excavation Damaged Zone
EIR	Effective ionic radius
EPA	Environmental Protection Agency
ESF	Electrostatic field
FCM	Fracture Continuum Model
FFEC	Flowing Fluid Electrical Conductivity
GDSA	Geologic Disposal Safety Assessment
HF	Hydraulic Fracturing
HLW	High-Level Radioactive Waste
HotBENT	High temperature effects on bentonite buffers
HTPF	Hydraulic Testing of Pre-existing Fractures
ICP-AES	Inductively Coupled Plasma-Atomic Emission Spectrometer
JAEA	Japan Atomic Energy Agency
KAERI	Korea Atomic Energy Research Institute

KICT	Korea Institute of Civil Engineering and Building Technology
KIGAM	Korea Institute of Geoscience and Mineral Resources
LANL	Los Alamos National Laboratory
L-ASCM	LLNL Automated Surface Complexation Model
LBNL	Lawrence Berkeley National Laboratory
LLNL	Lawrence Livermore National Laboratory
L-SCIE	LLNL Surface Complexation/Ion Exchange
LVDT	Linear Variable Differential Transformer
MAE	Mean absolute error
NM	Nelder-Mead
NMM	Numerical Manifold Method
NUMO	Nuclear Waste Management Organization of Japan
OGS	OpenGeoSys
PA	Performance Assessment
PCA	Principal component analysis
PFC	Particle Flow Code
PFLOTRAN	A Massively Parallel Reactive Flow and Transport Model for Describing Surface and Subsurface Processes
R&D	Research and Development
RSD	Relative Standard Deviation
SA	Sensitivity Analysis
SAFENET	Safety Implications of Fluid Flow, Shear, Thermal and Reaction Processes within Crystalline Rock Fracture NETWORKS
SCM	Surface Complexation Model
SEM	Scanning electron Microscope
SFWD	Spent Fuel Waste Disposition
SFWST	Spent Fuel Waste Science & Technology
SIMFIP	Step-rate Injection Method for Fracture In-situ Properties
SIT	Specific interaction theory
SJB	San Juan Bautista

SNF	Spent Nuclear Fuel
SNL	Sandia National Laboratories
THM	Thermo-Hydro-Mechanical
THMC	Thermal, Hydrological, Mechanical and Chemical
TM	Thermal-Mechanical
TUBAF	Technical University Bergakademie Freiberg, Germany
UFDC	Used Fuel Disposition Campaign
UFZ	Zentrum für Umweltforschung (Helmholtz Center for Environmental Research), Germany
WSM	World Stress Map
XRD	X-ray diffraction
XRF	X-ray Fluorescence



## 1.0 GOAL AND OUTLINE

The U.S. Department of Energy Office of Spent Fuel Waste Disposition (SFWD) established the Spent Fuel Waste Science & Technology (SFWST) Program (formerly the Used Fuel Disposition Campaign) program in fiscal year 2010 (FY10) to conduct the research and development (R&D) activities related to storage, transportation and disposal of used nuclear fuel and high-level nuclear waste in the U.S. The mission of the SFWST is:

*To identify alternatives and conduct scientific research and technology development to enable storage, transportation and disposal of used nuclear fuel and wastes generated by existing and future nuclear fuel cycles.*

Disposal R&D work packages directly support the following SFWST objectives:

- Develop a fundamental understanding of disposal system performance in a range of environments for potential wastes that could arise from future nuclear fuel cycle alternatives through theory, simulation, testing, and experimentation.
- Develop a computational modeling capability for the performance of storage and disposal options for a range of fuel cycle alternatives, evolving from generic models to more robust models of performance assessment.

Crystalline rocks have been considered as a potential host medium for deep geologic disposal of nuclear waste by several countries (e.g., Korea, Japan, China), and are being studied at several underground research laboratories. For example, granite rocks have been investigated at the Fennoscandian Shield, Sweden (Martin and Christiansson, 2009), at the Grimsel Test Site, Switzerland (Hadermann and Heer, 1996), and in the Beishan area, China (Cao et al., 2017). Such rocks have advantageous features for waste isolation including their high mechanical stability, low permeability (without fractures), high thermal conductivity, and widespread geologic occurrence.

Crystalline disposal work packages are aimed to advance our understanding of long-term disposal of used fuel in crystalline rocks and to develop necessary experimental and computational capabilities to evaluate various disposal concepts in such media. The research topics of interest are identified in the research plan (Wang et al., 2014) and the SFWST Campaign R&D Roadmap (Sevougian et al., 2019). FY23 work was focused on:

- Assist the geologic disposal safety assessment (GDSA) team to develop a robust repository performance assessment model.
- Provide the GDSA with a basic “minimal” set of process models and model feeds to support the GDSA near-term goal.
- Develop a basis for process modeling that enables streamlined integration with system modeling resulting in feeds to GDSA.
- Consolidate model parameter data, especially thermodynamic data, to ensure more consistent usage of the data across the project.
- Considering the existence of different approaches taken by various researchers, understand how well the models are developed in terms of pedigree and rigor.
- Fully leverage international collaborations for data collection and model development and validation.
- Closely collaborate with other work packages, especially those on disposal in argillite and engineered barrier system design.

The FY23 work continued to focus on: (1) better characterization and understanding of fractured media and fluid flow and transport in such media, and (2) designing effective engineered barrier systems (EBS) for waste isolation.

The FY23 work for the Crystalline Disposal R&D work packages covers the following research topics:

- Understand and quantify radionuclide interactions with corrosion products, especially understand the whole process from surface adsorption to irreversible structural incorporation.
- Understand and quantify bentonite erosion, suspension, and clogging and their impacts on fracture permeability and radionuclide transport.
- Understand fluid flows in low-permeability media, e.g., gas migration in water-saturated compacted bentonite materials.
- Continue development of new-generation buffer materials/waste package materials; understand thermal limits of buffer materials.
- Continue development of the discrete fracture network (DFN) model, especially account for the effect of regional stress and thermal stress on fracture aperture and permeability; and develop the corresponding reduced order model for GDSA, e.g., using machine learning.
- Continue development and demonstration of a workflow for field data synthesis and flow modeling in fractured media.
- Develop geophysical and well-testing techniques and laboratory rock testing capabilities for characterizing fractures and inflows; reduce the uncertainties of key flow parameters in the excavation disturbed zone (EDZ).
- Continue process model demonstration and validation using the data collected through international collaboration.

This report summarizes work accomplished in FY23 for the Crystalline Disposal R&D work packages. The report is outlined as follows, covering topics from engineered barrier material performance to far-field flow and transport:

- Chapter 1 reiterates the overall goal of the crystalline DR work packages (SNL).
- Chapter 2 documents the development and testing of a triaxial rock-mechanical system for laboratory EDZ characterization (LBNL).
- Chapter 3 documents the work on transmissive fracture characterization using an in-situ borehole testing technique and numerical modeling (LBNL).
- Chapter 4 presents a method for geometric characterization of a single transmissive fracture (LBNL).
- Chapter 5 documents the work on understanding of thermal-hydrological-mechanical couplings in a single fracture (DECOVALEX 2023 Task G) (LBNL, SNL).
- Chapter 6 documents the work on understanding of the effects of fracture geometry on fluid flow, transport, and chemical reactions in fracture networks (LBNL, LANL).
- Chapter 7 focuses on bentonite erosion, coagulation/flocculation, and clogging in a fractured crystalline rock (LANL).
- Chapter 8 documents the work on gas migration in water-saturated compacted bentonite (SNL).
- Chapter 9 documents the study of radionuclide interaction with thermally altered bentonite and iron oxides (LLNL).
- Chapter 10 proposes saponite as a new buffer material for high temperature and high pH repository environments (SNL).
- Chapter 11 documents the work on the application of machine learning in the prediction of solution thermodynamic properties (LLNL).
- Chapter 12 provides an overall summary of FY21 accomplishment for Crystalline Disposal R&D work packages (SNL).
- Chapter 13 provides the list of references.

- Appendix A provides an evaluation of the current status of tasks identified in SFWST R&D roadmap (SNL).

The results documented in this report represents the major portion of the work conducted in FY23 for the Crystalline Disposal R&D work packages but not all the work. The work not reported includes the development of a new generation of buffer materials and the effect of microbial reactions on bentonite stability. The related work will be reported later as it becomes available for public release.



## 2.0 LABORATORY CORE EXPERIMENTS FOR CHARACTERIZATION OF EXCAVATION DISTURBED ZONE

### 2.1 Introduction

Geologic disposal of high-level radioactive waste (HLW) relies on both a natural barrier formed by rock formations and an engineered barrier system (EBS) in isolating the waste from biosphere. In most repository designs, emplacement tunnels will be backfilled with bentonite material, serving as an engineered barrier, to provide mechanical buffering for the waste canisters, additional retention capacity, and thermal stability (Meunier et al., 1998; Bourg et al., 2003; Sellin and Leupin, 2013). After waste emplacement, both natural rock barrier in the excavated disturbed zone (EDZ) (including fractures, cracks) and the bentonite backfill will be heated due to the radionuclide decay, triggering complex coupled THMC processes at the bentonite-rock interface. When hydrated, bentonite can expand several times its original volume, leading to the formation of a dense, impermeable barrier. The swelling characteristics allow bentonite to fill and seal rock fractures, reducing the potential for fluid migration (Bian et al., 2019). Bentonite can also undergo chemical interactions with the minerals present in the rock fractures (Arcosa et al., 2003). For example, exchangeable cations in the bentonite, such as sodium or calcium ions, can be exchanged with cations in the rock, leading to alteration of the mineralogy and potentially forming new minerals under repository conditions. These chemical interactions may further enhance the sealing properties of the bentonite-rock fracture system.

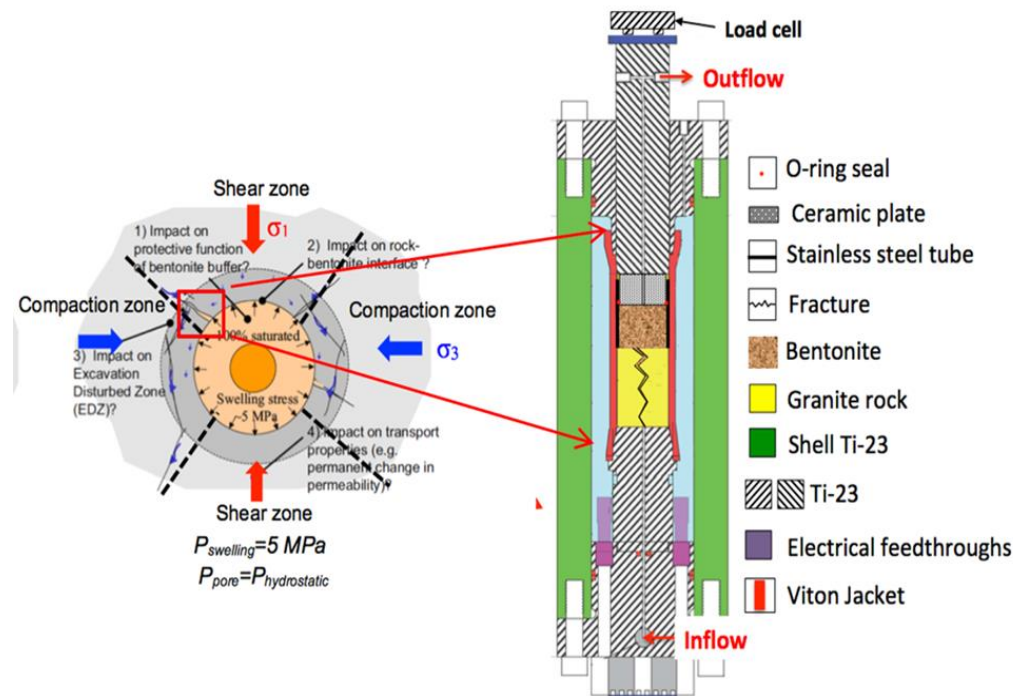


**Figure 2-1.** Conceptual model of potential long-term coupled THMC processes at EBS-EDZ interface (left, revised from Birkholzer et al., 2007) and schematics of the laboratory test on bentonite-rock interactions (right).

While radionuclide retardation behavior of each element of the EBS and natural host rock has been characterized and predicted, the coupled THMC processes and prediction of long-term performance of each element are greatly complicated by the bentonite-rock interactions at their interface. A better understanding on the bentonite-rock interactions and THMC processes (including fine particle migrations) at the interface requires systematic laboratory investigations using stacked bentonite and rock under *in-situ* stress, hydrological, thermal and chemical conditions.

In FY22, we applied the dedicated triaxial loading system for characterizing bentonite permeability and swelling pressure. We also conducted experiment to investigate the bentonite-rock fracture interactions and sealing of micro-scale rock fracture by hydrated bentonite (Figure 2-1). In FY23, we continued the experiment under elevated temperature and showed the considerable thermal impact on the stacked bentonite-rock fracture system and a bentonite sealing capability. We also fabricated a new sample holder so that fracture geometry and aperture can be well-controlled and applied in the loading system. We then conducted a new set of experiments on bentonite stacked with a large mm-scale flat fracture to investigate the water infiltration rate and thermal impacts. This chapter describes the lab system modification, materials used, experimental method and procedures, and results obtained so far.

## 2.2 Bentonite Characterizations

### 2.2.1 Permeability Evolution

The experiment was conducted using a stainless-steel tube (1.500'' (3.81 cm) long, 1.244'' (3.16 cm) inner diameter, and 1.5'' (3.81 cm) outer diameter). The Wyoming bentonite MX-80, which is used at the HotBENT field site, was compacted at an average dry density of 1.45 g/cm<sup>3</sup> and a gravimetric water content of 5.3%, similar to the field conditions (see the top right image in Figure 2-2). As shown in Figure 2-2, the compacted bentonite is composed by large (cm size) grains and powder, representing very heterogeneous geometry before the test. The top and the bottom of the tube are capped with a 1-cm-thick porous ceramic disc with an O-ring seal on the side (the middle right image in Figure 2-2). The porosity and permeability of the ceramic discs (Soilmoisture, CA) are 0.45 mD and 8.8 mD, respectively. The average pore size is 2.5 μm, which is smaller than the minimum bentonite particle size measured from sieving of different mesh sizes.

According to the field-site groundwater compositions, synthetic brine (electrical conductivity of the brine =  $1.33 \times 10^{-2}$  S/m, pH = 6.5) was prepared for these flow experiments (Table 2-1). The compacted bentonite and the two ceramic discs were stacked in a Viton rubber sleeve and emplaced in the loading cell. Then, we applied a constant 725 psi confining stress and an initial 540 psi axial stress to the sample. We then injected brine from the bottom and maintained a constant water pressure at 290 psi. This pressure was used to investigate the bentonite hydration, swelling and potential bentonite particle migration at the bentonite-rock interface in the presence of high-permeability fracture, which is similar to the value applied at the HotBENT field and laboratory tests. We closely monitored the Linear Variable Differential Transformer (LVDT) reading and controlled its variations by adjusting the axial stress, so that a minimum deformation of the stacked system (0.01% strain) was achieved.

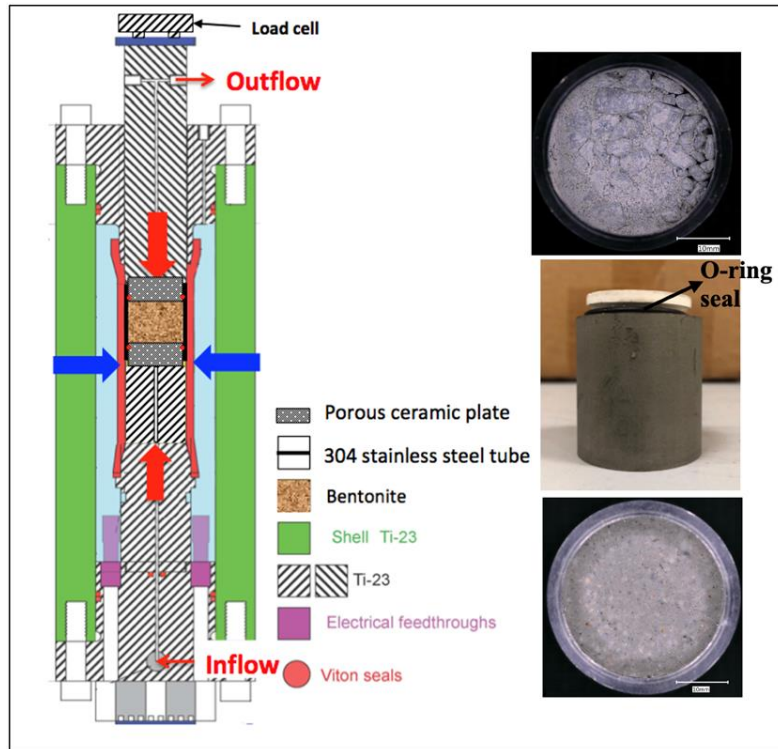


**Figure 2-2.** Schematic of the laboratory experiment used for characterization on bentonite permeability and swelling pressure (left). Photograph of the compacted bentonite before test (top right), the sample holder and ceramic disc seal (middle right), and the compacted bentonite after hydration test (bottom right).

**Table 2-1.** Chemical composition of the artificial groundwater used in the tests.

<b>Cations</b>		(mg/L)
Na+	0.846 mM	19.458
Ca+2	0.190 mM	7.61
Sr+2	2.63 μM	0.23
K+	6.11 μM	0.239
Mg+2	1.22 μM	0.03
Mn+2	0.08 μM	0.005
<b>Anions</b>		(mg/L)
F-	0.268 mM	5.091
Cl-	0.385 mM	13.648
SO4-2	0.067 mM	6.437
HCO3-	0.453 mM	27.64

The bentonite permeability was determined based on the applied differential pressure, water injection rate, and permeability of the ceramic discs. We sequentially quantified the bentonite permeability at 25°C and

elevated temperature 90°C. Figure 2-3 shows the water infiltration rate vs. time during water injection at constant 290 psi under the two tested temperatures. As shown in Figure 2-3(a), the water infiltration rate decreased with time from  $4.5 \times 10^{-4}$  mL/min to  $2.0 \times 10^{-4}$  mL/min after 4 days. After 8 days, brine was collected from the outlet after hydrating the bentonite. Meanwhile the infiltration rate remained being relatively constant at  $1.7 \times 10^{-4}$  mL/min. At this point, we stopped water injection, released water pressure and axial stress to 0 psi and monitored the load cell readings for bentonite swelling pressure after hydration. The load cell was calibrated using the weight of a metal block used with the loading frame, and the bentonite swelling pressure was calculated as 2.6 MPa from the calibrated load cell reading and the sample surface area.

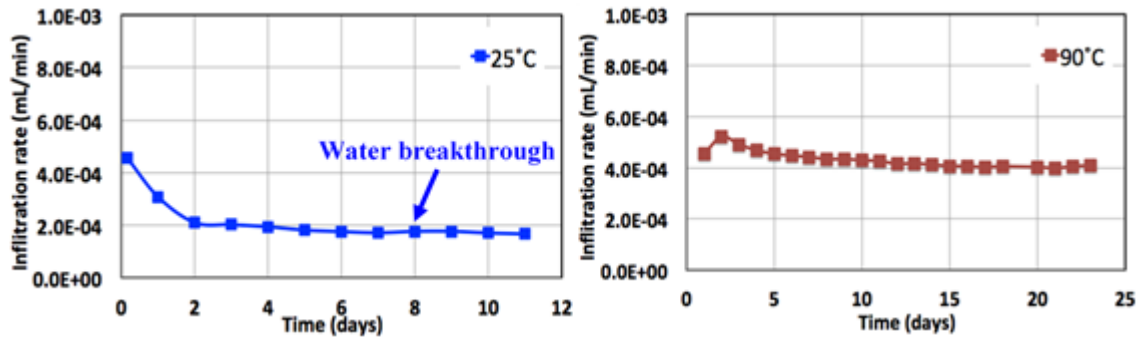


**Figure 2-3.** Water infiltration rate measured during bentonite permeability tests for water injection at 290 psi under 25°C and 90°C.

After the swelling pressure was measured at 25°C, we re-injected water at 290 psi, increased the axial pressure to 540 psi and heated the bentonite sample up to 90°C by using heating bands wrapped over the vessel. Figure 2-3(b) presents a graph of the water infiltration rate under 90°C, which was stable at  $4 \times 10^{-4}$  mL/min after injection for 14 days. The infiltration rate, shown in Figure 2-3, was used to calculate bentonite permeability changes vs. time at 25°C and 90°C. Assuming Darcy's law and fluid flow through a multi-layer system (Figure 2-4), the equivalent permeability of the multi-layer system vs. permeability of each layer can be computed by Eq. (2-1). With the  $k_{\text{equivalent}}$  measured from the water infiltration rate and applied differential pressure, the bentonite permeability was calculated and presented in Figure 2-5. The calculated bentonite permeability after hydration was 28.5 nD at 25°C and 23.6 nD at 90°C, respectively. The bentonite swelling pressure, following the previous steps, was 3.26 MPa under 90°C, higher than the swelling pressure measured at 25°C. This higher bentonite swelling pressure is caused the observed reduced permeability under the elevated temperature. The bottom right image in Figure 2-2 is the photograph of the bentonite after the heating and hydration tests, showing more homogenous structure than on the top right image taken before the experiments. This homogenization of the sample was caused probably by equalization of the inter-particle distance by clay swelling, and also the collapse of large pore space by both swelling and mechanical compaction by the applied stress.

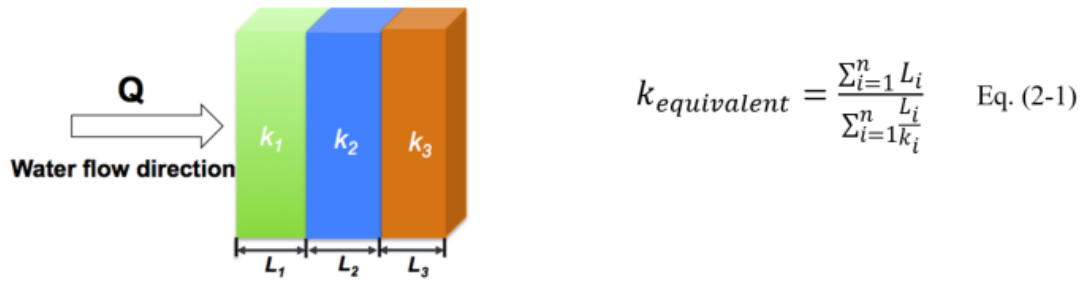


**Figure 2-4.** Schematics of water flow through a multi-layer system including the compacted bentonite and ceramic disc, and the equation used to calculate the equivalent permeability.

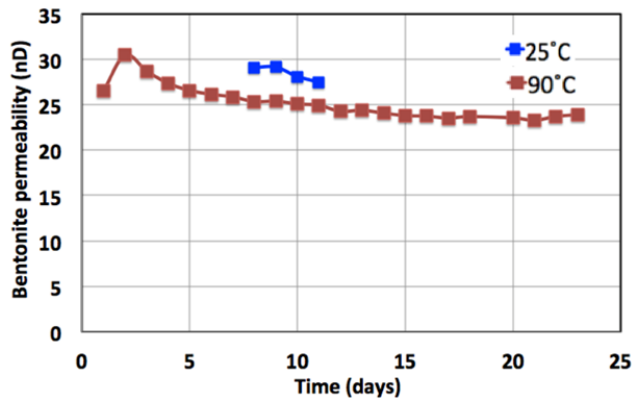


**Figure 2-5.** Bentonite permeability estimated by Eq. (2-1) under 25°C and 90°C.

## 2.2.2 Effluent Water Chemistry

Figure 2-6 presents the concentration of major chemical elements and variations with time in the effluent water measured from the bentonite permeability tests under 25°C and 90°C. The concentrations of Na, Mg, Si and K are higher than those in the injecting water, which can be attributed to the leaching from bentonite after hydration. Temperature changes did not impact the concentrations of Na and Mg, while spike of Si and K concentrations can be observed under 90°C. More detailed analysis, including the chemical compositions of bentonite will be conducted to better understand the observed changes in effluent water chemistry.

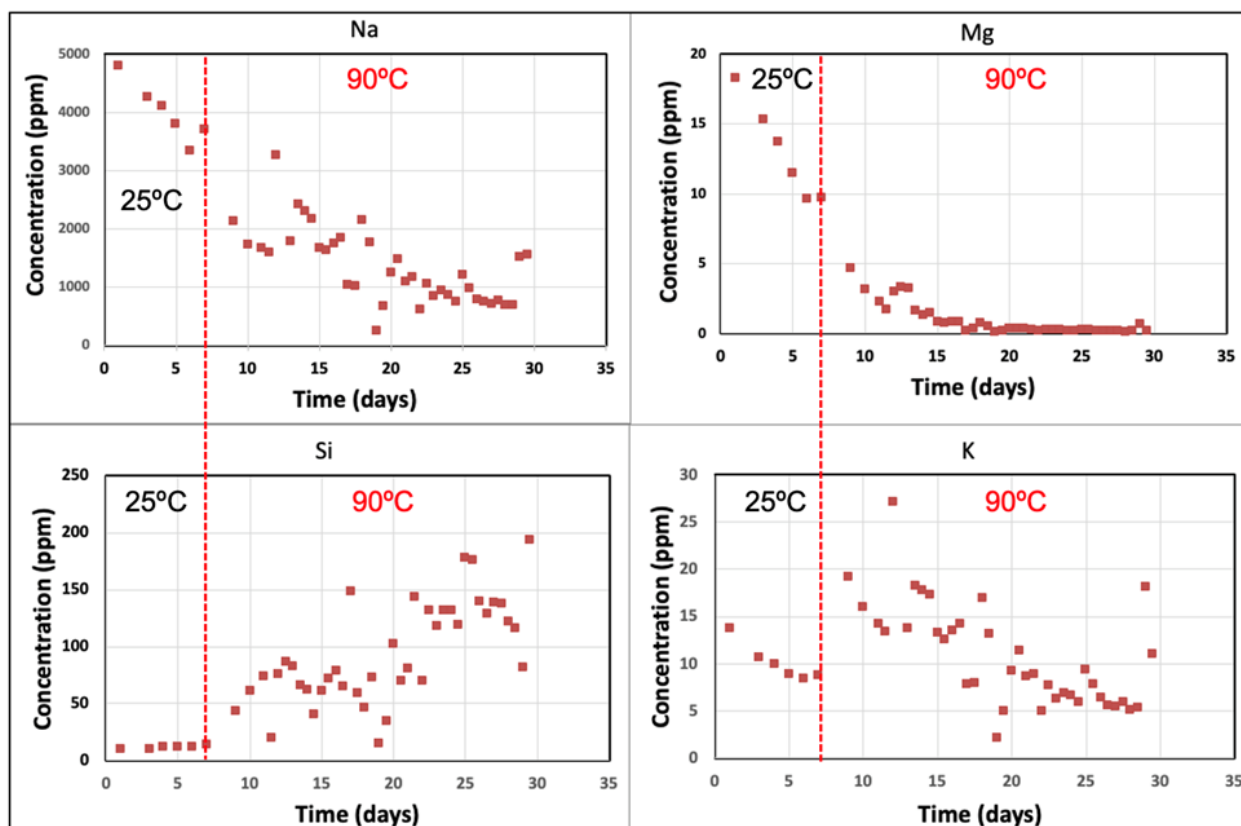


**Figure 2-6.** Effluent water chemistry as a function of time during the bentonite permeability and swelling pressure test. The red dash lines delineate the changes in temperature when water samples were collected.

### 2.3 Fracture Characterization

Using a Grimsel rock core sample, we induced a tensile fracture along the long axis by Brazilian splitting. Figure 2-7(a) is the photograph of the fractured rock sample. We applied a shear offset along the fracture by 2 mm to create an open fracture. The resulting, extruding ends at the top and bottom surfaces were removed by grinding. Figure 2-7(b) is the X-ray CT image showing the fracture and the rock matrix. Figures 2-7 (c) and (d) are the microscope images showing the surface geometry of each half of the sample. Note the roughness (or fracture surface variation) is up to 5.7 mm. We then saturated the fractured sample with brine and measured its permeability under a 725 psi confining stress. A stainless steel hose clamp was used outside of the rubber sleeve to secure the rock sample to avoid any displacement along the fracture during the preparation and the experiment. Figure 2-8 shows the correlation between injected water flow rate and the differential pressure along the sample. The water permeability was calculated to be 156 mD. Assuming the cubic law,  $k_f = a^2/12$ , the fracture hydraulic aperture ( $a$ ) can be estimated from the measured permeability ( $k_f$ ) to be 1.3  $\mu\text{m}$ .

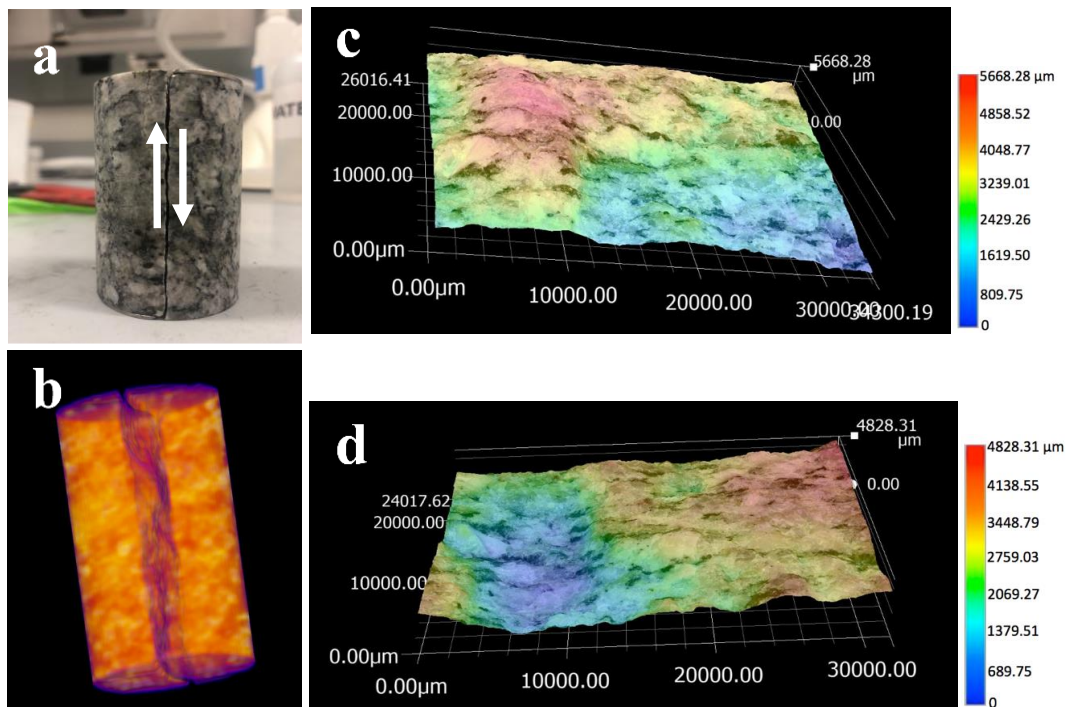


**Figure 2-7.** (a) Photograph of the fractured sample from Brazilian splitting test; (b) CT image of the rock sample and fracture; (c) and (d) are microscope images on the fracture surface geometry.

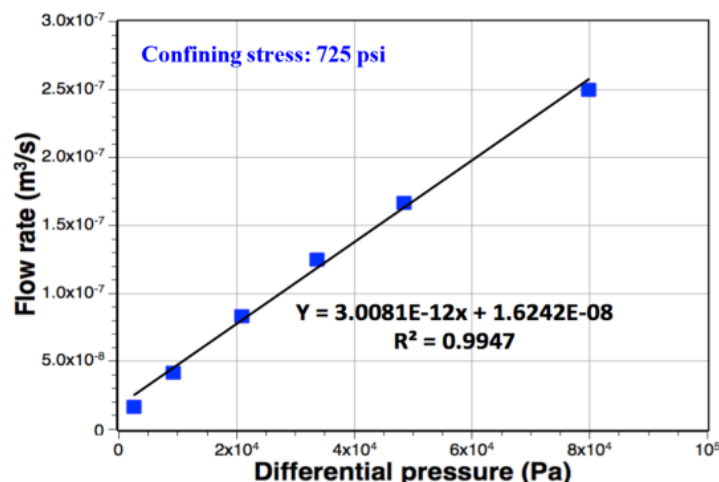


**Figure 2-8.** The relationship of water flow rate vs. differential pressure applied to the fractured sample. The linear equation, shown on the figure, was used to calculate fracture permeability.

## 2.4 Bentonite-Fracture Interactions

### 2.4.1 Permeability Evolutions at 25°C

After detailed characterization of the bentonite and the fractured rock samples, we stacked both in a Viton rubber sleeve, as shown by Figure 2-9. The X-ray CT image (Figure 2-9a) presents how the top ceramic disc, the stainless steel holder and the compacted bentonite, and the fractured rock sample were assembled. A hose clamp was used outside of the rubber sleeve to stabilize the test column. During the experiment, we applied an initial axial stress of 540 psi (3.7 MPa), a confining stress of 725 psi (5 MPa) to the stacked bentonite-rock column, and injected brine from the bottom at 290 psi (2 MPa). During the experiment, the axial stress was adjusted to minimize overall deformation of the system. The blue plot in Figure 2-9(b) shows a graph of the water infiltration rate vs. time during water injection, in which the infiltration rate ranged from  $7.18$  to  $8.84 \times 10^{-5}$  mL/min for 19 days. After 10 days of water injection, water breakthrough was observed at the outlet, resulting in a relatively stable infiltration rate afterward. The equivalent permeability of the stacked system was calculated from the applied differential water pressure and infiltration rate, as shown by the green squares and a line in Figure 2-9(b). Using Eq. (2-1) and permeability of the ceramic disc and bentonite, the fractured rock permeability was determined and presented in Figure 2-9(c). The average permeability of the stacked column and the fractured rock sample are 85 nD and 0.45  $\mu$ D, respectively.

The calculated permeability of the fractured rock sample in this experiment (0.45  $\mu$ D) is over 5 orders of magnitude lower than the previously calculated permeability of the fractured sample without an adjacent bentonite layer (156 mD), indicating considerable bentonite particle migration into the open fracture and clogging of the flow pathway. The measured fracture rock permeability is similar to the rock matrix permeability. As shown in Figure 2-9(c), under the same confining stress (725 psi), the measured rock

matrix permeability was  $0.31 \mu\text{D}$ . The fractured rock permeability is close to the matrix permeability, indicating the sealing of fracture after bentonite hydration and swelling.

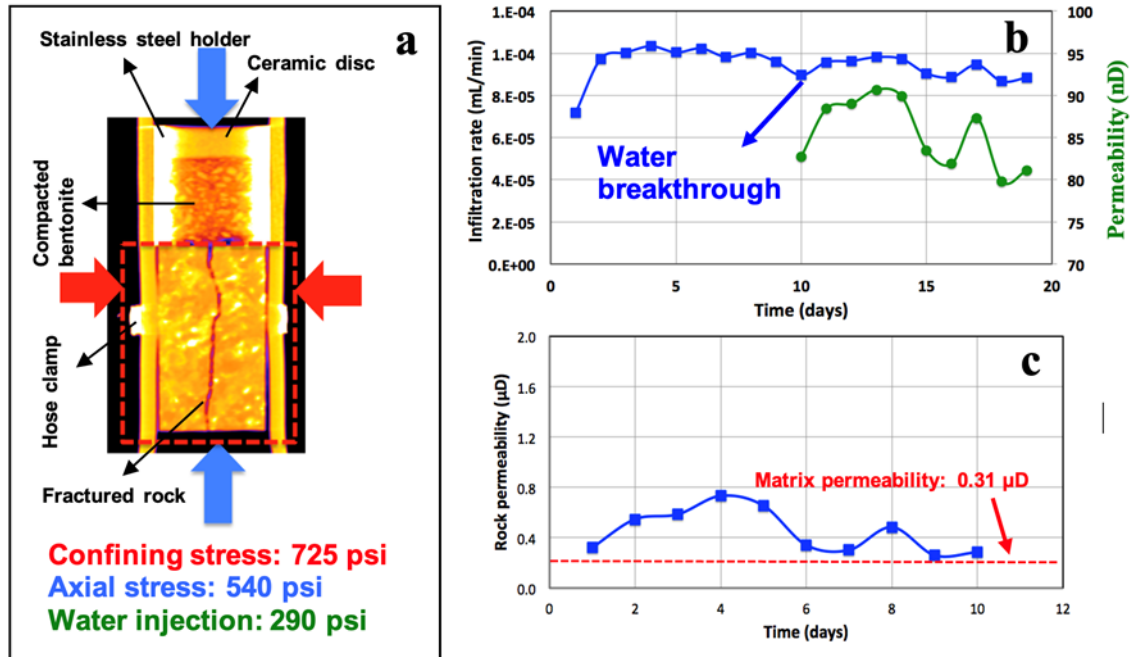


**Figure 2-9.** (a) The CT image showing the stacked bentonite-rock settings and applied stress conditions during the water flow through test; (b) Water infiltration rate vs. time measured during water injection at 290 psi, and permeability variations of the stacked system; (c) The permeability of the fractured sample calculated from Eq. (2-1) and comparison with intact core permeability measured under the same stress conditions.

## 2.4.2 Permeability Evolution at $90^\circ\text{C}$

After the experiment on stacked bentonite with the rough rock fracture, we increased the system temperature up to  $90^\circ\text{C}$  without dismantling or rebuilding the sample and investigated the thermal impact on the permeability evolution. We maintained the sample water injection pressure of 290 psi, the same confining and axial stress. Figure 2-10(a) shows the water infiltration rate as a function of time under  $90^\circ\text{C}$ , and Figure 2-10(b) compares the column permeability under  $90^\circ\text{C}$  vs.  $25^\circ\text{C}$ . Once heated, the water infiltration rate spiked up to  $4.3 \times 10^{-4}$  mL/min and then gradually decreased and stabilized at  $3.0 \times 10^{-4}$  mL/min. The corresponding column permeability decreased from 140 nD to 100 nD.

It is noted in Figure 2-10(b) that the column permeability measured under  $90^\circ\text{C}$  is higher than the value of  $\sim 85$  nD measured under  $25^\circ\text{C}$ . The bentonite permeability measured with confined boundaries in Section 2.2, i.e., without rock fracture indicate small impact from the elevated temperature. After heating, bentonite sealing performance of bentonite in the stacked system involving a rock fracture seems to be compromised.

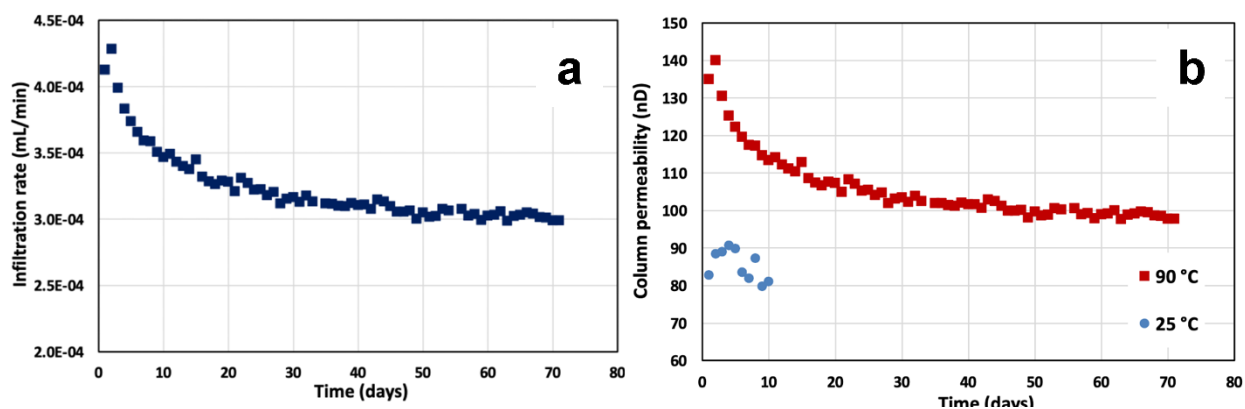


Figure 2-10. (a) Water infiltration rate measured from the stacked column tests under 90°C and (b) comparison of column permeability measured at 25°C and 90°C.

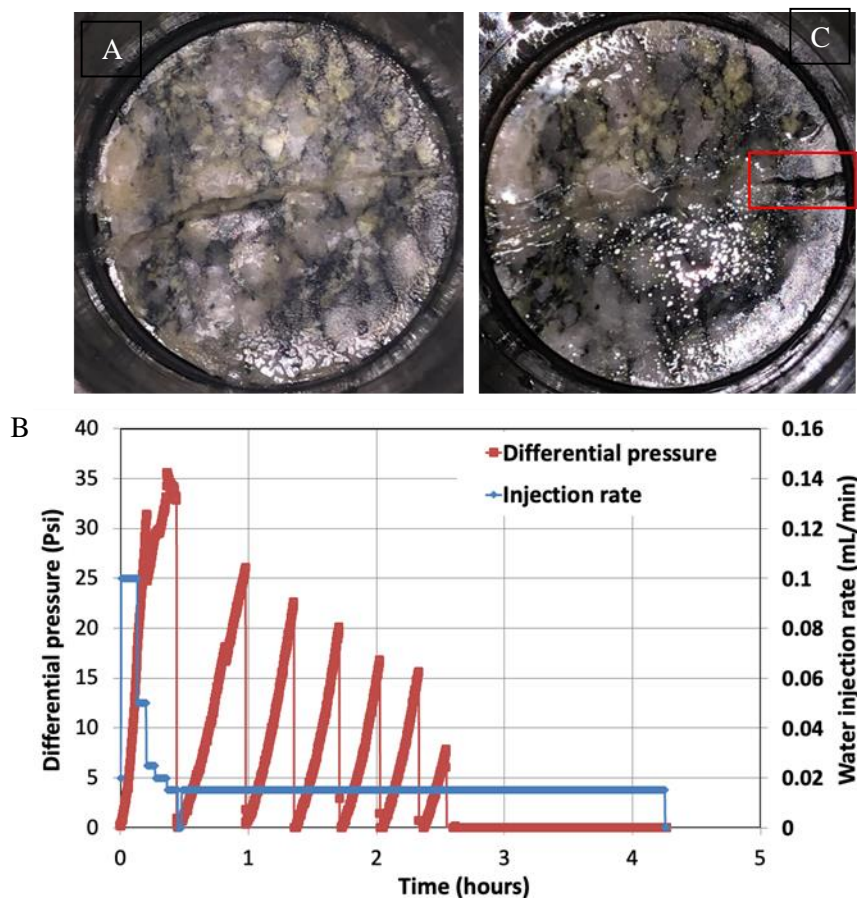
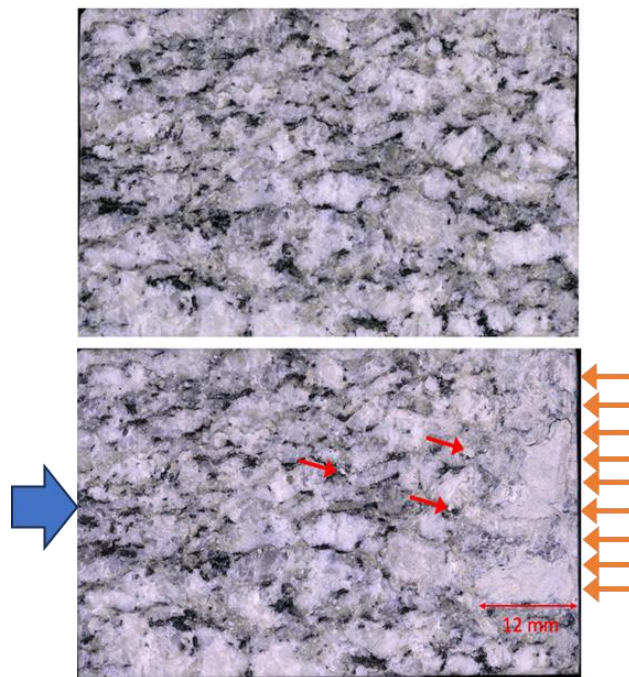


Figure 2-11. (a) Photograph of the fractured rock sample after the experiment; (b) Pressure and flow rate of water injection in the clogged rock sample; (c) Photograph of the rock sample after water breakthrough.

After the experiment, we recovered the rock samples, and Figure 2-11(a) is photograph of the fracture and rock surface in contact with bentonite, showing clearly that fracture surface was completely clogged by bentonite. We then injected water from 0.015 to 0.1 mL/min to the clogged rock sample under the axial stress of 540 psi (3.7 MPa), confining stress of 725 psi (5 MPa), and room temperature. Figure 2-11(b) presents the injection flow rate and a corresponding differential pressure between the inlet and outlet of the sample. Initially the clogged fracture held up to 35 psi differential pressure, which then dropped to zero quickly. The fracture then appeared to reseal, with the differential pressure building up to 25 psi again after ~0.5 hours as water injection continued, followed by another quick pressure release. After 7 cycles the differential pressure was close to zero (limited by the pressure gauge resolution at low pressures) indicating a cleared flow path for water was created. Figure 2-11(c) shows photograph of the rock sample after the water breakthrough test and depicts the clean open fracture zone (marked by the red box) and removal of bentonite particles.



**Figure 2-12.** Microscope image of the fracture surface: (a) before and (b) after the water flow through test in stacked bentonite-rock fracture column. In (b), the blue arrow indicates the water flow direction under 290 psi and orange arrows indicate the bentonite swelling direction.

Figure 2-12 compares the microscope images of the 2D rock surface along the long axis (a) before and (b) after the stacked column test. In Figure 2-12(b), the blue arrow indicates the water flow direction under 290 psi and orange arrows indicate the bentonite swelling direction. The swelling of bentonite can surpass the water pressure and invaded fracture up to 1.2 cm. Some particles can be seen almost half deep into the fracture; however, these scattered particles may not contribute much to the fracture permeability reduction. The majority of permeability reduction could be attributed to the clogging at the fracture entrance and ~1 mm deep into the fracture.

### 2.4.3 Effluent Water Chemistry in Stacked Bentonite-Rock System

Figure 2-13 depicts the temporal trends of major chemical elements in the effluent water measured from the stacked bentonite-rock tests under 25°C and 90°C. Overall, the concentrations of Na, Mg, Si and K decreased with time, which was not likely impacted by the temperature change.

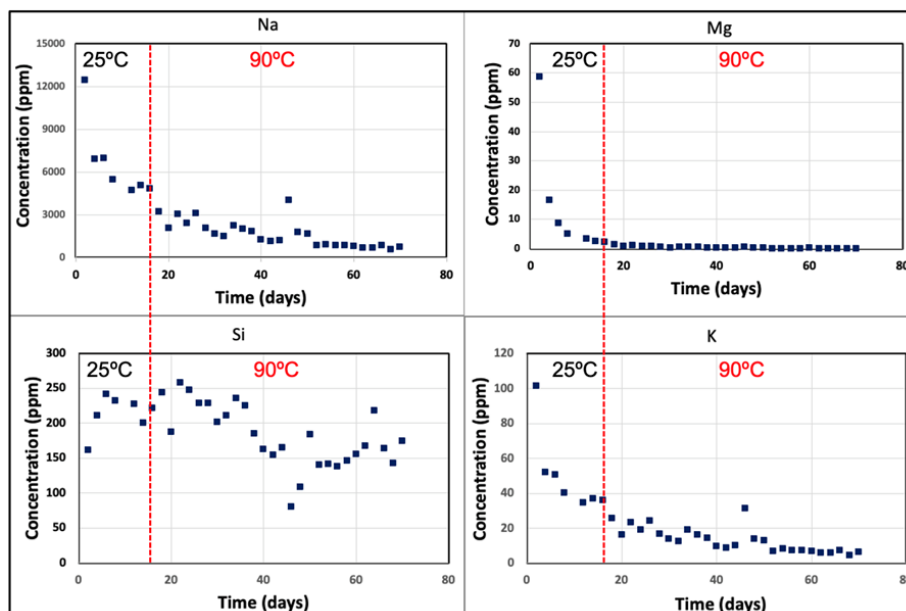


**Figure 2-13.** The concentration of major elements in the effluent water as a function of time and temperature.

## 2.5 Bentonite-Flat Fracture Tests

We have shown in Section 2.4 the clogging of tight and rough fracture and permeability reduction by bentonite swelling and particle migration. We also showed an increase of permeability of the stacked bentonite-rock fracture under elevated temperature, indicating potential compromised performance of bentonite buffer in the presence of a fracture. In this section, we further investigate the bentonite-fracture interactions and potential impacts of fracture on bentonite performance by including a wide and flat fracture in the stacked system.

We first fabricated two chip samples from the rock block from Grimsel granite, as shown in Figure 2-14. The two rock chips have very flat surface and are 5 cm long, 2.5 cm wide and 0.5 cm thick. A custom sample holder was designed and manufactured for the experiment.

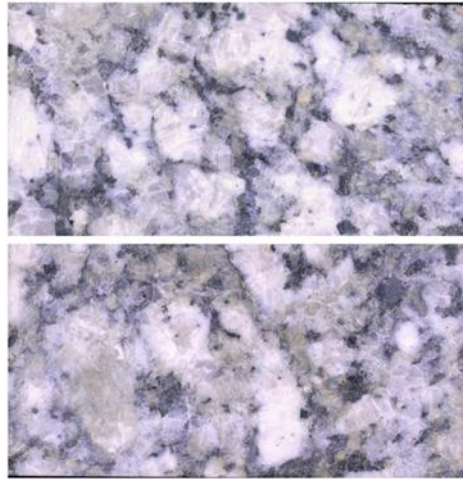


**Figure 2-14.** Photographs of the rock chip samples used for stacked bentonite-flat fracture tests.

### 2.5.1 Fracture Sample Holder and a Testing System

Figure 2-15 shows a new sample holder and its emplacement in the triaxial loading system. The sample holder is composed of a stainless-steel cylinder (3.81 cm diameter and 5 cm long) with an internal cuboid slot, so that the two rock discs can be inserted (shown on image #3 in Figure 2-15). There are two 1/16 inch hemi-circle grooves fabricated so that two rubber sleeves can be inserted, establishing a gap of 1.5 mm between the two rock discs. Two stainless steel plates were inserted between the sample holder wall and the rock discs so that rock discs were pushed against the rubber sleeves. On top and below the holder, two slit discs (images #2 and #4 in Figure 2-15) were assembled with the holder using two bolt threads, leaving a 3 mm wide slot to allow for bentonite intrusion and water flow. Before the experiment, the slot in the top disc was filled with granulated bentonite and powder, then the fracture sample holder was stacked with compacted bentonite on top (image #1 in Figure 2-15). The bentonite was compacted with the same initial dry density (1.45 g/cm<sup>3</sup>) and initial water content (5%) in Sections 2.2 and 2.4.

During the experiment, a 1,000-psi axial stress was applied to compress bentonite against the fracture. Additional 500 psi confining stress was applied to the system, allowing for water flow through both the fracture and compacted bentonite (see the schematic images of the loading system in Figure 2-15). A small water inject rate was used initially to hydrate the bentonite. Once the pressure was built up, water injection pressure was maintained constantly at 290 psi. The water infiltration rate, LVDT and loading cell readings were monitored.

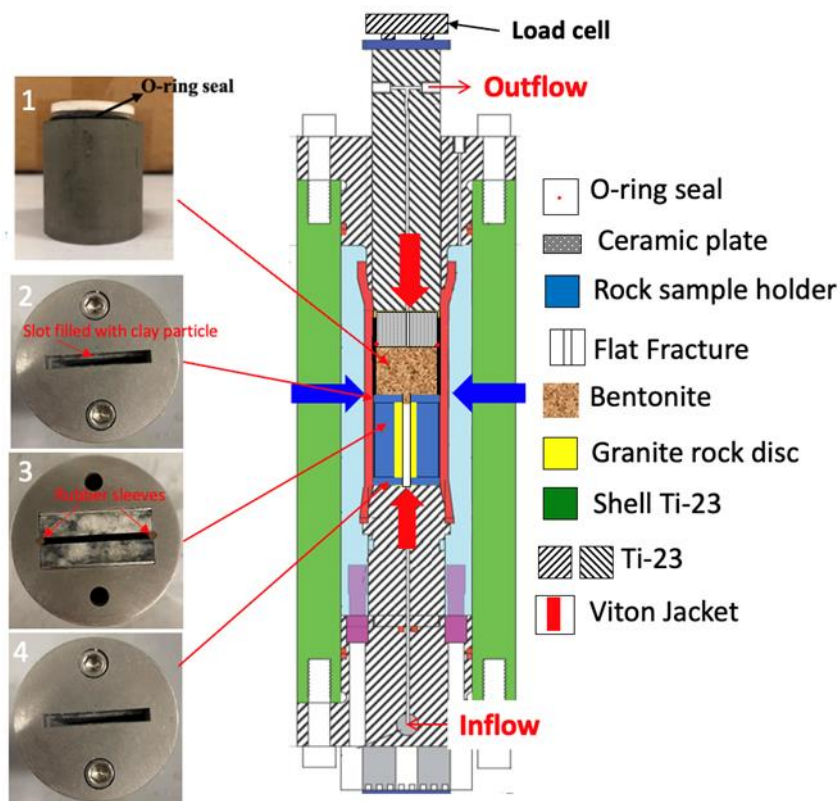


**Figure 2-15.** Photograph of the new sample holder and schematic of the settings for stacked bentonite-flat fracture tests.

### 2.5.2 Infiltration Rate Evolution at 25°C

Figure 2-16 depicts the water infiltration rate after water breakthrough of the effluent as a function of time under 25°C. Results from two tests are presented, including bentonite stacked with the wide and flat fracture (this test, blue triangles) and bentonite stacked with the tight (1.3  $\mu\text{m}$  aperture) and a rough fracture, described in Section 2.4 (red squares). The water infiltration rate varied from 1 to  $1.4 \times 10^{-4}$  mL/min in the flat fracture test, higher than the tests stacked with a tight and rough fracture at  $\sim 9 \times 10^{-5}$  mL/min. The blue dash line indicates the predicated water flux based on bentonite and ceramic permeabilities (given in Section 2.2), which is close to the measured water infiltration rate from bentonite stacked with a tight and rough fracture. In this case, the compact bentonite performs favorably to seal the fracture while maintaining the geometry integrity and buffer performance. By comparison, the increased water infiltration rate in bentonite stacked with the 1.5 mm wide and flat fracture indicates pronouncedly the compromised bentonite performance. The big fracture provided some extra space for bentonite swelling, the ‘leakage’ of compacted bentonite into a large fracture, which deteriorated the integrity of a bentonite buffer because of loss of materials and swelling capability.

The two experiments clearly showed the limitation of a bentonite buffer in sealing fracture after hydration, which may be critically important for the evaluation of the EBS performance in nuclear waste repositories. While sealing of small fractures (e.g., microscale cracks) by bentonite swelling is applaudable, the presence of large fractures (mm-scale fracture) at the EDZ-EBS interface could be a threat to the buffer performance,

which need to be well assessed, managed, and plugged. The current results may help optimization of the engineering design of bentonite properties, installation techniques, and a repository design to maximize its sealing efficiency.

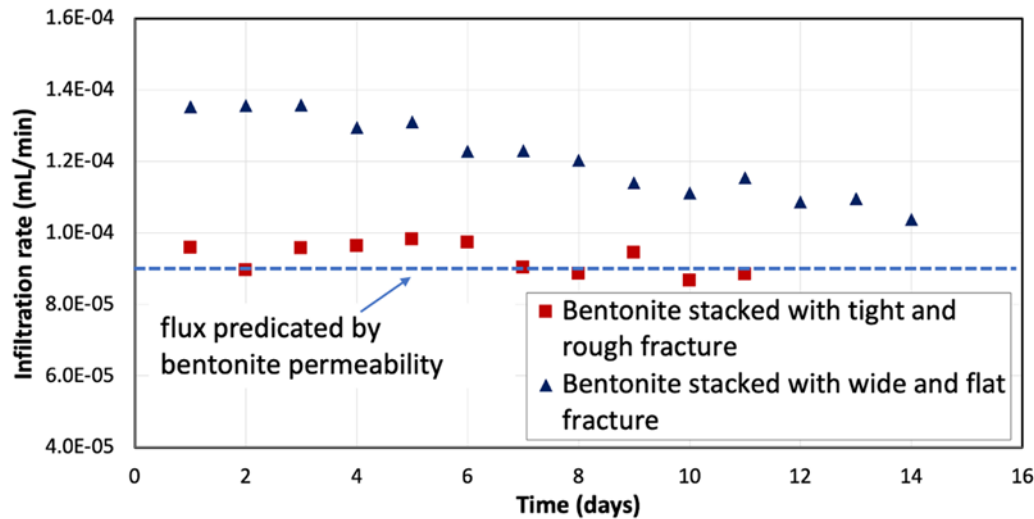


**Figure 2-16.** Water infiltration rate vs. time obtained from experiments on bentonite stacked with tight and rough fracture (red square) and bentonite stacked with wide and flat fracture.

## 2.6 Conclusions

In FY23, we modified the dedicated twin-cell triaxial loading system so that it could be used for (1) bentonite sample characterization, including determination of permeability and a swelling pressure, and (2) investigations of the bentonite-rock interaction and a fracture permeability evolution. Two sets of experiments on bentonite stacked with tight and rough fracture were completed under ambient (room) and elevated temperature. The water infiltration rate was monitored for permeability evolution. Under ambient temperature, the fracture permeability was reduced over 5 orders of magnitude. Images of the fracture surface showed that hydration caused considerable bentonite particle migration and fracture clogging due to swelling. It was shown that calculated permeability of stacked bentonite-fracture system was close to measured bentonite permeability, indicating that bentonite could maintain good sealing characteristics in the presence of tight (1.3  $\mu\text{m}$  aperture) and rough fracture. After heating of the system to 90°C, a 65% increase in stacked column permeability was observed, indicating that the bentonite sealing capability was compromised.

We also fabricated a new rock sample holder, which can be applied to the loading system for testing bentonite-fracture interactions with well-controlled surface geometry and aperture. We used a flat 1.5 mm aperture fracture, stacked with the bentonite, and investigated the water infiltration rate under ambient temperature. Comparison to the bentonite stacked with a tight and rough fracture showed that water infiltration rate in bentonite stacked to a 1.5 mm fracture is 20-50% higher. The presence of a large fracture provided extra space for bentonite swelling and deteriorated the integrity of bentonite buffer geometry and its sealing capability.

New experiments are on-going under 90°C to further investigate the temperature impact on the water infiltration rate in bentonite stacked with a large fracture and its buffering capability. After the experiment, the fracture and bentonite sample will be recovered, fracture permeability will be measured independently, and additional post-experiment measurements will be carried out to assess the fracture surface geometry and a bentonite particle distribution. We also plan to investigate the impact of injected water chemistry on bentonite swelling, bentonite particle migration and clogging, and water infiltration rates in the stacked system.

## 3.0 DOWNHOLE CHARACTERIZATION OF STRESS AND FRACTURES IN CRYSTALLINE ROCKS

### 3.1 Introduction

Crystalline rock is one of several potential geologic environments that have been considered for long-term disposal of nuclear waste due to their inherent low permeability. One key challenge in evaluating the safety case for crystalline rock is that fractures present within these rocks may serve as transmissive pathways for radionuclide transport. The 2019 update to the SFWST research and development (R&D) roadmap (Servougian et al., 2019) identified that improved site characterization techniques are needed for investigations of crystalline repository systems, especially to characterize fractures and their hydrogeologic properties. Such data are needed to develop accurate DFN models, which have also been used to model fluid flow for enhanced geothermal systems and evaluate the potential for leakage from geologic CO<sub>2</sub> sequestration sites.

In FY20, we have conducted three SIMFIP tests in 2.4 m long sealed sections at 485.2, 505.9 and 515.1 m depths in the COSC-1 borehole that was drilled through foliated and fractured metamorphic rocks of the COSC. Focus was to investigate *in-situ* the role of discontinuities on the hydromechanical performance of a crystalline rock at a depth analogue to a repository host rock by conducting direct and coupled measurements of borehole pressure, injection flowrates and fractures three-dimensional displacements. In FY21, we conducted the COSC-1 experiments to characterize the *in-situ* stress tensor. The local state of stress and fracture permeability variation were directly estimated in response to mechanical opening and shear monitored in the field. We developed a method to calculate the stress heterogeneity in a fracture network by using a profile of SIMFIP hydromechanical tests. Indeed, the orientation of the vectors measured by a SIMFIP sensor reflects well the true orientation of the activated fracture's movement that can be used to estimate the orientation and magnitude of the stress tensor. We showed that profiling SIMFIP tests along a borehole allows for estimating the stress heterogeneity along a borehole. Further analysis suggested that significant stress variations relate to the contrasted borehole geology, i.e., intact rock, crosscut by one single fracture or by a fracture zone. In details, our modeling results suggest that there may be a link between (i) stress concentrations and the size of the minimum block volume in a fractured zone, and (ii) stress dissipation and fracture stiffness.

In FY21 and FY22, we continued exploring how to input these observed *in-situ* fracture responses into generic fracture network models of the host rock close and away from the repository tunnels. We first developed a new approach to *in-situ* estimate fractured rock elastic properties from SIMFIP measurements, as well as the link between these elastic properties and the development of stress heterogeneity within a fractured hard rock. We compared these observations with published data from the Forsmark site, which is located within the same type of fractured crystalline rock. We showed how fractures with the same elastic stiffness but with a different orientation experience a highly contrasted response to an elastic loading. This generates stress and strain gradients at intersections between fractures that may favor flow paths developments. Comparison with other field data also allowed for evaluating the uncertainties associated with the SIMFIP borehole estimations. One result is that the SIMFIP approach may offer a reasonable *in-situ* estimate of fractured hard rock elastic properties at the multimeter scale. Another key result is that elastic dilatant shear allows for flow in initially closed fractures below the breakdown pressure. Second, we explored the potential links between stress heterogeneity and flow channeling in generic fracture networks close and away from a nuclear disposal drift in crystalline rock. We used the fracture network geology from the COSC-1 borehole as well as the local stress and fractures properties estimations from the SIMFIP tests to propagate the stress variations to the fracture network scale. We considered a fully saturated hydromechanical undrained model with and without a horizontal tunnel excavated at a depth of 500 m. We

explored the link between stress heterogeneity and flow at the fracture network scale. We analyzed how natural stress perturbations superimpose to the stress re-distribution around the drift configuration. We highlighted the development of low stress zones generated by strain/displacement gradients developing on interacting fractures. We showed how information on fractures displacement versus pressure analyzed from the *in-situ* SIMFIP tests may help suggesting scenarios for the development of potential leakage flow paths extending several tunnels' diameters away. We calculated that such scenarios may occur under "limited" stress variations of a few mega-pascals. We suggested that, given their relatively low magnitude, these stress and strain gradients developing on fractures may not only occur following a gallery excavation phase, but be active during the lifetime of repository site. Indeed, thermal heating of the gallery walls or remote impacts related to climate changes may, for example, be sufficient to vary these gradients, and, thus, drive the potentially long-term evolution of leakage flow paths. We suggested that such effects may produce significant thermo-poro-elastic response of fractures and eventual fractures creep.

In FY23, we first conducted research on evaluating how borehole three-dimensional displacements help better constrain the local full stress tensor (i.e., the three principal stresses orientations and magnitudes) in a borehole. We show that displacements measurements give information on rock behavior that, in other techniques, is unknown and requires the application of simplifying assumptions, which are often not satisfied. The full stress tensor can be characterized by one SIMFIP test, which is not the case of the usual hydrofracturing (HF) methods, which rely on combinations of datasets obtained at multiple depths. Therefore, we conducted a series of tests along one borehole designed to estimate the local stress heterogeneity. Based on the COSC-1 tests, we estimated a 10-to-20° and a 2-to-14 MPa variations in principal stresses orientations and magnitudes.

Secondly, we have worked on relating the variability between tests to fracture heterogeneity while the classical methods rely on assumptions of homogeneity and linear increase of the *in-situ* stress with depth, conditions unlikely to be met in fractured crystalline rocks. This work required some additional fully coupled hydromechanical modeling to conduct a solid sensitivity study to model parameters previously used in FY21 and FY22. In detail, we made borehole nearfield models to analyze the borehole displacements versus pressure and estimate some elastic properties of the intact rock and of the fractures. Then, we made larger models to analyze the transient evolution of fractures pore pressure and displacements during the entire testing sequence. We suggest a conceptual spatial-temporal evolution of crystalline rock hydromechanical properties evolution during the growth of a macro-fracture from the borehole near field to deeper in the host rock.

Finally, we present some preliminary results of creep triggered on a secondary fault affecting a gabbro formation at 68 m depth in a new experimental borehole deployed in the San Andreas fault area (San Juan Bautista, CA). The interesting point is that creep was triggered by earthquakes distant from the instrumented fault. These new data are relevant to address the concern that seismic events on faults close or even distant to a repository site may induce secondary fracture shear movements across canister positions. Moreover, these new data bring insights on weak loadings that could impact stress and strain gradients developing on fractures during the lifetime of a repository site.

### **3.2 Three-Dimensional Displacement Measurements in a Deep Borehole in Scandinavian Caledonides**

Three-dimensional borehole displacement measurements were carried out to explore the interplay between the geological structures and stress at ~500m depth in the COSC-1 borehole drilled into foliated high-grade metamorphic rock located in the central Scandinavian Caledonides (Figure 3-1). This is the first time that the SIMFIP method, which allows for simultaneous and continuous measurement of borehole fracture displacement during a high-pressure fluid injection, was used at such significant borehole depth. Three contrasting borehole sections were investigated, namely an intact rock section, a section intersected by a flowing fracture and a section intersected by a non-flowing fracture. In the experimental procedure, an

injection borehole section sealed by inflatable packers is pressurized until a micrometer scale borehole movement is triggered. Mainly normal opening of fractures is observed at the early stages, followed by increasing shearing with repeated activation cycles as the tests proceed (Figure 3-2). Analyses of downhole pressure and fracture slip with an inversion method allows estimation of the full stress tensor, whose orientation is reasonably consistent with the  $N120^\circ$  maximum horizontal stress trend deduced from borehole breakout analyses at greater depths in the same borehole. Finally, we show that natural fractures induce a variation of stress orientation and magnitude of 10-to- $20^\circ$  and 2-to-14MPa between tests, which may significantly affect the shallow crustal stress and hydrogeology (Table 3-1).

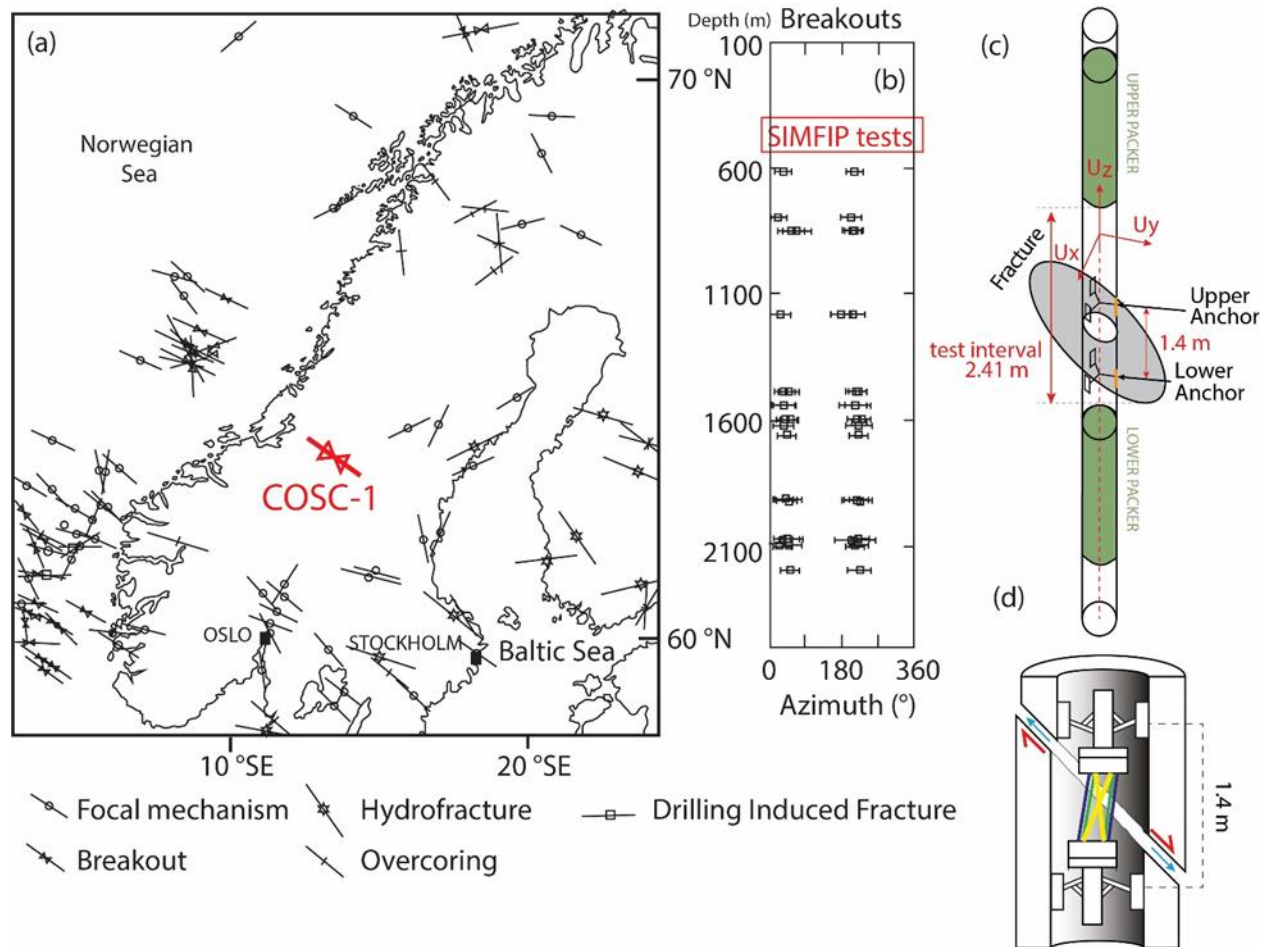


**Figure 3-1.** Location of the COSC-1 borehole on (a) the World Stress Map (WSM) of Fennoscandia (stress indicators from the WSM after Heidbach et al., 2008). (b) Schematic location of the SIMFIP tests on the COSC-1 borehole log of breakouts mapped by Wenning et al. (2017). (c) SIMFIP probe deployed at COSC-1 (d) Details of the SIMFIP cage.

Figure 3-2 shows a synthesis of the observed borehole displacements variations common to all the three tested intervals in COSC-1 borehole. Displacements are related to the injection pressure and to the amount of water leakage into the stimulated fractures. Indeed, during each test, the protocol involved repeated low-to-high pressure cycles, associated with a progressive increase in the cumulated volume of water injected in the fractures with time in repeated cycles (see Figure 3-4 for the intact rock test). At low injection pressures, there was the  $(80-150) \cdot 10^{-6}$  m horizontal chamber wall displacement in all the tests. In the intact rock, this displacement was preceding the fracture initiation at 16.7MPa. In the other tests, it was observed below 8.5-to-10.0 MPa, mainly during the first cycle when little injection water is leaking into the preexisting natural fracture(s). This horizontal displacement is related to the transversal elongation of the rock associated with the axial shortening of the borehole pressurized section sealed between the two SIMFIP packers (Figure 3-2). At high injection pressures and low injected water volume, water leakage into the formation is characterized by a dominant vertical displacement. This was observed during the short duration constant flowrate tests in the intact rock where a progressive transition from sub-horizontal to vertical displacements was observed (Figure 3-2c-d). At the fracture breakout of 16.7 MPa, displacements were still mainly horizontal, but they progressively turn to sub-vertical during the following reopening cycles. This is in good agreement with the creation and reopening of the flat-lying fracture observed on borehole acoustic log after the test (Figure 3-2c-d). In the two initially fractured intervals, displacements rotate to a sub-vertical direction for pressure between 8.5 and 14.4 MPa. It should be noted that the displacement vectors are not exactly perpendicular to the fracture planes in all three tests, indicating a minor shear component during this activation period characterized by a low injection water volume (see Figure 3-4b for ex.). This shows that fracture reactivation is dominated by a mode 1 opening during this period (Figure 3-2c-d). At high injection pressure and after significant water flow into the fractures, an increasing reverse shear component was developed on the stimulated fractures. This occurs at about the same pressure of 13.5-to-14.4 MPa in all three tests. In the intact rock case, this happens when the fluid-driven hydrofracture has grown large enough to behave in the same way as the natural fractures stimulated in the other two tests (Figure 3-2e). This shows that as the fracture stimulated patch volume is increasing with time and with the amount of injected fluid, the activation mode evolves from mode 1 to the mixed mode, with the fracture hydromechanical development being more dependent on the far-field stress tensor.

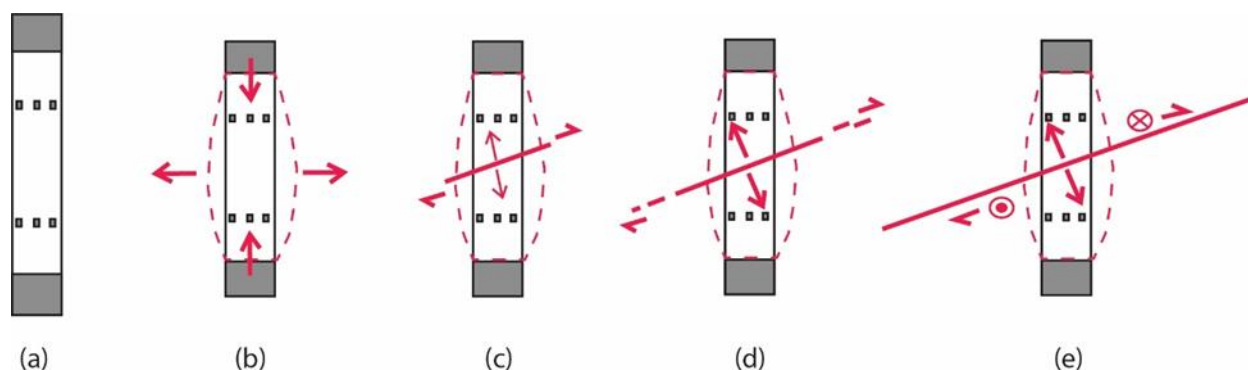


**Figure 3-2.** Synthesis of the observed fracture activation mechanisms. (a) Pre-test status of the SIMFIP double packers sealed borehole interval. (b) Reversible interval response below the breakout pressure. (c) and (d) Fracture initiation at breakout pressure and during the following reopening pressure cycles. (e) Fracture slip after several stimulation cycles.

The stress state is computed following the protocols on dislocation analysis during fluid injection and its application to stress inversion. The protocol uses: (a) the SIMFIP displacement vectors, (b) an estimation of the activated fracture normal stress based on the measured injection pressure and (c) an estimation of the vertical stress calculated at the test depth using the density log. We project the measured displacement vector on the activated fracture plane that is given by borehole acoustic logging. We considered that the measured displacement has a slip and a component normal to the fracture plane or a dilation component. The dilation is considered to not affect the orientation of the slip, and consequently, not affecting the orientations and magnitudes of the *in-situ* stress state during the inversion. The results are characterized by a 10-to-20° and by a 2-to-14 MPa variations in principal stresses orientations and magnitudes (Table 3-1). Typical ranges of uncertainties in stress magnitude and orientation given by classical HF methods are tens of MPa and 5° to 20°, respectively. The full stress tensor can be characterized by one SIMFIP test, which is not the case of the usual methods, which rely on combinations of datasets obtained at multiple depths. In addition, the SIMFIP clearly shows a variability between tests that relates to fracture heterogeneity while the usual methods rely on assumptions of homogeneity and linear increase of the *in-situ* stress with depth, conditions unlikely to be met in fractured crystalline rocks.

**Table 3-1.** Summary of stress estimations.

Test Nbr. [Depth]	Vector	$\sigma_1$		$\sigma_2$		$\sigma_3$		$\sigma_v$	Activated fault		Slip		Pressure
		<i>dd/d</i>	<i>MPa</i>	<i>dd/d</i>	<i>MPa</i>	<i>dd/d</i>	<i>MPa</i>		<i>MPa</i>	<i>dd</i>	<i>d</i>	<i>dd/d</i>	
1 [484 486.4]	EF	252/10	42.1	352/46	12.6	153/43	12.3	13.3	247	13	71/ -13	TF	16.7
	JK	234/10	44.4	324/5	16.6	77/79	12.4				44/ -12	TF	14.2
	PQ	246/10	42.2	5/71	12.5	153/17	12.0				60/ -13	TF	17.4
	QR	255/9	38.6	163/13	34.9	19/74	11.0				138/ -5	TF	17.2
	VW	299/44	16.4	206/2	13.4	114/47	10.6				-59/ 8	N	16.4
	A1B1	279/19	32.9	11/7	32.7	121/70	10.7				-13/ -3	TF	13.5
2 [513.9 516.3]	UV <sub>1</sub>	349/38	20.4	252/9	16.3	150/51	10.2	14.1	270	10	-17/3	N	14.4
	UV <sub>2</sub>	319/4	16.4	50/20	15.4	217/70	14.0		110	59	-17/ -45	TF	14.4
	UV <sub>3</sub>	285/10	25.0	17/8	18.0	130/75	12.0		270 110	10 59	-17/3 17/45	N TF	14.4
3 [503.7 506.2]	NO	235/51	14.9	335/8	13.9	70/38	12.9	13.8	288	12	-118/ 9	N	13.5
	NO	292/9	28.6	24/11	16.8	163/77	13.8				63/ -9	TF	13.5

(*dd* – dip direction; *d* – dip; TF – Thrust Fault; N – Normal Fault)

### 3.3 Deep Borehole Observations and Modeling of Crystalline Rock Hydromechanical Property Evolution During the Development of a Macro-Fracture

Understanding how initially intact rock properties evolve into fractured-rock properties under pressure is crucial for deep boreholes applications in crystalline rock. Here, we used fully coupled hydro-mechanical numerical code to model borehole displacement, fluid pressure and flow measurements conducted in sections sealed by a double-packer system at an ~500m depth in the COSC-1 borehole drilled into foliated high-grade metamorphic rock (Figure 3-3).

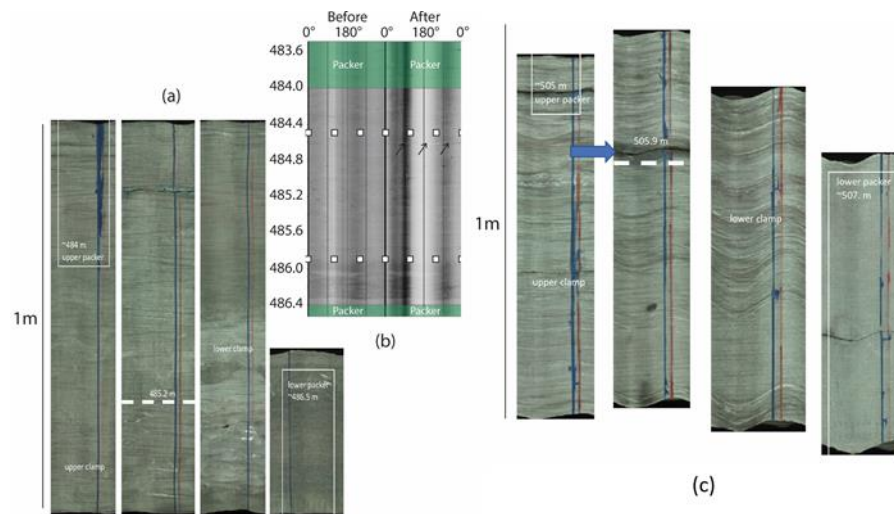


**Figure 3-3.** (a) Intact rock section cores showing foliated metamorphic rock. (b) Acoustic image log of the tests' interval geology before and after the SIMFIP tests (white squares are the locations of the SIMFIP sensor's clamps; black arrows show the main geological structures of the intervals). (c) Open fracture (blue arrow) section cores.

We first considered the axial section displacement measurement versus the section pressure variation during the first seconds-to-minutes until fracturing or fracture re-opening (Figure 3-4a colored sections). Figure 3-4b demonstrates three successive phases of displacement variations in the intact rock section. There is an initial reversible axial contraction followed by irreversible contraction after fracturing pressure and finally axial extension after conducting repeated fracture reopening pressure cycles. It is only during that last phase that water starts leaking into the formation. In the initially fractured section, where fractures are closed, the initial contraction is larger than in the previous case, and larger is the extension associated to the fractures opening. In the initially fractured section with an open fracture, no contraction is observed. A large axial extension correlates with injection pressure. Using the reversible contraction phase, an intact rock bulk modulus is estimated to be  $80 \pm 20$  GPa (Figures 3-5 and 3-6). In the initially fractured section, models show an about 40 GPa decrease of the equivalent fractured rock modulus compared to estimations from the intact rock section. Models that figure the section as continuous blocks bounded by macro-discontinuities give a block modulus of  $40 \pm 10$  GPa, and discontinuities normal and shear stiffness of 30 and 3 GPa/m, respectively. In the initially open fracture section, we get fracture stiffness values that are ten times less than in the closed fractured section.

In a second modeling phase, we consider the evolution of pressure, normal and tangential fracture displacements versus time during the intact and open fracture rock tests duration (Figure 3-7). We find that the fractures properties previously estimated reasonably, can be used to explain the measured transient hydromechanical response (Table 3-2 and Figures 3-8 and 3-9). We show that in addition to elastic properties, a low fracture friction angle or a large deviatoric stress overestimate the measured shear displacements and slightly underestimate the fracture normal opening. Indeed, the best match is when the two tests are modeled with the same state of stress, but with the contrasts in fractures elastic properties deduced from the first modeling phase. In other words, it these results demonstrate that contrasts in fractures properties may induce a heterogeneity in borehole stress. Figure 3-4 shows an example of borehole displacements, fluid and packer pressure and injection flowrate during the test conducted in the initially intact rock section.

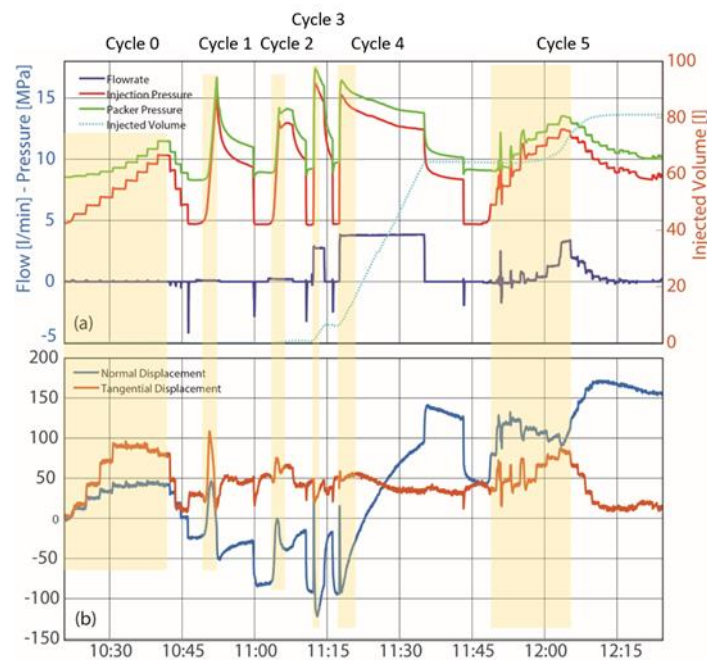


**Figure 3-4.** Evolution of chamber axial displacement during the intact rock HF test. (a) Packer and chamber pressure, injection flowrate and cumulated injected volume. (b) Displacement (in micrometers) normal and tangential to the created fracture (since the fracture is subhorizontal, the normal displacement is taken as the borehole axial displacement).

We developed three-dimensional models of fractures intersecting the three borehole intervals using the distinct element code 3DEC (Figure 3-5 and 3-7). The code was used for a fully coupled hydromechanical analysis of the fracture movement induced by the injections. A small model was first built to study the borehole wall axial displacement versus pressure (Figure 3-5). A larger model was then conducted to study the time evolution of fracture displacements during the entire tests (Figure 3-7). We assume that the complex opening of the fractures observed in the field corresponds to a fault rupture that is described by a generalized Coulomb failure criterion, including the possibility for failure in shear and in tension. The elastic hydromechanical response of the fracture is also included in the numerical model.

Injection of fluid leads to a change of pressure and fluid flow in the stimulated fracture, and consequently, to a change in stress over the fault surface, with a resulting change in aperture. It is assumed that the cubic law can be used to describe fluid flow in the fault:

$$Q = -\frac{b_h^3 \cdot w}{12\mu} \Delta P \quad (3-1)$$

where  $Q$  is the flow rate (m<sup>3</sup>/s),  $\Delta P$  is the increment in fluid pressure (Pa),  $\mu$  is the viscosity of fluid (Pa.s),  $w$  is the fracture width (m), and  $b_h$  is the hydraulic aperture (m), which is defined:

$$b_h = b_{ho} + \frac{\Delta\sigma'_n}{k_n} + \Delta u_s \cdot \tan \psi \quad (3-2)$$

where  $b_{ho}$  (m) is the initial aperture at zero normal stress,  $\Delta\sigma'_n$  is the increment in effective normal stress,  $\Delta u_s$  (m) is the shear slip increment,  $k_n$  is the fracture normal stiffness (GPa/m) and  $\psi$  is the dilation angle (°). Dilation occurs only as the fracture slips. The hydraulic aperture is linked to the fracture permeability as follows:

$$k = \frac{b_h^2}{12} \quad (3-3)$$

Experimental and numerical analyses have showed that the cubic law is adequate to simulate fluid flow and hydromechanical effects along smooth surfaces (Brown, 1989; Zheng et al., 2019).

Numerical simulations of flow are based on the fluid domain network structure, in which each domain has a uniform fluid pressure and can communicate with the neighboring domains. Thus, the fluid flow is governed by the difference in pressure between adjacent domains. At each time step ( $\Delta t$  in seconds), the fluid pressure ( $P$  in Pa) is updated considering the net fluid flow and the domain volume change ( $\Delta V$ ):

$$P = P_0 + K_w Q \frac{\Delta t}{V} - K_w \frac{\Delta V}{V_m} \quad (3-4)$$

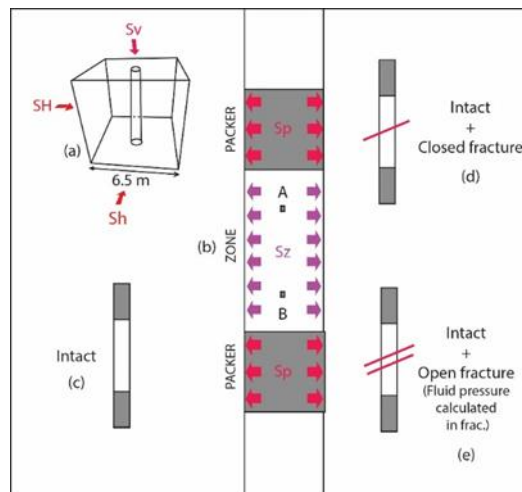
where  $P_0$  is the initial fluid pressure,  $K_w$  (Pa) is the fluid bulk modulus, and  $V_m = (V_t + V_{t-1})/2$  with  $V_{t-1}$  and  $V_t$ , the domain volumes (m<sup>3</sup>) at previous ( $t-1$ ) and new ( $t$ ) times, respectively.

We used two different fluid flow modes to reproduce the observed fluid pressures:

- A variable permeability model (i.e., the cubic law with a value of hydraulic aperture that changes with the evolution of fault normal displacement). This flow model was used to model the initially open fracture, and
- A variable permeability model activated at failure. We use the “crack flow model” implemented in 3DEC to simulate fluid flow in the activated parts (due to local shear or tensile failure) of the fracture plane but prevent flow from occurring in the remaining elastic parts. This assumption is used to model the hydromechanical responses of the initially intact rock interval.

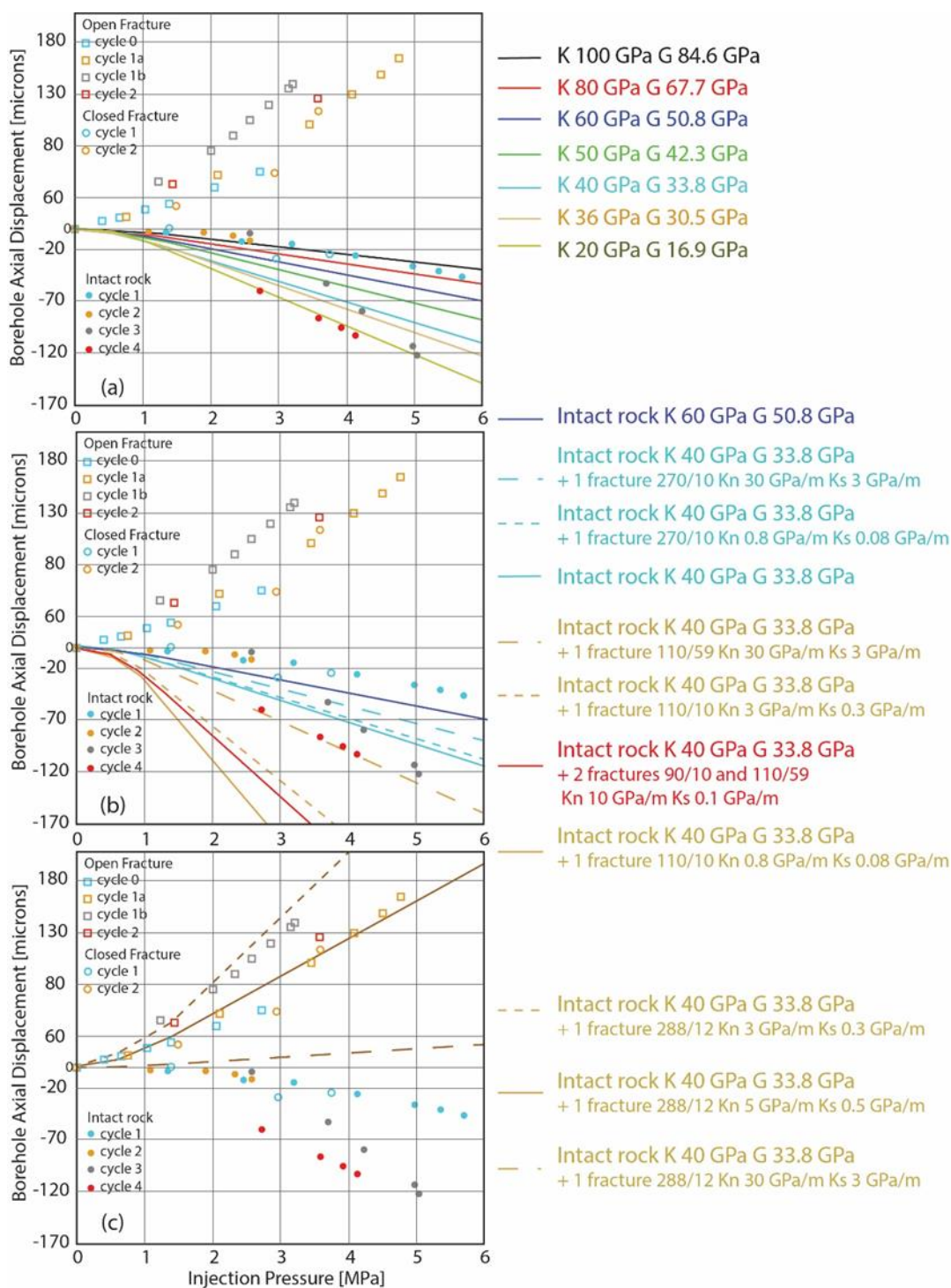
The fracture and intact rock properties used in the model were first estimated using the small borehole nearfield model. The host rock is assumed to be linear elastic. The host rock matrix is considered impermeable. Fracture stiffness  $K_n$ , and  $K_s$  are estimated from matching model results to the initial reversible parts of the measured displacement-vs-pressure curves. An initial hydraulic aperture is given to initiate the model. It is incrementally actuated during calculation iterations. Fracture friction, cohesion and

tensile strength values were adjusted until a best match is observed between calculated and measured displacements. We applied the median stress field estimated in Section 3.2 to all the model' boundaries. In the small model, the injection pressure and the packer pressures were modeled as stress boundary conditions applied to the borehole wall (Figure 3-5). In the large model, the field injection was simulated by applying the injection flowrate at the model's fracture grid point with coordinates (0, 0, 0) (Figure 3-7), which theoretically represents the measured time-history of injection flowrate imposed in each interval during the *in-situ* tests. Using the small model, we compared calculated borehole axial displacements to measured ones (Figure 3-6). In the large model, normal and shear displacements of fractures and pore pressure were calculated at the injection point and compared to field measurements (Figures 3-8 and 3-9). First, the model is run to equilibrium to establish the initial static stress and pressure conditions. Then, the injection flowrate is applied.

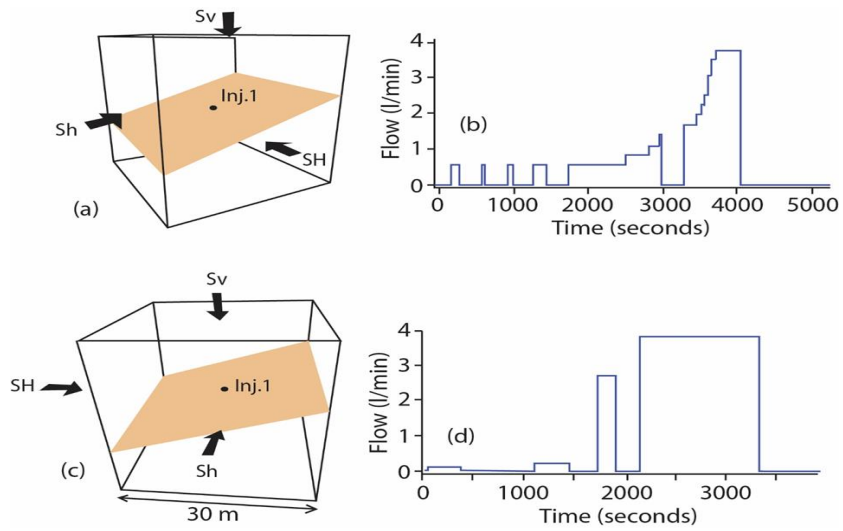


**Figure 3-5.** Small scale 3DEC numerical model used to estimate rock properties from chamber axial displacement versus pressure. (a) Model boundary conditions. (b) Stress boundary conditions applied in the borehole to figure both packer and chamber pressure increase during tests. (c) to (e) different rock geologies considered in models.

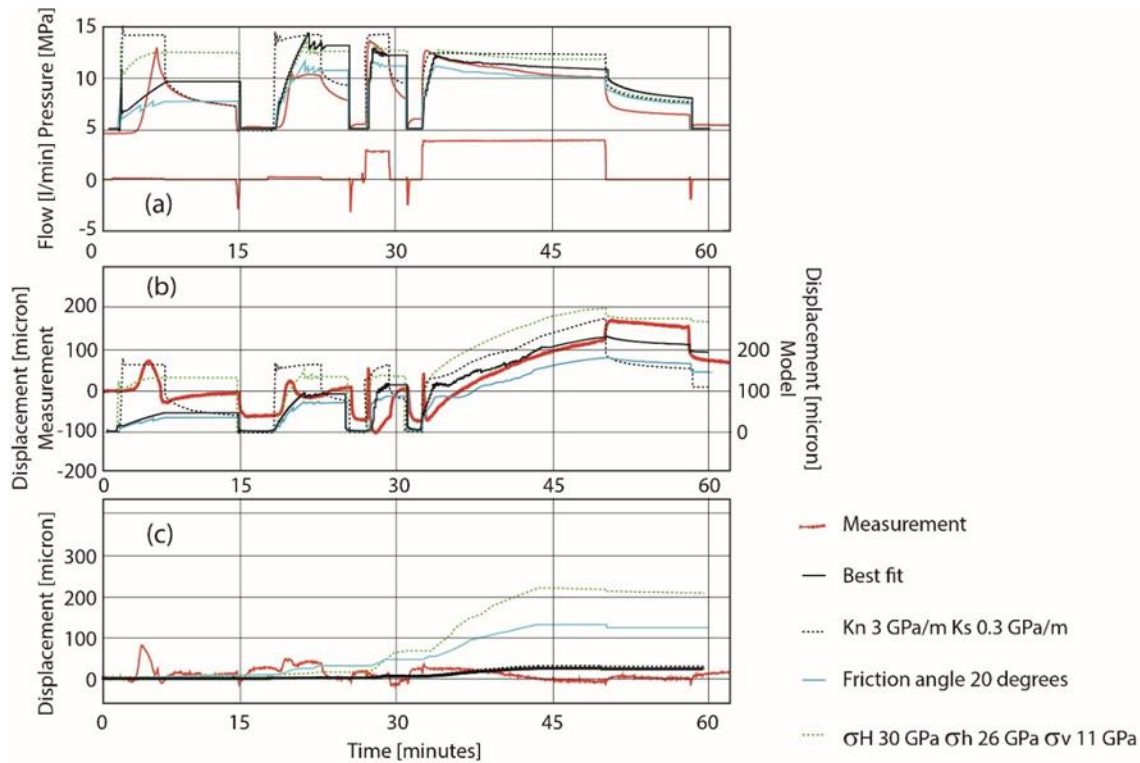
Figure 3-6 shows the results of the numerical analysis of the measured borehole wall axial displacements using the small model (which was shown in Figure 3-5). In Figure 3-6(a), we consider the elastic response of an intact rock chamber (Figure 3-5c) for different elastic bulk moduli. We found that the best match to the intact rock test data during injection cycle 1 before fracturing, is for an intact rock modulus of 80-to-100 GPa. We observed that after fracturing the best match is for a bulk modulus that decreased to 20-to-36GPa during cycle 4. In Figure 3-6(b), we consider the elastic response of a closed fracture (Figure 3-5d). We found that before the fracture activation, there was no significant difference in the chamber elastic response compared to the intact rock case (see how the experimental points of cycle 1 for the closed fracture align with those for intact rock). When the fracture is activated, there is a drastic change in the chamber displacement response to pressure which switches to an axial extension similar to the chamber response of the initially open fracture case. Thus, in both the activated closed fracture (cycle 2 closed fracture in Figure 3-6b) and the opened fracture case (Figure 3-6c) best match for fracture properties of 3-to-5GPa/m and 0.3-to-0.5GPa/m for the normal and shear stiffnesses respectively.



**Figure 3-6.** Borehole axial displacement versus chamber pressure. Circles and squares are measurements picked on the experimental displacement curve periods figured for example in yellow in Figure 3-4 (same type of picks were conducted on closed and open fracture tests). Curves show the results of the numerical sensitivity study of borehole axial displacement to rock properties (axial displacements are calculated with the model setting shown in Figure 3-5).

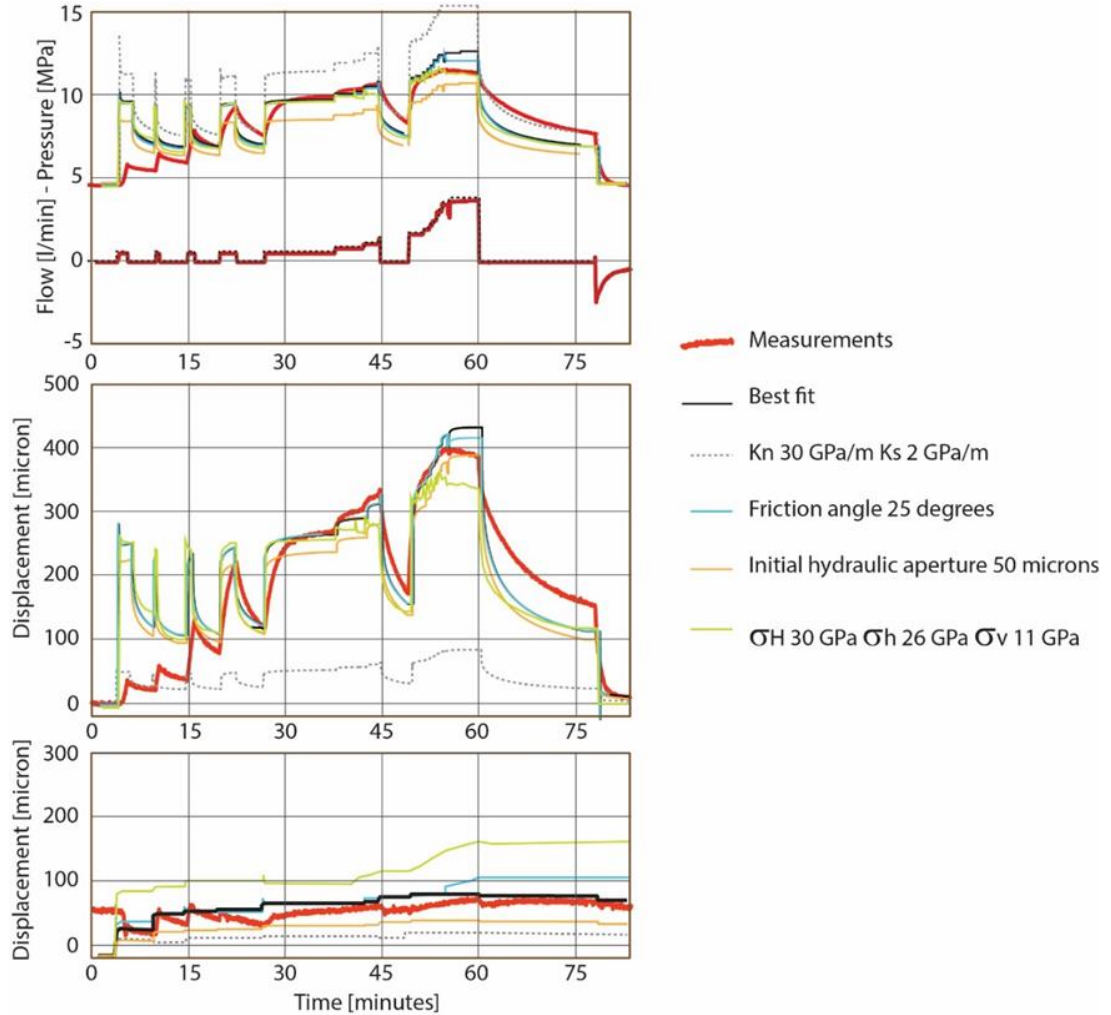


**Figure 3-7.** Model setting to analyze the transient evolution of injection pressure, fracture normal and tangential displacements during the entire intact rock and open fracture tests. (a) Intact rock tests where the HF plane is initially considered as a closed fracture at the onset of the model. This plane will only open at failure triggered by pressure increase induced by injecting the flowrate history (b) at the injection point Inj.1. (c) Open fracture model setting and (d) flowrate history injected at point Inj.1 in the model.



**Figure 3-8.** Intact rock HF propagation sensitivity to rock and stress properties. (a) Injection pressure (upper graphs) and flowrate imposed in the model (lower graph). (b) Fracture normal displacement. (c) Fracture tangential displacement. Best fit model properties are given in Table 3-2.

Figure 3-8 shows that the fracture's displacement and injection pressure observed during the intact rock fracturing test are reasonably reproduced for the model's parameters summarized in Table 3-2. The initial injection cycle is poorly reproduced because of the application of the simplified fracture physics considered in the model. Indeed, the chamber's displacements measurements illustrate a much more complex mechanical damage effect progressively evolving in a macro-fracture (this damage and the fracture localization physics are not considered in the model). We also found that the best fit was for a closed fracture with no cohesion and no tensile strength. Increasing cohesion or tensile strength does not change the results (except if values are taken above 10MPa where no failure is modeled). It appears that rupture is driven by the permeability law applied in the model. This law only allows flow calculation in the rupture in tension or in shear fracture patches. Model shows that when fracture's elastic properties are reduced, there is more fracture normal displacement. When fracture friction angle or deviatoric stress are increased, there is more tangential displacement.



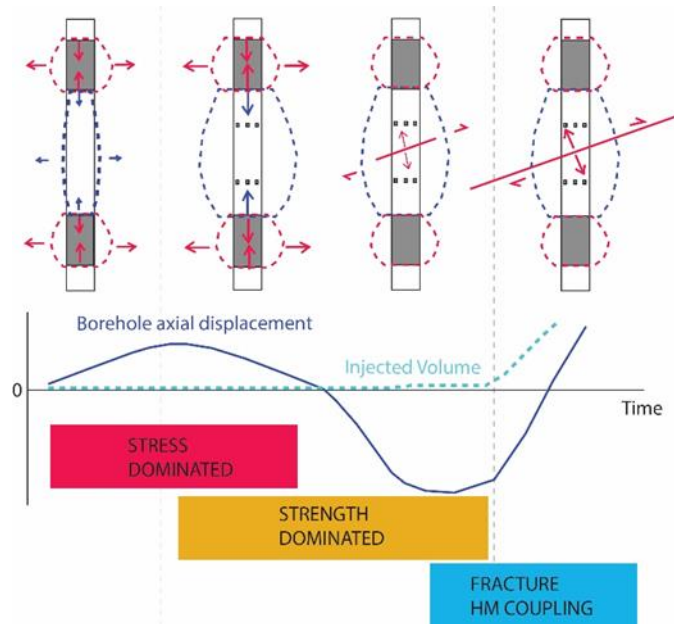
**Figure 3-9.** Open fracture test sensitivity to rock and stress properties. (a) Injection pressure (upper graphs) and flowrate imposed in the model (lower graph). (b) Fracture normal displacement. (c) Fracture tangential displacement. Best fit model properties are figured in Table 3-2.

Figure 3-9 shows that the fracture’s displacement and injection pressure observed during the open fracture test are reasonably reproduced for model’s parameters given in Table 3-2. Increasing the natural fracture stiffness reduces the normal opening and increases the fluid pressure. A larger initial hydraulic aperture induces a smaller injection pressure and normal displacement. A lower friction angle favors rupture above 10MPa but triggers more shear displacement than measured. A larger deviatoric stress also favors rupture above 10MPa but underestimates the normal displacement and strongly overestimates the shear displacement.

**Table 3-2.** Best fit properties for numerical models shown in Figures 3-8 and 3-9.

Parameters	Units	Intact rock	Open fracture
Bulk modulus of rock ( $K$ )	GPa	50	33.3
Shear modulus of rock ( $G$ )	GPa	33.8	25
Rock density ( $\rho_r$ )	kg/m <sup>3</sup>	2800	2800
Fault elastic stiffness ( $k_n, k_s$ )	GPa/m	20, 1	3.3, 0.17
Friction angle	(°)	25	25
Cohesion/Tensile strength	(MPa)	(0,0)	(0,0)
Initial hydraulic aperture ( $a_{ho}$ )	µm	0	10
Dilation angle ( $\psi$ )	Degree	5	5
Initial fluid pressure ( $P_o$ )	MPa	6.2	6.2
Fluid Bulk modulus ( $K_w$ )	GPa	2	2
Fluid density ( $\rho_f$ )	kg/m <sup>3</sup>	1000	1000
Fluid viscosity ( $\mu_f$ )	Pa.s	0.001	0.001
Stress ( $\sigma_1, \sigma_2, \sigma_3$ )	(MPa)	(14.8, 14.0, 13.0)	(14.8, 14.0, 13.0)

Finally, we observe that leakage into an initially intact crystalline formation only occurs after several repeated fracturing pressure cycles (Figure 3-10). We identify that, before fracturing, a near borehole surface effect must be overcome, where natural cracks are small and deformations dominated by stress tensor's variations caused by the influence of chamber and packer pressures. Fracturing initiation is causing damage and weakening of the intact rock elastic properties but no leakage since all the fluid entering the growing cracks is back-flowing at the end of stimulation cycles. We suggest that this transient state is dominated by strength and by the drastic change in the elastic properties of the rock, both controlling fracture growth and leakage. Finally, when a macro-fracture grows deeper into the rock, deformation and flow are steadier and dominated by fracture's hydromechanical parameters and eventual connection with other existing fractures.



**Figure 3-10.** Conceptual model of damage evolution toward a hydraulic macro-fracture growth in crystalline rock during a borehole hydraulic test.

### 3.4 New Field Experiments to Study the Crystalline Fault and Fractures Permeability Variations Induced by Weak Aseismic to Seismic Loadings at Relevant Nuclear Repository Depths

There is a concern that seismic events within or close to a repository site may induce secondary fracture shear movements across canister positions. Depending on the magnitude and velocity of the secondary shear displacement and on the orientation and location of the intersecting fracture relative to the canister, such a shear displacement could jeopardize the integrity of the canister. It is thus of crucial interest to nuclear waste authorities to study permeability changes in response to either local small magnitude or remote large magnitude earthquakes, which need to be better understood and predicted. Here we show a new fault displacement instrument called Downhole Robotic Stress Analyzer (DORSA) and a new field experiment site set in granite rocks both designed to get relevant data about fault and fractures permeability variations induced by weak aseismic or seismic loadings. The site was developed within a collaboration with the Nuclear Waste Management Organization of Japan (NUMO). We present some preliminary results highlighting the instrument capabilities and the order of magnitude of fault displacements recently observed following: (i) a magnitude 3.6 earthquake sequence that occurred at a 4 km depth on the San Andreas fault close to the area where the experimental site is deployed, and (ii) the Mw 7.8 Turkey tele-seismic earthquake.

The DORSA instrument has been developed based on the strong LBNL experience of using SIMFIP probes installed in boreholes for monitoring three-dimensional displacement. This instrument was developed to fulfill the following requirements related to a subsiding area overlying an intensively pumped aquifer:

- Large tens-of-centimeter displacements;
- Possibility to distribute the measurements along a borehole;
- Long-term monitoring of several months-to-years;
- Deployment in cased boreholes;
- Relatively low-cost and ruggedized instrument.

The DORSA is made of two anchoring zones connected to each other by aluminum tube and the 3D sensor (Figures 3-11a and 3-11b). The anchoring zones are made of two 1-m long stiff bars that are pressed against the borehole wall by a 1-m long air-inflatable rubber packer. Each anchor is inflated and fixed independently. This is allowing to deflate only one anchor when it is eventually necessary to reset the sensor that is getting out of range due to long-term increasing displacements. The 3D sensor is made of two platforms linked by 6 legs set in 6 different directions (Figure 3-12b). One platform is attached to the upper anchor. The other one is attached to the lower anchor. Legs are connected to the platform with ball or spherical joints. Legs are made with displacement sensors that are electric-based LVDT sensors from TE Connectivity Company (HR 200 model), with a +/-5mm range and 0.1 micrometer resolution. The aluminum tubes that connect each platform to the anchors are considered fully rigid, while the 3D sensor is ultra-compliant. Thus, the DORSA is measuring the displacements variations along the 6-legs linking the two platforms. These legs displacements correspond to the displacements of the upper and lower anchors that are induced by borehole wall displacements related to fault movements if the DORSA is set across the fault zone. The distance between the two anchoring points has been set to 4.6 m for the NUMO tests. A compass fixed on the top anchor allows for orienting the measurements. Above the upper anchor, the electronic unit of the legs displacement sensors is installed. The DORSA is connected to the borehole head with an electric line to convey power to the sensors and to convey the sensors signal to the surface, two pneumatic lines to inflate the anchors and a steel cable to hold the probe during deployment. Displacement signals are recorded at the ground surface with a National Instrument DAQ M system connected to a computer. An in-house software made with LabView software automatically converts the 6 legs displacements into the  $(x, y, z)$  displacements and  $(R_x, R_y, R_z)$  rotations of the DORSA- $\alpha$  upper anchor relative to the lower anchor. The output is a 7- column data file (.csv format), the first column being the date and time, the 6 remaining ones being the three-dimensional displacements and rotations.

In detail, the three-dimensional DORSA sensor is a 6-degree of freedom (DOF) displacement sensor. Since displacements depend on the surrounding rock subsidence, they are unknown. We use the legs length variation to solve the position and orientation of the upper mobile platform relative to the lower platform considered fixed. To determine the forward kinematics of the upper platform, a set of strongly coupled nonlinear equations is applied, because there is no a closed form solution for this set of equations. We use the Nelder–Mead (NM) algorithm to search the value of the variables  $(x, y, z, R_x, R_y, R_z)$  position of the moving platform satisfying the 6-legs length variations. The NM algorithm is a direct searching method for a nonlinear minimization problem.

The instrument was built and calibrated at LBNL. It is measuring the relative three-dimensional displacements and rotations between two anchoring points eventually clamped to two fault or fracture compartments. In the laboratory, 0.01-to-10 micrometer displacements were applied to the DORSA sensor in different orientations, highlighting a sensor's resolution of  $10^{-7}$  to  $10^{-8}$  micrometers and a very low range of background noise with a coefficient of variation  $<1\%$ .

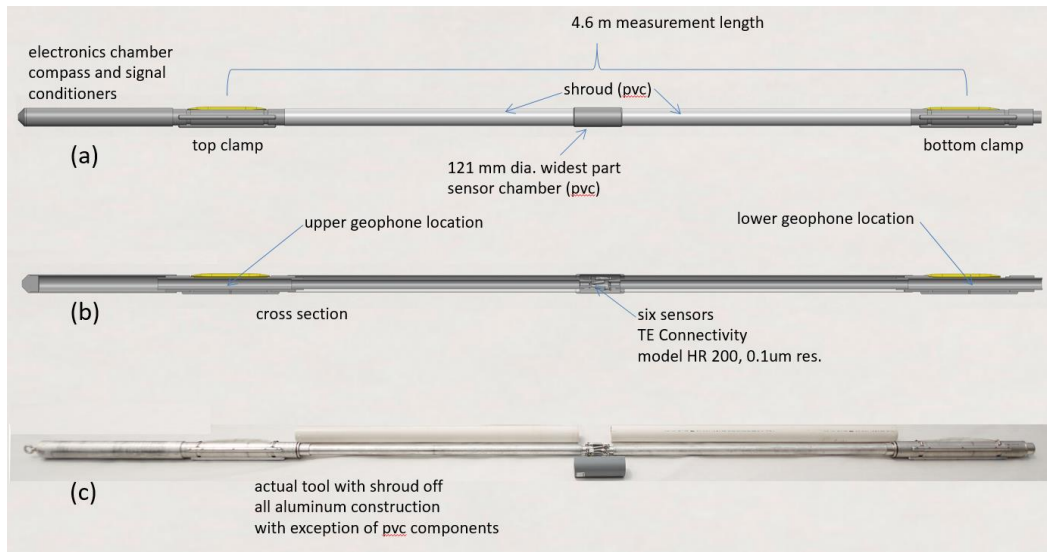


**Figure 3-11.** Schematic of a DORSA probe prepared for long term monitoring of fault movements: (a) Model view of the instrument with its protective PVC shroud. (b) Cross section of the instrument showing the 3D-sensor centered between the two anchoring packers. Each packer will be instrumented with a Silicone Audio 3 axis accelerometer to capture seismic waves. (c) Built instrument ready for deployment in the NUMO field experiment.

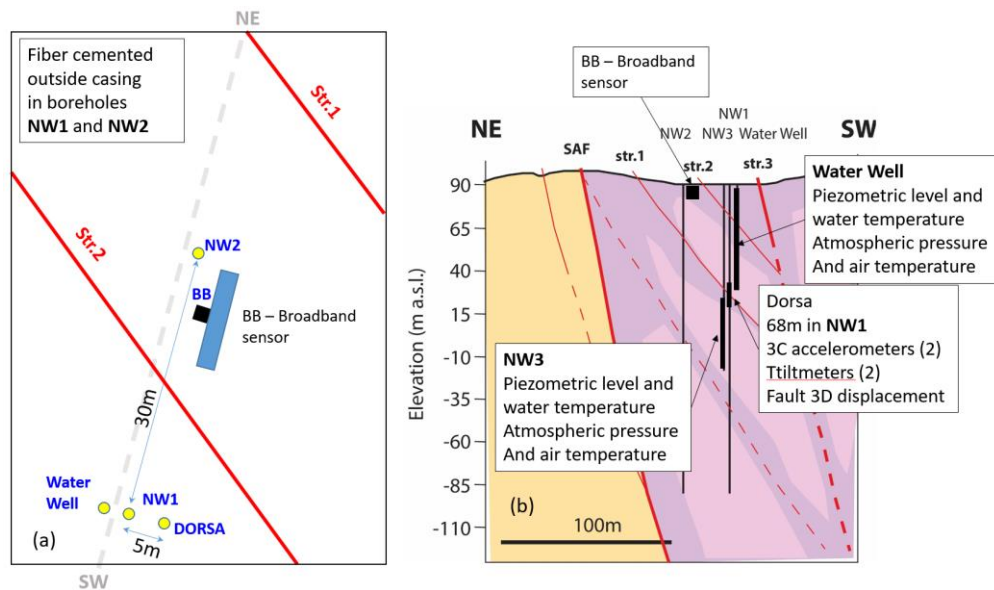


**Figure 3-12.** (a) Map of the instrumented NUMO San Andreas field site. (b) Vertical cross section showing boreholes instruments layout.

The DORSA was installed at a 68 m depth in a vertical borehole crosscutting a small secondary fault close to that San Andreas fault trace (Figure 3-12 for the detailed borehole geology and Fig 15a to see the site on a larger scale). Since December 2022, the DORSA has been permanently recording fault displacements. Here, we extracted two periods of interest that show:

- The fault response to the local January 19, 2023, Mw 3.6 San Juan Bautista earthquake sequence, and
- The fault response to the February 6, 2023 Mw 7.8 Turkey tele-seismic earthquake.

On January 19, 2023, the DORSA displayed a significant displacement variation starting 36 minutes after the San Juan Bautista (SJB) Mw 3.6 earthquake (Figures 3-13 through 3-16). This signal occurred while there was no rainfall. DORSA signal was 8 minutes and 15.15 seconds long (Figure 3-13b). It initiated as a slow change in the displacements' trend for 7 minutes and 44.44 seconds, followed by a sudden acceleration lasting 31.31 seconds. During the acceleration period, the amplitude of Eastern, Northern and Vertical fault displacements were 297, 123 and 22  $10^{-6}$  m, respectively (Figure 3-13b). This corresponds to a displacement vector length of 322  $10^{-6}$  m and a displacement velocity of 11 micrometer/second.

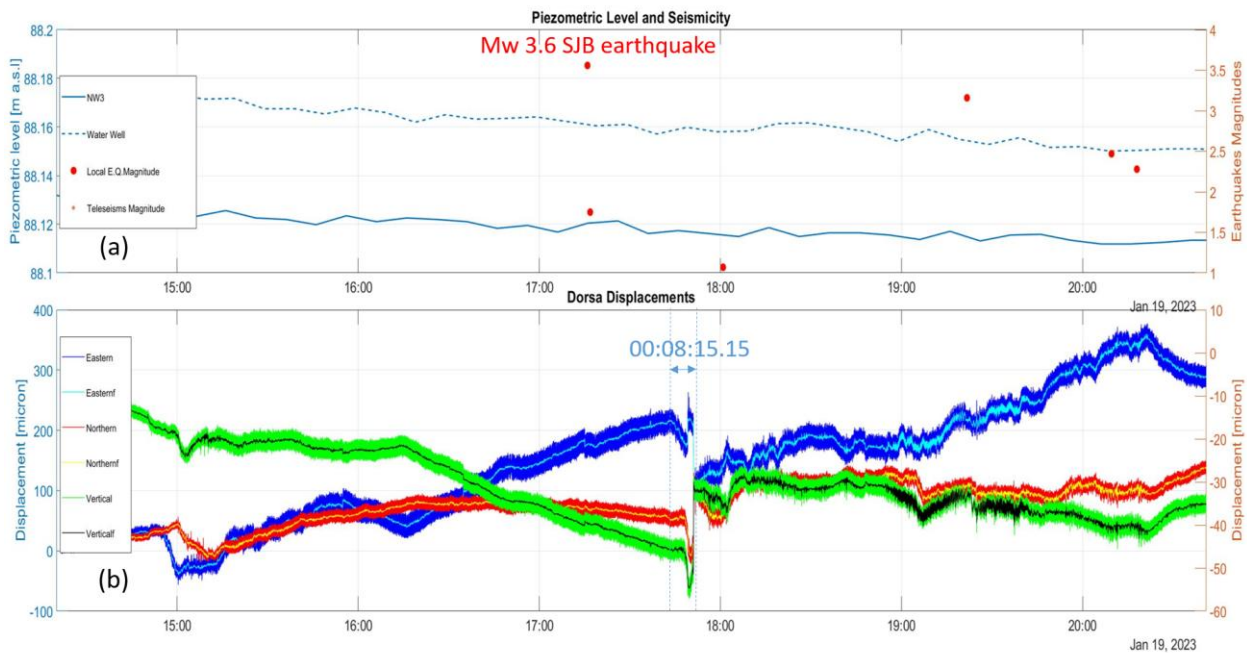


**Figure 3-13.** DORSA displacements vs time during the SJB Mw 3.6 earthquake sequence: (a) Piezometric levels in NW3, Water well, and seismicity. (b) Strand 1 Eastern, Northern and Vertical-up displacement vs time.

Figure 3-14 shows that the three-dimensional relative displacements of fault compartments are sub-horizontal with a slight vertical component. Displacements follow two main trends:

- A general contraction trend that was N050° to N070°. This trend is consistent with the N064° maximum horizontal stress ( $S_{hmax}$ ) estimated on the site. This trend is characterized by the fault hanging wall (red curve) slowly moving eastward and the fault footwall (brown curve) moving westward, and
- Episodic displacement events subparallel to the fault. The main one was the 8 minutes and 15.15 seconds long shown in Figure 3-13. In Figure 3-14d, this event is characterized by a fast displacement from 'l' to 'm', in good accordance with a right lateral strike slip movement on the fault.

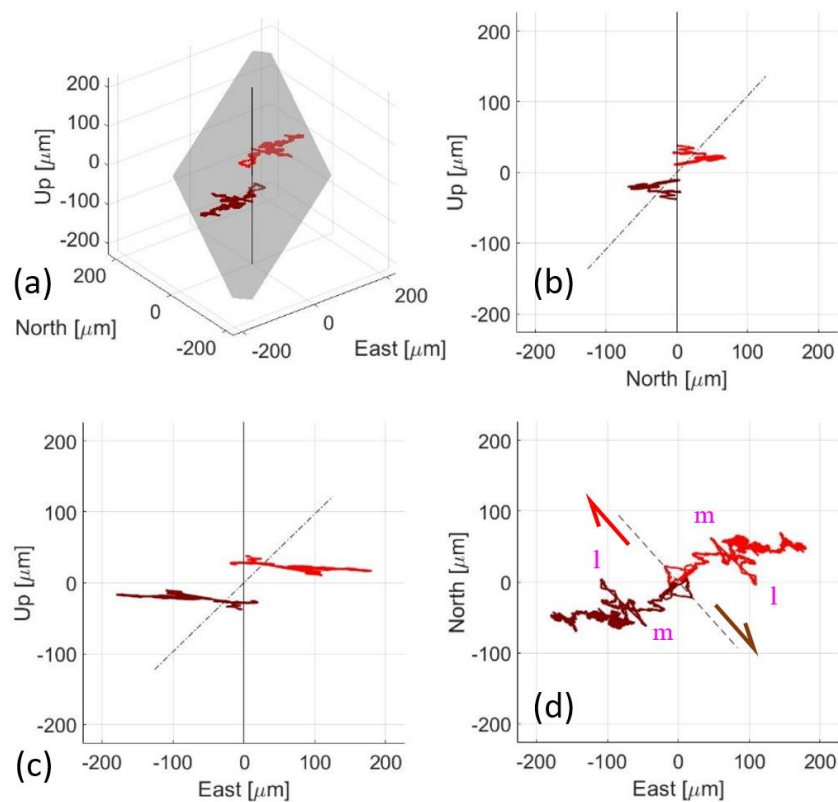


**Figure 3-14.** Three-dimensional variations of the DORSA displacements during the SJB earthquake period shown in Figure 3-15 (red curve is the displacement of the upper DORSA anchor clamped to the fault hanging wall and brown curve is the displacement of the lower DORSA anchor clamped to the fault foot wall): (a) Three-dimensional view (grey surface is strand 1 fault). (b) and (c) are vertical plane views. (d) Horizontal plane view. The dashed line is the strand 1 fault plane projection.

In Figure 3-15, we have converted the DORSA displacements into displacements normal and tangential to the fault surface. Then, we have picked displacement values at key changes in displacements (magenta lines in Figure 3-15b). This allows for defining displacement vectors between two consecutive picked values. There is a migration of displacements from the parallel-to- $S_{Hmax}$  NE-SW trend ( $\vec{fg}$ ,  $\vec{gh}$  and  $\vec{ij}$  in Figure 3-15a-b) to mainly right-lateral strike slip during the main creep event (vectors  $\vec{jk}$ ,  $\vec{kl}$  and  $\vec{lm}$  in Figure 3-15a-b). During the initial period, the fault was slightly closing. The creep event is characterized by a  $50 \cdot 10^{-6}$  m opening. Interestingly, the compression zone on the Mw 3.6 event's beach ball displays an EW average trend that is consistent with the  $\vec{gh}$  vector orientation at the onset of the DORSA signal deviation from the  $S_{Hmax}$  trend (Figure 3-15a-b).

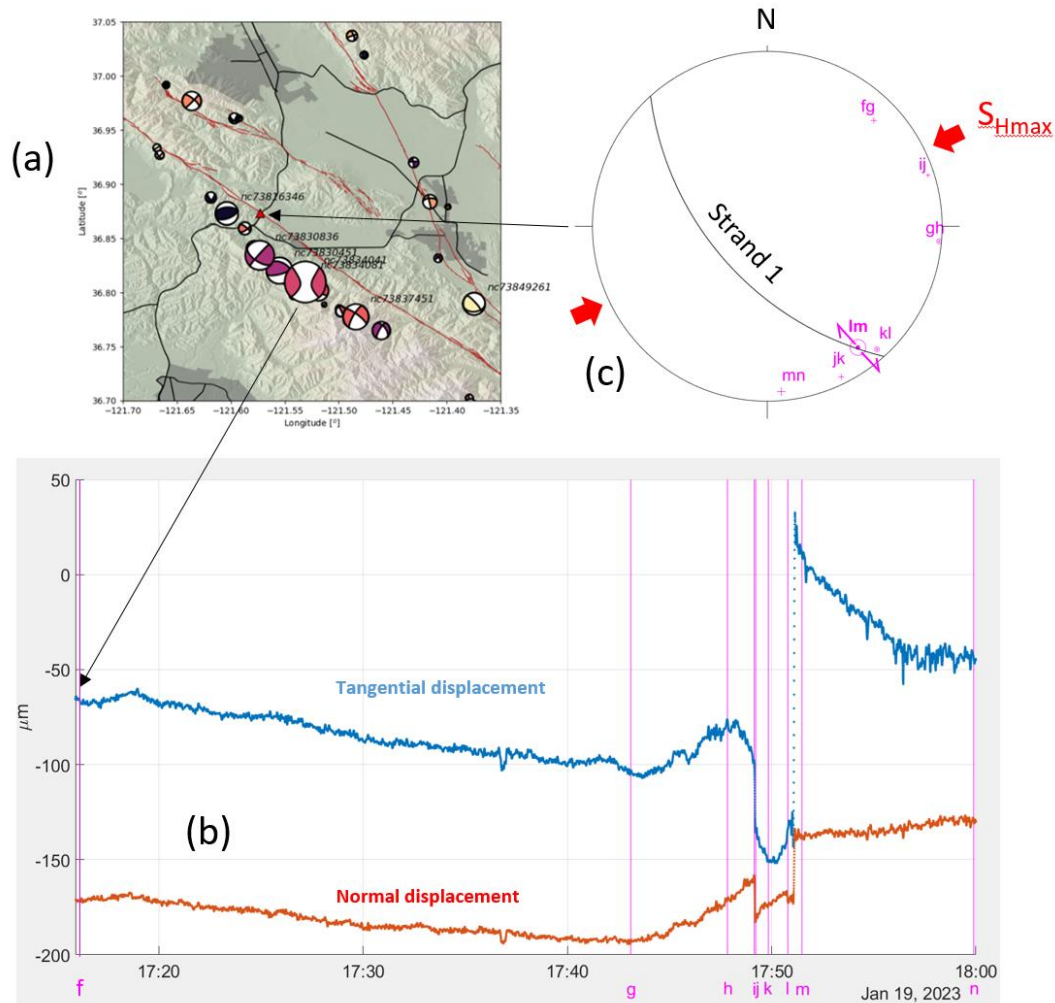


**Figure 3-15.** Comparison of DORSA creep event with SJB Mw 3.6 event: (a) Earthquakes location. (b) Fault normal and shear displacement variation with time (Mw 3.6 event occurred at magenta line 'f' on the left of the graph). Magenta lines are where displacements were picked to define the vectors plotted in Figure 3-15c. (c) Stereographic lower hemisphere projection of displacement vectors (dark semi-circle is the projection of strand 1 fault plane).

On February 6, 2023, the DORSA recorded a signal that could apparently be related to the Mw 7.8 Turkey earthquake (Figure 3-16). Nevertheless, some electric malfunction of the DORSA is altering the signal (blue arrows in Figure 3-16). The tele-seismic waves start being recorded at line ‘m’ on the left of Figure 16a-b. Displacements apparently started deviating from the Shmax NE-SW trend at line ‘p’ when there was the arrival of the large amplitude surface waves. This surface wave shaking period is characterized by displacement tangential to the fault ( $\overline{pq}$ ). Figure 3-16b shows that a 25-to-50  $10^{-6}$  m opening occurred.

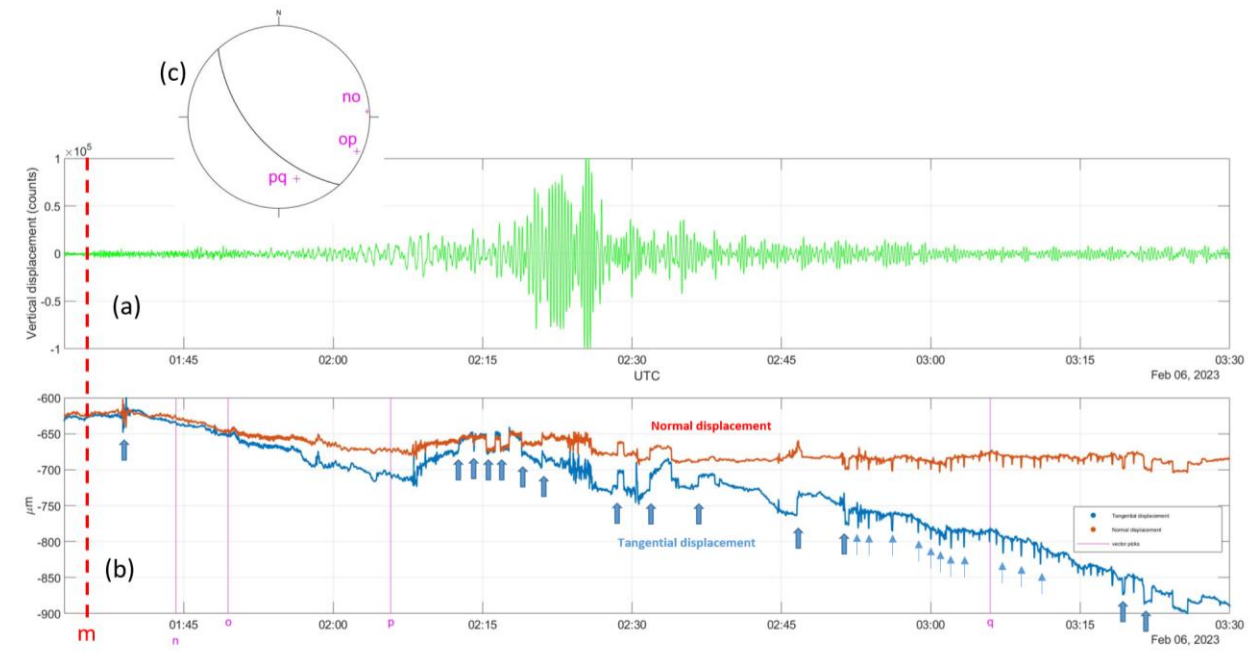


**Figure 3-16.** Dorsa response to the Mw 7.8 Turkey tele-seismic earthquake: (a) Vertical displacement recorded at the broad band seismic sensor on the NUMO site (arbitrary unit). (b) Fault normal and shear displacement variation with time. Magenta lines indicate the times when displacements were picked to define the vectors plotted in Figure 3-16(c). Blue arrows show electric malfunction of the DORSA sensor (fixed since these observations). (c) Stereographic lower hemisphere projection of displacement vectors (dark semi-circle is the projection of strand 1 fault plane).

### 3.5 Conclusions

LBNL scientists conducted monitoring experiments and analyzed direct downhole data of flow, pressure and displacements with both inversion methods and fully coupled hydromechanical forward numerical models. Experiments were conducted to highlight the activation sequence of fractures in crystalline rocks at an ~500 m depth in the COSC-1 borehole. Mainly flat-lying fractures subparallel to foliation open under variations of the normal effective stress in a slightly reversed stress regime were detected. Fractures first open at an injection pressure in a range of the sub-vertical minimum principal stress. This opening preceded a reactivation of reverse shear that occurred at higher injection pressure and after several water injection cycles. All tests show this evolution of fracture activation from mode 1 to a mixed mode as the stimulated

water volume increased. Adding the borehole displacement measurement to a standard HF or hydraulic tests on pre-existing fractures (HTPF) test allowed for defining an early test period where fracturing mainly depends on the minimum principal stress, and a later test period where the fracture hydromechanical response was more dependent on the triaxial far-field stress tensor. Using the slip vector triggered on fracture plane during this latter period, we estimated for the present case the three principal stresses orientations and magnitudes with a 10-to-20° and a 2-to-14 Mpa variation between tests. These are typical ranges of uncertainties in stress magnitude and orientation given by classical HTPF method, likely because of a limited number of tests. The estimated maximum horizontal stress orientation is consistent with the N120° trend deduced from breakouts mapped in the same COSC-1 borehole at greater depths. It should also be noted that the SIMFIP approach proves its utility to determine stress in areas where no such borehole-induced fractures are observed.

Displacement measurements also show the strong influence of borehole wall deformation on the onset of fracture activation, and until breakdown pressure. After several fracture reopening cycles, this influence vanishes, and displacements are mainly driven by hydromechanical movements of the fractures. We find that borehole wall displacement before the fracturing pressure can be used to estimate intact rock and fracture properties such as the bulk and shear moduli and the fracture normal and shear stiffness. They can also be used to quantify the evolution of these properties during a HF test. Key result is that a mechanical weakening phase is preceding flow into the deeper host rock, or in more practical words that several stimulation cycles are needed to trigger flow through the borehole mechanical damage zone.

Perspectives are to develop more advanced fully coupled hydromechanical models of flow associated to the critical evolution of borehole nearfield damage toward deeper rock macro-fracture growth in crystalline rock. In our current models, we “only” focused on modeling the borehole axial-vs-pressure displacement to estimate the rock properties. Here we will model both borehole axial and radial displacement, and their variations with pressure and with time. In addition to considering the models sensitivity to rock properties, we will also look at the sensitivity of borehole wall displacements to different state of stresses.

In parallel, we will start quantitative numerical modeling of fault creep induced by weak loadings such as seismic waves from distant earthquakes. In this preliminary work, we will explore how to tune the 3DEC code on the DORSA observations of fracture creep triggered by off fault earthquake. Moreover, we may also deploy a DORSA across a fault in an underground gallery in Switzerland, and to monitor the eventual fault displacement induced by a gallery excavation conducted nearby.

## 4.0 GEOMETRIC CHARACTERIZATION OF A SINGLE TRANSMISSIVE FRACTURE

### 4.1 Introduction

To gain more insight into the nature of the fracture flow observed at the COSC-1 well, core from depths corresponding to the flowing fractures was provided to LBNL, and laboratory experiments were conducted to determine fracture transmissivity  $T$  in multiple directions for naturally fractured core samples (Dobson et al., 2016, 2017; Zheng et al., 2018, 2019; Guglielmi et al., 2020). The three primary goals of the lab experiments were to:

1. Examine  $T$  changes with effective stress,
2. Compare lab-scale  $T$  values to field-scale values obtained from FFEC logging
3. Look for anisotropy in fracture  $T$

A novel experimental set up enabled flow through a transverse fracture to be specified in four directions, using a range of effective stresses representative of *in-situ* conditions, and differential pressure across the core to be measured. Flow experiments through an artificial fracture were done to verify that the laboratory procedure works. Then flow experiments were conducted on several naturally fractured cores selected from the depth intervals where FFEC logging identified flowing fractures. Experimental results for two cores were examined in detail, including developing a numerical model of the fracture planes and conducting numerical simulations of the laboratory flow experiments.

CT scans of cores provide maps of fracture aperture  $b(I, J)$ , where  $I$  and  $J$  are pixel indices in orthogonal directions across the fracture face, under conditions of zero confining stress. It is useful to compare aperture distributions obtained from different cores, and for the same core before and after a series of flow experiments in which confining stress is cycled from minimum to maximum values and back. The ultimate goals are to determine whether aperture distribution permanently changes as a consequence of experiencing a range of confining stress, and to gain understanding of how changes in aperture distribution  $b$  relate to changes in transmissivity  $T$ , and consequently to flow patterns through the fracture.

### 4.2 Visualizing Aperture Distribution

The most straightforward visualization of the aperture distribution is as a color map, as shown in Figures 4-1 and 4-2 for cores 211-2 and 401-1, for pre- and post-flow-experiment conditions. For both cores, the images have been rotated to match the orientation of numerical models described in previous reports. The color-map display is very good for providing an overall assessment of the differences between aperture distributions. For core 211-2 (Figure 4-1), aperture decreases significantly over most of the core between pre- and post-flow conditions, but at some point in time, a small chunk of the upper surface of the core broke off, and in post-flow conditions, sits loosely on the lower half, creating an extremely large aperture shown in bright red in the upper left portion of the core. For core 401-1 (Figure 4-2), aperture does not change much between pre- and post-flow conditions.

The color-map is not so good for answering quantitative questions, such as, does aperture change by a uniform amount between pre- and post-flow conditions? Positioning the core in the CT scanner is not precise enough to subtract aperture values pixel by pixel, so other methods must be used to address such questions.

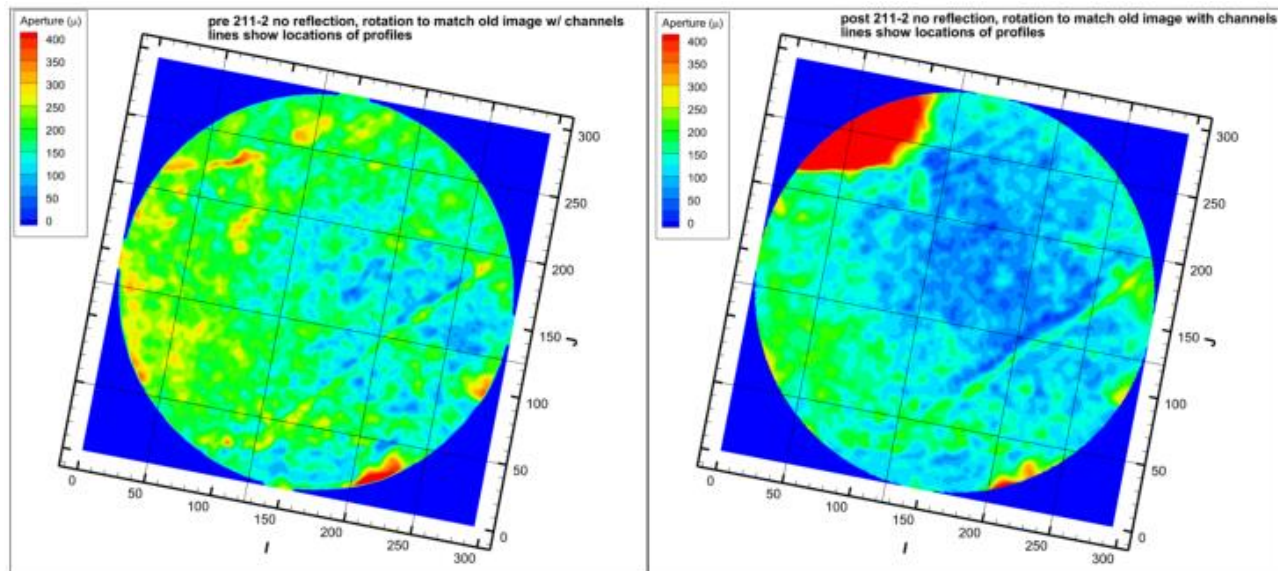


Figure 4-1. Core 211-2 pre-flow (left) and post-flow (right) aperture distributions. The black lines show the locations of aperture profiles.

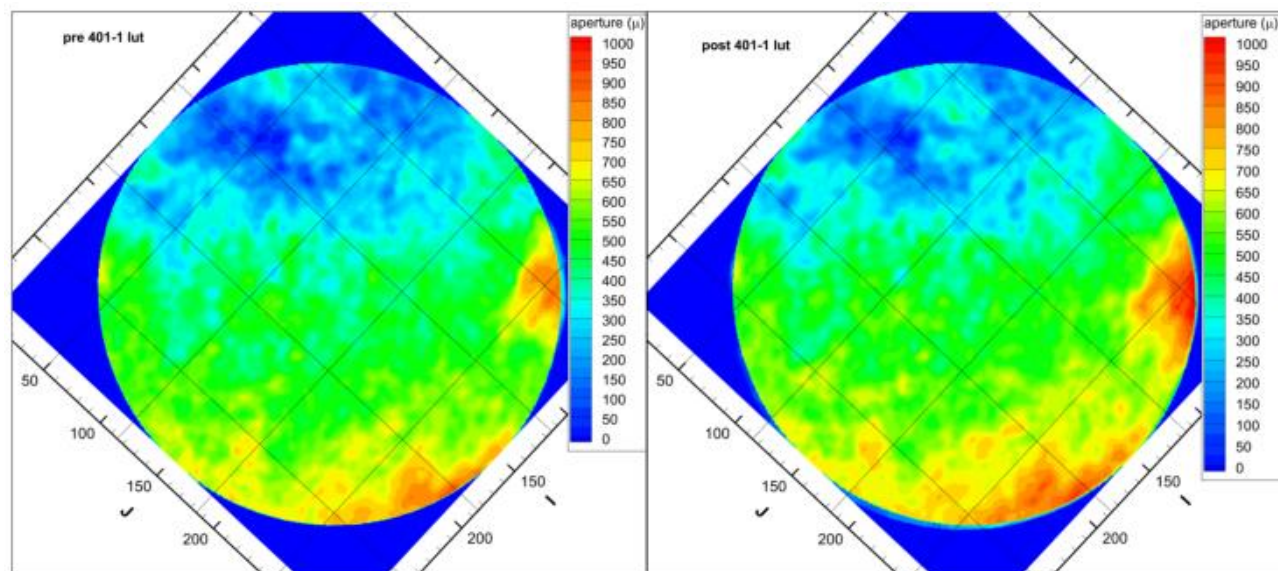


Figure 4-2. Core 401-1 pre- and post-flow aperture distributions. The black lines show the locations of aperture profiles.

Figures 4-3 through 4-6 shows profiles of aperture across the cores for the maps shown in Figures 4-1 and 4-2. The CT scans just provide a single  $b$  value for each (I,J) location in the fracture plane, but here  $-b/2$  and  $+b/2$  are plotted, to make aperture visualization easier.

For core 211-2 (Figures 4-3 and 4-4), the overall decrease in aperture is apparent, as is the isolated large increase associated with the broken chunk. Moreover, it is obvious that the aperture does not uniformly decrease. In some places, initially large apertures decrease more than initially small apertures, creating a more uniform aperture distribution (e.g., the low-I region of the  $J = 125$  profile in Figure 4-3; the high-J region of the  $I = 200$  profile in Figure 4-4). In some places there is very little aperture change, and in a few places beyond the broken chunk, aperture increases. If the aperture distribution were strongly anisotropic, it could manifest as a contrast in profile character between the I- and J- direction profiles, but this does not appear to be the case.

For core 401-1 (Figures 4-5 and 4-6), the lack of aperture change between pre- and post-flow conditions is apparent. In most places, the post-flow aperture is slightly bigger. As for core 211-2, there does not appear to be much contrast in the character of the profiles in the I- and J-directions.

The aperture profiles illustrate nicely that the small-scale variability in core 211-2 is more significant (i.e., bigger) relative to average aperture diameter than it is for core 401-1. In core 401-1, whole-core-scale variation dominates the aperture distribution.

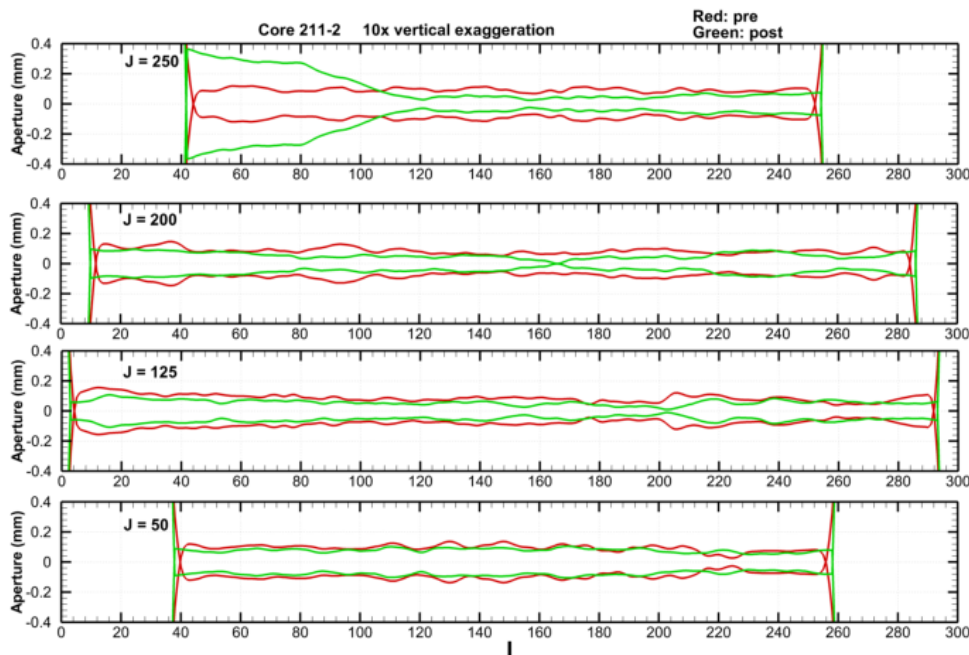


**Figure 4-3.** Profiles in the I direction for selected J values (see Figure 4-1) for core 211-2.

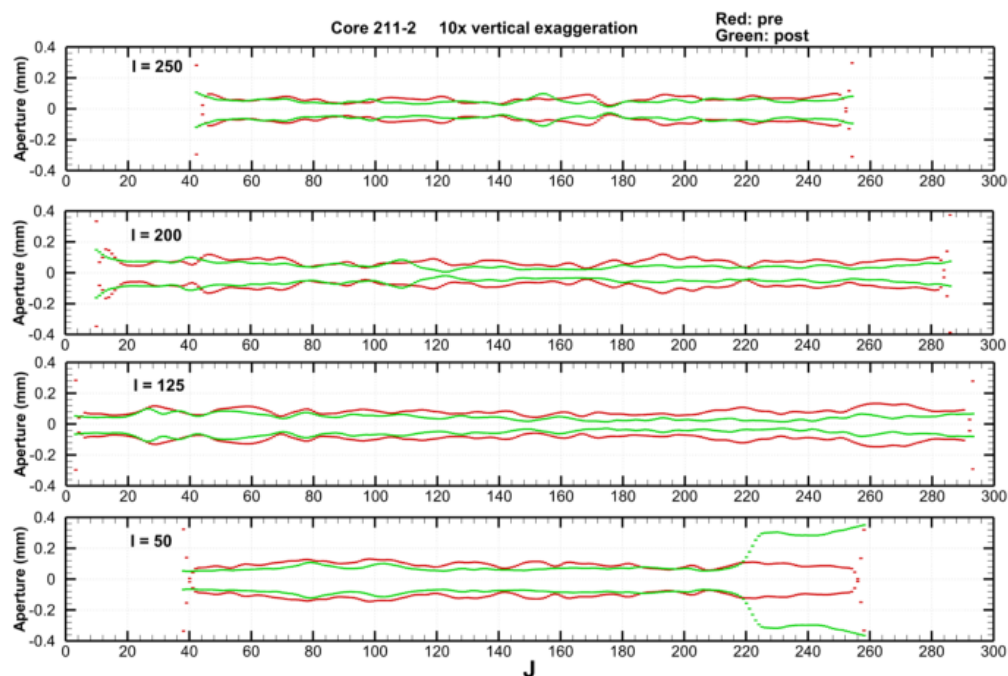


Figure 4-4. Profiles in the J direction for selected I values (see Figure 4-1) for core 211-2.

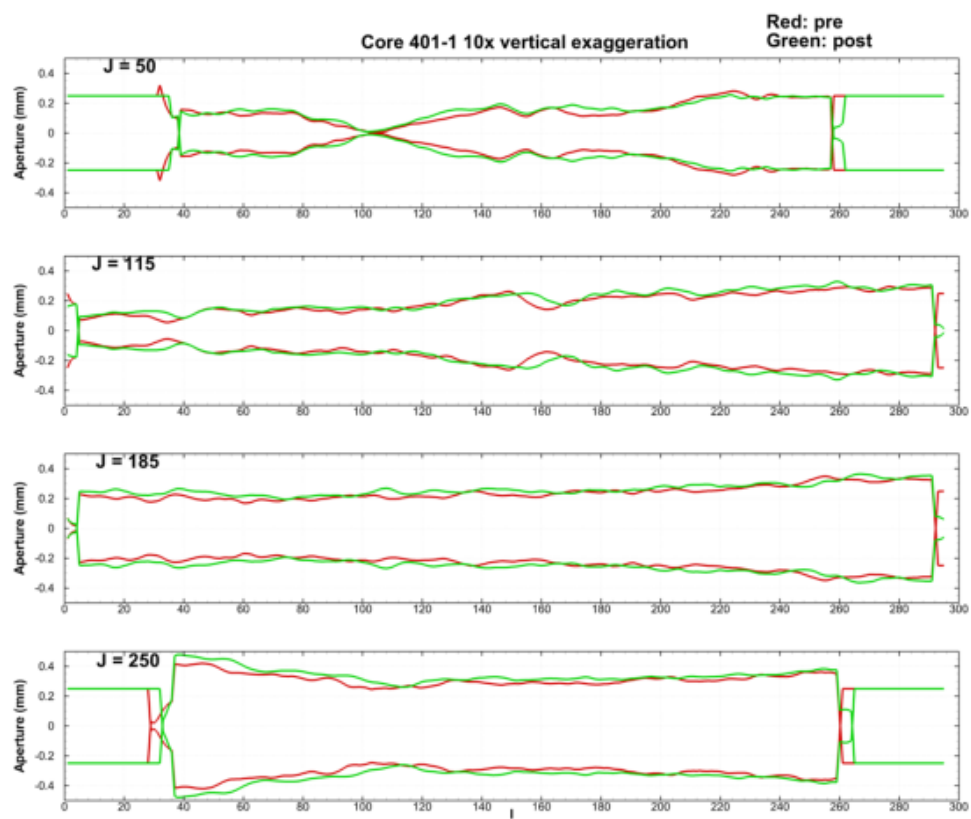


Figure 4-5. Profiles in the I direction for selected J values (see Figure 4-2) for core 401-1.

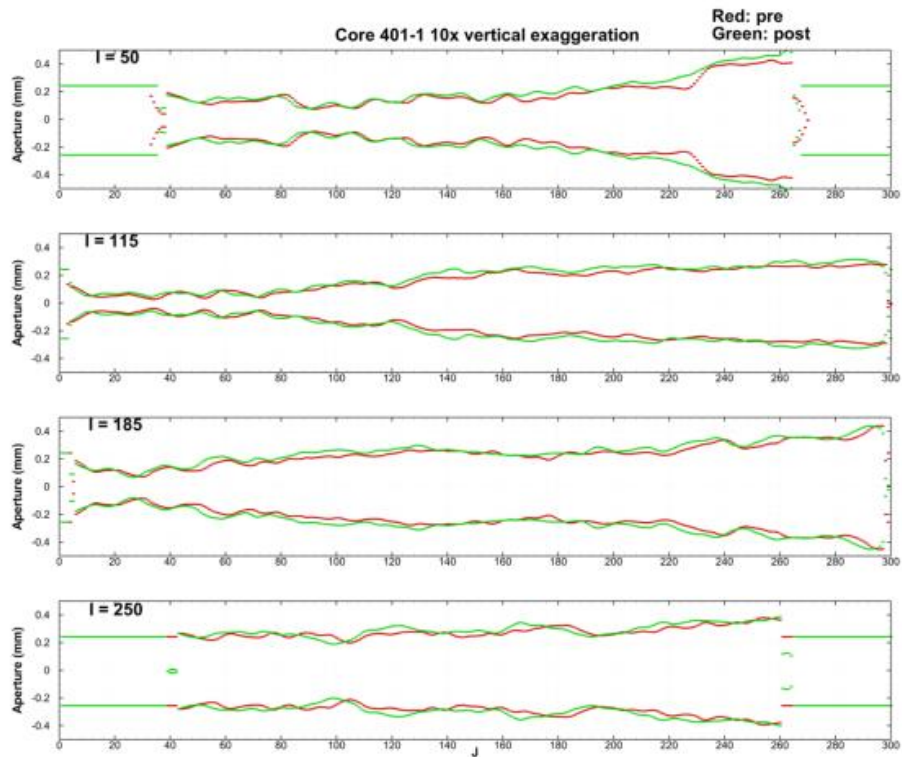


Figure 4-6. Profiles in the J direction for selected I values (see Figure 4-2) for core 401-1

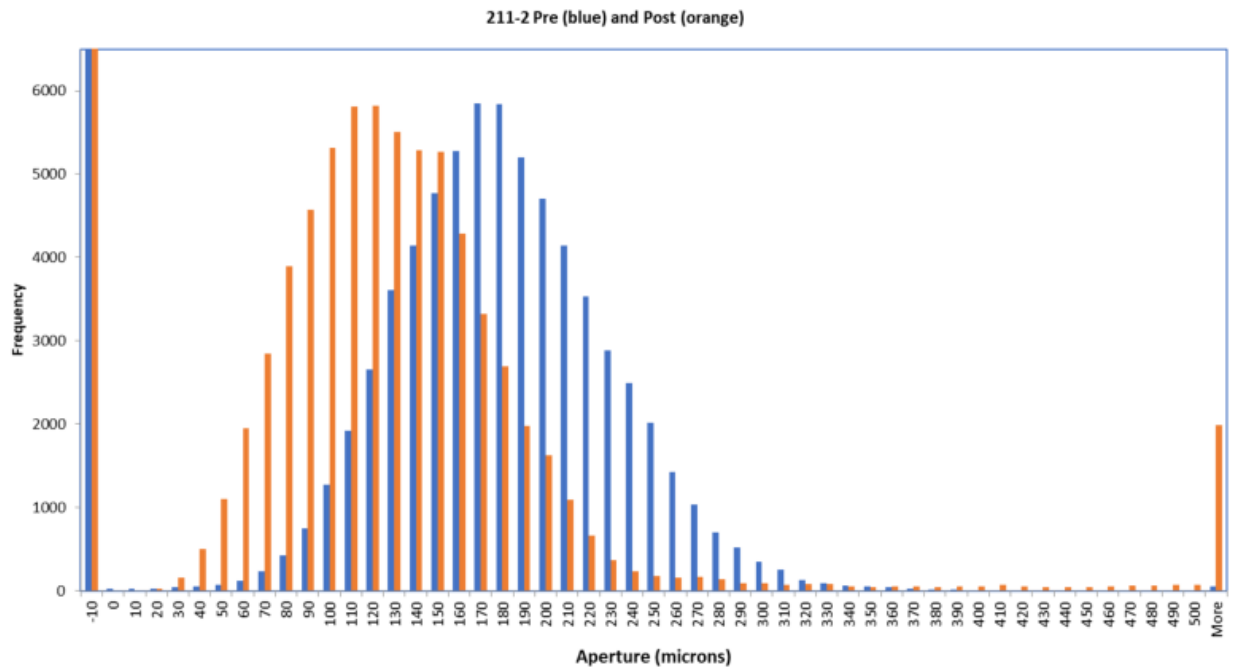
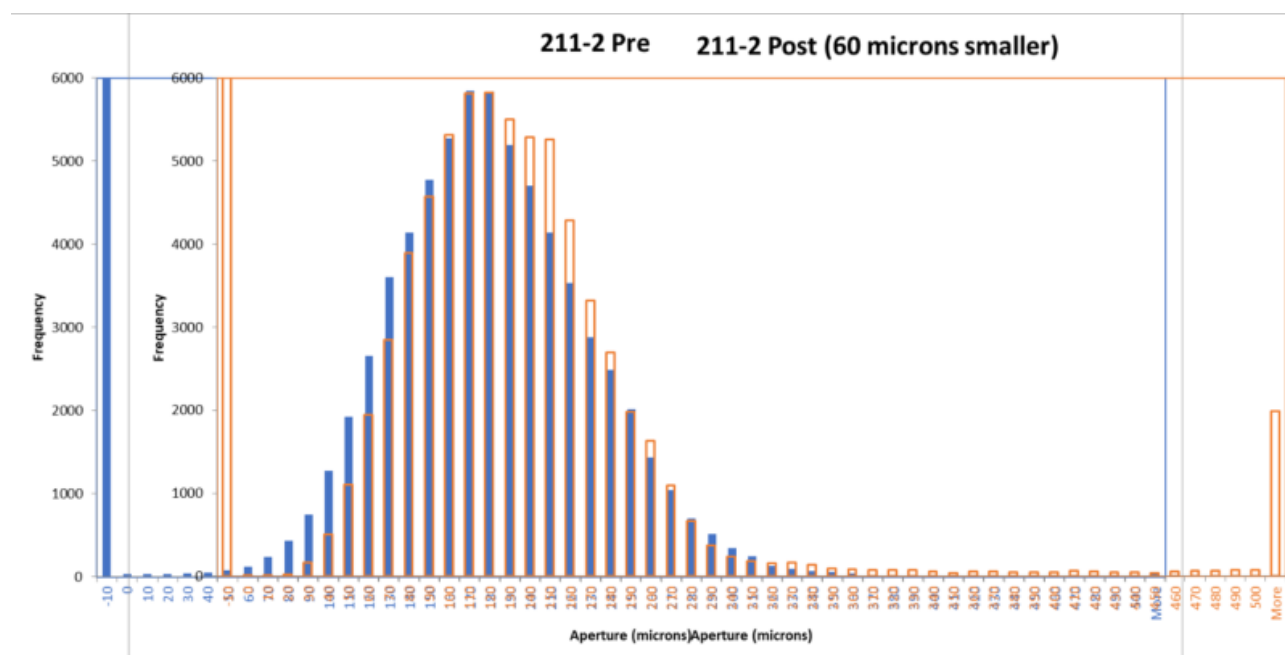


Figure 4-7. Core 211-2 histograms of aperture for pre-flow (blue) and post-flow (orange) conditions.

Figure 4-7 shows the histograms of aperture distribution for core 211-2, for pre-flow and post-flow conditions. The aperture distribution has generally maintained its shape, while shifting to smaller values overall. The broken chunk shows beyond the 500-micron upper limit of the histogram. The peaks at -10  $\mu\text{m}$  are not physical, but represent background values in the CT scans (note dark blue backgrounds in Figures 4-1 and 4-2).

More quantitative comparison between pre- and post-flow histograms can be made by shifting the horizontal axes until the peaks of the two histograms match, as shown in Figure 4-8. A shift of 60 microns aligns the peaks, and illustrates how the aperture distribution has changed. For the post-flow conditions, the left limb of the peak is overall sharper, and the right limb has a shoulder, which may be related to a slight opening adjacent to the broken chunk. The sharp left limb indicates that as the fracture overall closes, the smallest apertures do not close as much, which implies that asperities will not form as much as would be predicted by a uniformly closing fracture. This in turn suggests that there will be not as much of a tendency for preferential flow as there would be with a uniformly closing fracture.



**Figure 4-8.** Core 211-2 histograms of aperture for pre-flow (blue) and post-flow (orange) conditions, with the post-flow histogram shifted 60 microns to the right.

Figure 4-9 shows the histograms of aperture distribution for core 401-1, for pre-flow and post-flow conditions. The aperture distribution has generally maintained its shape, while shifting to slightly larger values overall. The peaks at -20  $\mu\text{m}$  are not physical, but represent the background value.

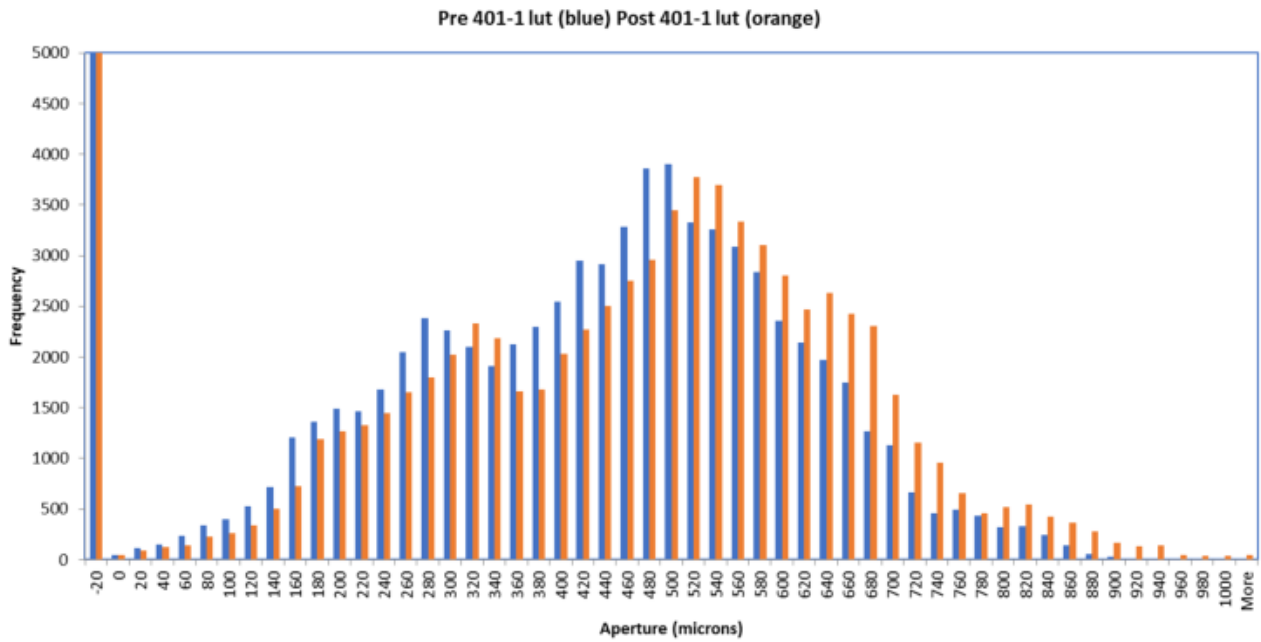


Figure 4-9. Core 401-1 histograms of aperture for pre-flow (blue) and post-flow (orange) conditions.

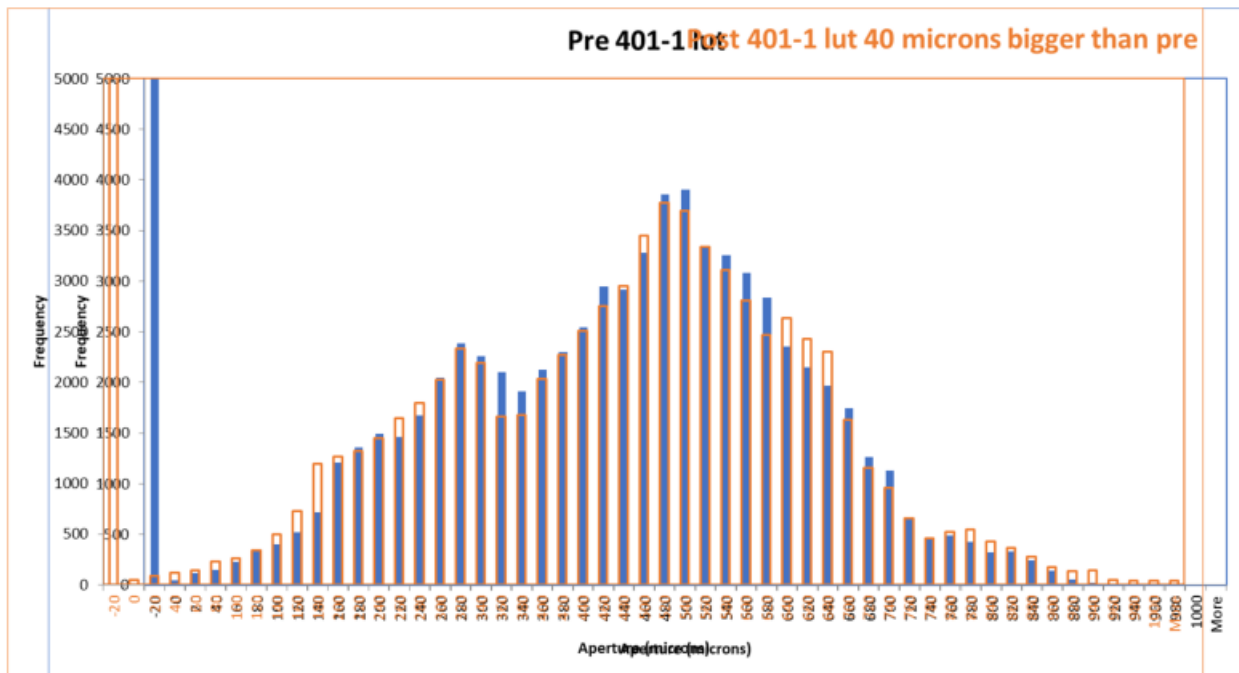


Figure 4-10. Core 401-1 histograms of aperture for pre-flow (blue) and post-flow (orange) conditions, with the post-flow histogram shifted 40 microns to the left.

Figure 4-10 shows the pre- and post-flow histograms with the horizontal axis shifted by 40 microns to match the histogram peaks. The overall shape of the two histograms are quite similar, indicating that a relatively uniform opening has occurred. Note that the range of the histogram plot for core 401-1 is 0-1000 microns, whereas for core 211-2 it is 0-500 microns (and except for the broken chunk, the range is about 0-350 microns). Hence, the percent shift is much smaller for core 401-1 ( $40/1,000 = 4\%$ ) than for core 211-2 ( $60/350 = 17\%$ ).

### 4.3 Conclusions

Different methods of visualizing aperture distribution are useful for different purposes. Color maps illustrate general behavior, profiles demonstrate detailed mechanisms, and histograms provide insights into collective behavior, all of which provide distinct information that is useful for interpreting aperture distribution changes and their consequences for flow experiment results.

For FY24, we plan to continue examining CT scans of aperture distributions, including before-flow-experiment and after-flow-experiment scans, to assess the effects of exposing the core to the cycle of increasing then decreasing confining stress that occurs during flow experiments. Particularly, it will be important to separate physical effects from different processing techniques.

## 5.0 UNDERSTANDING THERMAL-HYDROLOGICAL-MECHANICAL PROCESSES IN A SINGLE FRACTURE

### 5.1 Introduction

Fractures are ubiquitous in crystalline rocks. For the safe disposal of nuclear waste in crystalline rocks, the opening and shearing of natural fractures, as well as the creation of new fractures need to be understood and, if possible, controlled. For example, the opening of natural fractures or the creation of new fractures may provide additional transport paths, increase permeability of the crystalline rocks, and have a negative impact on the safety of the nuclear waste disposal. The shearing of fractures can lead to dilation of localized fracture segments, increasing permeability or even leading to seismic events.

The shearing (slip) of fractures is caused by shear stress exceeding the threshold of the shear strength due to mechanical loading, fluid flow, and temperature effects. The physics of shearing involves not only two interfaces (planar or rough) sliding along each other that satisfies a certain friction law, but also a dynamic change of contact states and/or contact locations.

Depending on the scale under consideration, fractures show different geometric and physical features. Figure 5-1 show a discrete fracture network (DFN) at the reservoir scale (m-10 km - Figure 5-1a), a rough fracture network (mm-m - Figure 5-1b), a dominant fracture at the core scale (mm-cm - Figure 5-1c), and a damage zone at micro grain scale ( $\mu\text{m}$ -mm -- Figure 5-1d).

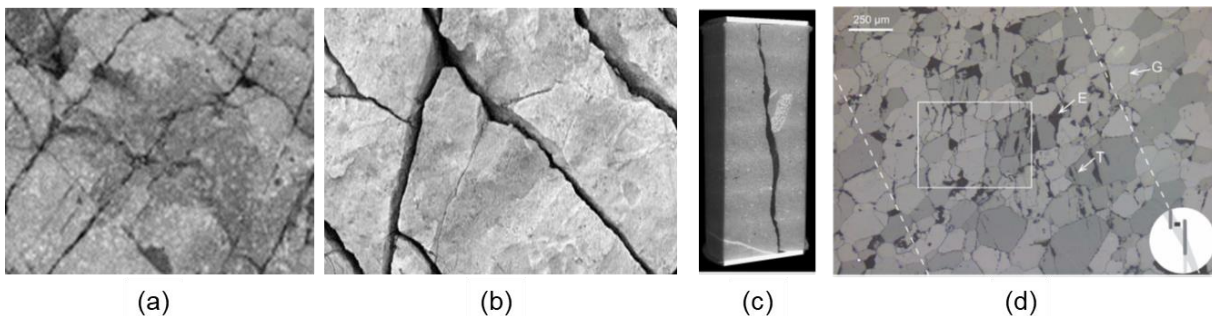


**Figure 5-1.** Fractures at different scales: (a) a DFN (m-10 km), (b) discrete rough fractures (mm-m), (c) a dominant fracture at the core scale (mm-cm, Ajo-Franklin et al., 2018), and (d) a damage zone at micro-grain scale ( $\mu\text{m}$ -mm, Cheng and Wong, 2018).

At the outcrop scale (Figure 5-1a), fractures appear to be very thin relative to their lengths, forming a network. Zooming into a smaller scale (Figure 5-1b), the fractures are no longer straight lines, they appear to be quite rough. At the core scale for a single fracture (Figure 5-1c), the fracture asperities may exhibit various shapes, corners, or distributions, which may not be described by common statistical functions. Continuing to zoom into the micro-grain scale (Figure 5-1d), a fracture, as a damage zone, can be considered as a granular system in which grain boundaries may or may not be cemented. Therefore, fractures can be classified into three categories based on their geometrical features: (1) dominant fractures with non-negligible widths and mineral fillings (finite-thickness porous zones), (2) discrete thin fractures forming networks, and (3) rough interfaces and granular systems (Hu et al., 2017a; Hu and Rutqvist, 2020a, 2020b, 2021).

Depending on the scale, the shearing of fractures may be controlled by different geometric or multiphysical features. At the discrete network scale, the shearing of fractures is controlled by their intersections (Hu and Rutqvist, 2021). At the asperity scale of a single fracture, the shearing is governed by the major asperities (Hu and Rutqvist, 2020a). At the granular scale, the shearing may be governed by abnormal geometric (e.g., sharp corners) and physical (e.g., softer or weaker minerals) features.

In a nuclear waste repository, the shearing behavior of fractures may be affected by temperature or temperature gradients. Thermal shearing of rock fractures may occur when an increase in temperature in the host rock generates a thermal gradient along with uneven thermal expansion of the rock asperities, leading to shearing of the fractures. Such shearing of fractures can result in potentially large changes in the fracture permeability via changing the connectivity of a fracture network and/or apertures of single fractures. In the presence of fluid or reactive fluids in fractured-porous media, thermal shearing is further complicated by thermal pressurization, changes in fracture friction, dissolution, precipitation, and pressure solution, which result from temperature gradient. Thus, thermal shearing is a very important process to be considered in the assessment of the long-term performance of a geological nuclear waste repository.

Models that explicitly account for discrete fractures can be categorized depending on the geometric representation of the fractures. Two types of models exist for the modeling of the mechanics of fractures:  $n$ -dimensional solid element models (Rutqvist et al., 2009), and discontinuous interface models where fractures are modeled as interfaces between discontinuous rock blocks (Lisjak et al., 2016). The  $n$ -dimensional solid element models (Rutqvist et al., 2009) can be used to represent fractures with non-negligible apertures. But when fracture apertures are much smaller than their lengths, the use of  $n$ -dimensional solid elements becomes computationally expensive. By comparison, the discontinuous mechanical interface model for discrete fractures has been proven to be promising for analyzing coupled processes in fractured porous media where fracture contact dynamics (dynamic changes of contact locations and contact states) can be considered (Hu et al., 2016, 2017b; Hu and Rutqvist, 2020a).

Modeling of coupled processes in fractures at the microscale has only been attempted in recent years. For example, modeling coupled processes in a single fracture was a part of the international DEvelopment of COupled Models and their VALidation against Experiments (DECOVALEX) project (Bond et al., 2017; Birkholzer et al., 2019). The models were categorized into 2D simplified models, statistical models, and homogenized models. In these models, geometric features (such as asperities along fractures and grains) are either not represented explicitly, or approximated by spheres or rectangular grids. Because real contacts along rough surfaces cannot be accurately captured, numerical modeling of coupled processes at the microscopic scale has only recently been attempted. To develop understanding of fracture dynamics at a microscale, a microscale model has been recently developed and applied for analyzing fractures at the micro asperity scale as well as in granular systems (Hu and Rutqvist, 2020a,b).

In this section, we will use a series of numerical experiments involving shearing of fractures, thermal slip of fractures, and hydrological-mechanical coupling within a single fracture to answer the following scientific questions:

- *How do the intersections impact the shearing of a fracture network? Can we simplify the shearing (slip) of fractures in a DFN? We will show that multiple fractures in a neighborhood can possibly be represented equivalently by a single larger fracture mechanically.*
- *How do the asperities affect the thermal slip of single fractures?*
- *How do the stress and fluid pressure affect the aperture and permeability of a fracture?*

To answer these questions, we conduct numerical simulations using (a) a novel code based on the Numerical Manifold Method (NMM) and (b) a commercial software FLAC3D for multiscale thermal-mechanical analysis, (c) COMSOL Multiphysics™ software. We used the NMM to conduct numerical simulations for scenarios of two or several intersecting fractures to test a hypothesis of using a major path(s) to simplify complex DFNs. The results are benchmarked with FLAC3D simulations to provide confidence in the proof-

of-concept of the new approach—i.e., the simplified DFN approach. Then, we applied FLAC3D to model the thermal-slip experiment for the Step 3 of DECOVALEX Task G, with a comprehensive sensitivity analysis of key parameters such as the friction angle and the thermal expansion coefficient. Finally, we used COMSOL Multiphysics™ software investigate the effect of stress and fluid pressure on porosity and permeability changes.

## 5.2 Multiscale Modeling of Shearing of Fractures

### 5.2.1 Fundamentals of NMM

The NMM (Shi, 1992) is based on the concept of “manifold” in topology. In NMM, independent meshes for interpolation and integration are defined separately. Based on this approach, an initially one-time generated, non-conforming mesh can be used and flexible local approximations can be constructed and averaged to establish global approximations for both continuous and discontinuous analyses.

In NMM, independent mathematical and physical covers are defined. A mathematical cover is a set of connected patches that cover the entire material domain. For example, we can use a quadrilateral patch, a circular patch, or a rectangular patch as a mathematical cover (e.g., patches A, B, C in Figure 5-2). Features such as the density and shape of these mathematical patches define the precision of the interpolation. The physical patches are mathematical patches divided by boundaries and discontinuities, determining the integration fields. The union of all the physical patches forms a physical cover. For example, physical patch C is the entire model domain, while physical patch B is the intersection of the mathematical patch B and the physical domain which is divided by the boundaries. Physical patch A (divided from mathematical patch A by boundaries) is further divided into physical patches  $A_1$  and  $A_2$  by the inner discontinuity. The overlapping areas by multiple physical patches are defined as elements. As a result, the model domain  $\Omega$  is discretized into five elements:  $A_1BC$  (the overlap of physical patches  $A_1$ , B and C),  $A_1C$ ,  $A_2C$ , BC, and  $C$ . From Figure 5-2, we can see that the shape of the mathematical patches can be arbitrary; the relative locations of mathematical patches at the model domain can also be arbitrary (only if satisfying  $\Omega \subset AUBUC$ ), and the number of physical patches on each element can also be arbitrary.

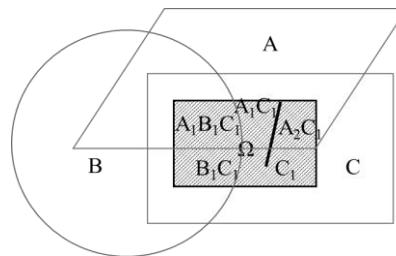
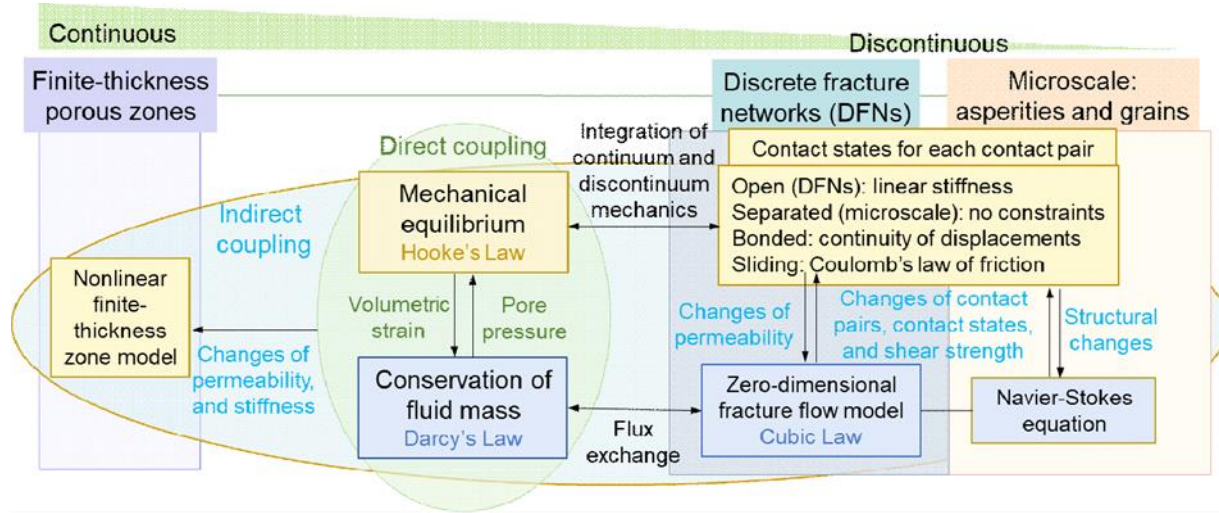


Figure 5-2. NMM mathematical and physical meshes.

The NMM (Shi, 1992; 1996), based on the theory of mathematical manifolds is a promising method for analyzing both continuous and discontinuous media. In the past two decades, NMM has been successfully applied to analyze mechanical processes in geologic media involving higher-order interpolation, fracture propagation, wave propagation across fractured media, slope stability, fracturing of sandstone and microscale mechanics of deformable geomaterials with dynamic contacts (Hu and Rutqvist, 2020b). For fluid flow analysis, the NMM has also been successfully applied to the analysis of moving interface problems such as free surface flow (Wang et al., 2014, 2016). The authors have previously developed a

series of models for the analysis of flow and fully coupled processes of fractured porous media at different scales (Hu et al. 2016, 2017a,b; Hu and Rutqvist, 2020a).

Figure 5-3 illustrates a high-level summary of the modeling capabilities for simulating fractures as finite-thickness porous zones, DFNs, and microscale asperities and grains. Radiating from the direct coupling of conservation of solid momentum and conservation of fluid mass, discontinuum mechanics with the calculation of dynamic contacts is applied to the two discontinuous scales, i.e., the DFNs and microscale



**Figure 5-3.** Overview of the multi-scale coupled processes models based on the NMM.

asperities and grains. In addition, different direct and indirect couplings were applied to assess features of constitutive behavior and physical laws for different scales.

## 5.2.2 Discontinuous Fracture Model in NMM

### 5.2.2.1 Contacts of the Discontinuous Fractures

The mechanical state of a fracture is complicated. A fracture may have several segments and every segment from the two sides of this fracture (a contact pair) has three possible contact states: open, bonded, or sliding. When sliding or shearing occurs, contact pairs (i.e., the locations where contacts occur) may be altered. Corresponding to these three contact states for each contact pair, different boundary constraints are applied. When a fracture segment (a contact pair) is open, a linear constitutive behavior is assumed:

$$\delta\sigma'_f = k_f \llbracket u_f \rrbracket \quad (5-1)$$

where  $\sigma'_f$  denotes a tensor of the effective stress in both normal and tangential directions of a segment of a fracture,  $k_f$  is the stiffness tensor of the segment, and  $\llbracket u_f \rrbracket$  is the jump of displacements in both normal and tangential directions of the fracture segment. When  $k_f$  is set as zero, a mechanically open fracture can be described.

When a segment of a fracture is bonded, the distance and relative shear displacement between the two sides of the segment is assumed to be zero, satisfying:

$$d = 0 \quad \cap \quad \llbracket u_s \rrbracket = 0 \quad (5-2)$$

where  $d$  is the time-dependent normal distance between the two surfaces of the fracture segment, and  $\llbracket u_s \rrbracket$  is the relative displacement between the two surfaces in the direction along the contacting face.

When a segment of a fracture is sliding, Coulomb's law of friction is satisfied in the tangential direction, while the normal distance between the two surfaces of the fracture segment should be zero:

$$d = 0 \quad \cap \quad F_s = F_n' \tan(\varphi) \operatorname{sgn}(\llbracket u_s \rrbracket) \quad (5-3)$$

where  $F_s$  is the contact force in the direction of the sliding face,  $F_n'$  is the effective normal contact force by considering fluid pressure,  $\varphi$  is the friction angle, and  $\operatorname{sgn}(\llbracket u_s \rrbracket)$  denotes the direction of  $F_s$  that depends on the direction of relative shear displacement. When sliding occurs along the two surfaces of a fracture, the locations of contacts change with time, possibly leading to changes of contact pairs as well as contact states among several segments of this fracture (Hu and Rutqvist, 2020a; 2021).

So far, we have described a fracture segment (a contact pair) in open, bonded and sliding contact states. In dynamic conditions, these contact states may be changed as follows:

- If a fracture segment was open, but became bonded later, constraints in Equation (5-2) should be added.
- If the fracture segment was open, but is in a sliding state afterward, constraints in Equation (5-3) should be added.
- If a fracture segment was bonded but becomes open later, the constraints in Equation (5-2) should be removed.
- If a fracture segment was bonded but transfers to a sliding state, we need to consider one condition: in order to initiate sliding of A and B against each other, the force in the direction of contacting face  $F_s$  needs to be larger than the shear strength  $S$ . The shear strength may consist of frictional force (satisfying Coulomb's law of friction) and cohesive force  $F_{cohe}$ . This criterion for shearing a bonded fracture segment in the direction along its contact face can be expressed as:

$$F_s > S = F_n' \tan(\varphi') + F_{cohe} \quad (5.4)$$

where  $\varphi'$  is the internal friction angle, which determines the threshold of transition from stick to shearing.

- If Equation (5-4) is satisfied, the fracture segment is transferred from bonded to sliding state. Comparing Equations (5-2) and (5-3), we find that the constraint in the direction normal to the contacting face should be retained, while in the sliding direction, the constraint needs to be changed.
- If a fracture segment was in a sliding state, but becomes open, constraints in Equation (5-3) should be removed. If it becomes bonded, the constraints should be modified in the direction along the fracture segment so that no relative shear displacement will occur.

With Equations (5-1) through (5-4), we are able to describe the three different contact states of a fracture segment, dynamic changes of these contact states, and criteria that need to be satisfied for the changes of the contact states.

### 5.2.2.2 Geometric Representation

An important issue for the calculation of discrete fractures is *how to simulate intersections of fractures*. Figure 5-4 depicts a geometric representation of two fractures that intersect each other and one triangular mathematical mesh. As we can see, the two intersecting fractures divide the triangle into four different blocks (A, B, C, D). In this case, contact states satisfying constraints described by Equations (5-1)-(5-3)

will be applied to the four pairs of parallel interfaces (interfaces between A and B, C and D, B and C, and A and D) to account for the opening, bonded and sliding states of the surfaces of each fracture.

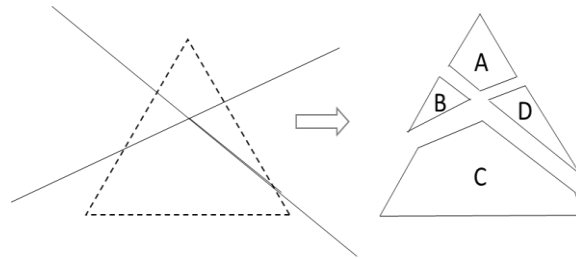


**Figure 5-4.** Geometric representation of an element divided by two intersecting fractures.

Fractures in open and bonded states or alterations between these two states are easier to simulate because this case does not require a change of contact pairs. It is assumed that a fracture is approximated by two surfaces that are parallel at the beginning, but these two surfaces can be non-parallel after deformation and motion, or opened. This capability is included in the algorithm.

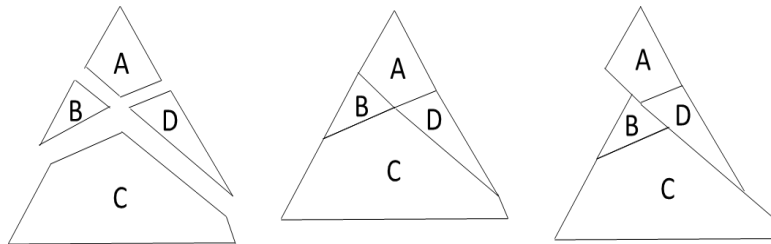


**Figure 5-5.** Geometric representation of open, bonded and sliding contact states for elements divided by intersecting fractures.

It is a challenging problem to simulate shearing along fractures because shearing leads to dynamic changes of contacts between different elements. As shown in Figure 5-5, when the four blocks A, B, C, D are in contact (i.e., the fractures are completely bonded), the contact pairs are A and B, B and C, C and D, and A and D. However, when sliding (slip) occurs at one of the fractures, the contact pairs become A and B, B and C, B and D, C and D, D and A. By using a rigorous contact algorithm that updates contact pairs at each time step, sliding along fractures can be rigorously and explicitly represented.

### 5.2.2.3 NMM Calculation of Shearing Discontinuous Fractures

#### Updating Contact Pairs

As demonstrated in Section 5.2.2.2, a fracture is approximated by two surfaces that are initially parallel. After shearing, the contact pairs (i.e., where contacts occur exactly) will be updated. This may involve changes of contact locations on the same contact elements or contact between different elements. The latter results in changes between zero and non-zero values at the off-diagonal elements of the calculating matrix.

#### Enforcement of Contact Constraints

The distance and displacement constraints for bonded and sliding states are imposed by using penalty methods (Shi, 1992). The penalty method is based on the concept of constructing a penalty function  $g$  to penalize the deviation from the displacement constraint  $c(u)$ . The key to effectively using the penalty

method is to choose a reasonable value for the penalty parameter. We assumed that a significantly stiff spring applied to the deviation of a constraint associated with the displacements. Therefore, the stiffness of the spring becomes the penalty parameter  $p$ . Minimization of deviation of the displacement constraint can be achieved by minimizing the potential energy associated with the work done by the penalty spring. The potential energy  $\Pi_c$  generated by the penalty spring to enforce the constraint can be generally expressed as:

$$\Pi_c = g c(u) = \frac{1}{2} p c^2(u) \quad (5-5)$$

The second constraint, i.e., Coulomb's law of friction is imposed directly by constructing the potential energy:

$$\Pi_{friction} = g c(u) = -F_s \cdot u_s \quad (5-6)$$

Note that (1) because Equation (5-6) includes a dot product, it requires the calculation of projecting shearing force on the sliding face, and (2) on the two sides of the sliding face, the absolute shear displacements are different due to sliding (as a relative displacement).

#### Iteration for Contact State Convergence

Within each time step, iterations may be carried out several times and pre-estimated contact states may be adjusted until the enforced contacts reach convergence. In a dynamic process, contact pairs may change continuously (Hu and Rutqvist, 2020b). For the same contact pair (a segment of fracture discretized by a numerical mesh in NMM), the three possible states may change dynamically. Thus, for every iteration within a time step, the global equilibrium equations are solved with the enforcement of contact constraints from the pre-estimated contact states. At this point, the contact states are re-evaluated to check for consistency with the pre-estimated contact states. If they are consistent for every contact pair, the calculation proceeds to the next time step. If they are not consistent, the contact states will be adjusted, and the calculation is looped back to re-solve the equilibrium equations until such consistency (i.e., convergence) is achieved.

### **5.2.3 Simplified DFN Model – Proof of Concept**

In this section, we present a step-by-step analysis of shearing of intersecting fractures. We first start with investigating two intersecting fractures with different intersecting scenarios. Based on the results of simulations of two intersecting fractures, we hypothesized that a network of discrete fractures may be presented using a simplified model of one or a few major path(s) if the two intersecting angles ( $\alpha$  and  $\beta$ ) at one intersection satisfy certain conditions. To test this hypothesis, we conducted a number of simulations involving a different number of major path(s). We conducted most of the simulations by using both the NMM and FLAC3D, which showed excellent agreement. In this section, we show the NMM results for all the examples and selectively plotted the comparison with FLAC3D results using a few typical examples. For all examples, we use the same domain size and mechanical boundary conditions: the bottom of the domain is fixed, while a vertical loading of 10 MPa is applied on the top. On the left and right boundaries, horizontal loadings of 5 MPa are applied.

#### **5.2.3.1 Shearing of Two Intersecting Fractures**

We first begin with three different scenarios of two intersecting angles with orientations of  $60^\circ$  and  $-60^\circ$ , and  $45^\circ$  and  $-60^\circ$  (as shown in Figure 5-6, top row). The difference between the second and third scenarios is that in the 2nd scenario the two intersecting fractures cut through each other, whereas in the 3rd scenario only the tip of the  $-60^\circ$  fracture intersects with the  $45^\circ$  fracture. We used the NMM to simulate the shear displacements of each fracture in each scenario and compared the results of shear displacement with an analytical solution (Pollard and Segall, 1987), where only the shearing of a single fracture is considered.

The purpose of such comparison is to show the impact of intersection of each single fracture by showing the deviation of shear displacements from the analytical solution of a single fracture. The results are shown in Figure 5-6 (bottom row).

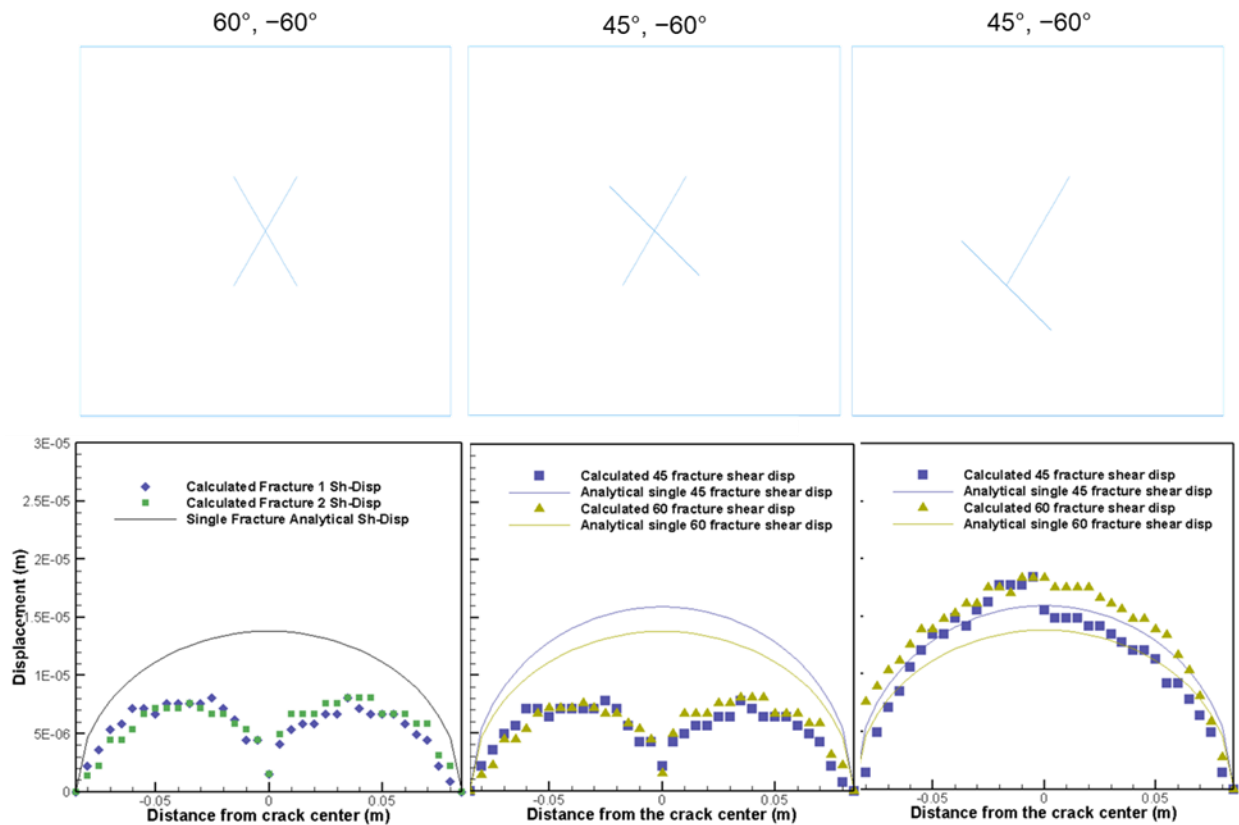


**Figure 5-6.** Three scenarios of geometry (top row) and NMM calculated shear displacements (bottom row) of two intersecting fractures with orientations of  $60^\circ$  and  $-60^\circ$  (left),  $45^\circ$  and  $-60^\circ$  (middle and right).

As can be seen from Figure 5-6 (bottom row, left), when two intersecting fractures are oriented symmetrically ( $60^\circ$  and  $-60^\circ$ ) and cut through each other, each fracture is divided into two sub-fractures and shearing of either fracture is prohibited at the intersection due to symmetry. As a result, the shear displacement profile of each fracture is broken into two nearly symmetric sub-circles where the highest shearing occurs in the middle part of each sub-fracture. The slight asymmetry is because the vertical loading is only applied from the top and the bottom boundary is fixed. Slightly adjusting one of the fractures from  $60^\circ$  to  $45^\circ$  does not intrinsically change the distribution of shear displacement (Figure 5-6, middle column). We still observe the same sub-fracture shearing behavior of both fractures, despite that there is no symmetric distribution of shear displacements between the sub-fractures. If the  $45^\circ$  fracture intersects with the  $-60^\circ$  fracture only at the tip of the  $-60^\circ$  fracture (shown on the right of Figure 5-6), we see that the distribution of the shear displacement of the  $-60^\circ$  fracture exhibits similar results to that of a single  $-60^\circ$  fracture with larger values in average. The  $45^\circ$  fracture shows a jump in the displacement adjacent to the intersection whereas the other part of the  $45^\circ$  fracture remains almost undisturbed by the intersection. Thus, the 3rd scenario provides a basis to further investigate this question: if two intersecting fractures do not completely cut through, the intersection plays a minor role in the shearing of both fractures.

We further simulated two scenarios of two intersecting fractures with orientations of  $45^\circ$  and  $60^\circ$ , as shown in Figure 5-7. In the first scenario, the two fractures cut through each other, and in the second scenario, the  $45^\circ$  fracture only intersects with the tip of the  $60^\circ$  fracture. We used both NMM and FLAC3D to calculate the shearing of these two scenarios. The meshes that were used in NMM and FLAC3D are shown in Figure 5-7.

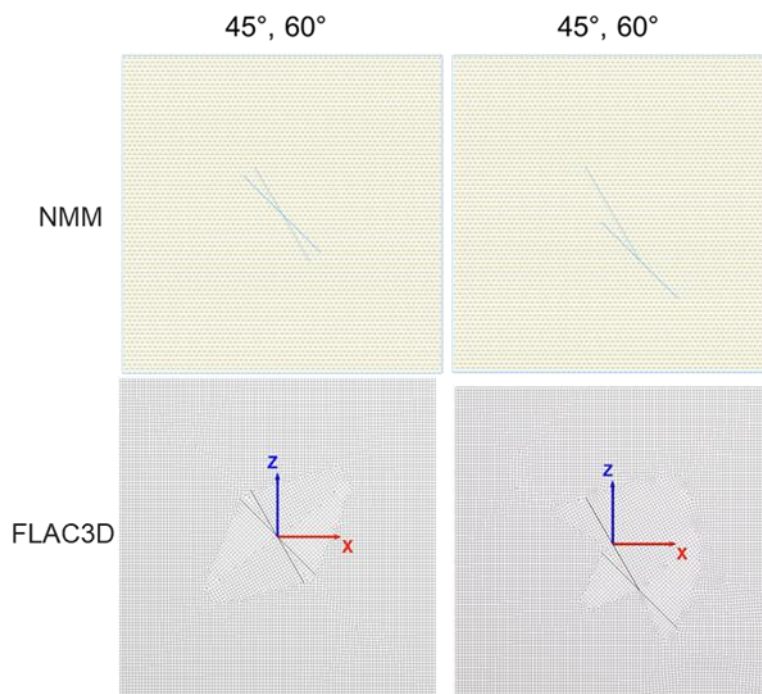


**Figure 5-7.** Two scenarios of two intersecting fractures with orientations of  $45^\circ$  and  $60^\circ$ : NMM mesh (top row), FLAC3D mesh (bottom row).

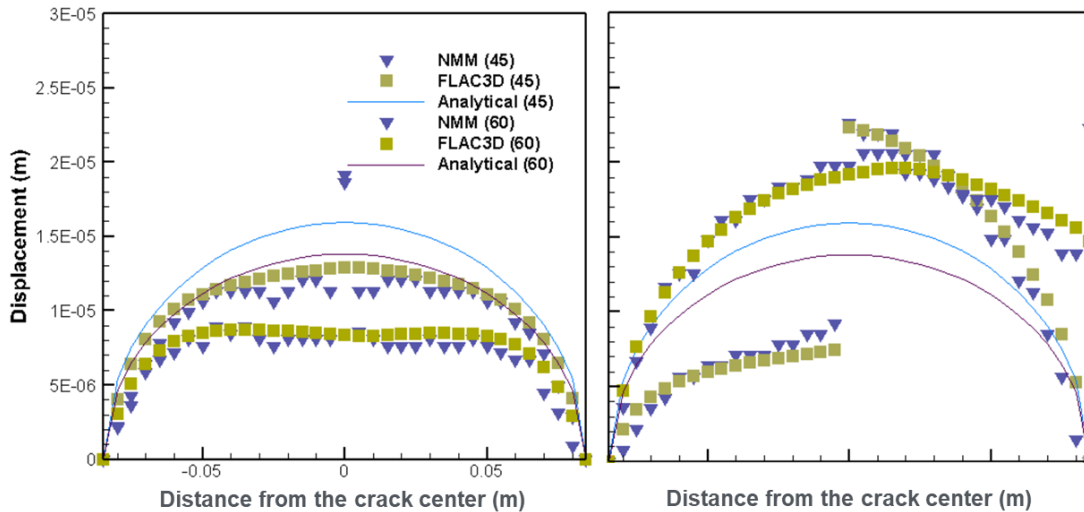


**Figure 5-8.** Shear displacements calculated by NMM and FLAC3D for the two scenarios of two intersecting fractures with orientations of  $45^\circ$  and  $60^\circ$  (geometry and meshes are shown in Figure 5-7).

The results of the NMM and FLAC3D for these two scenarios are shown in Figure 5-8. The two simulators yielded consistent results for both fractures in both scenarios, which provides confidence for the interpretation. For the first scenario, we see that either of the two fractures is no longer divided into two sub-fractures. Instead, the two fractures exhibit similar shearing behavior as the single fractures. The magnitude of shearing is much smaller than for both single  $45^\circ$  and  $60^\circ$  fractures. For the second scenario, we see that the shearing of the  $60^\circ$  fracture and the lower right extent of the  $45^\circ$  fracture both increased because each of these two fractures functions as an extended fracture path for the other to slip along in comparison to intact rock to break through in the case that is provided by the analytical solution. In contrast, shearing of the upper left part of the  $45^\circ$  fracture is surpassed, thus it is decreased from the case of the analytical solution. In addition, the intersection at the  $45^\circ$  fracture causes a significant jump in shearing.

### 5.2.3.2 Simplifying Intersecting Fractures with Major Path(s)

Based on the simulation results obtained for different scenarios of two intersecting fractures, we have one important question to ask:

- *Can we simplify the intersecting fractures with major path(s)?*

Figure 5-9 lists nine possible scenarios of two intersecting fractures with fixed orientations in 2D, where the two intersecting angles are denoted as  $\alpha$  and  $\beta$ . For these nine scenarios: (a) represents the two fractures cutting through each other; (b) and (c) represent the same intersecting condition with  $\alpha < 180^\circ$  and  $\beta > 180^\circ$ ; (d)-(g) represent the same intersecting condition with  $\alpha < 180^\circ$  and  $\beta < 180^\circ$ ; and (h) and (i) represent the same intersecting condition with  $\alpha > 180^\circ$  and  $\beta < 180^\circ$ .

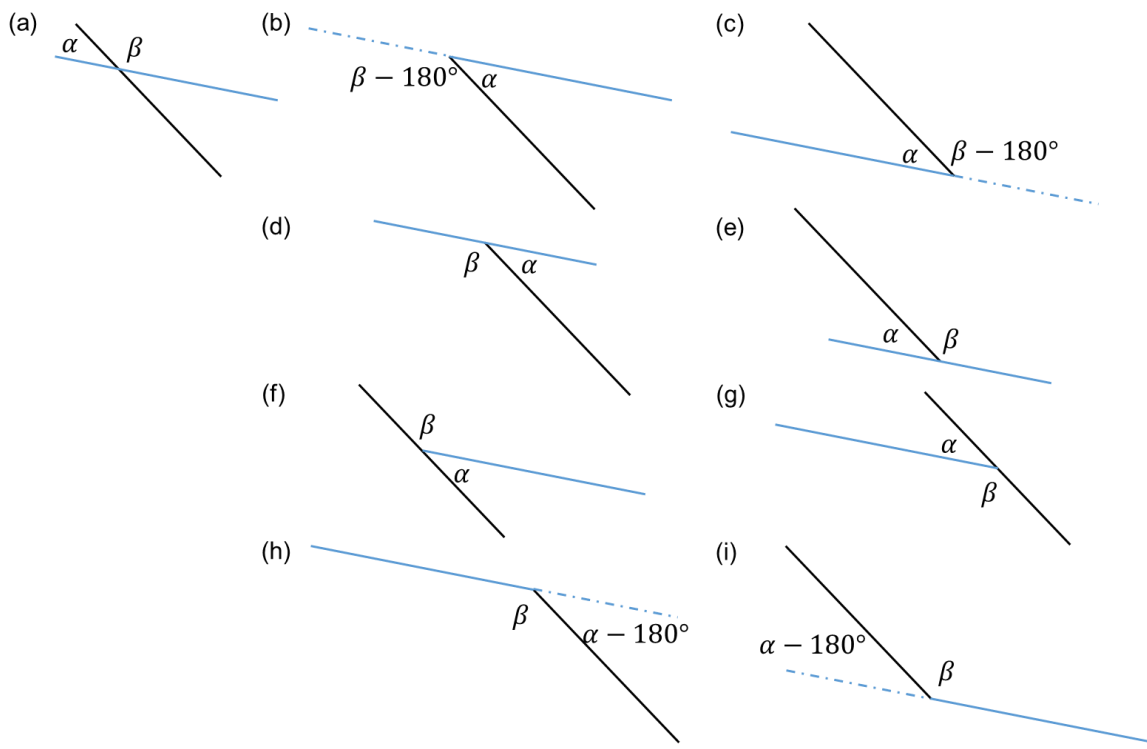


**Figure 5-9.** All the scenarios of two intersecting fractures in 2D.

We developed the following hypothesis:

If  $0 < \alpha - 180^\circ \ll \beta$  or  $0 < \alpha \ll \beta$ , the two intersecting fractures can be simplified as a major path.

This hypothesis can be valid if there are  $n$  pairs of two intersecting fractures forming a discrete fracture network (DFN), which satisfy  $0 < \alpha_i - 180^\circ \ll \beta_i$  or  $0 < \alpha_i \ll \beta_i$  ( $0 < i \leq n$ ).

In order to test this hypothesis, we conducted simulations for all the scenarios as shown in Figure 5-10. In all of these scenarios, we compared the results of stress and displacement distributions of intersecting DFNs (shown as blue lines) with those of hypothetical single major paths (shown as dashed yellow lines). The intersecting DFNs include two, four and five intersecting fractures with different intersecting angles.

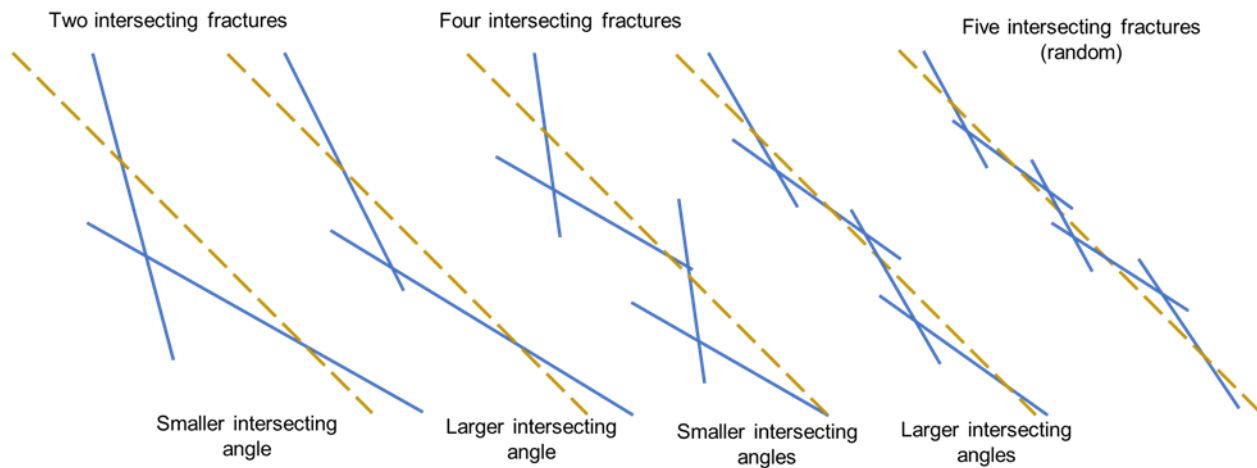


**Figure 5-10.** Intersecting fractures (blue lines) and hypothetical single major paths (yellow lines).

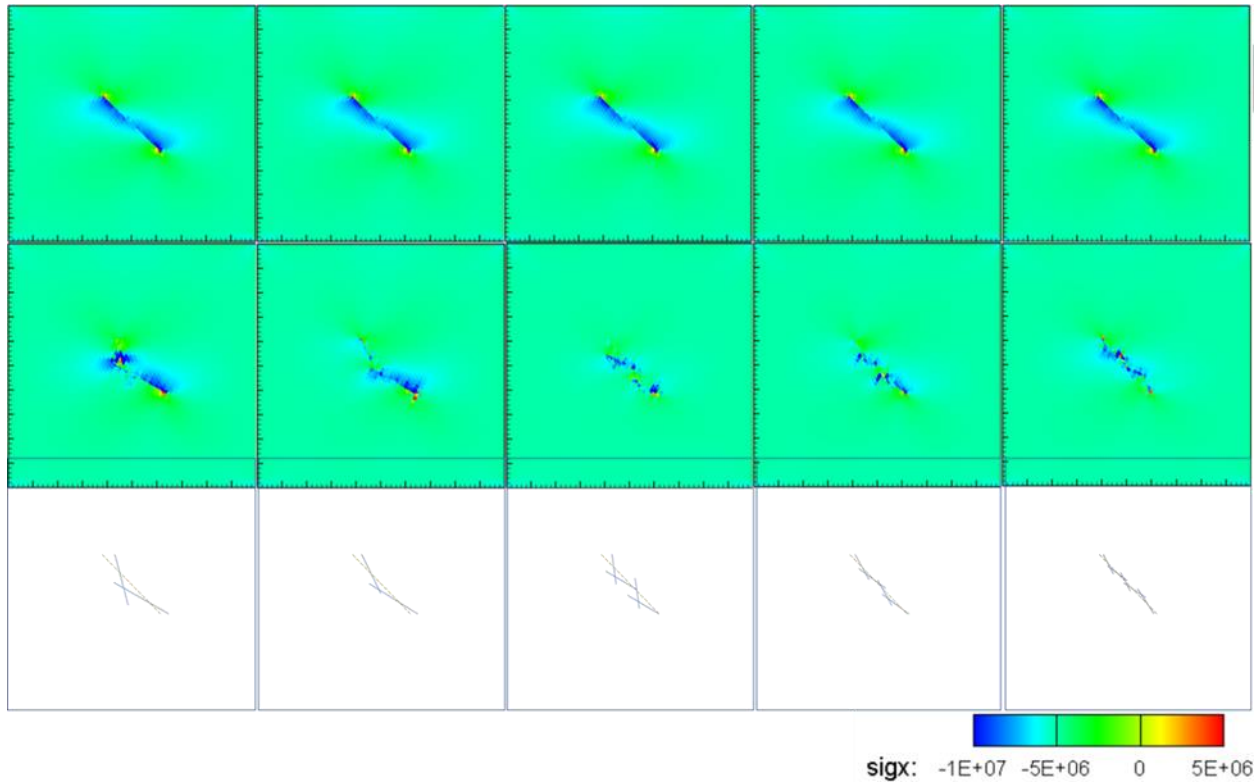


**Figure 5-11.** NMM calculated horizontal stress in domains involving a major path (top row) and DFNs (middle row) with geometry shown in the bottom row (units are Pascals).

We compared the distributions of the stress tensors as well as displacements for domains that contain DFNs against the results for domains that contain hypothetical single major paths. In Figure 5-11, we selectively show the results of the horizontal stress comparison. As we can see, despite the differences within local areas that are adjacent to the fracture tips and intersections, the intersecting DFNs do not exhibit intrinsic discrepancies in the stress distribution compared to the single major paths. Another interesting aspect that we observed is that, when there are more and shorter intersecting fractures (e.g., five intersecting fractures on the right), the intersections play a less important role than that of two intersecting fractures. This is perhaps due to the domain size effect. In summary, the simulations demonstrate that the hypothesis is valid when there is a single major path that can be simplified from a number of intersecting fractures satisfying the following conditions:  $0 < \alpha - 180^\circ \ll \beta$  or  $0 < \alpha \ll \beta$  for every two intersecting fractures.

Additionally, we investigated whether there are several major paths (MP) that can be simplified from DFNs that each subset of those satisfy  $0 < \alpha - 180^\circ \ll \beta$  or  $0 < \alpha \ll \beta$ . Figure 5-12 shows the scenarios involving two, four and six major path(s) that are hypothetically simplified from the DFNs and the geometry of the domain. We also extracted points from two profiles of the second scenario (middle column) to compare the results of the NMM and FLAC3D.

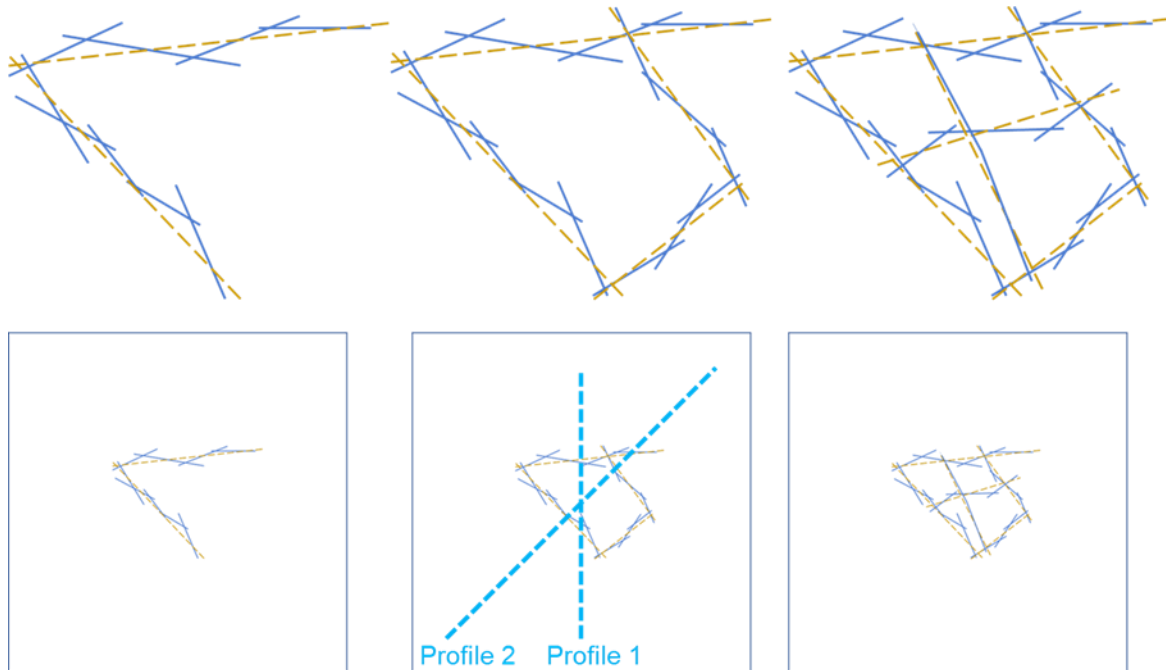


**Figure 5-12.** Geometry (top row) of intersecting fractures (blue lines) and hypothetical single major paths (yellow lines) and the simulation domain (bottom row).

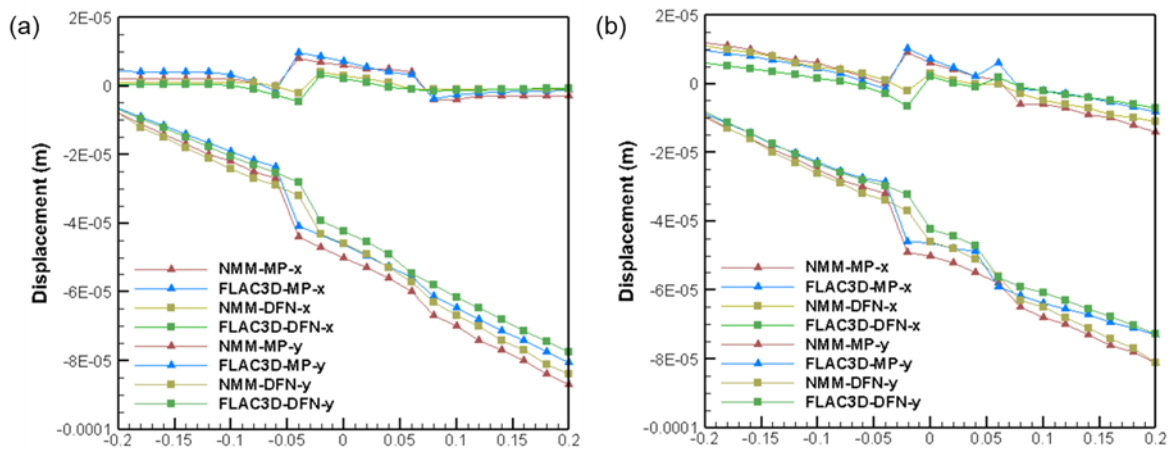


**Figure 5-13.** Comparison of displacement results between NMM and FLAC3D of (a) Profile 1 and (b) Profile 2.

The comparison of calculated displacements between NMM and FLAC3D for both Profile 1 and Profile 2 of the scenario that involves four major paths are shown in Figure 5-13. As we can see, (a) the results of NMM and FLAC3D are consistent, and (b) despite the local deviation of displacements due to intersections of intersecting short fractures, the overall distributions of displacements are consistent for the scenarios involving DFNs and major paths.

We further compared the stress distribution in domains that contain major paths (top row) and intersecting DFNs (middle row), which are shown in Figure 5-14. We see that the scenario that involves two major paths (left) results in a more significant difference of stress between the major path(s) and the DFNs due to stress concentration in local areas near the intersections. With the increase of the major path(s) and DFNs, less stress concentration is developed at the intersections. Instead, the stress is more concentrated at the outer boundaries and corners. It is also interesting to note that, populating more fractures or major paths near the center axes (from the middle column to the right column, Figure 5-14) does not release the stress concentration from the outer boundaries and corners under this specific loading condition and domain dimension, so that both hypothetical major paths (top) and DFNs domains exhibit the same behavior. The consistent distribution of stress for domains that contain major paths and for domains that contain DFNs demonstrate that the hypothetical major paths can be used to approximate the DFNs even if they intersect.

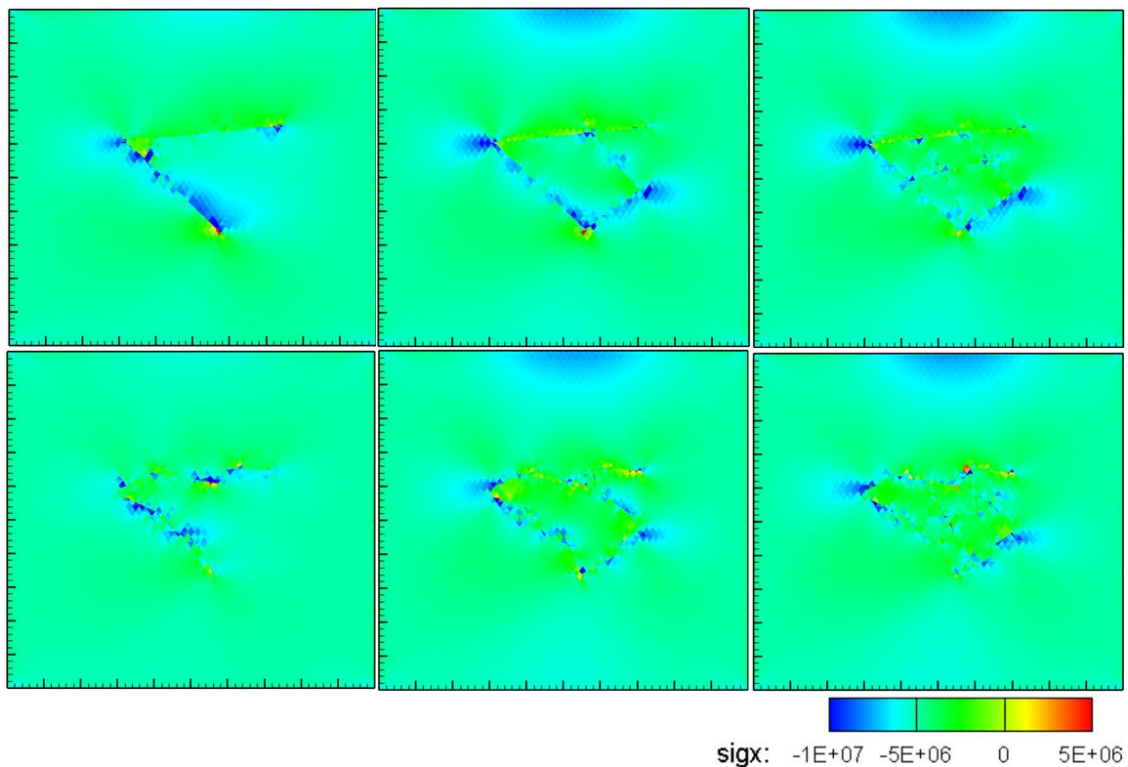


**Figure 5-14.** Calculated horizontal stress (unit: Pa) in domains involving intersecting major paths (top row) and intersecting DFNs (bottom row).

### 5.2.4 Discussion

In this section, we present the results of numerical simulations of different scenarios of shearing of two intersecting fractures, to test a hypothesis that single major paths may exist if the intersecting angles satisfy certain conditions. In order to test this hypothesis, we conducted simulations for scenarios from one major paths to six intersecting major paths and found that the displacements and stress distributions in the domains are consistent for DFNs and major paths, despite local stress concentrations and displacement jumps due to local intersections of short fractures. We also observed that increasing the number of DFNs or major paths in the center does not change the distribution fundamentally as the stress concentration primarily occurs at the outer boundaries and corners for this specific loading conditions and dimension. We assume that further increasing the number of DFNs (as shown in Figure 5-15), the hypothetical major paths are still valid. If increasing the number of DFNs with one more order beyond the right column of Figure 5-15, we may reach a domain that can be assumed as an equivalent continuum model. Thus, using major paths to represent complicated DFNs — we name this as the simplified DFN approach— provides an efficient approach to model the shearing and contact dynamics of fractures. This new simplified DFN approach can potentially reduce the computational load significantly that DFN approaches suffer without compromising the accuracy associated with capturing the stress concentration of individual fractures that may not be captured in equivalent continuum approaches. As a result, we showed that the simplified DFN approach can be used to fill the gap between the DFN and the equivalent continuum approach.

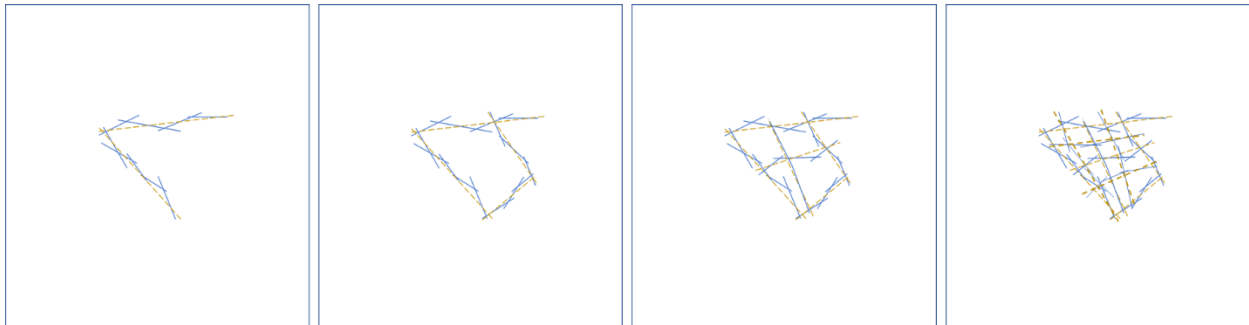


**Figure 5-15.** Increased number of DFNs (blue lines) and major paths (dashed yellow lines) in the center area.

However, in all the proof-of-concept numerical investigations, we assumed in advance the major path(s) for each DFN scenario. These pre-assumed major path(s) may not be the optimized ones—the optimized major paths represent the intersecting fractures with the least deviation of results such as shearing and normal displacements and stress. To obtain the optimized major path(s), we will need to compare different major paths for evaluating their consistency in terms of displacement and stress with the DFNs. With sufficient data and evaluation metrics, it will be promising to use machine learning to derive the optimized major paths.

## 5.3 DECOVALEX-2023 Task G

### 5.3.1 Work scope and team

DECOVALEX is an international research project comprising participants from industry, government and academia, focusing on development and understanding of models and codes in complex coupled problems in subsurface geological and engineering applications. DECOVALEX-2023 model comparison project runs from 2019 to 2023. The theme of Task G is Safety Implications of Fluid Flow, Shear, Thermal and Reaction Processes within Crystalline Rock Fracture NETWORKS (SAFENET). The focus of DECOVALEX-2023 Task G is to analyze the results of the laboratory scale experiment, designed to link micro-scale THMC effects acting on fracture surfaces and asperity contacts with emergent fracture properties such as permeability. The experimental task concept with increasing complexity is:

- Mechanical results that are derived from constant normal load (CNL) direct shear tests and constant normal stiffness (CNS) direct shear tests as well as high-resolution fracture surface scans (TUBAF);
- Thermal-mechanical results that are obtained from tri-axial tests conducted at KICT (Korea Institute of Civil Engineering and Building Technology) with focus on shear processes triggered by thermal stresses;
- THMC and HMC results that are obtained with the GREAT cell (University of Edinburgh) with focus on fundamental shear processes under complex 3D stress states.

These experiments will be conducted on typical granite samples with pre-existing well-characterized discontinuities. The experiments are complementary, allowing for inclusion and exclusion of hydraulics, permitting a clear separation of key processes. The experimental work is focused on characterizing displacements and permeability changes resulting from different thermal, mechanical and hydraulic loads on the system. It is expected that research teams will apply and develop existing constitutive models for fracture characterization, and hence improve fundamental physical understanding of these complex processes as well as improving modeling predictive capabilities.

The scientific task concept is:

- To further increase our understanding of THMC processes in crystalline and indurated rocks introducing new experimental concepts and modeling approaches, in particular concerning TM processes governing fluid flow through fracture networks under changing mechanical shear, thermal and geochemical gradients induced by heat generating waste emplacement;
- To derive better understanding of crystalline systems using unique multi-scale experimental data combined with state-of-the-art numerical modeling techniques and thereby improving environmental safety assessment knowledge and regulation.

The novelty of the task is a combination of novel experimental and modeling approaches for THMC coupled processes in brittle/crystalline rocks. The combined approach will further improve our understanding of fracturing processes including fracture networks. Moreover, the concept will allow for the transfer from experimental lab to an *in-situ* scale:

- Unique 3D stress control on fracture networks (GREAT cell);
- Thermal stress impact on pre-existing fracture surfaces (KICT lab);
- Combination of model calibration and “blind” prediction (for model validation) with measured data and long-term prediction for PA/SA impact evaluation.

There are seven teams participating in this Task, namely DynaFrac from Germany using the Particle Flow Code (PFC), LBNL using the NMM and FLAC3D, Korea Institute of Geoscience and Mineral Resources (KIGAM) from Korea using 3DEC, a joint team by Quintessa, University of Edinburgh and Radioactive Waste Management from United Kingdom using COMSOL, Institute of Rock and Soil Mechanics, Chinese Academy of Sciences from China using CASRock, Canadian Nuclear Safety Commission (CNSC) from Canada using COMSOL, Helmholtz Center for Environmental Research (UFZ) from Germany using a finite-element based code called OpenGeoSys (OGS), Technische Universität Bergakademie Freiberg (TUBAF) from Germany using OpenGeoSys, Sandia National Laboratory using COMSOL, PFLOTRAN and FRACMAN, and a new team joined in FY22-- Korea Atomic Energy Research Institute (KAERI) from Korea using TOUGH-3DEC.

### 5.3.2 LBNL Work for DECOVALEX 2023 Task G

Currently, investigations of thermal shearing have mainly been conducted using laboratory experiments. Figure 5-16 shows one of these experiments where a cubic granite sample with a single fracture in its diagonal (Figure 5-17a) is subjected to an increase in temperature under mechanically constrained conditions, thereby inducing thermal shearing (Figure 5-17b) (Sun et al., 2021). Such experiments offer valuable insights into the physics of thermal shearing via measurements of fracture displacements, acoustic emissions, stress changes, etc. However, such laboratory experiments can be time-consuming and hence cannot be readily repeated to examine different granite samples with different thermo-mechanical (TM) properties, which is necessary to assess the physics of thermal shearing. In addition, due to the difficulties in controlling some of the aspects in laboratory experiments, it is challenging to provide predictive understanding of thermal shearing if only using the experimental approach alone. For instance, the inability to control the asperity distribution of tensile-split fractures in laboratory tests hinders the evaluation of how fracture geometry influences thermal shearing, which is a critical factor in understanding this phenomenon.

Numerical modeling is a valuable tool to provide such a predictive understanding of the physics of thermal shearing. However, most numerical simulations up to date were performed by representing a fracture either as 2D rough surfaces or 3D flat surfaces. These simplifications may not capture the intrinsic behavior of shearing of 3D natural fractures, which are rough, because asperities can play a major role in shearing. Hence, it is necessary to employ a 3D rough fracture model to assess the physics of thermal shearing.

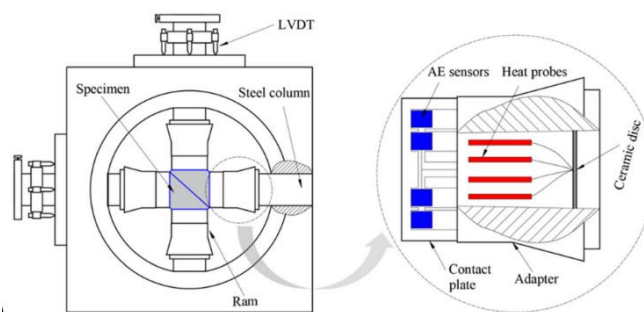


**Figure 5-16.** The experimental setup of thermal shearing of a single granite fracture (after Sun et al. (2021)).

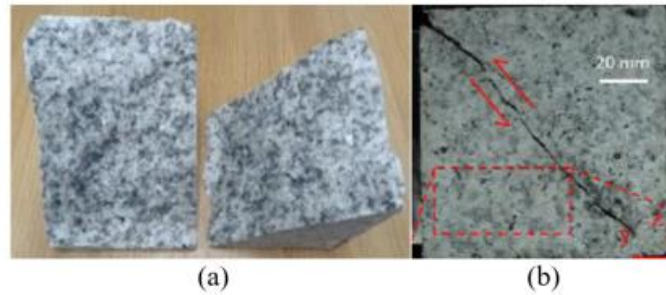


**Figure 5-17.** A granite sample with a single rough fracture (after Sun et al. (2023)): (a) the sample with a tensile-split rough fracture; (b) the sample during thermal shearing.

In this study, thermal shearing of a 3D rough fracture is numerically simulated, and the results are compared against measurements from a laboratory experiment (Sun et al., 2023), in order to identify key thermo-mechanical properties of the fracture and/or the host rock that control thermal shearing. FLAC3D (Itasca Consulting Group, 2020), was used to construct a 3D rough fracture model and to simulate its TM coupled behavior during thermal shearing. Details of the numerical modeling as well as the results of the simulation are provided in the following sections.

### 5.3.2.1 Modeling Fractures as Interfaces in FLAC3D

In order to model the mechanical interactions between separate surfaces (such as fractures) within the model domain, a methodology for modeling interfacial behaviors is necessary. FLAC3D can be used to simulate the interfaces with its built-in contact models. Figure 5-18 shows a detailed contact model, which consists of the normal (i.e.,  $k_n$ ,  $D$ ,  $T_s$ ) and tangential ( $k_s$ ,  $S$ ,  $S_s$ ) components. Detailed descriptions of each component are provided below.

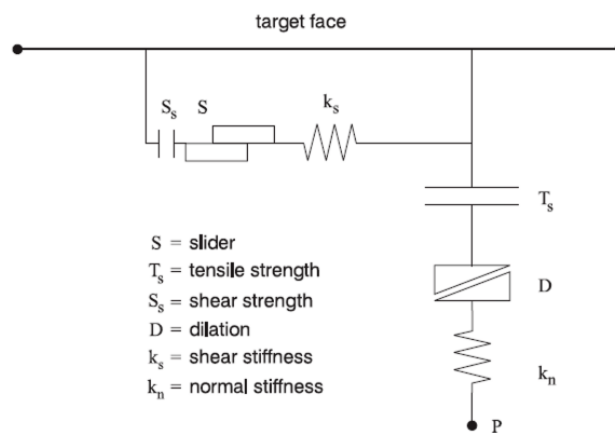


**Figure 5-18.** Modeling of interface behavior in FLAC3D (Itasca Consulting Group, 2020).

The tangential contact behavior is modeled with a linear shear spring; the contact shear force is generated when a node moves relative to the contacting surface in the tangential direction, as represented by the following equation:

$$F_s = k_s \Delta u_s A \leq F_{smax} \quad (5-7)$$

where,  $F_s$  is the contact shear force,  $k_s$  is the shear stiffness (i.e., stiffness of the shear spring),  $\Delta u_s$  is the relative displacement between the node and the surface, and  $A$  is the representative contact area of the node. This equation also indicates the maximum contact shear force,  $F_{smax}$ , which is determined from Coulomb's friction law, as shown in the equation:

$$F_{smax} = S + S_s A = (F_n - p_{pore} A) \tan \phi_I + S_s A \quad (5-8)$$

where  $S$  is the frictional (slider) strength (in the units of force),  $S_s$  is the shear strength, i.e., tangential cohesion (in the unit of stress),  $F_n$  is the normal force applied on the contact surface,  $p_{pore}$  is the pore pressure, and  $\phi_I$  is the friction angle between the node and surface materials.

Like the tangential contact behavior, the normal contact behavior is also modeled with a linear spring. The contact normal force develops when a node is detected with penetration to a contact surface in the model, and the magnitude of the normal force is linearly proportional to the penetration distance as shown in the following equation:

$$F_n = k_n u_n A + DA \geq F_{nmin} = T_s A \quad (5-9)$$

where  $F_n$  is the contact normal force,  $k_n$  is the normal stiffness (i.e., stiffness of the normal spring),  $u_n$  is the penetration distance,  $A$  is the representative contact area. Note that compression is positive for the contact normal force. The minimum normal force ( $F_{nmin}$ ) is specified as the tensile strength ( $T_s$ ) multiplied by the areas ( $A$ ). The normal contact calculation also includes a dilation component ( $D$ ), which is defined as follows:

$$D = k_n \left( \frac{(F_{s>max} - F_{smax})}{(k_s A)} \right) \tan \psi_I \quad (5-10)$$

where  $F_{s>max}$  is the shear force upon yielding before correction (i.e., predicted shear force above  $F_{smax}$ ), and  $\psi_I$  is the interface dilation angle. The term  $\left( \frac{(F_{s>max} - F_{smax})}{(k_s A)} \right)$  indicates plastic shear displacement; it is converted into plastic normal displacement by multiplying it with the tangent of the dilation angle,  $\tan \psi_I$ . Finally, the product is converted into the normal force by multiplying it with the normal stiffness,  $k_n$ .

The shear and normal interface stiffnesses are calculated as follows:

$$k_s = k_n = 10 \max \left( \frac{\left( \frac{K + 4\frac{G}{3}}{\Delta z_{min}} \right)}{\Delta z_{min}} \right) \quad (5-11)$$

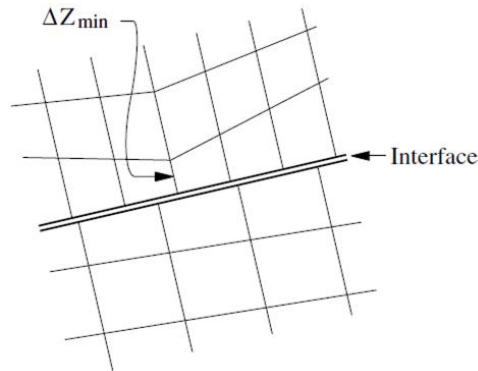


**Figure 5-19.** The smallest zone width ( $\Delta z_{min}$ ) near the interface (Itasca Consulting Group, 2020).

where  $K$  and  $G$  are the bulk and shear moduli of the interface materials, respectively. The values of the stiffer side of the interface are generally used to avoid excessive penetration. The smallest zone width,  $\Delta z_{min}$ , whose value is obtained after the mesh is created as the smallest mesh width at the interfaces, is defined as shown in Figure 5-19.

### 5.3.2.2 TM Coupling in FLAC3D

The FLAC3D was used for both nonlinear continuous-discontinuous mechanical analysis and THM analysis (Rutqvist, 2020; Sasaki and Rutqvist, 2021). Here, we describe the relevant results of simulations of TM coupling. The TM coupling in FLAC3D starts from the evaluation of thermal strains as shown below:

$$\underline{\underline{\dot{\epsilon}_T}} = \alpha_T \underline{\underline{\dot{T}}} \underline{\underline{I}} \quad (5-12)$$

where  $\underline{\underline{\dot{\epsilon}_T}}$  is the thermal strain rate tensor,  $\alpha_T$  is the linear thermal expansion coefficient, and  $\underline{\underline{\dot{T}}}$  is the rate of temperature change. The thermal strain is then substituted into the constitutive model to update stresses as shown in the following equation:

$$\underline{\underline{\Delta\sigma}} = H \left( \underline{\underline{\sigma}}, \underline{\underline{\dot{\epsilon}}}\Delta t - \underline{\underline{\dot{\epsilon}_T}}\Delta t \right) \quad (5-13)$$

The thermal strain increment  $\underline{\underline{\dot{\epsilon}_T}}\Delta t$  is subtracted from the total strain increment  $\underline{\underline{\dot{\epsilon}}}\Delta t$  to calculate an elastic strain increment, which is used to update stresses.

The thermal calculations are performed independently from the mechanical calculations (i.e., there is thermal (T) to mechanical (M) coupling through the thermal strain as shown above, but there is no M to T coupling), which is shown below:

$$\rho c_V \dot{T} = q_{TV} - \nabla \cdot \underline{\underline{q_{TS}}} \quad (5-14)$$

where  $\rho$  is the density,  $c_V$  is the specific heat capacity at constant volume ( $c_P$ , which is the specific heat capacity at constant pressure, can be used as well for most solids and liquids),  $q_{TV}$  is the volumetric heat

flux per unit volume, and  $q_{TS}$  is the surface heat flux per unit area provided through heat conduction, which is governed by Fourier's law as shown below:

$$q_{TS} = -\lambda_T \nabla T \quad (5-15)$$

where  $\lambda_T$  is the thermal conductivity.

### 5.3.2.3 FLAC3D Modeling of Thermal Slip of Fractures

Understanding of shear reactivation of pre-existing discontinuities for brittle host rocks is an area of considerable interest for radioactive waste disposal. In particular, the potential for existing features to undergo shear displacements and related changes in permeability as the result of coupled thermal, mechanical, and hydrological effects can all have significant impacts on repository safety functions (e.g., creating permeable pathways or, for very large displacements, mechanical damage of waste packages).

#### Model Geometry and Material Properties

The 3D fracture models created with FLAC3D are shown in Figure 5-20. The model dimensions for the flat fracture model are 10 cm by 10 cm by 10 cm with the fracture angle of 42°, whereas those for the rough fracture model are approximately 8 cm by 9.5 cm by 10 cm with the fracture angle of 45° from the horizontal plane. The model consists of the top and bottom wedges with the matching fracture interfaces, and the total number of “zones” (which is equivalent to linear stress and strain finite elements) was roughly 9,000 and 100,000 for the flat and rough fracture models, respectively. Figure 5-21 shows the details of the fracture interface, which is discretized with fine meshes in the case of the rough fracture model, so that the asperities of the tensile-split granite fracture can be reproduced in the model. The constructed model was assigned with the TM properties provided in Table 5-1 and with the fracture mechanical properties provided in Table 5-2. Mechanically, the rock wedges are assumed to be linear isotropic elastic without failure and the fracture interface was modeled with linear normal and shear springs (i.e., constant normal and shear stiffnesses) with the classic Coulomb friction failure criterion. It was assumed that the fracture has zero cohesion and thus resists shearing only by friction—which consists of two components: the intrinsic friction of the geomaterials as well as the asperity distribution in the case of the rough fracture model.

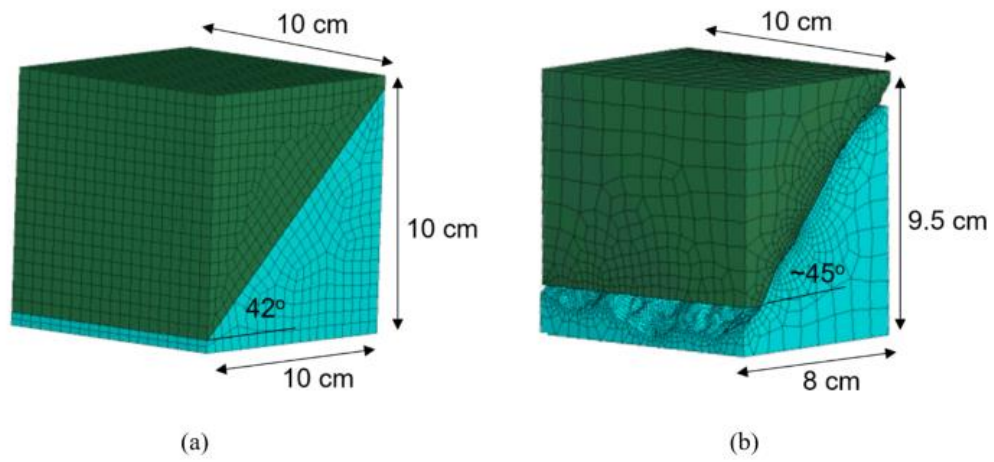


**Figure 5-20.** The dimensions of the (a) flat and (b) rough fracture models.

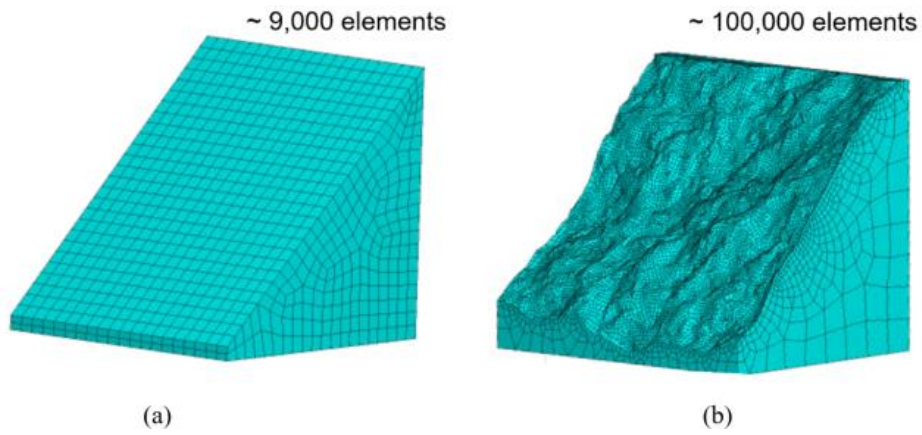


**Figure 5-21.** Overview of the fracture interface of the (a) flat and (b) rough fracture models.

**Table 5-1.** The TM properties of the host rock.

Host rock property	Value
Bulk density (kg/m <sup>3</sup> )	2609
Young's modulus (GPa)	55.09
Poisson's ratio (-)	0.275
Linear thermal expansion coefficient ( $\mu\epsilon/K$ )	6.49
Thermal conductivity (W/(m*K))	2.19
Specific heat (J/(kg*K))	645

**Table 5-2.** The mechanical properties of the fracture interface.

Fracture property	Value
Normal stiffness (GPa/mm)	5.509
Shear stiffness (GPa/mm)	5.509
Cohesion (MPa)	0
Friction angle (°)	30

### Simulation Steps

The simulations consisted of two steps: temperature only simulations with the flat fracture model, and mechanical only simulations with the rough fracture model. In the temperature only simulation, the temperature evolution measured during the experiment (Sun et al., 2021) was used to validate the temperature distribution calculated in FLAC3D. Figure 5-22 shows the boundary conditions specified for the temperature only simulation. At the top and bottom boundary, measured time-varying temperature evolution was directly specified, and on the lateral boundaries, convection boundary conditions were specified. The heat transfer coefficient at the left and right boundary was assigned a higher value than that for the front and back boundary, in order to match the experimental temperature evolution. Considering the coupling between thermal (T) and mechanical (M) processes is mostly one-way in this case (i.e., T impacts M), the temperature distributions that best matched the experimental data were then imported into the mechanical only simulation with the rough fracture model to simulate thermal shearing. Note that this was done to overcome the difficulty of conducting coupled TM simulation with the rough fracture model as thermal flux across finely-meshed rough fracture interfaces caused convergence failure.

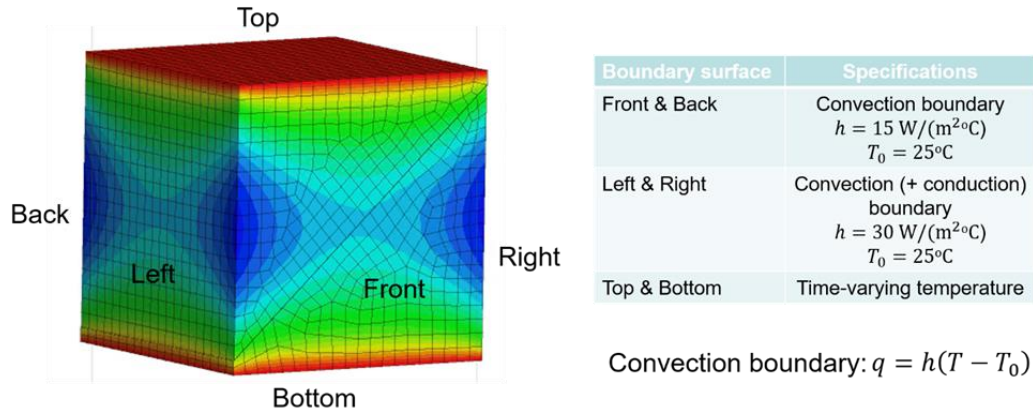


**Figure 5-22.** The boundary conditions for the thermal only simulation with the flat fracture model.

The mechanical only simulation was then carried out in two stages (Figure 5-23): the initial equilibrium stage and the thermal shearing stage. In the initial equilibrium stage, a lateral stress of 24.6 MPa and a vertical stress of 3 MPa were applied on the lateral and top boundaries, respectively, whereas the bottom boundary was prescribed with zero surface normal displacement (i.e., roller boundary condition). The out-of-plane boundaries were not applied with any stress or displacement boundary conditions. After equilibrium was achieved in this stage, the lateral stress boundary conditions were replaced with the roller boundary conditions and the temperature distributions obtained in the temperature only simulation were imported into the rough fracture model at 60-second intervals to induce thermal shearing along the fracture. The thermal shearing stage was simulated for 6,000 seconds.

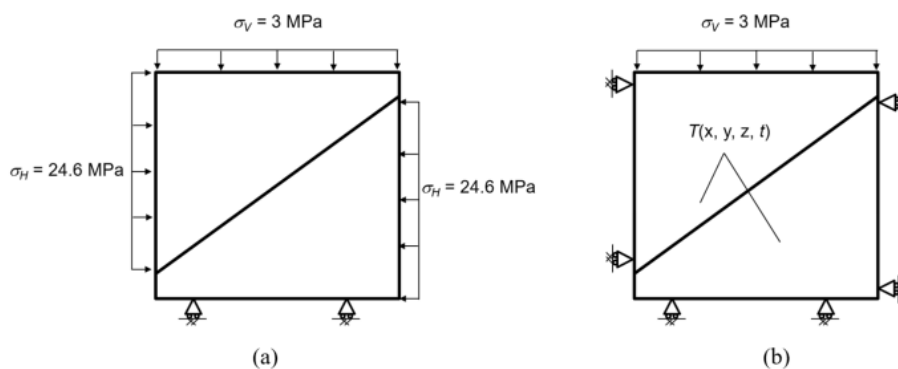


**Figure 5-23.** The boundary condition for the mechanical only simulation with the rough fracture model: (a) equilibrium stage; (b) shearing stage.

In the mechanical only simulation, the values of interface friction angle and the linear thermal expansion coefficient were varied to assess their effect on the thermal shearing (i.e., parametric study). Also, two model configuration cases were employed (Figure 5-24) as part of the parametric study: the mated and unmated interface cases. In the mated fracture case, the matching fracture interfaces on the top and bottom wedges were kept matched with each other during the equilibrium stage and then the following thermal shearing stage was implemented. In the unmated fracture case, on the other hand, the matching fracture interfaces were displaced relative to each other along the fracture plane direction ( $45^\circ$ ) by 2.83 mm and an initial equilibrium was achieved in this unmated configuration. The thermal shearing was then implemented. These two cases were simulated to assess the effect of mated and unmated fracture asperity on thermal shearing.

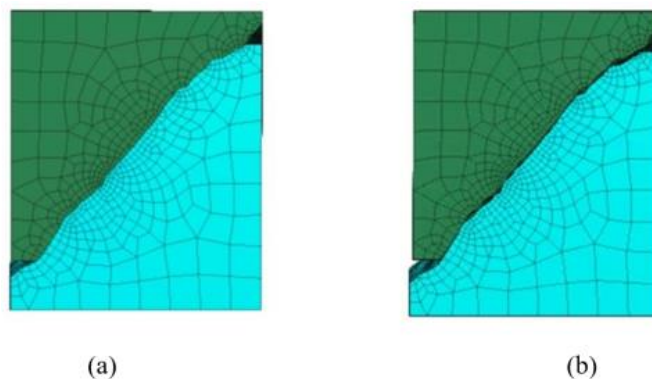


**Figure 5-24.** (a) Mated interface case; (b) unmated interface case.

5.3.2.4 Results

Figure 5-25 shows the data readout locations in the flat fracture model for comparing the measured and calculated temperature evolutions. The red points (T1 through T3) are located on the fracture interface, while the green ones (S1 through S6) are on the front boundary surface. This helps validate that the FLAC3D thermal calculations were done robustly by matching both the internal and surface temperatures.

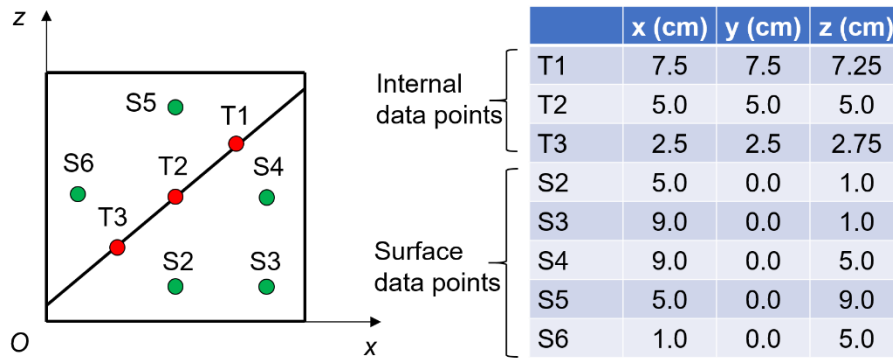


Figure 5-25. Data readout locations in the flat fracture model for the temperature validation.

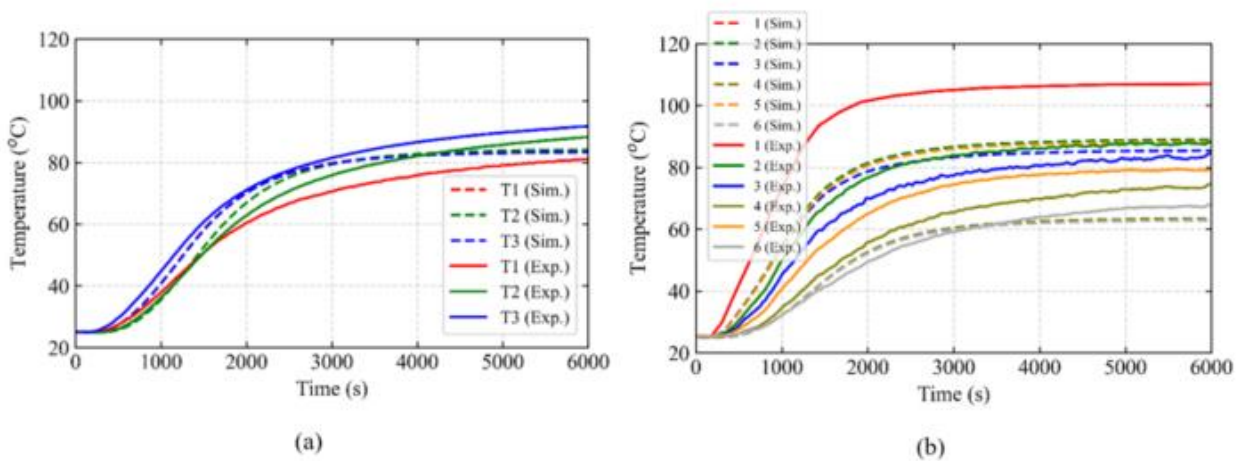
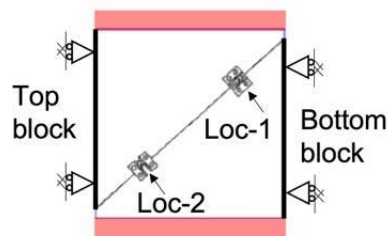


Figure 5-26. Results of the temperature comparison: (a) internal data points; (b) surface data points.

Figure 5-26 shows the results of the temperature comparison. It was found that the match at the internal data points was satisfactory, whereas the match at the surface data points was less, as the simulation overestimated the temperature at S3 and S5 particularly at the early times (~2,000 seconds). This means that the temperature change near the model boundaries was more sensitive to the applied boundary conditions than the temperature change away from the boundaries (e.g., T1-T3). However, this probably does not produce major problems to the thermal shearing modeling as the errors are relatively small and diminish toward the end of the timeframe (6,000 seconds). Hence, the calculated temperature distributions were used to specify temperature change in the rough fracture model in the following mechanical only simulation.

In the mechanical only simulation, the normal and shear displacements along the fracture interface were calculated and compared at the two locations on the boundary surface indicated in Figure 5-27. In addition to the interface displacements, the change in the normal stress at the lateral boundary on the bottom wedge during thermal shearing was also compared.



**Figure 5-27.** Data readout locations for the fracture displacements. The precise locations were estimated from Figure 3 and Figure 5c of Sun et al. (2023).

#### Mated Fracture Case

##### **Interface friction = 40°**

Figure 5-28 shows the results of the thermal shearing stage for the mated rough fracture model when the interface friction angle was set to 40°. It was found that this simulation case could not match the experimental results by a large margin, as the shear displacement was significantly underestimated, and the normal displacement and lateral boundary stress change were significantly overestimated. This shows that the rough fracture model resisted thermal shearing and did not slip as expected, indicating that the friction angle needs to be reduced to match the experimental data, which was done in the next simulation case.

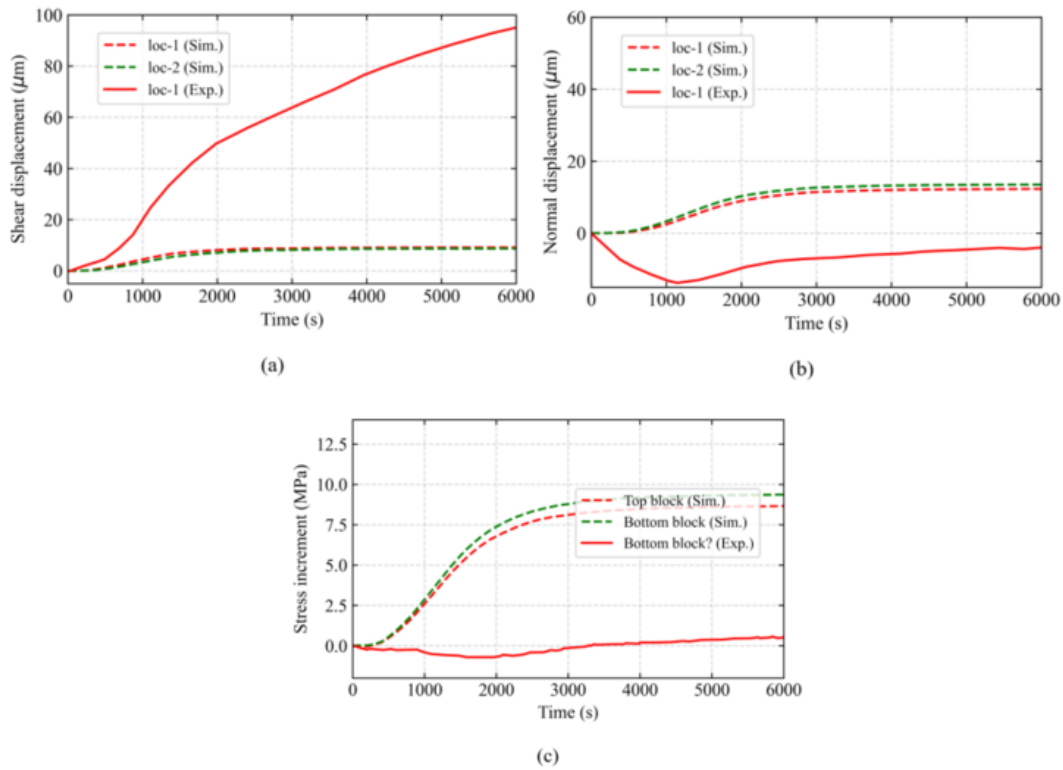


**Figure 5-28.** Results of the thermal shearing comparison (mated fracture case, interface friction angle = 40°): (a) interface shear displacement; (b) interface normal displacement; (c) normal stress at the lateral boundary.

### Interface friction = 30°

Figure 5-29 shows the results of the thermal shearing stage for the mated rough fracture model when the interface friction angle was set to 30°. It was found that reducing the interface friction angle from 40° to 30° did not improve the match between the simulation and experimental observations. The shear displacement along the interface decreased rather than increased (relative to the 40° results), which was against expectation, whereas the lateral boundary stress decreased as expected (indicating the stress release due to the interface slip). This contradiction suggests that the interface slip was concentrated at areas near the lateral boundary and such localized slip near the boundary reduced the potential of slippage in the middle part of the interface where the measurement was taken.

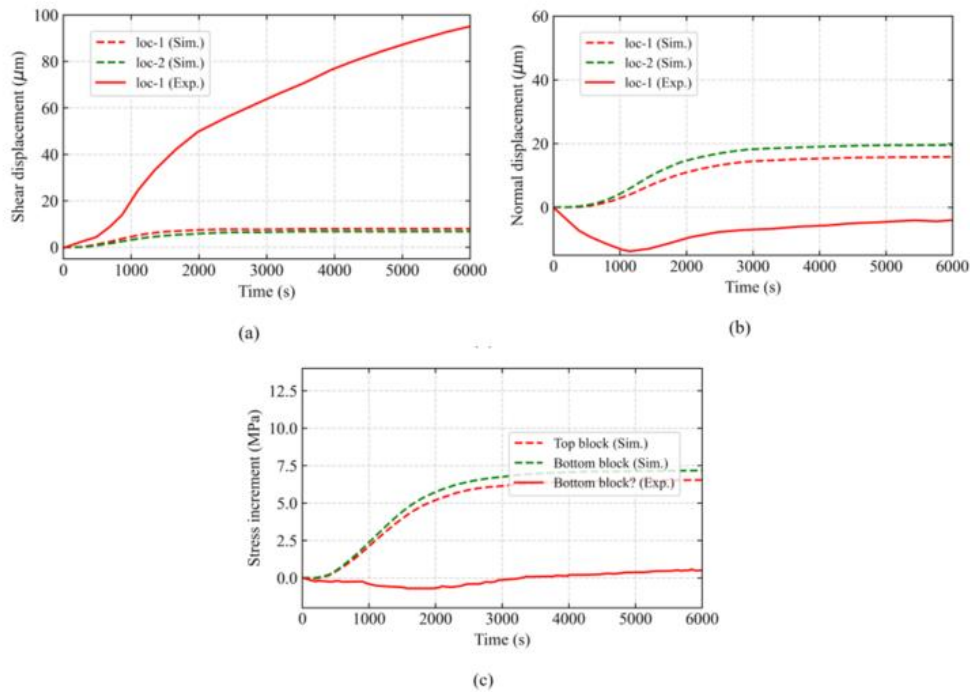


**Figure 5-29.** Results of the thermal shearing comparison (mated fracture case, interface friction angle = 30°): (a) interface shear displacement; (b) interface normal displacement; (c) normal stress at the lateral boundary.

### Interface friction = 25°

Figure 5-30 shows the results of the thermal shearing stage for the mated rough fracture model when the interface friction angle was set to 25°. This and the previous results show that reducing the interface friction angle alone was not effective in matching the experimental data. However, the lateral boundary stress decreased further as expected and the shear displacement remained relatively unchanged compared to the 30° case. As discussed in the 30° results, this suggests that interface slip was indeed enhanced by reducing the friction angle, but it was concentrated near the lateral boundary. This localized slip near the boundary (and localized slip resistance in the middle part of the interface) is attributed to the asperity of the rough fracture surface, which is addressed in the unmated interface case shown later.

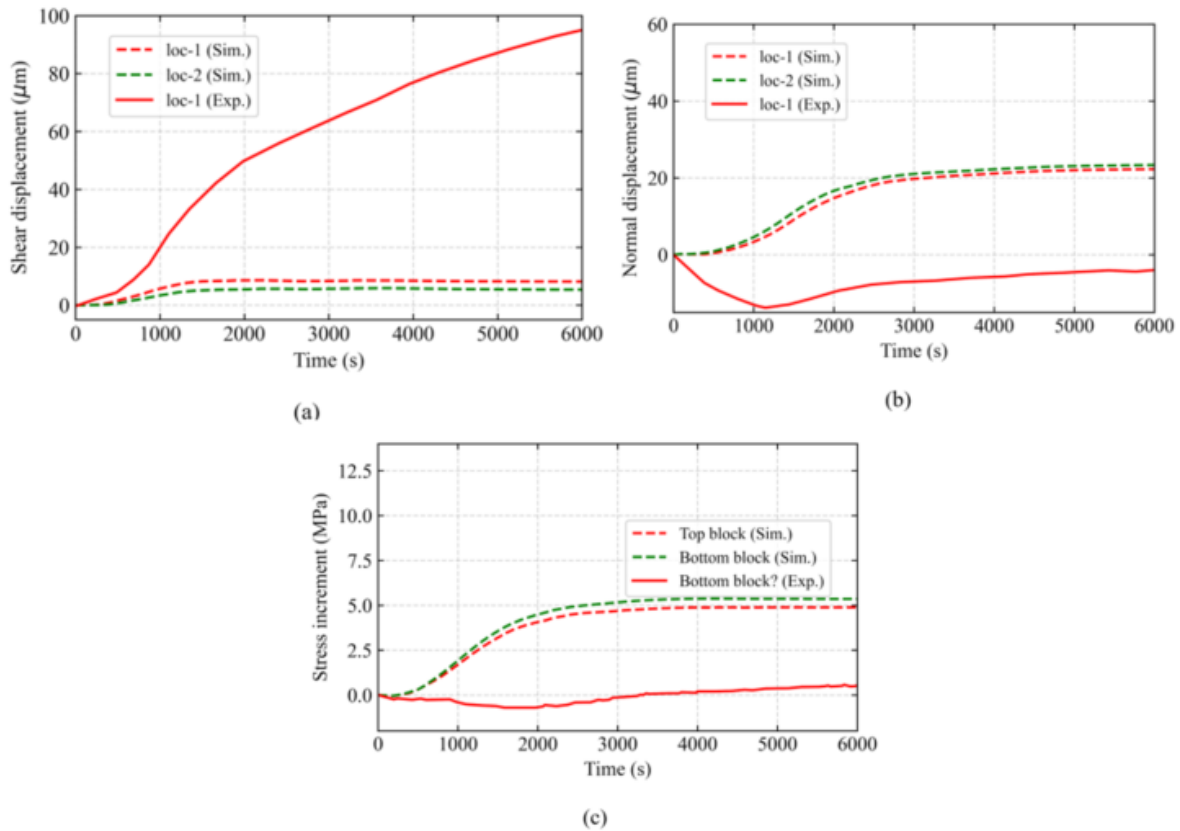


**Figure 5-30.** Results of the thermal shearing comparison (mated fracture case, interface friction angle = 25°): (a) interface shear displacement; (b) interface normal displacement; (c) normal stress at the lateral boundary.

**Thermal expansion coefficient = 13e-6 (K<sup>-1</sup>)**

Figure 5-31 shows the results of the thermal shearing stage for the mated rough fracture model when the thermal expansion coefficient was increased from 6.49e-6 (K<sup>-1</sup>) to 13e-6 (K<sup>-1</sup>) (the interface friction angle was set to 30°). Enhanced interface slip was expected as greater thermal expansion would cause greater displacements during temperature increase. However, it was found that the interface shear displacement was relatively unchanged compared to the 6.49e-6 (K<sup>-1</sup>) case, whereas the interface normal displacement and lateral stress significantly increased. This suggests that the interface asperity increased due to thermal expansion and that prevented slip from occurring. Thus, it is important to look into the effect of asperity, which is addressed in the following section by examining the unmated interface modeling case.

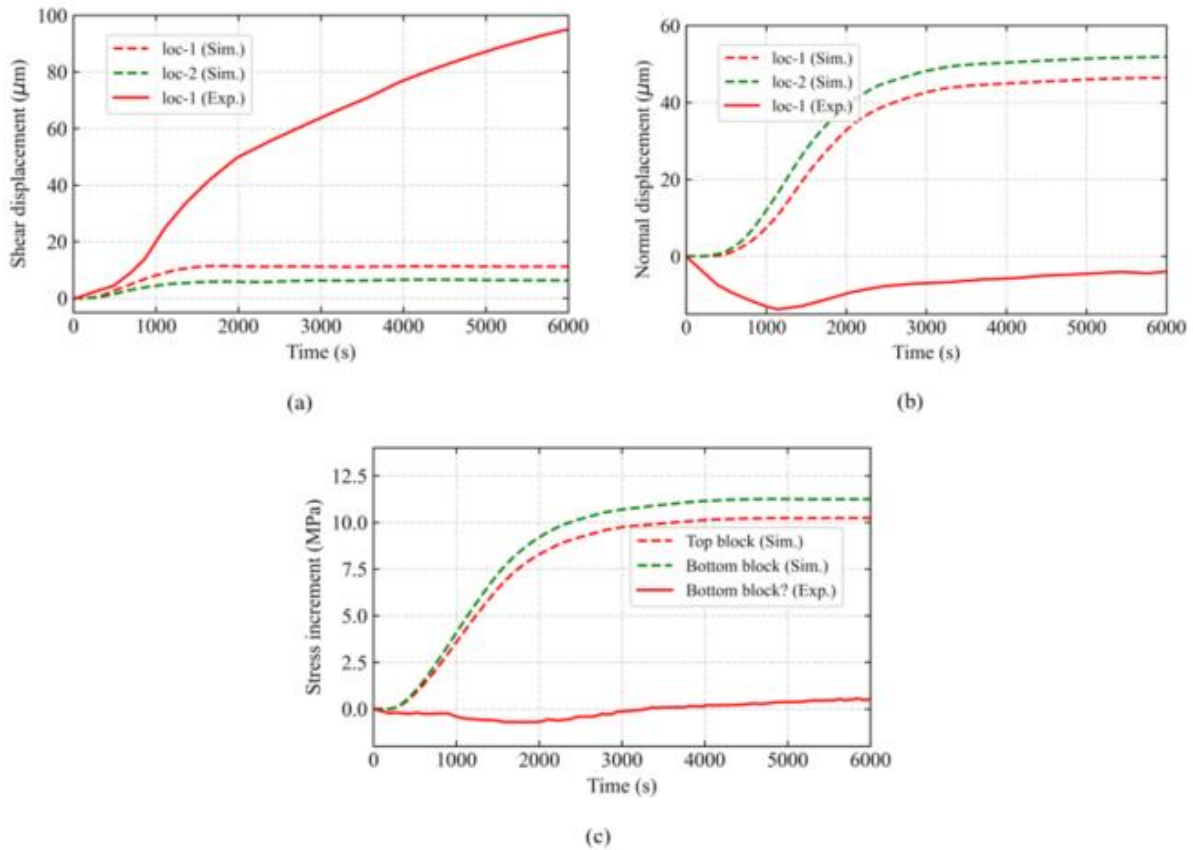
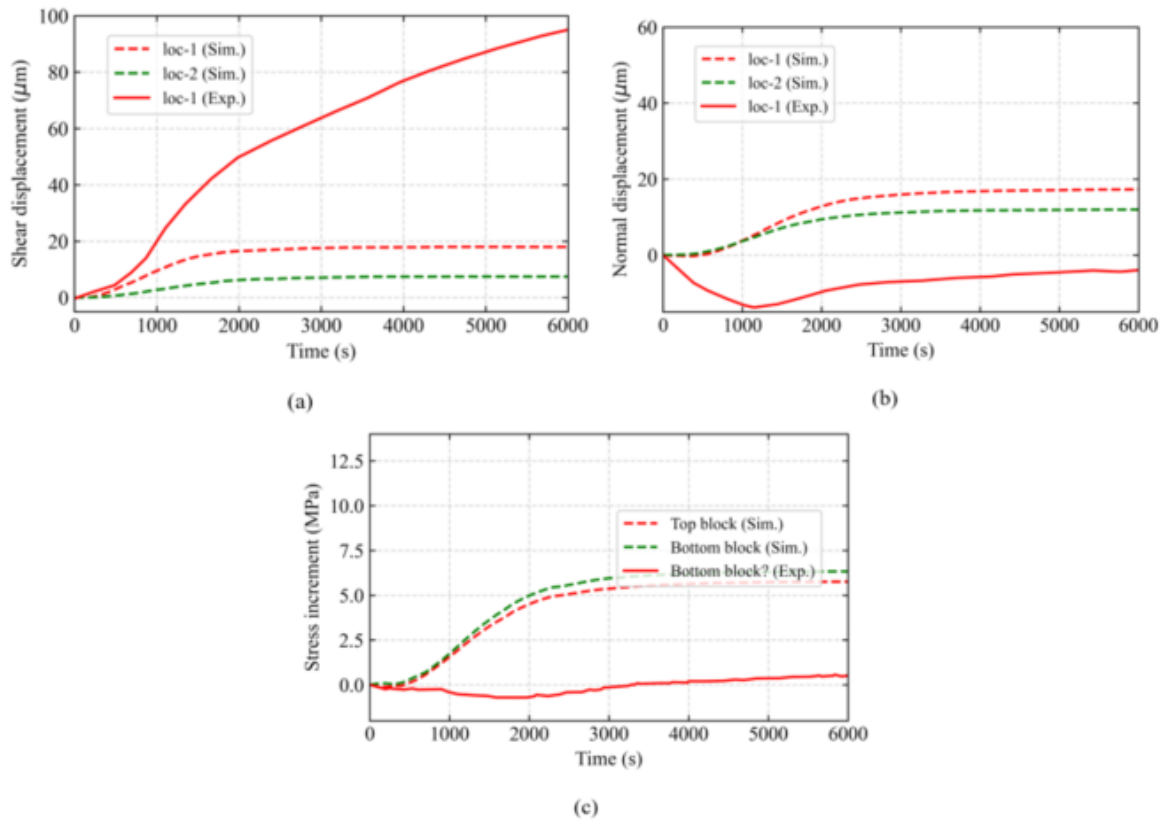


**Figure 5-31.** Results of the thermal shearing comparison (mated fracture case, thermal expansion coefficient =  $13 \cdot 10^{-6}$ ): (a) interface shear displacement; (b) interface normal displacement; (c) normal stress at the lateral boundary.

### Unmated Fracture Case

#### Interface friction = $40^\circ$

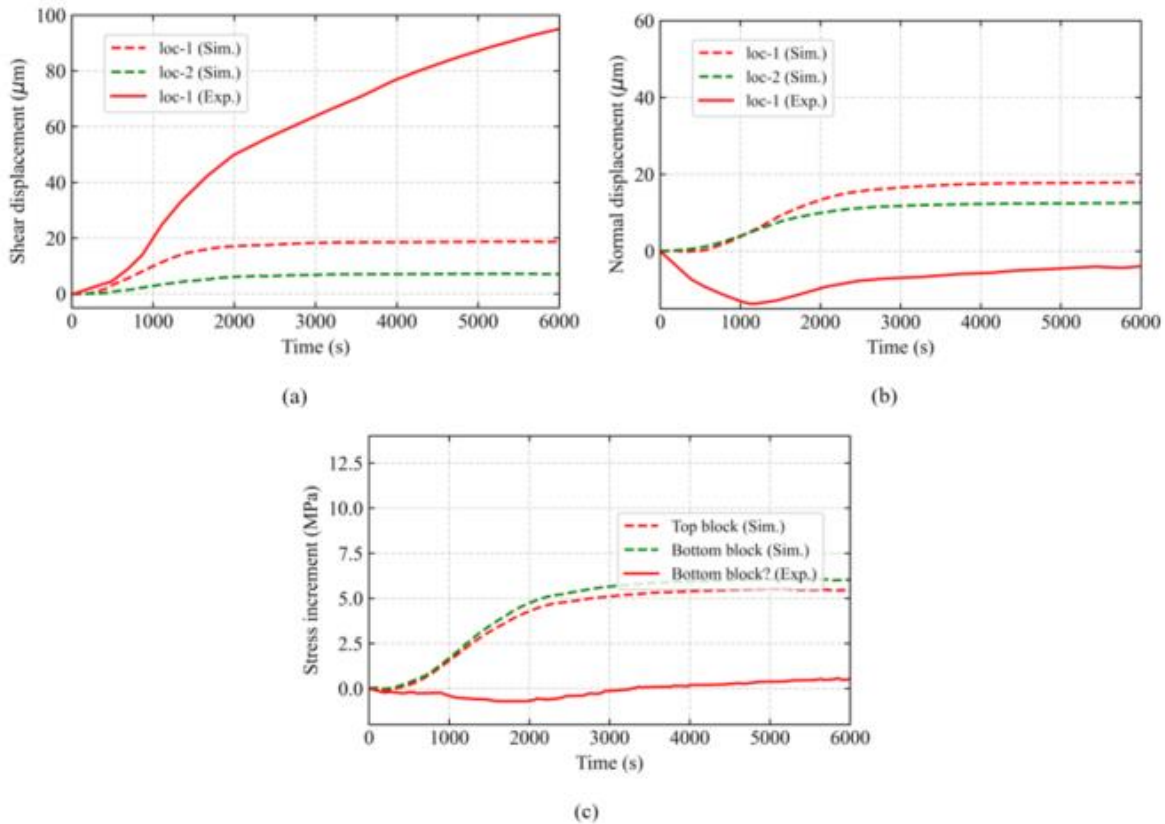
Figure 5-32 shows the results of the thermal shearing stage for the unmated rough fracture model when the interface friction angle was set to  $40^\circ$ . It was found that the unmated interface configuration improved that match against the experiment compared to the corresponding mated interface case, as the interface shear displacement significantly increased (by as much as 100%), and the lateral stress decreased by approximately as much as 3 MPa. The interface normal displacement remained relatively unchanged. This indicates that the interface asperity indeed has a significant impact on the thermal shearing.



**Figure 5-32.** Results of the thermal shearing comparison (unmated fracture case, interface friction angle =  $40^\circ$ ): (a) interface shear displacement; (b) interface normal displacement; (c) normal stress at the lateral boundary.

### Interface friction = $30^\circ$

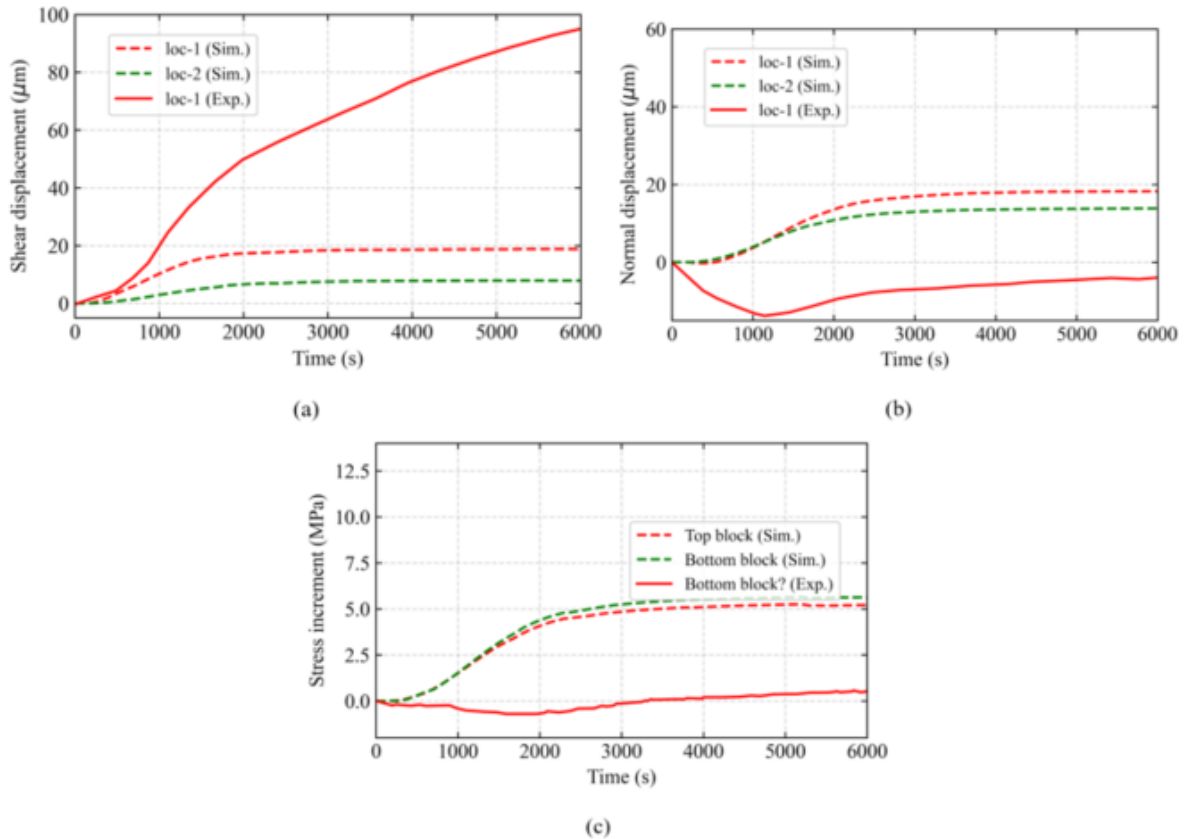
Figure 5-33 shows the results of the thermal shearing stage for the unmated rough fracture model when the interface friction angle was set to  $30^\circ$ . The same trend, which was discussed in the unmated case with  $40^\circ$  friction angle, was found in these simulations, i.e., the unmated configuration led to increased interface shear displacement and decreased lateral stress change, indicating the effect of mated/unmated asperity on thermal shearing.



**Figure 5-33.** Results of the thermal shearing comparison (unmated fracture case, interface friction angle = 30°): (a) interface shear displacement; (b) interface normal displacement; (c) normal stress at the lateral boundary.

### Interface friction = 25°

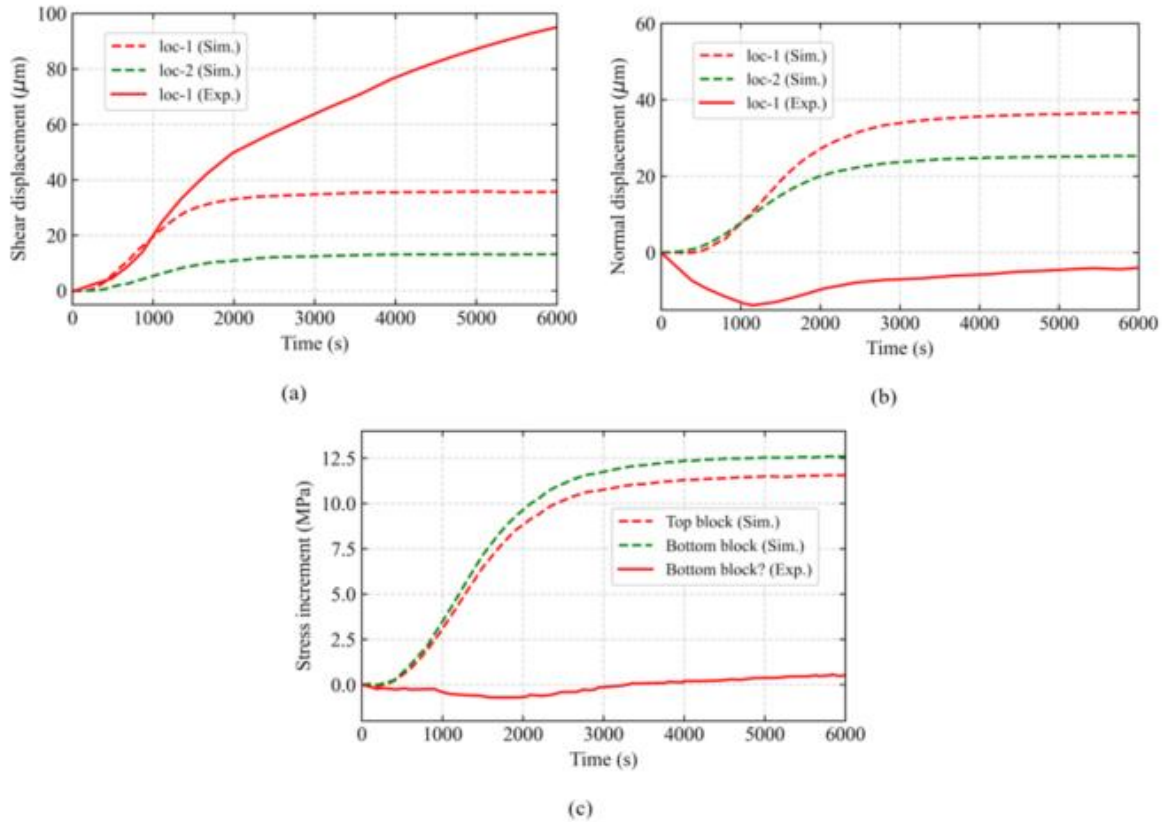
Figure 5-34 shows the results of the thermal shearing stage for the un-mated rough fracture model when the interface friction angle was set to 25°. The same trend discussed in the un-mated cases with 40° and 30° friction angle applies to these results, i.e., the un-mated configuration led to increased interface shear displacement and decreased lateral stress change.



**Figure 5-34.** Results of the thermal shearing comparison (unmated fracture case, interface friction angle =  $25^\circ$ ): (a) interface shear displacement; (b) interface normal displacement; (c) normal stress at the lateral boundary.

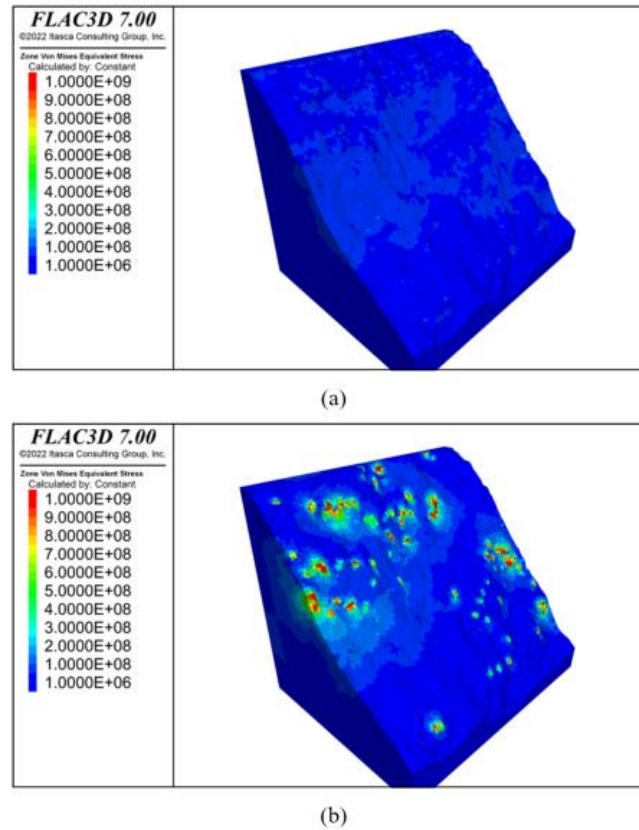
**Thermal expansion coefficient =  $13\text{e-}6$  ( $\text{K}^{-1}$ )**

Figure 5-35 shows the results of the thermal shearing stage for the un-mated rough fracture model when the thermal expansion coefficient was set to  $13\text{e-}6$ . It was found that while the interface shear displacement significantly increased in the un-mated configuration, as was the case for the other un-mated results presented earlier, the lateral stress also increased, which is opposite to the trend discussed in the earlier un-mated results. This is probably caused by enhanced thermal expansion altering interface asperity, which made the area in the middle part of the interface (where displacement measurements were taken) more prone to slip and the area near the lateral boundary (where the stress measurements were taken) decreased, resulting in the abovementioned shear displacement and stress change trends. This suggests that thermal shearing is sensitive to changing of the asperity distribution due, in this case, to the change in the thermal expansion coefficient.



**Figure 5-35.** Results of the thermal shearing comparison (unmated fracture case, thermal expansion coefficient =  $13 \cdot 10^{-6}$ ): (a) interface shear displacement; (b) interface normal displacement; (c) normal stress at the lateral boundary.

We further calculated the distributions of von Mises stress on the interface asperity, as shown in Figure 5-36. It was found that von Mises stress level in the mated fracture case was predominantly below 100 MPa (Figure 5-36a) whereas it exceeded 1,000 MPa at concentrated locations in the unmated fracture case (Figure 5-36b). This von Mises stress level should be large enough to cause failure in granite.



**Figure 5-36.** The distributions of von Mises stress on the fracture asperity: (a) mated fracture case; (b) unmated fracture case.

### 5.3.2.5 Discussion

Results presented in the above sections show that the experimental data could not be quantitatively reproduced by changing interface friction angle, thermal expansion coefficient, or interface configuration (i.e., mated or unmated interface), although in general the thermal expansion coefficient and interface configuration can have a greater impact on the thermal shearing than the interface friction angle. Both parameters alter the interface asperity. In theory, the effective interface friction angle is expressed as follows (Goodman, 1989):

$$\phi_{eff} = \phi_{\mu} + i \quad (5-16)$$

where  $\phi_{eff}$  is the effective interface friction angle,  $\phi_{\mu}$  is the intrinsic interface friction angle, and  $i$  is the (average) asperity angle. In this study, the friction angle  $\phi_{\mu}$  was found to have a relatively minor effect on thermal shearing. This indicates that the interface asperity  $i$  had a greater impact on thermal shearing than the intrinsic friction angle if it is set between 25° and 40°.

Assuming the asperity-associated friction of 30° or higher, intrinsic friction angles of 25° and 40° lead to similar yet very high total friction coefficients, which both may not be realistic. Indeed, the intrinsic

interface friction coefficients of single crystals such as quartz-quartz, Quartz-feldspar and feldspar-feldspar frictions are unknown, which depend on the crystal structures, temperature and water chemistry. Thus, single-crystal experiments that determine those intrinsic friction values would be useful for applying accurate modeling input.

In addition, in this study the rock wedges were assumed to be elastic, and no failure was considered. But it was shown that interface asperity should have failed due to stress concentration. Thus, it may be important to include rock damage and/or failure in thermal shearing modeling to be able to capture the increased shearing displacement that was observed in the experiment.

### 5.3.3 SNL Work for DECOVALEX 2023 Task G

The DECOVALEX 2023, Task G modeling and analysis work at SNL continued with hydro-mechanical simulations of intact and fractured samples. The simulations were made using problem specifications in McDermott et al. (2018) and Fraser-Harris et al. (2020). Modeling results were compared with experimental data from the GREAT cell (Geo-Reservoir Experimental Analogue Technology) experiments (McDermott, 2018). The GREAT cell is a laboratory experimental setup designed to recreate subsurface conditions to a depth of 3.5 km on 200 mm diameter rock samples containing fractures. The experiments support validation of modeling results. For the simulations documented in this section, COMSOL Multiphysics™ software version 6.0 was used. Two modeling cases were considered: Step 1a, mechanical case, with solid body deformation only; and Step 2a, coupled hydro-mechanical case, with fluid flow in a fracture surrounded by impermeable matrix.

Fracture network analysis is of importance to the study of migration of radionuclides away from a geological nuclear waste repository in fractured rock. Recent studies included evaluation of the characterization methods: Fracture Continuum Model (FCM) and Discrete Fracture Network (DFN) model (Hadgu et al., 2017). The study allowed understanding of different characterization methods suitable for use in geologic disposal of nuclear waste in crystalline host rock. Use of fracture network models in the evaluation of experimental data is documented in Iwatsuki et al. (2020) and Hadgu et al. (2022). Understanding the mechanical-hydrological-chemical response of single fracture and fracture network under stress would provide better understanding of the behavior of the repository and its surroundings with time. Such work was started in DECOVALEX 2015 and reported in Wang (2017). DECOVALEX 2023 Task G is a continuation of the work in DECOVALEX 2015. The main objective of the present study is to conduct preliminary research work to combine the previous work on fractures with rock mechanics.

DECOVALEX-2023 Task G is on: Safety Implications of Fluid Flow, Shear, Thermal and Reaction Processes within Crystalline Rock Fracture NETWORKS (SAFENET). The task is conducted in steps in order of increasing complexity using benchmark exercises and experimental data. This report describes the mechanical and hydro-mechanical portions of SAFENET.

As discussed above, two modeling cases are presented in this report. Section 5.3.3.1 describes Step 1a, which is the mechanical case. Modeling of solid body deformation (no fracture) under different loading conditions is presented. Comparisons of modeling results with experimental data are made. Section 5.3.3.2 describes Step 2a, the coupled hydro-mechanical case. Modeling of a single fracture under coupled external loading and fluid flow through a fracture is presented. The work is summarized in Section 5.3.3.3.

#### 5.3.3.1 Step 1a: Modeling of Surface Deformation of a Solid Body

For the solid body deformation only (i.e., no fracture) case (Step 1a), experiments were made for synthetic rock analogs and a greywacke sample. This report discusses simulations made for one of the synthetic samples, a homogeneous artificial sample (opaque amorphous thermoplastic polymer). The simulations assumed an elastic material with impermeable matrix. The selected sample was represented as a cylinder with 200 mm diameter and 200 mm height. Representation of the numerical model as given in McDermott

et al. (2018) is shown in Figure 5-37. Material properties used for the simulations are given in Table 5-3. Both axisymmetric loading and triaxial loading conditions were considered. For axisymmetric loading:  $\sigma_1 = 10$  MPa,  $\sigma_2 = 8$  MPa,  $\sigma_3 = 8$  MPa. For triaxial loading:  $\sigma_1 = 10$  MPa,  $\sigma_2 = 8$  MPa,  $\sigma_3 = 2$  MPa. Boundary Condition: zero circumferential-displacement boundary conditions along the vertical lines that define the sample circumference intersection with the x- and y-axes. Zero displacement in the z-direction across the entirety of the sample base. The simulations were steady-state (stationary in COMSOL).

**Table 5-3.** Material Properties used in modeling for Step 1a

Parameter	Sample	Unit
Elastic Modulus	3.85	GPa
Poisson's ratio	0.4	-

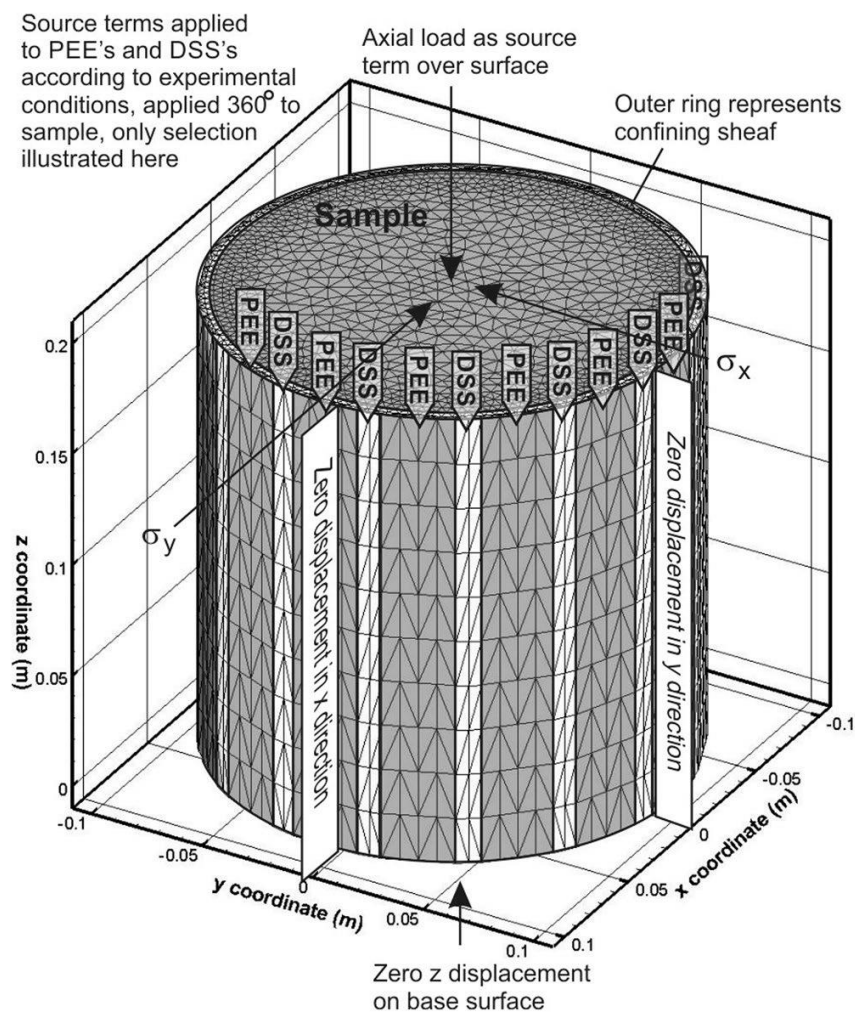


**Figure 5-37.** Conceptual representation of the numerical model for Step 1a. (McDermott et al., 2018)

## Modeling of Axisymmetric Case

Figure 5-38 shows COMSOL modeling mesh for the triaxial loading case. External loads on the surface of the sample for axisymmetric loading (Step 1a) are illustrated in Figure 5-39. COMSOL modeling results for axisymmetric loading are given in Figure 5-40. The results represent the loading conditions for the axisymmetric case and the boundary conditions. Larger surface displacement is indicated in the top part of the sample due to the higher vertical load.

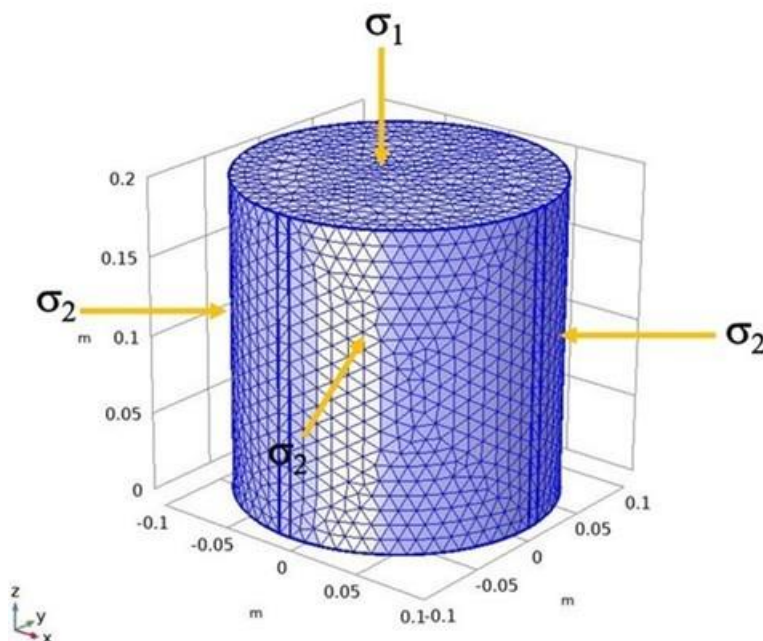


Figure 5-38. COMSOL Mesh for axisymmetric loading (Step 1a)

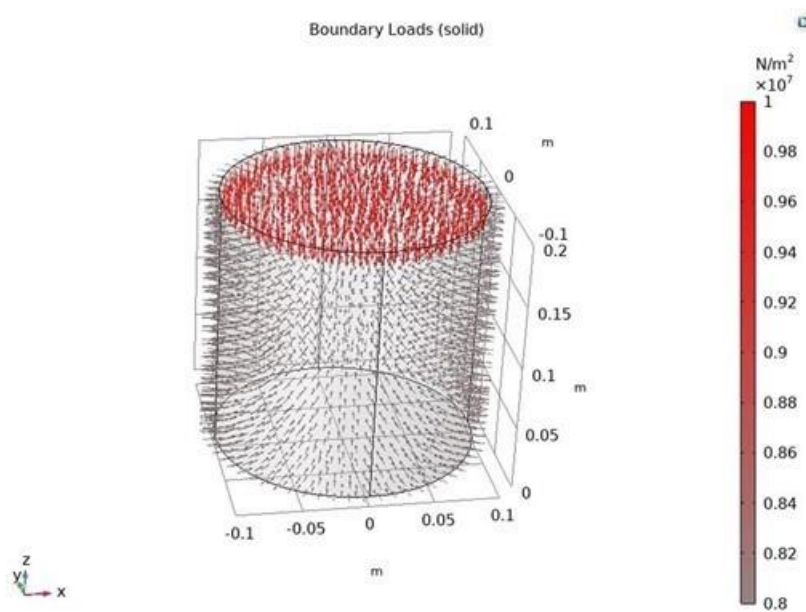
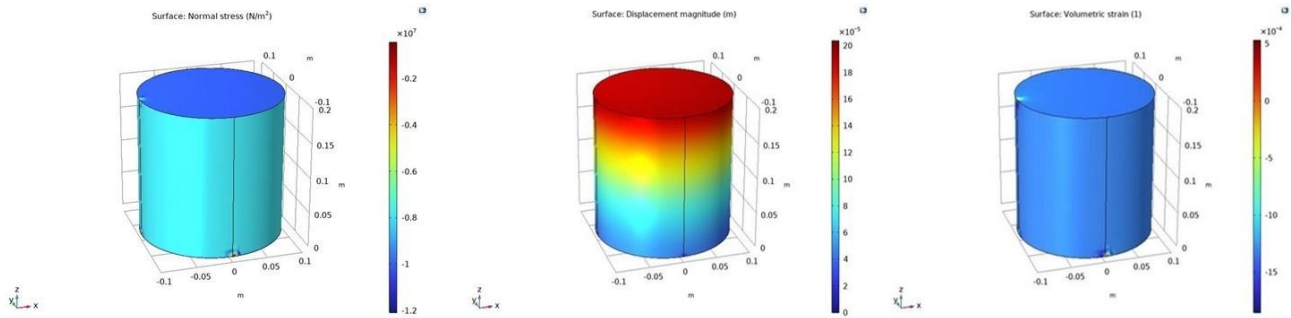


Figure 5-39. Boundary loads for axisymmetric loading (Step 1a)



**Figure 5-40** Step1a results for axisymmetric loading: a) surface normal stress (N/m<sup>2</sup>); b) surface displacement (m); c) surface strain

## Modeling of Triaxial Case

The horizontal loading conditions are different for the triaxial case. Figure 5-41 shows COMSOL mesh for triaxial loading (Step 1a) of the uniform resin sample case, along with directions of the loads. To obtain a true horizontal triaxial loading around the circumference of the sample, Equation 5-16 was applied. Equation 1.1 allows distribution of loads around the circumference of the cylinder. The circumference was subdivided into 16 parts and loading was applied corresponding to the specified representative angle.

$$\sigma = \frac{\sigma_2 + \sigma_3}{2} + \frac{\sigma_2 - \sigma_3}{2} \cos(2\theta) \quad (5-16)$$

Results for Step 1a triaxial loading are shown in Figures 5-42 and 5-43. The results in Figure 5-42 represent external triaxial loading and the relevant boundary conditions. The results show an even horizontal distribution of loads, representing a true triaxial case. The horizontal loading for this case has more contrast than the axisymmetric case (i.e.,  $\sigma_2 = 8$  MPa ,  $\sigma_3 = 2$  MPa) and thus, higher displacement. Figure 5-43 shows triaxial loading results of volumetric strain around the circumference of the sample at 0.065 m radius. Like McDermott et al. (2018), the figure shows a close match between model and experimental results. Note that the selected model and mesh are simplified and do not include all experimental details such as the containing sheaf. Further improvements in the modeling results could be made by including more experimental details and using mesh refinement.

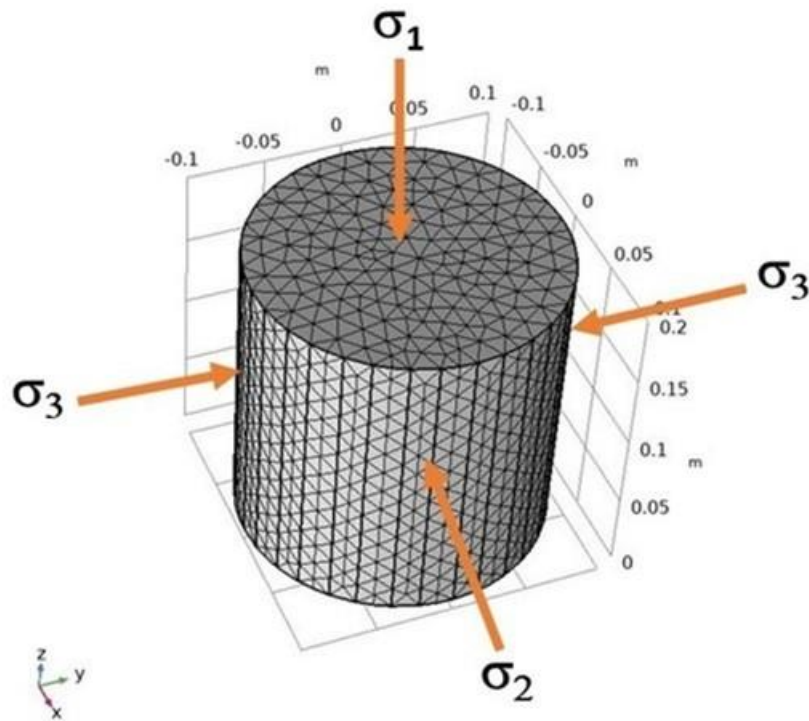


Figure 5-41. COMSOL mesh for triaxial loading (Step 1a)

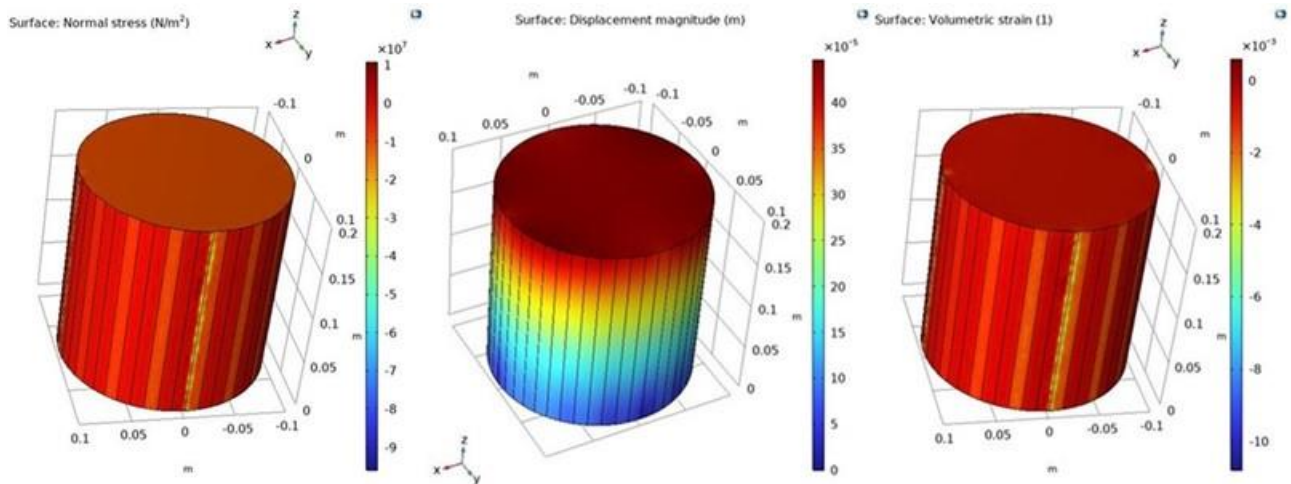
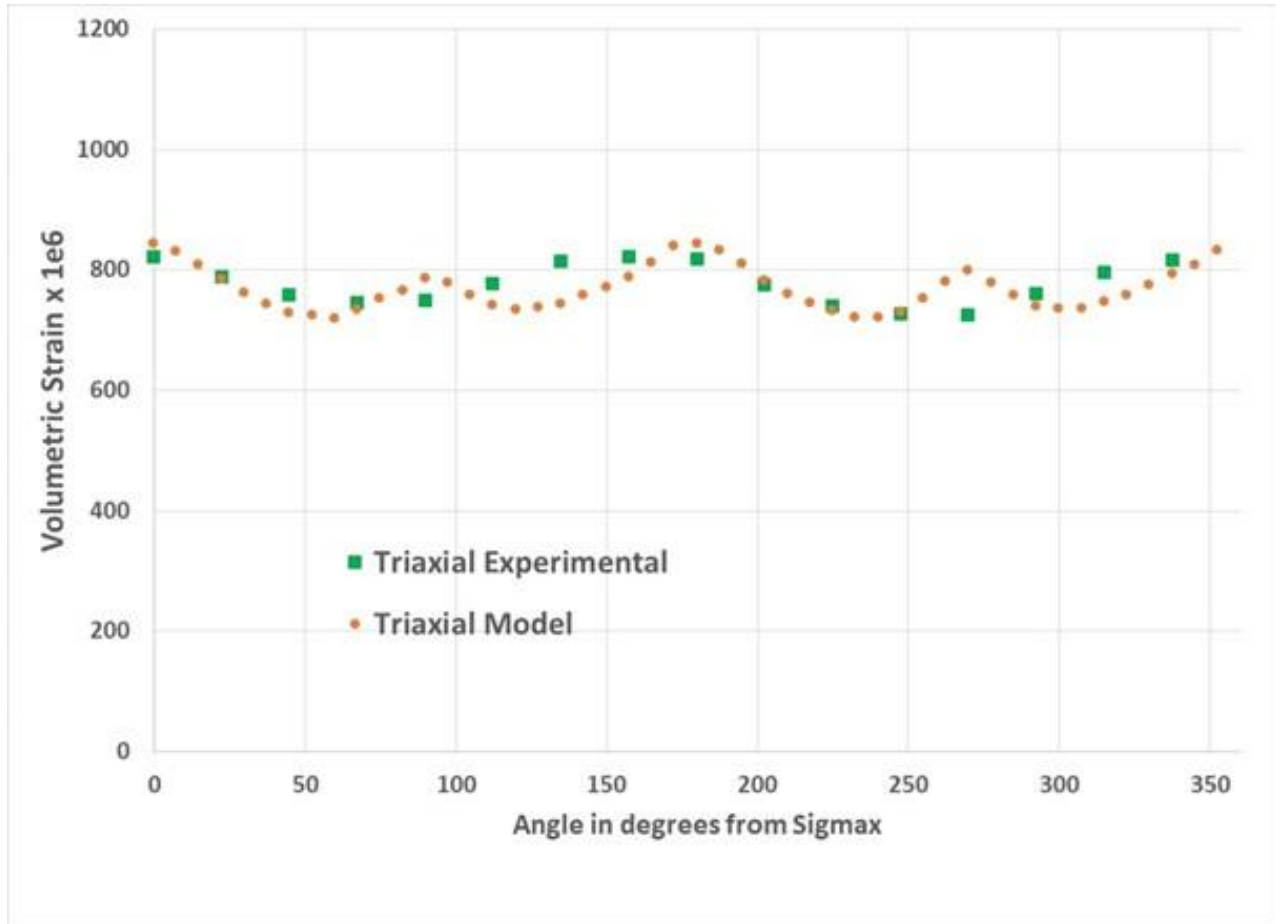


Figure 5-42. Step 1a results for triaxial loading: a) surface normal stress; b) surface displacement; c) surface volumetric strain



**Figure 5-43.** Step1a results for triaxial loading : Volumetric strain - model and experimental

### 5.3.3.2 Step 2a: Coupled Hydro-Mechanical Modeling

For the coupled hydro-mechanical case (Step 2a), a planar (smooth) fracture in an elastic material was assumed. The fracture was represented as a spring foundation using Hooke's law. In COMSOL the spring condition is represented as:

$$\mathbf{f}_s = -K \cdot (\mathbf{u} - \mathbf{u}_0) \quad (5-17)$$

where  $\mathbf{f}_s$  is a force/unit area,  $\mathbf{u}$  is the displacement deforming the spring, and  $K$  is a stiffness matrix.  $\mathbf{u}_0$  is an optional deformation offset, which describes the stress-free state of the spring.

For Step 2a simulations, the sample geometry and material are similar to Step 1a, but with a vertical fracture included in the middle of the sample. The sample is represented as a cylinder with 200 mm diameter and 200 mm height. At the center of the sample is a 3 mm hole that runs from the top of the sample to a vertical height of 125 mm. Following Fraser-Harris et al. (2020) fluid is injected into the bottom of the hole. Material properties used for the simulations are shown in Table 5-4. The loading conditions for

triaxial loading were:  $\sigma_1 = 10$  MPa,  $\sigma_2 = 8$  MPa,  $\sigma_3 = 4$  MPa. In this case  $\sigma_3$  has higher loading than in Step 1a. As in Step 1a the circumference was subdivided into parts and loading was applied corresponding to the specified representative angle using Equation 5-16. For fluid flow through the fracture Darcy flow was assumed. Flowrate and outlet pressure were as specified in Fraser-Harris et al. (2020). Flow was applied at inlet, which is the bottom of the 3 mm hole at a rate of 25 ml/min ( $4.2 \times 10^{-7}$  m<sup>3</sup>/s). Pressure was applied at outlet, which for this work was taken to be the entire bottom of the sample. For this work the outlet pressure is set at 3.45 MPa. The simulations were steady state (stationary in COMSOL).

For fracture permeability evaluation, the Cubic law was assumed:

$$K = b^2/12 \quad (5-18)$$

where  $b$  is hydraulic aperture (m) and  $K$  is fracture permeability (m<sup>2</sup>). In the COMSOL simulations the fracture aperture ( $b$ ) was used as a coupling term between the mechanical and fluid flow processes. The aperture can be calculated using flowrate and pressure difference between the fracture inlet and outlet from:

$$b = \sqrt[3]{\frac{12 \cdot \mu \cdot Q \cdot L}{\Delta P \cdot W}} \quad (5-19)$$

where  $Q$  is the volumetric flow rate ( $4.2 \times 10^{-7}$  m<sup>3</sup>/s),  $w$  is the fracture width (0.2 m) along the sample axis,  $b$  is the fracture aperture (m),  $\mu$  is the dynamic viscosity of the fluid assumed in each case to (0.00103 Pa·s),  $\Delta P$  is the fluid pressure difference (Pa), and  $L$  is the fracture length in the direction of the flow (0.075 m)

## Model Results

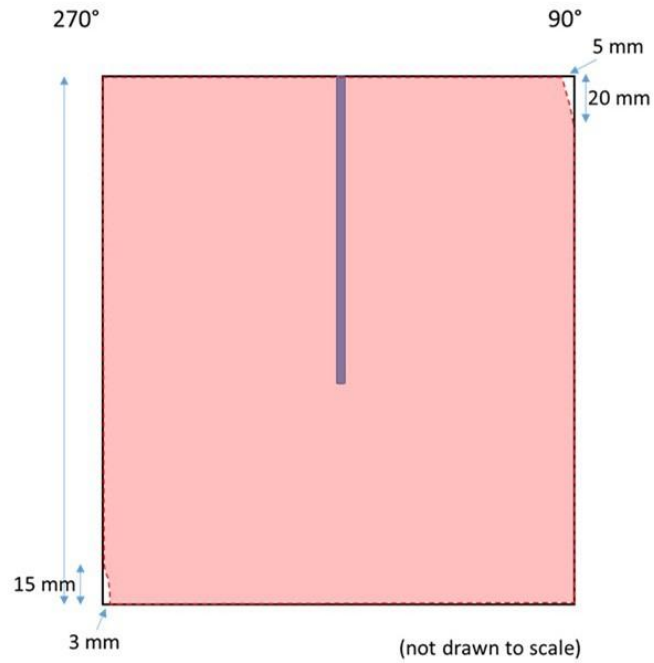
Preliminary simulations were conducted to estimate fracture hydraulic aperture and fracture permeability using Equations 5-19 and 5-18, respectively. Following Fraser-Harris et al. (2020) the COMSOL model was setup with a vertical borehole and a central fracture. Figure 5-44 shows a cross-section at the center of the cylinder from Fraser-Harris. Figure 5-45 shows the corresponding setup in COMSOL. The simulation mesh is shown in Figure 5-46. As in Fraser-Harris et al. (2020), the external horizontal loading positions with respect to the fracture were varied to estimate fracture permeability as a function of stress conditions. For the current work preliminary estimates for a position with  $\sigma_2$  perpendicular, and  $\sigma_3$  parallel to the fracture axis (Position B) are discussed. Position B is given in Figure 5-47.

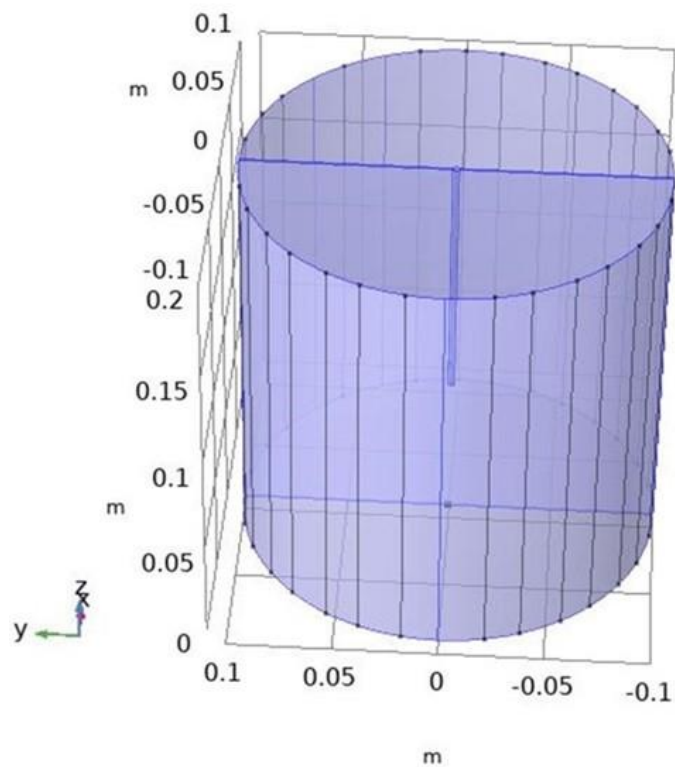
Results for Step 2a triaxial loading are shown in Figures 5-48 to 5-51. The results represent external triaxial loading for Position B, the boundary conditions and fluid flow in the fracture. The results also represent the presence of the fracture. Figure 5-48 shows normal and shear stress on the surface of the sample. Figure 5-49 shows x-component stress and y-component stress on the fracture surface, representing the loading conditions. Figure 5-50 shows results for strain and displacement on the surface of the fracture.

Figure 5-41 shows model results for pressure on the fracture surface. As was done in Fraser-Harris et al. (2020) rough estimates of fracture hydraulic aperture and fracture permeability were obtained using the pressure difference between the hole inlet and the outlet (bottom of fracture). For Position B the estimated hydraulic aperture is  $1.2 \times 10^{-5}$  m, and the corresponding fracture permeability is  $1.19 \times 10^{-11}$  m<sup>2</sup>. As with Step 1a, the selected model and mesh are simplified and do not include all experimental details. Further improvements in the modeling results could be made by including more experimental details, changing loading conditions around the circumference of the cylinder, and applying optimal mesh refinement. Further analysis will be conducted to refine the model results, and to conduct simulations at other loading positions. Simulations results will also be compared to experimental data and other modeling studies.

**Table 5-4.** Material Properties used in modeling for Step 2a

Parameter	Sample	Fracture	Unit
Elastic Modulus	3.85	0.3	GPa
Poisson's ratio	0.4	0.4	-

**Figure 5-44.** Representation of fracture for Step 2a: Fraser-Harris et al. (2020, Figure 11) for Position B



**Figure 5-45.** Representation of fracture for Step 2a: COMSOL model

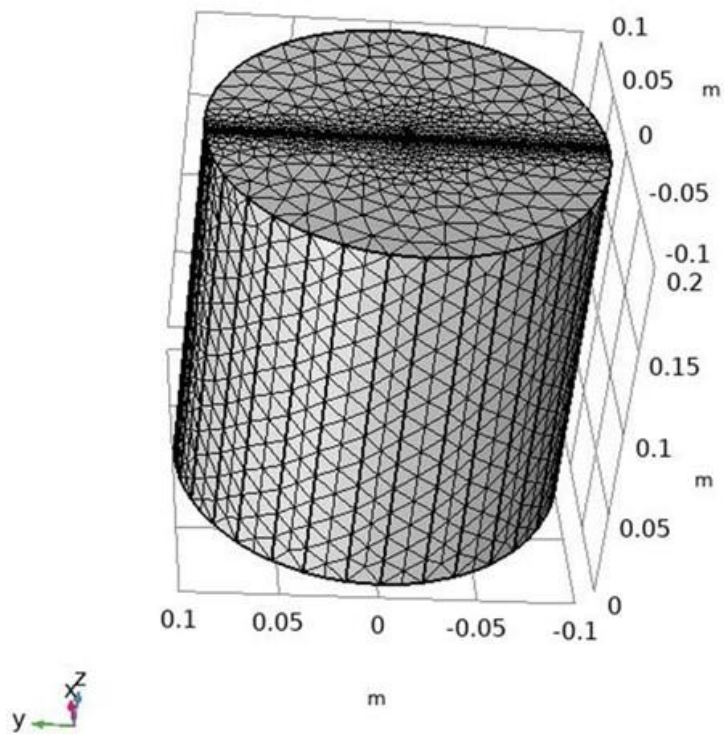


**Figure 5-46.** COMSOL mesh for Step 2a

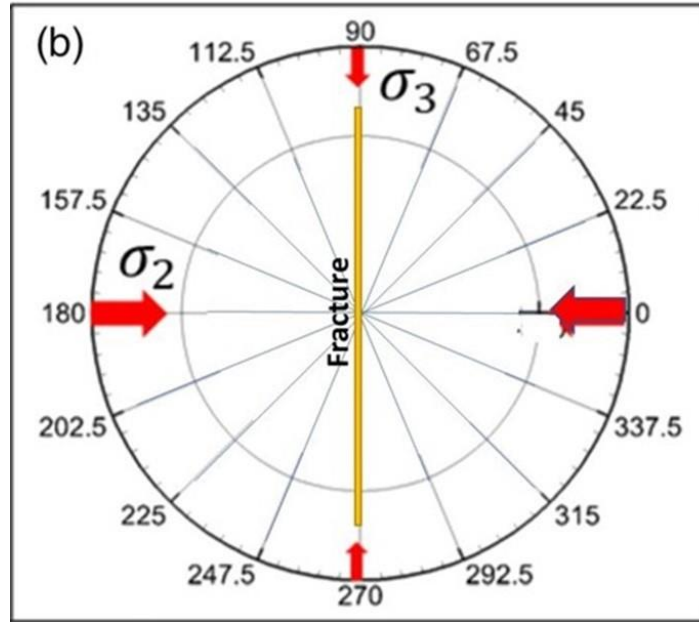


Figure 5-47. Step2a triaxial loading: loading position B

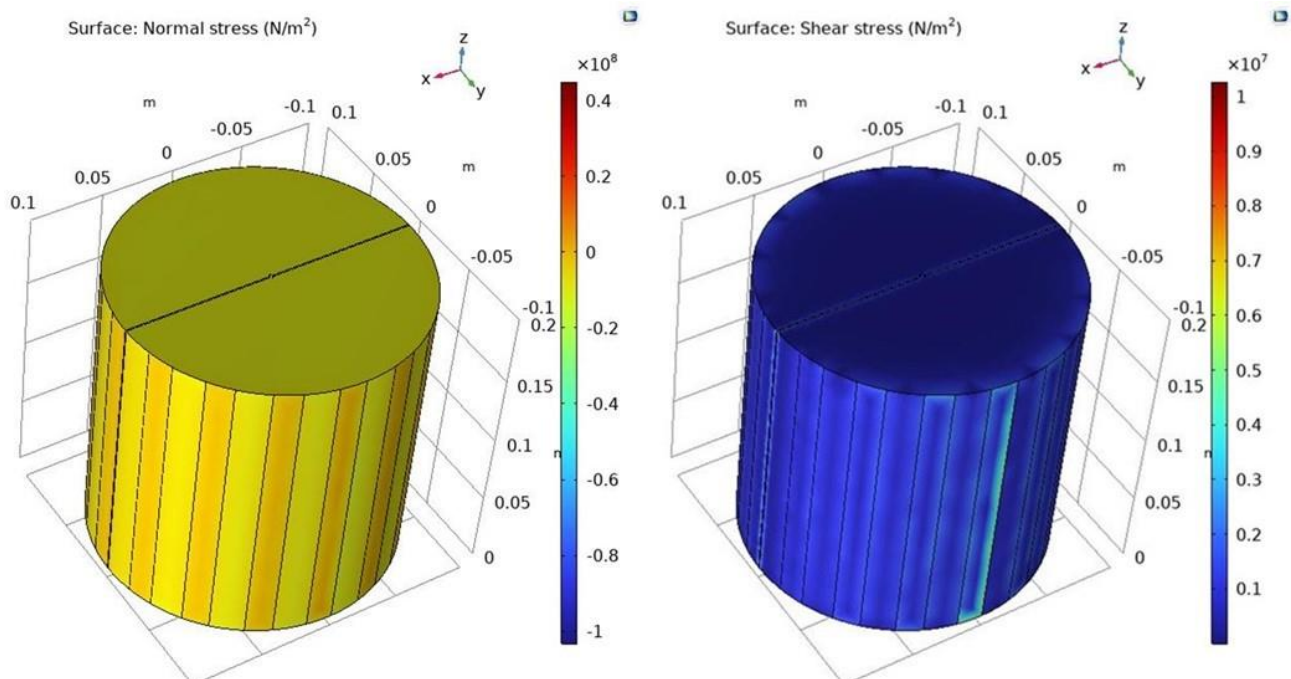
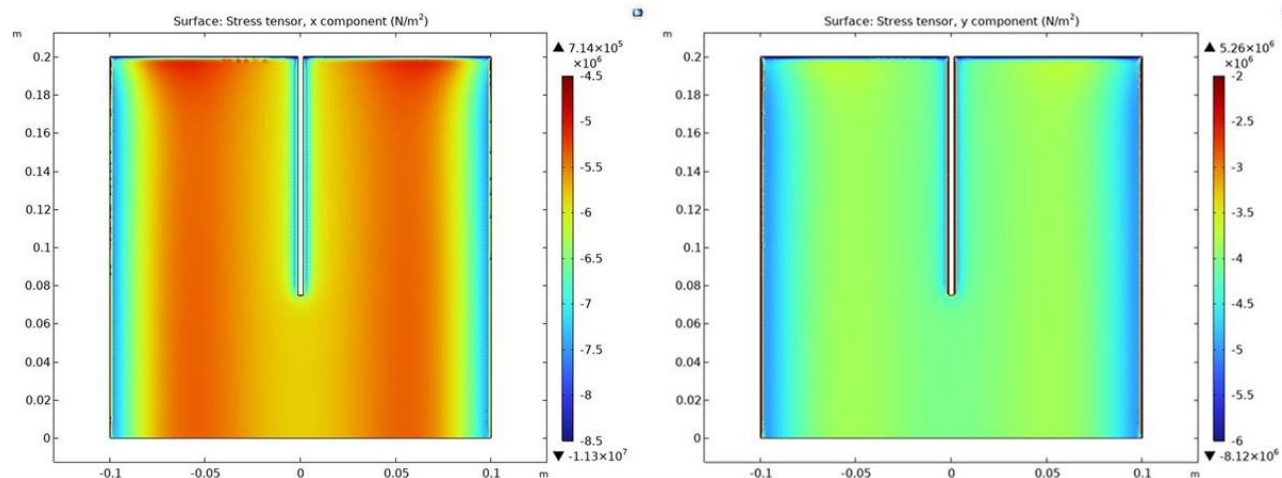
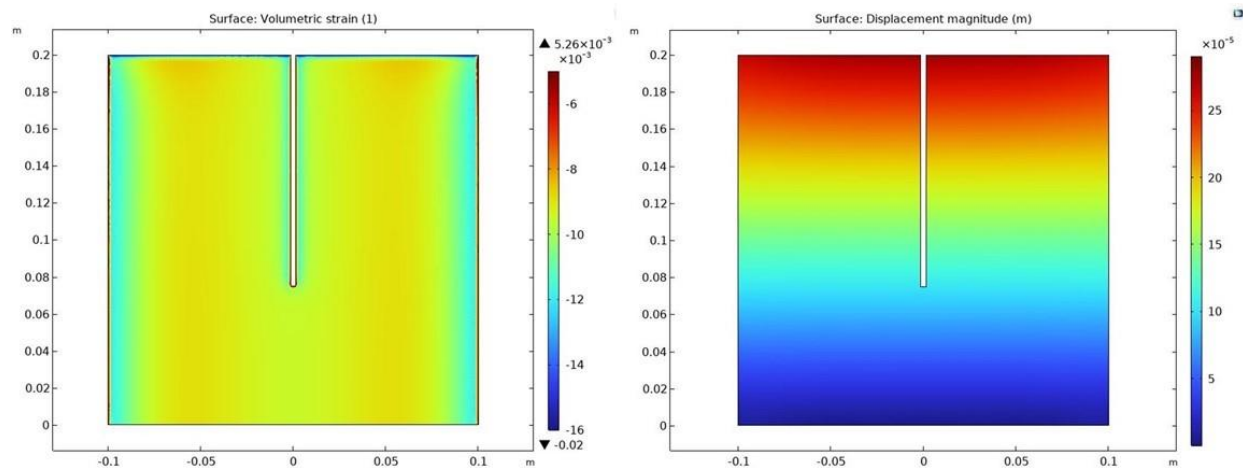


Figure 1.12. Model results for fracture position B, Step 2a. a) surface normal stress; b) surface shear stress



**Figure 5-49.** Model results for fracture position B, Step 2a - stress on fracture surface. a) x-component; b) y-component



**Figure 5-50.** Model results for fracture position B, Step 2a: a) fracture surface strain; b) fracture surface displacement

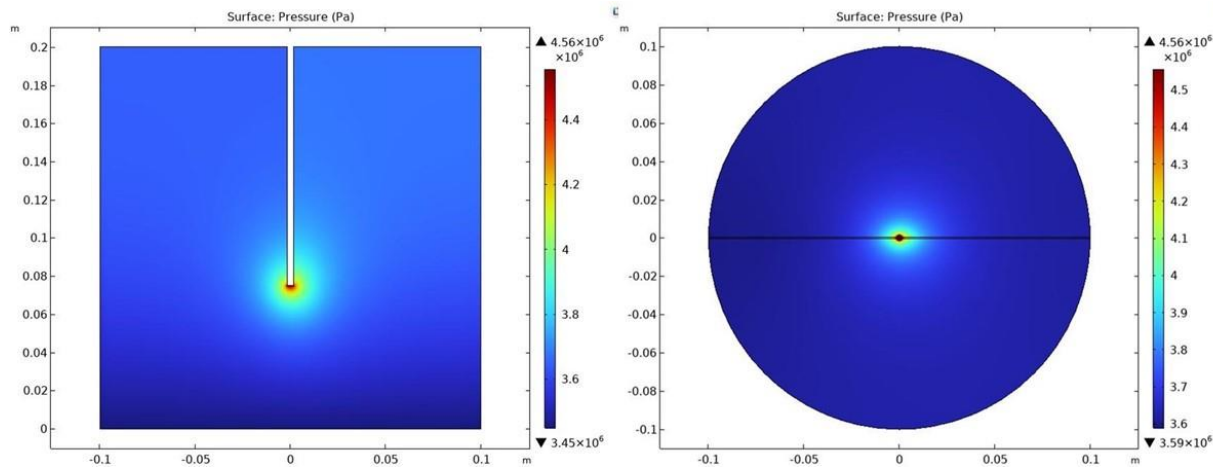


**Figure 5-51.** Model results for fracture position B, Step 2a: pressure on fracture surface - a) Z-Y plane at  $X = 0$ ; b) Z-X plane at  $Y = 0$

## 5.4 Conclusions

In FY23, LBNL used the NMM model and FLAC3D to conduct a number of numerical simulations to analyze (a) shearing of intersecting fractures, and (b) thermal slip of single fractures for DECOVALEX Task G step 3. The key findings from those simulations are:

- The intersections of fractures do not fundamentally change the shearing of two intersecting fractures if the intersecting angles satisfy certain conditions.
- A new simplified DFN model was developed to simplify modeling of the slip of fracture networks by using major path(s). The model was verified based on several examples involving different numbers of major path(s). This new simplified DFN model is promising to serve as a new conceptual model which is complementary to the existing models to characterize DFNs.
- The parameter sensitivity study for thermal slip of fractures suggests that a more refined intrinsic friction angle may affect the shearing behavior of a rough fracture. In addition, damage of asperities may explain the increased shearing of single rough fractures as observed in the KICT experiment for DECOVALEX Task G.

Using COMSOL Multiphysics™ software, SNL conducted simulations for DECOVALEX 2023 Task G Step 1a, mechanical case, with solid body deformation only and Step 2a, hydro-mechanical case, with fluid flow in a fracture surrounded by impermeable matrix. For the mechanical only case (Step 1a) an intact uniform resin sample was subjected to axisymmetric and triaxial loading conditions. Stress, strain and displacement results were obtained for the different loading conditions. Comparison of circumferential strain model results closely match laboratory experimental data for the axisymmetric loading case. For the hydro-mechanical modeling case (Step 2a) a cylindrical uniform resin sample with a single vertical fracture was subjected to triaxial external loading and fluid flow. The fluid flow was introduced to the fracture using a central hole. The COMSOL model includes coupled solid mechanics and Darcy flow. For the current work a selected loading position with respect to the fracture axis was selected. Stress, strain and

displacement results were obtained for the coupled problem. In addition, pressure changes in the fracture between the fluid inlet and outlet were recorded. The results were used to estimate hydraulic aperture and fracture permeability using the Cubic law.

## 6.0 UNDERSTANDING FLOW, TRANSPORT AND CHEMICAL REACTIONS IN FRACTURE NETWORKS

### 6.1 Introduction

Fractured rock formations are widely encountered in the subsurface, with fractures providing the main pathways for fluid flow and contaminant transport in low permeability rocks (Viswanathan et al., 2022). Understanding flow behavior in these systems is of great importance in various fields, including geology, hydrology, and environmental engineering, with specific applications ranging from CO<sub>2</sub> sequestration (Jenkins et al., 2015) to the long-term storage of spent nuclear fuel (Follin et al., 2014; Selroos et al., 2002). The hydraulic aperture of a fracture is a critical parameter controlling fluid flow in connected fracture networks because the individual apertures determine the hydraulic conductivity of each fracture, and therefore, influence the overall permeability of the connected network (Lang et al., 2014; Witherspoon, Wang et al., 1980; Witherspoon, Wilson, et al., 1980; Zimmerman & Bodvarsson, 1996). Larger aperture fractures provide less resistance to flow, i.e., larger hydraulic conductivity, and conventional wisdom suggests that larger apertures ought to therefore lead to higher volumetric flow rates, faster fluid flow and transport of contaminants. However, such changes in fluid flow properties require corresponding changes in the driving force of the system. Consider the case of a single fracture where inflow and outflow boundaries are prescribed constant flow rate boundaries (mass or volumetric). Under these conditions, a uniform decrease in aperture is accompanied by a corresponding increase in the flow velocity since the total amount of fluid flowing through the fracture is fixed by the boundary but the total volume decreases. Given less space, the fluid must increase velocity due to volume conservation. Similarly, a uniform increase in the fracture aperture is accompanied by a corresponding decrease in the flow velocity for consistent reasons. Conversely, under Dirichlet, or constant pressure boundary conditions, each boundary of the fracture is held at a prescribed pressure for flow to be solved. According to Darcy's Law, an increase in the aperture must result in an increase in the volumetric flux and corresponding velocity because the pressure gradient does not change under these boundary conditions. What is unclear, however, is the interplay and feedback between changes in hydraulic aperture within the context of an interconnected network, and, in particular, when pressure is the primary driving force as is a common operational setup, which is what we consider and address here.

Previous research has shown that the relationship between individual fracture aperture, aperture distribution, and flow and transport behavior at the network scale is complex and depends on the specific properties of the network (Council et al., 1996; National Academies of Sciences et al., 2020). Multi-scale heterogeneities are intrinsic aspects of fracture networks in nature and have been shown to play a key role in network scale flow and transport properties. Relevant length scales range from sub-fracture size, such as those related to surface roughness and asperities, to inter-fracture aperture heterogeneity, to network-scale attributes such as fracture topology and intensity. Most studies have concluded that in-fracture aperture variability, whether natural or caused by external stress, can have significant effects on fluid flow and transport in a single fracture (Hanna & Rajaram, 1998; Cardenas et al., 2007; Dang et al., 2019; Hyman et al., 2021; Kang et al., 2016; M. Wang et al., 2016; Zhou et al., 2018; de Dreuzy et al., 2012; Frampton et al., 2019; Makedonska et al., 2016; Pandey et al., 2015). Within the context of network flow, there is substantially less research than at the single fracture scale (Hyman et al., 2016, 2020, 2019; Kang et al., 2020, 2019a; Lei et al., 2017; Garipov et al., 2016; Maillot et al., 2016; McClure et al., 2016; Tran & Jha, 2021; Sweeney & Hyman, 2020). Nonetheless, a common finding amongst these studies is that when the aperture distribution widens, e.g., due to different fractures opening and closing from stress, flow channelization increases. Yet, the theoretical understanding for these changes and their impact on upscaled transport properties has not been addressed. The interdependence of multi-scale physical and hydraulic

properties with anomalous flow and transport behavior has also been well documented by many previous researchers (e.g., Berkowitz & Scher, 1997; Edery et al., 2016; Kang et al., 2020, 2019b, 2017, 2015; Roubinet et al., 2013; Sherman et al., 2021; Z. Wang et al., 2021).

Coupled with flow and transport, fluid mixing, chemical reactions and the associated mineral dissolution and precipitation in fracture networks are also important processes that need to be considered in many applications. Mineral dissolution and precipitation may change fracture apertures and therefore fracture permeability. Previous studies focusing on the role of mineral precipitation on fracture permeability considered relatively simple permeability models based on a set of parallel fractures with permeability described by the cubic law (Witherspoon et al., 1980; Steefel and Lasaga, 1994; Zimmerman and Bodvarsson, 1996; Steefel and Lichtner, 1998). Fewer studies have considered intersecting fracture networks (Hyman and Jimenez-Martinez, 2018; Hu et al., 2016; 2017a,b), and only one to our knowledge has considered mineral precipitation or coupled mineral dissolution and precipitation in these environments (Feng et al., 2019). Other studies have focused on characterization of intersecting fracture networks in which precipitation has occurred, including Crandall et al. (2017).

A significant number of numerical models have been applied to analyze fluid flow (Hu et al., 2016; Hyman and Jimenez-Martinez, 2018), mechanics (Hu et al., 2017a,b), and hydro-mechanical (Hu et al., 2017a,b; 2020a,b;) processes in DFNs. A recent review paper by Laubach et al. (2019) highlights many of the important topics with regard to fractured rock systems, and they noted that the topic of mineral precipitation in these systems was relatively neglected. Noiriel et al (2021) considered mineral precipitation in fractured rock but did not consider the role of mixing (fractures split rather than converge), or that of gas phase transport. Jones and Detwiler (2019) examined precipitation in a single fracture, although they did not consider the role of mixing or gas phase transport.

In this section, we will investigate the effects of fracture-to-fracture aperture heterogeneity on fluid flow and transport in the context of complex fracture networks. We will begin with an analytic derivation providing a counter-intuitive prediction that the highest flow rates and fastest travel times in networks occur when inter-fracture aperture heterogeneity is low, not necessarily those networks with higher apertures as previously thought. We will then demonstrate, explore, and characterize these effects at the network scale using a series of high-fidelity three-dimensional discrete fracture network (DFN) models coupled with flow simulations and Lagrangian particle tracking. In addition, we will investigate the interplay between the geometric features of fracture networks (asperities and intersections) and mineral precipitation and its effect on porosity and permeability changes.

## 6.2 Characterizing the Impacts of Multi-Scale Heterogeneity on Solute Transport in Fracture Networks

### 6.2.1 Theoretical Background

We begin by considering a series of three fractures where flow is driven by Dirichlet pressure boundary conditions and steady-state flow and solute transport times can be solved analytically for this system using Darcy's Law. We choose this problem because it isolates how changing a single fracture aperture in a series affects flow and transport at the network scale. Consider first the cross-sectional flow rate in the network, neglecting gravity, given by

$$Q = \frac{b_h^3}{12\nu} \frac{p_0 - p_1}{\rho L} \quad (6-1)$$

where  $\nu$  is kinematic fluid viscosity,  $p_0$  and  $p_1$  are boundary pressures,  $\rho$  is fluid density,

$$L = l_1 + l_2 + l_3 \quad (6-2)$$

and the aperture of the network is given by the harmonic average of the individual apertures, which are denoted by the subscript  $i = 1,2,3$ ,

$$b_h^3 = \frac{3}{\frac{1}{b_1^3} + \frac{1}{b_2^3} + \frac{1}{b_3^3}} \quad (6-3)$$

We can then calculate the velocities in each of the fractures. If we choose values for the unknowns in this system, namely,  $l_i, p_0, p_1, \rho$ , and  $v$ , we can explore the behavior further. Assume that  $l_1 = l_2 = l_3 = 1$  m,  $p_0 = 1.1$  MPa,  $p_1 = 1.0$  MPa,  $\rho = 997$  kg/m<sup>3</sup>, and  $v = 8.93 \times 10^{-7}$  m<sup>2</sup>/s. Without loss of generality, assume the first and third fractures in the series have apertures of  $10^{-4}$  m and we systematically vary the aperture in the second fracture from  $2 \times 10^{-5}$  m to  $5 \times 10^{-3}$  m. For each aperture, we analytically solve for the advective travel times of particles through the network.

Figure 6-1 shows the results plotted as a function of the aperture of the second fracture. Any decrease or increase beyond a small amount in the aperture of the middle fracture results in a delay in the particle breakthrough times relative to the case where the middle fracture has the same aperture as the left and right fractures. So even if the system has a larger harmonic average due to that larger second fracture apertures relative to  $10^{-4}$  m, there is a delay due to the velocity decreasing in the second fracture caused by the larger aperture of the second fracture. One can make a similar argument using Bernoulli's principle in pipe flow where a large pipe is connected to a smaller pipe, driven by an excess pressure (Levi, 2023). Attempting to increase the flow rate out of the second pipe by changing the size of the first is a futile task as the velocity limit of the system occurs when the pipes are equal diameter. The question then becomes, how does such a phenomenon manifest at network scale in fracture networks and is it possible that networks with greater permeability have slower transport times through them?

$$v_i = \frac{Q}{b_i} \quad (6-4)$$

and the advective travel time in each fracture is

$$t_{fi} = \frac{l_i}{v_i} \quad (6-5)$$

Thus, the total advective travel time is

$$t_f = t_{f_1} + t_{f_2} + t_{f_3} \quad (6-6)$$

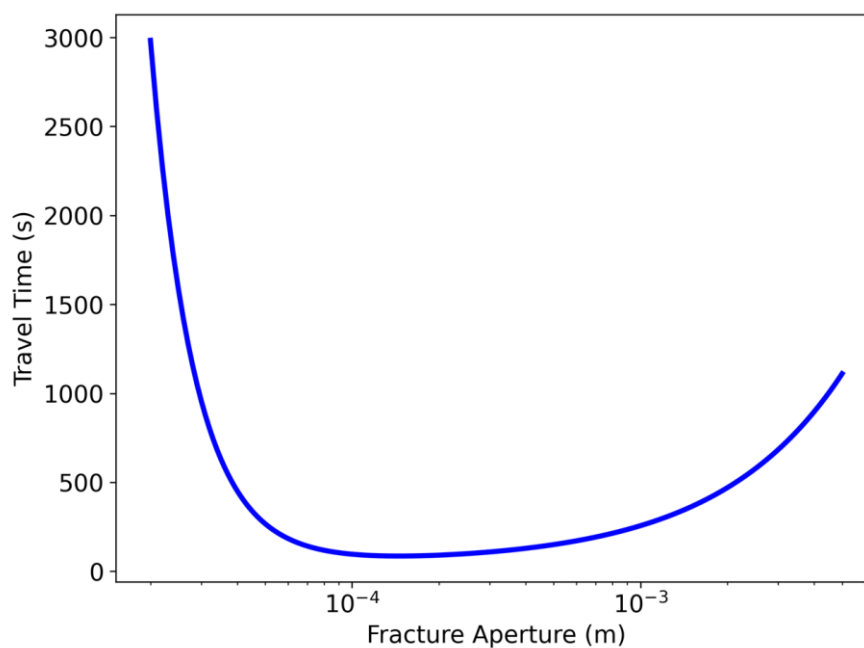


**Figure 6-1.** Analytical solution for advective particle travel time as a function of the second fracture aperture in a three-fracture series. The first and third fractures in the series have the same aperture of  $10^{-4}$  m.

### 6.2.2 DFN Simulations

We use the *dfnWorks* (Hyman et al., 2015) software suite to generate, mesh, and resolve flow and particle transport on three-dimensional fracture networks with increasing complexity. Comprehensive details and methods of the discrete fracture methodology and *dfnWorks* can be found in the original paper and have been published extensively. The networks we consider are “semi-generic” meaning that they do not represent a particular field site, but their attributes are loosely based on field observations. Once the networks are generated and meshed, we solve for the steady-state pressure field and volumetric flow rates of an incompressible fluid by invoking Dirichlet boundary conditions using *PFLOTRAN* (Lichtner et al., 2015), which uses a two-point flux finite volume approach. The governing equation we adopt is Reynold's equation, which is linear in the pressure gradient. Solute transport within each DFN is simulated using a Lagrangian approach, where a plume of purely advective, non-reactive particles trace pathlines through the fluid velocity field within the network (Makedonska et al., 2015). Each simulation in the following sections uses 100,000 particles and their initial locations are uniformly placed along the fractures that intersect the inflow boundary plane. The travel times of particles exiting the domain is recorded and the probability density function of the travel time distribution (i.e., the breakthrough curve) is empirically constructed.

Further details of the flow and transport approach, including governing equations, can be found in Hyman et al., (2015). In order that we retain a singular focus to this study, we assume that the apertures follow a smooth parallel plate assumption. Recent advances allow for in-fracture aperture variability to be incorporated into DFN network scale models, but our goal is to isolate changes at the fracture scale not smaller scales, so we assume that fracture apertures are uniform within individual fractures.

## 6.2.3 Results

### 6.2.3.1 Single Percolation Path

In this section, we consider DFNs with the same 43 fractures and geometry, with only one percolation path through the network (Figure 6-2). By doing this, we can isolate the effects of changing and increasing apertures on flow and transport along particle trajectories forced to enter and exit each fracture in the DFN and assess if and how the phenomenon described in Section 6.2.2 translates to systems with many more fractures.

The DFN is generated using a truncated power law distribution with radii  $r$  and a decay exponent  $\alpha$ , which is a commonly measured field quantity (Bonnet et al., 2001),

$$p_r = (r, r_0, r_u) = \frac{\alpha \left(\frac{r}{r_0}\right)^{-1-\alpha}}{r_0 \left[1 - \left(\frac{r_u}{r_0}\right)^{-\alpha}\right]} \quad (6-7)$$

where  $r_u$  and  $r_0$  are the upper and lower radius cutoffs, respectively. We use values  $r_u = 10.0$  m,  $r_0 = 2.0$  m, and  $\alpha = 2.0$ . The fractures are represented by randomly oriented discs, mimicking a disordered fractured media (Hyman & Jimenez-Martinez, 2017). The same flow problem is solved as the following sections in this paper. Namely, Dirichlet pressure boundary conditions, with an inflow pressure of 2.0 MPa and outflow pressure of 1.0 MPa. Because the governing equations are linear, modifying the pressure values does not change the phenomenology of the flow and transport in terms of the velocity field structure, but merely shifts particle arrival times in one direction or the other depending on how the gradient is changed.

Figures 6-2a,b,c show three DFNs under consideration in this section. The total domain length is 300 m and each non-boundary fracture is intersected by exactly two other fractures, while the boundary fractures are connected by one other fracture and the adjacent inflow or outflow boundary. Three different suites of fracture apertures are considered. First, those where all fractures have the same hydraulic aperture  $b_0 = 1.1 \times 10^{-4}$  m. Then, two suites of realizations where we only allow fracture apertures greater than  $b_0$ . We restrict the aperture to be higher because we are mostly interested in the phenomenology described in Section 2.2, where both the effective permeability and the travel time increase. We accomplish this by initially generating an aperture distribution using a log-normal distribution, with defined mean and variance. If an aperture value that is generated results in an aperture less than  $b_0$ , we simply flip the sign of the difference and add it to  $b_0$ , hence we end up with apertures greater than  $b_0$ . Since the mean fracture aperture varies each realization as a result of this generation approach, we generate 30 networks for each suite. We quantify this heterogeneity using the coefficient of variation,  $CV = \sigma/\mu$ , where  $\sigma$  is the population standard deviation and  $\mu$  is the population mean. One ensemble of 30 realizations has  $CV = 17.73$ , and the other ensemble has  $CV = 6.17$ , which we hereafter refer to as relatively high and low heterogeneity, respectively, noting these values are relative to each other and not a particular field site.

Figure 6-2d shows the BTCs for the high heterogeneity, low heterogeneity, and constant aperture transport simulations, shaded with 95% confidence intervals for the former two. When the aperture heterogeneity between the individual fractures is low, there is early first arrival of particles relative to the constant aperture case. However, when the heterogeneity is increased, there is a delay in arrival relative to the constant case, even though in both suites there are no fractures with apertures less than  $b_0$  meaning a more permeable network exhibits higher solute residence times than a less permeable network due to differences in fracture-to-fracture aperture.

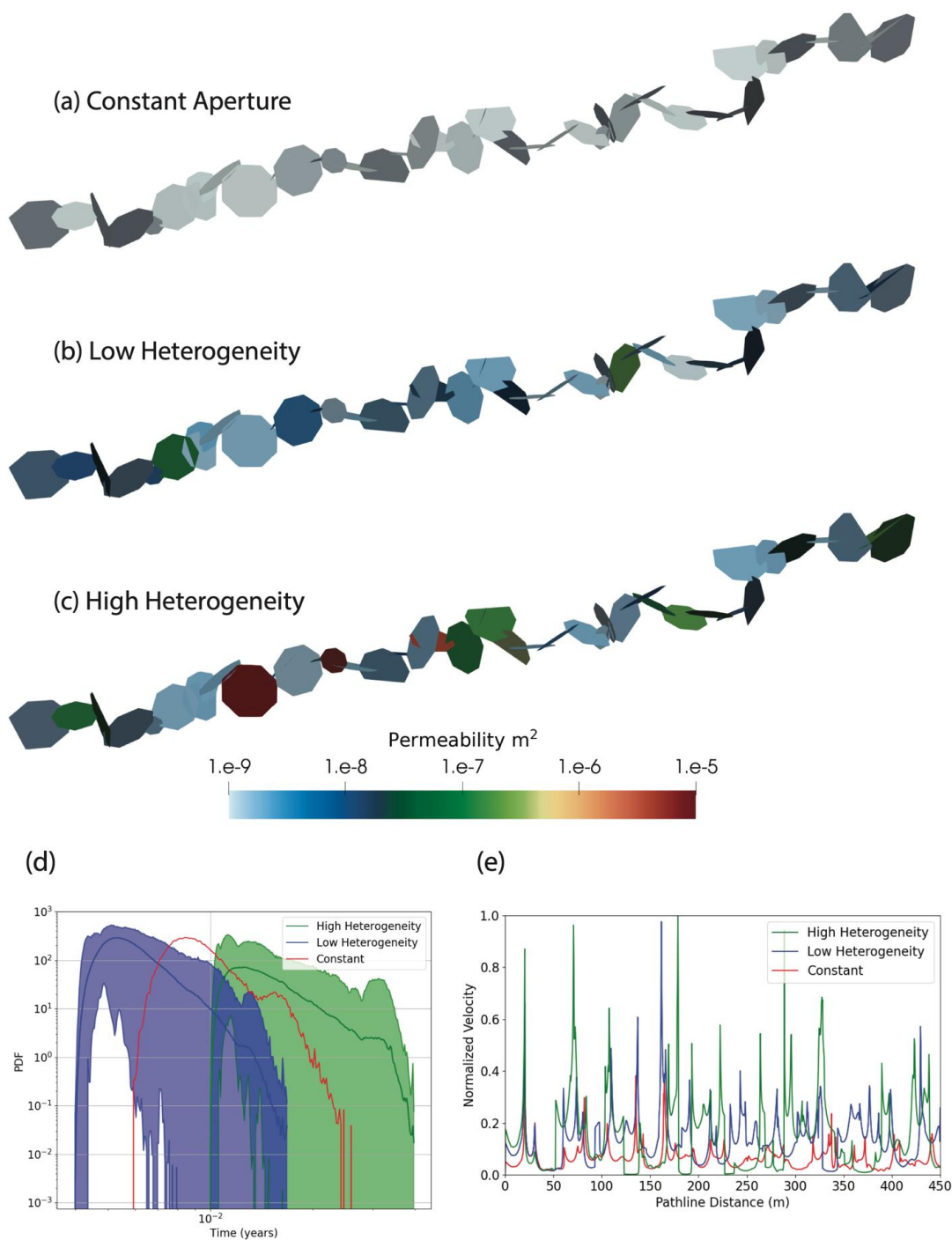


**Figure 6-2.** (a) DFN with constant fracture apertures; (b) DFN with relatively low fracture-to-fracture aperture heterogeneity; (c) DFN with relatively high fracture-to-fracture aperture heterogeneity; (d) Particle breakthrough curves for ensembles of DFNs shown in (b) and (c), as well as constant case (a); (e) Velocity as a function of path line distance for randomly selected particles in each type of DFN.

Figure 6-2e shows normalized particle velocities plotted as a function of path line distance for three individual particle trajectories (one randomly selected from each network suite). Note the trajectories are not necessarily one-to-one comparisons because particles are not guaranteed to take the same trajectory through an individual fracture or experience the same fractures at the same path line distance. Several striking features are evident. Each trajectory shows considerable velocity variability corresponding to changes in fracture residency. The constant aperture network shows the least amount of variability relative to the other cases. The particle trajectory from the high heterogeneity network records the highest velocities, but also the lowest, reaching values close to zero several times. The particle trajectory from the low heterogeneity network is consistently higher than the constant case and does not experience the same dramatic drops close to zero velocity that the higher heterogeneity case does.

These results extend the phenomena discussed in Section 6.2.2 with the three-fracture series and elucidate the expected variability depending on the actual fracture aperture encountered in different networks. In summary, if particles are confined to a single percolation path in a sparsely fractured network, the transport times are closely linked to the variation in fracture-to-fracture aperture.

### 6.2.3.2 Multiple Percolation Paths

In this section, we consider DFNs with multiple percolation paths, but with different densities. First, we consider a DFN with relatively low density/few percolation paths, which we define here as any connected pathway of fractures that connects the inflow and outflow boundaries, and then we consider a DFN with relatively high density/many percolation paths. Note that “high” and “low” are used as relative terms for the networks considered and are not meant to be quantitative outside of the comparison presented herein.

To generate these networks, we again employ a truncated power law distribution, where the fractures are represented as planar ellipses. For these networks we assume  $\alpha = 1.8$ ,  $r_0 = 1$  m, and  $r_u = 10$  m. The networks are generated in a cubic domain with sides of length 50 m. For consistency, we again refer to a constant baseline aperture case where all of the fractures have constant aperture of  $b_0 = 1.1 \times 10^{-4}$ , but also generate ensembles of 10 realizations each with relatively high and low aperture heterogeneity, but again restrict the fracture apertures to only be greater than  $b_0$  using the same approach previously described.

Similar to previous work (e.g., Hyman et al., 2020), we measure the density of the networks using the percolation parameter  $p$  as defined by de Dreuzy et al., (2012):

$$p = \frac{N}{L^2} \int_{r_0}^{r_u} dr \min(r, \alpha L) p_r(r) \quad (6-8)$$

For this set of generation parameters, the critical percolation threshold,  $p_c$ , defined as the minimum number of fractures required such that there is a connected cluster of fractures that spans the entire domain, is  $\approx 750$  fractures. We can further define a non-dimensional percolation parameter,  $p' = p/p_c$  where  $p$  is the number of fractures inserted into the computational domain during network generation. We only consider DFNs where the entire network connects the inflow and outflow boundaries, i.e., isolated fractures and clusters of fractures are not retained in the final networks. Hence, the final number of fractures in the DFNs is not equivalent to  $p$ . Nevertheless,  $p'$  is a useful metric because it places all the networks into a relative context (Hyman et al., 2020).

#### Low Density, $p' = 3$

For the relatively low density DFNs, we choose a value of  $p' = 3$ , which results in an initial seed of 2250 fractures in the generation. Using a randomly initialized seed, we end up with a DFN with 184 fractures after isolated fractures are removed (see Figure 6-3a). Similar to before, we generate two ensembles of the same network structure with different fracture-to-fracture aperture heterogeneities where the apertures are

only allowed to be greater than  $b_0$ . For these networks, we generate 10 realizations of each. The relatively high heterogeneity ensemble has  $CV = 35.07$  and the relatively low heterogeneity ensemble has  $CV = 9.74$ . We also include an example with constant aperture and the same flow and transport problem is solved as in Section 6.2.3.1.

Figure 6-3a shows the network under consideration colored by fracture number. It is clear that there are more percolation paths through the network compared to the network in Section 6.2.3.1., but still relatively few compared to the network in the next section. Figure \ref{multi}b shows the BTCs for the high heterogeneity, low heterogeneity, and constant DFN realizations. Both high and low ensembles show similar first arrival times, which are nearly the same as the constant aperture network.

The scaling of the tail in the BTCs are quite different (see Figure 6-3b). The high heterogeneity DFNs show heavy/long tails that decay quite slowly (slope -0.80) relative to both the low heterogeneity DFNs (slope -1.42) and the constant aperture DFN (slope -2.14). The tails of the low heterogeneity DFN BTCs show scaling behavior in between and different than the constant DFN and high heterogeneity DFNs.

From a Eulerian point of view, we can investigate how much of the domain is actively flowing using the flow channeling density indicator  $d_Q$  presented by (Maillot et al., 2016)

$$d_Q = \frac{1}{V} * \frac{(\sum_f S_f * Q_f)^2}{(\sum_f S_f * Q_f^2)} \quad (6-9)$$

whose definition is inspired by the participation ratio developed in solid state physics (Bell et al., 1970; Edwards & Thouless, 1972) and has been adapted for use in the geosciences as well (Andrade et al., 1999; Davy et al., 1995, 2010). In the equation for  $d_Q$ ,  $Q_f$  is one-half the absolute value of the total volume of fluid exchanged by a fracture  $f$  with its neighbors and  $S_f$  is the fracture surface area and  $V$  is the total size of the domain. This measure is very similar to the fracture intensity (total fracture surface area per unit volume), defined by

$$P_{32} = \frac{\sum_f S_f}{V} \quad (6-10)$$

Note that if  $Q_f$  is uniform across all fractures, then  $d_Q = P_{32}$ . Comparing the two previous equations shows that  $d_Q$  is a measure of active  $P_{32}$  or flowing  $P_{32}$  and the ratio  $d_Q/P_{32}$  is the percentage of the network with significant flow.

For the low density DFNs, this value does not change greatly, with mean  $d_Q/P_{32}$  values of 0.352, 0.360, and 0.375 for the high heterogeneity, low heterogeneity, and constant DFNs, respectively. The logical explanation for this result is that the particles in the different DFN suites are being transported through many of the same fractures in the low-density network. This explanation also aligns with the fact that there are few transport pathways.

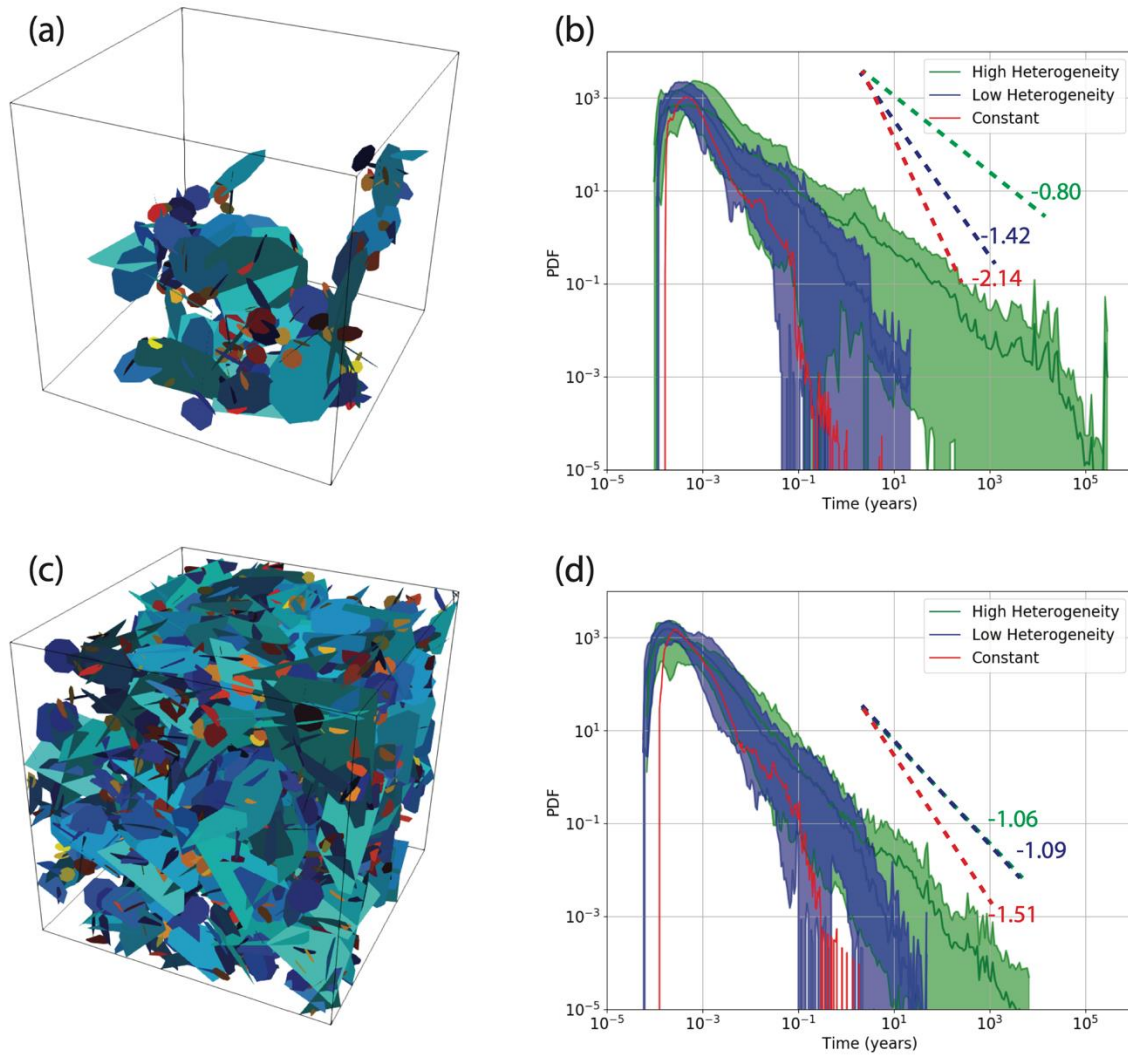


**Figure 6-3.** (a)  $p' = 3$  DFN (b) Particle breakthrough curves for ensembles of high and low aperture heterogeneity DFN shown in (a). 10 realizations of each high and low were generated and the curves are shaded with 95% confidence intervals. (c)  $p' = 5$  DFN (d) Particle breakthrough curves for ensembles of high and low aperture heterogeneity DFN shown in (c). 10 realizations of each high and low were generated and the curves are shaded with 95% confidence intervals.

### High Density, $p' = 3$

For the relatively high density DFNs, we choose a value of  $p' = 5$ , which results in an initial seed of 3750 fractures in the generation. Using a randomly initialized seed, we end up with a DFN with 1428 fractures after isolated fractures are removed (Figure 6-3c). 10 realizations of relatively high and low inter-fracture aperture heterogeneity networks are again generated, along with a network with constant fracture aperture. For these networks, the high heterogeneity ensemble has  $CV = 31.78$  and the relatively low heterogeneity ensemble has  $CV = 5.97$ .

Figure 6-3d shows the BTCs for the high heterogeneity, low heterogeneity, and constant DFN realizations for the relatively dense network. Both high and low ensembles again show similar first arrival times, which are slightly earlier than the constant aperture network, but not substantially so. The scaling of the tail in the BTCs are now quite similar between the high and low heterogeneity DFNs, with slopes of -1.06 and -1.09, respectively. The BTC of the constant DFN decays faster than both the high and low heterogeneity DFNs, but is within the 95% confidence intervals of both up until  $10^{-1}$  years. For the high density DFNs,  $d_Q/P_{32}$  mean values decrease as  $CV$  is increased, indicating an increase in flow channeling. The  $d_Q/P_{32}$  values for the high heterogeneity, low heterogeneity, and constant DFNs are 0.225, 0.278, and 0.326, respectively.

#### 6.2.4 Discussion

We have investigated the impact of fracture-to-fracture aperture heterogeneity on flow and transport in variable density fracture networks using high fidelity flow modeling and Lagrangian particle tracking in DFN models. Our results point to several interesting points previously not discussed in the fracture literature or that might be re-interpreted in light of the findings of this study.

In terms of transport, when particles are forced to sample the extent of the fracture-to-fracture aperture heterogeneity, there is a significant effect on both the timing of the initial breakthrough and the tailing behavior of the particle breakthrough that could be classified as anomalous. As the fracture network density, and subsequently the number of percolation paths, is increased, the initial breakthrough behavior is less dependent on the inter fracture aperture heterogeneity. Our results suggest that in the denser networks there is a greater degree of flow channeling as the  $CV$  is increased, hence changes in the fracture-to-fracture aperture heterogeneity are partially negated by changes in flow channeling, which explains why the breakthrough behavior of particles is similar between high and low heterogeneity ensembles. When there are relatively few percolation paths, however, the tailing behavior shows a strong dependence on the inter fracture aperture heterogeneity, with heavy and long tails in cases with high  $CV$ . Increasing the fracture network intensity to the point where there are many percolation paths washes out most of the effects of inter-fracture heterogeneity because the particles are no longer forced to sample the aperture heterogeneity present in the networks. At the extreme case where there is only one percolation path, the effects of aperture heterogeneity are amplified to the point where initial breakthrough times are heavily dependent on the degree of variation, here measured by  $CV$ . When apertures are increased in networks with a single percolation path, it is possible to actually delay the solute first arrival times due to strong velocity fluctuations from high fracture-to-fracture aperture changes, which is consistent with counter-intuitive analytical expectations. We only considered networks where the fracture apertures were increased relative to a constant baseline to probe this behavior.

Previous research has studied the link between fracture-to-fracture aperture heterogeneity from different perspectives than what we have done here and could be re-interpreted in light of our results. For one aspect, it has been published that under anisotropic mechanical stress fields, aperture distributions may widen and become more variable (Kang et al., 2019a; Lei et al., 2017; Sweeney & Hyman, 2020; Garipov et al., 2016; McClure et al., 2016; Tran & Jha, 2021). If the network is short circuited relative its original topology via connected shear fractures, one can expect early arrival times of solutes relative to the original network. We suggest this is less a consequence of apertures actually increasing, but the fact that given equivalent stress conditions, the connected fractures are likely similar in apertures, which would result in a low aperture heterogeneity pathway through the network, especially in sparser networks with few percolation paths. A second aspect to consider is with respect to flow channeling. Separate studies have looked at the relationship between flow channeling and network density (Hyman et al., 2020) and fracture-to-fracture aperture heterogeneity (Hyman et al., 2016; Kang et al., 2020). In the case of network density, the relationship between flow channeling and network density was shown to be negatively correlated, while for fracture-to-fracture aperture heterogeneity the relationship is positively correlated. Our results show that at low network

density, the degree of flow channeling is relatively unaffected by changes in the fracture-to-fracture aperture heterogeneity, whereas at high network density flow channeling does indeed increase, which is consistent with Kang et al., (2020). As alluded to in the previous paragraph, this is an important aspect to consider because the degree of flow channeling tells us how much of the network velocity field the particles are sampling as they traverse the network structure. In the case where the network density is high and the aperture heterogeneity is also high, the increase in flow channeling signifies that much of the network is not actually contributing to the flow and transport. Consequently, changes in the fracture apertures are not likely to have as dramatic effects as they do in sparser networks.

Changes in both fracture-to-fracture aperture heterogeneity and network density have strong effects on flow and transport in fracture networks, which we characterized using a flow channeling metric and breakthrough behavior of particles. This study was limited to theoretical considerations but could be extended to natural or engineered fractured systems in the future, which could elucidate these relationships further. Much of the energy production around the world is from subsurface fractured systems (Viswanathan et al., 2022). Tapping into these energy sources often involves stimulating them with high aperture fractures, which then connect to natural fracture networks. Our results suggest this should be done carefully because creating a system with large differences in fracture aperture could have the opposite of the intended effect in terms of energy production.

### **6.3 Effects of Geometric Features on Reactive Transport and Mineral Precipitation in Fracture networks**

To understand how geometric features affect reactive transport and mineral precipitation, we investigated reactive transport in discrete rough intersecting fracture networks leading to precipitation of secondary carbonate phases. The scale that is considered in this study is on the order of meters, although the results could be applicable to smaller and larger scale systems with adjustment for the width and permeability of the fracture zones. We considered a scenario where fluid mixing provides the necessary supersaturation for carbonate precipitation. We considered flow in a subsurface fracture network within which only single-phase flow occurs. A single initial permeability is adopted for the discrete fracture zone with the assumption that the fracture itself is filled with crushed and granulated material such that it can be considered locally as a porous medium. Mineral precipitates that accumulate in the pore space of the fracture gradually reduce permeability. This example is used primarily to investigate the effects of fluid mixing in intersecting fractures.

#### **6.3.1 CrunchFlow for Modeling Reactive Transport**

The reactive transport behavior of intersecting fracture networks was investigated in 2D with the software CrunchFlow (Steefel et al., 2015). CrunchFlow (or CrunchTope) is a general-purpose multicomponent reactive transport simulator to handle advective, diffusive, and dispersive transport, and an arbitrary number of mixed equilibrium and kinetic reactions. CrunchFlow is able to simulate single-phase flow in heterogeneous domains, including fracture flow (e.g., Steefel and Lichtner, 1998). Using a photograph of fractured granite (Figure 6-4a), we added an additional fracture to increase the interest of the simulation (computational grid shown in Figure 6-4b). The same fractured rock was considered previously by Hu and Ruqvist (2021). The fractures were conceptualized as a set of segments with arbitrary distributions of asperities along the fractures in 2D into the plane shown in Figure 6-4. Thus, as in Steefel and Lichtner (1994) and Steefel and Lichtner (1998), the interface between the fractures and the adjacent rock matrix is also a plane into the page.

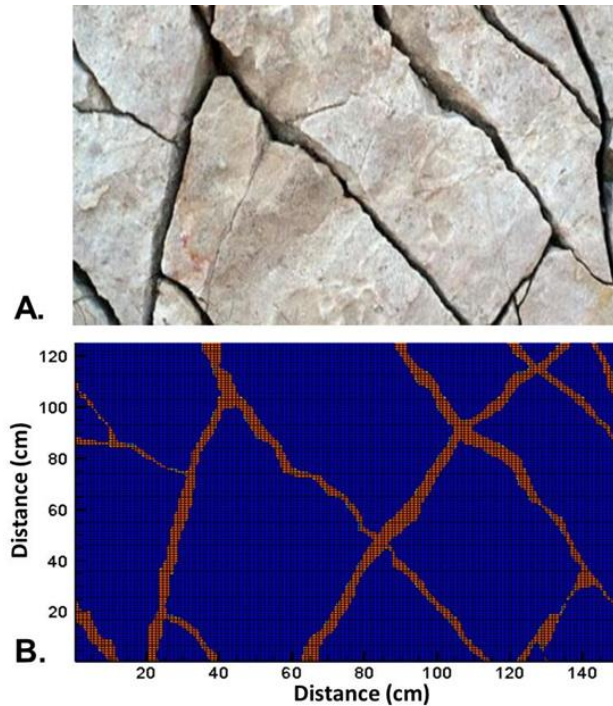


**Figure 6-4.** A. Photograph showing intersecting rough fractures in granite (top). B. Computational grid developed from the photograph, with an additional fracture added to increase the interest of the simulation. The mixing simulations discussed below consider a horizontal domain measuring 160 by 128 cm with a uniform grid spacing of 1 cm, while the critical zone simulations consider a vertical domain measuring 200cm in Z (height) and 62 cm in X discretized with 1.0 and 0.25 cm spacing respectively.

### 6.3.2 Reactive Transport Approach

The software CrunchFlow (Steeffel et al., 2015) is used to solve the following multicomponent reactive transport equation given by

$$\frac{\partial(\phi S_L C_i)}{\partial t} = \nabla \cdot (\phi S_L D_i^* \nabla C_i) - \nabla \cdot (\phi S_L v C_i) - \sum_{r=1}^{N_r} \nu_{ir} R_r - \sum_{m=1}^{N_m} \nu_{im} R_m - \sum_{l=1}^{N_g} \nu_{il} R_l \quad (6-11)$$

where  $C_i$  is the concentration of the  $i$ th species;  $\phi$  is the porosity;  $S_L$  is the liquid saturation;  $D_i^*$  is the combined dispersion-diffusion coefficient in porous media;  $v$  is average linear velocity;  $\nu_{ir}$ ,  $\nu_{im}$  and  $\nu_{il}$  are the stoichiometric coefficients for  $N_r$  aqueous reaction,  $N_m$  mineral reactions, and  $N_l$  gas reactions at  $R_r$ ,  $R_m$ , and  $R_l$  rates, respectively. For mineral dissolution and precipitation, a TST-type rate law is used to describe both magnesite and forsterite:

$$R_m = -A_m k_m \left[ 1 - \frac{Q}{K_{eq}} \right] \quad (6-12)$$

where  $A_m$  is the reactive surface area ( $\text{m}^2 \text{m}^{-3}$ ),  $k_m$  is the rate constant ( $\text{mol m}^{-2} \text{s}^{-1}$ ), and the convention used is that the rate is positive in the case of precipitation. For the mixing simulations, however, only magnesite precipitation is considered, because forsterite is not present. The porosity  $\phi$  is updated according to the evolving mineral volume fractions  $\phi_m$  as a result of reaction according to

$$\phi = 1 - \sum_1^{N_m} \phi_m \quad (6-13)$$

### 6.3.3 Flow Simulations

Darcy's Law is used to calculate flow velocities in the fracture network. As our focus here is on mixing in a general subsurface environment, we simulated single phase flow with the assumption that the fracture zones shown in Figure 6-4 consist of coarsely crushed rock that can be described with a single initial permeability value.

The first set of simulations investigating the role of fluid mixing was based on a computational domain measuring 160 by 128 centimeters and used a constant 1 cm grid spacing (Figure 6-4b). In these simulations, the fractures are zones consisting of permeability of  $10^{-13} \text{m}^2$  that contrasts with the rock matrix permeability of  $2.5 \times 10^{-19} \text{m}^2$ . The value of permeability of the fracture zone is close to what has been reported for fractures and shear zones at Yucca Mountain by Chen et al (2022) (about  $5.0 \times 10^{-13} \text{m}^2$ ). Following the approach in many subsurface treatments, mixing simulations considered only single-phase flux,  $q$ , described by the classical Darcy's law:

$$q = -\frac{k}{\mu}(\nabla p) \quad (6-14)$$

where  $k$  and  $\mu$  are permeability and the dynamic viscosity. In the simulations in which the porosity evolves due to geochemical reactions, permeability was updated according to:

$$k = k_0 \frac{\phi^3}{\phi_0^3} \quad (6-15)$$

where  $k$  is permeability and  $k_0$  and  $\phi_0$  are initial permeability and porosity, respectively. Darcy's law was used to calculate the flow velocities, satisfying  $q = \phi v$ . In the single flow simulations, the initial porosity of the fractures is assumed to be 0.20. Combining Equations (6-11) through (6-15), we consider advection, multicomponent diffusion and chemical reaction in fractured porous rocks where permeability can be changed due to changes of porosity as a result of chemical reaction.

### 6.3.4 Simulations of Mixing

In the simulations designed to investigate the role of fluid mixing in intersecting fractures, differing geochemical boundary conditions are used on either side of the dashed white mixing line along the lower boundary (Figure 6-5 and Table 6-1). Fractures (shown in tan) consist of higher permeability zones ( $10^{-13} \text{m}^2$ ) cutting through lower permeability rock matrix ( $2.5 \times 10^{-19} \text{m}^2$ ). A net pressure gradient of 7813 Pa/m was applied from bottom to top across the domain, with the X-Y domain considered to be perpendicular to the gravitational vector (i.e., no gravity effects on the advection). The sides of the domain are considered no-flow, making the fractures along the left and right essentially dead-end pores. The aqueous diffusion coefficient is assumed to be  $10^{-9} \text{m}^2 \text{s}^{-1}$ . Thus, diffusive exchange with the rock matrix was included in the simulations, but the effect was minor because of the abundant reactive material assumed to be present in the fracture system itself, and because the rock matrix diffusivity was assumed to be low.

The mineral precipitation reaction we considered involved the Mg-carbonate mineral magnesite ( $\text{MgCO}_3$ ) formed from the aqueous species  $\text{Mg}^{2+}$  and  $\text{CO}_3^{2-}$ . Two scenarios were considered: 1) a case in which both segments of the lower boundary were  $< -0.45 \log Q/K_{\text{eq}}$  with respect to magnesite, and 2) a case in which the left segment was close to equilibrium with respect to magnesite.

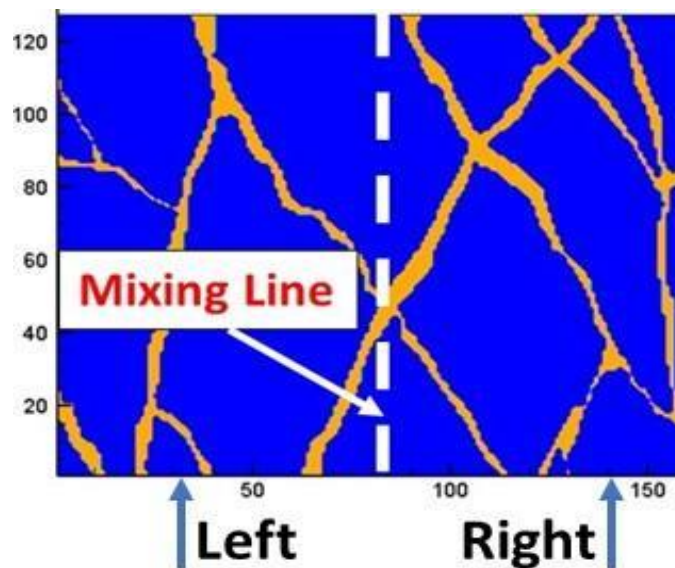


**Figure 6-5.** Schematic of computational domain showing a discrete rough fracture network and the mixing line in dashed white. Differing geochemical boundary conditions are used along the lower boundary on either side of the dashed white line. Flow is from bottom to top.

The geochemical boundary condition in Table 6-1 designated “Left” extends between 0 and 80 cm along the lower boundary, while the boundary condition designated “Right” extends from 80 to 160 cm. The boundary conditions are chosen to achieve magnesite supersaturation due to mixing between fractures originating from the left and right intersect at about 50 cm above the lower boundary.

**Table 6-1.** Geochemical boundary conditions used on lower boundary for mixing simulation. Units for the magnesium, sodium, and chloride ions are in molarity (M).

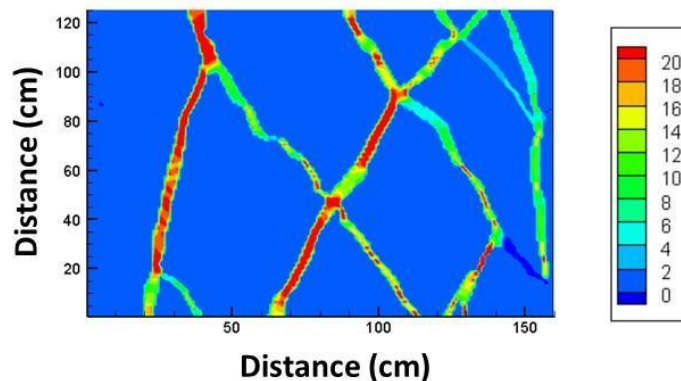
	Left Boundary	Right Boundary	Initial
pH	7.8	8.2	7.5
pCO <sub>2</sub> (bars)	0.02	0.0005	0.0003
Mg <sup>++</sup> (M)	0.0001	0.0008	0.00001
Na <sup>+</sup> (M)	0.1	0.1	0.1
Cl <sup>-</sup> (M)	0.1	0.1	0.1
Magnesite Saturation ( $\log Q/K_{\text{eq}}$ )	-0.567	-0.457	-3.980

Table 6-2 gives the kinetic parameters used in the simulations. The value for the magnesite rate constant is representative of what was found in various experimental studies (e.g., Giammar et al., 2005; Xiong and Giammar, 2014; Steefel and Yang, 2021). The value for reactive surface area in the fractures represents a reasonable value for coarsely crushed material, which is then treated as an equivalent porous and permeable medium. Magnesite is allowed to form without a nucleation barrier according to the rate law given in Equation 6-12.

**Table 6-2.** Rate constant and reactive surface area for the mixing simulations.

	Rate Constant ( $k_m$ ) mol m <sup>-2</sup> s <sup>-1</sup>	Reactive Surface Area ( $A_m$ ) m <sup>2</sup> m <sup>-3</sup>	Initial Mineral Volume Fraction m <sup>3</sup> m <sup>-3</sup>
Magnesite	10 <sup>-8</sup>	100	0.00

The permeability distribution shown in Figure 6-4a and the net pressure head gradient of 7,813 Pa/m leads to a distribution of Y velocities shown in Figure 6-6. The variations in velocity along the extent of the fractures are due to the combination of the variable thickness of the fracture zones and the fluid mixing where two fractures join to form a single fracture, as in the upper left portion of the domain. Where two fractures intersect, the flow is split between the two fracture extensions, as in the intersecting fracture set at about 50 cm from the lower boundary in the Y direction along the mixing line shown in Figure 6-6.



**Figure 6-6.** Initial velocity distribution (m<sup>3</sup> m<sup>-2</sup> yr<sup>-1</sup>) in the fractures for the single-phase flow mixing case.

In the first set of mixing simulations, magnesite is undersaturated along the entire length of the lower boundary (i.e., in both the “Left” and “Right” sectors shown in Figure 6-5; see Table 6-1). Thus, supersaturation is only achieved by mixing, which occurs primarily at the fracture intersection occurring at about  $X = 80$  cm and  $Y = 50$  cm.

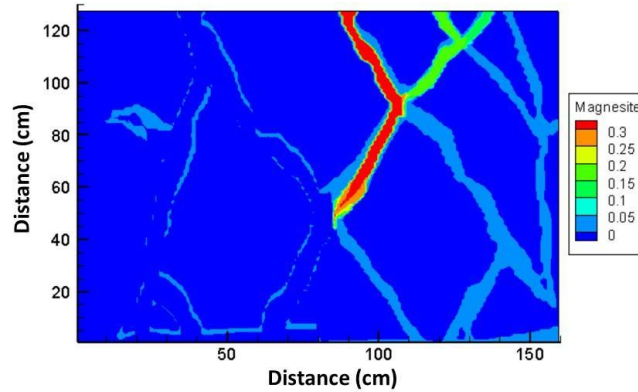


**Figure 6-7.** Magnesite supersaturation  $\log\left(\frac{Q}{K_{eq}}\right)$  developed above fracture intersection at approximately  $X = 80$  cm and  $Y = 50$  cm due to mixing. Flow is from bottom to top. The lower boundary is undersaturated with respect to magnesite.

The question arises whether the supersaturation developed on the upper right limb of the two intersecting fractures is due to geochemical or flow effects? This can be easily tested by switching the geochemical boundary conditions in Table 6-3 (“Left Boundary” and “Right Boundary”). When this is done, the supersaturation develops in the same area, indicating that the discrete zone of supersaturation is driven by the fracture flow characteristics rather than the geochemistry (result not shown). Similarly, in the next intersection at about  $X = 110$  cm and  $Y = 95$  cm, the magnesite precipitation rate is different on either segment following this intersection. The generalization here is that discrete fracture segments can develop distinct geochemical characteristics depending on the fracture flow geometry and rates.

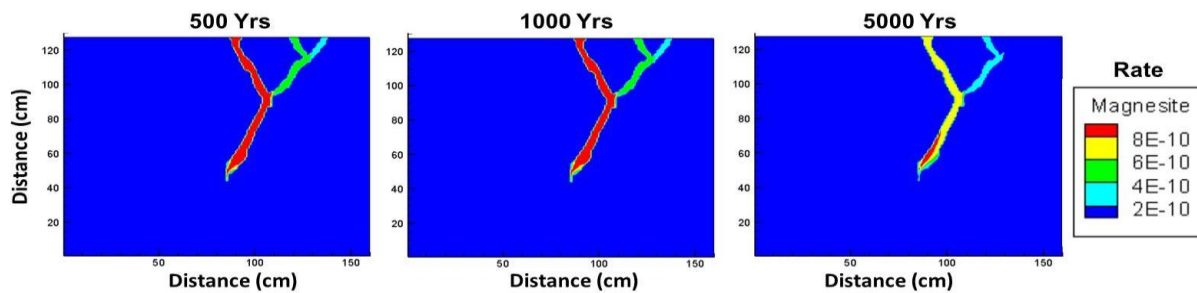


**Figure 6-8.** Precipitation rate ( $\text{mol m}^{-3} \text{s}^{-1}$ ) of magnesite over time driven by supersaturation.

As with the magnesite saturation plot in Figure 6-8, switching the geochemical boundary conditions has no effect on the results. Thus, one may conclude that the precipitation zone is controlled by the greater flux coming in from the fracture on the lower left, driving the reaction products to the right on the upper side of the fracture intersection. The precipitation of magnesite in the fracture causes a reduction in absolute porosity shown in Figure 6-9.

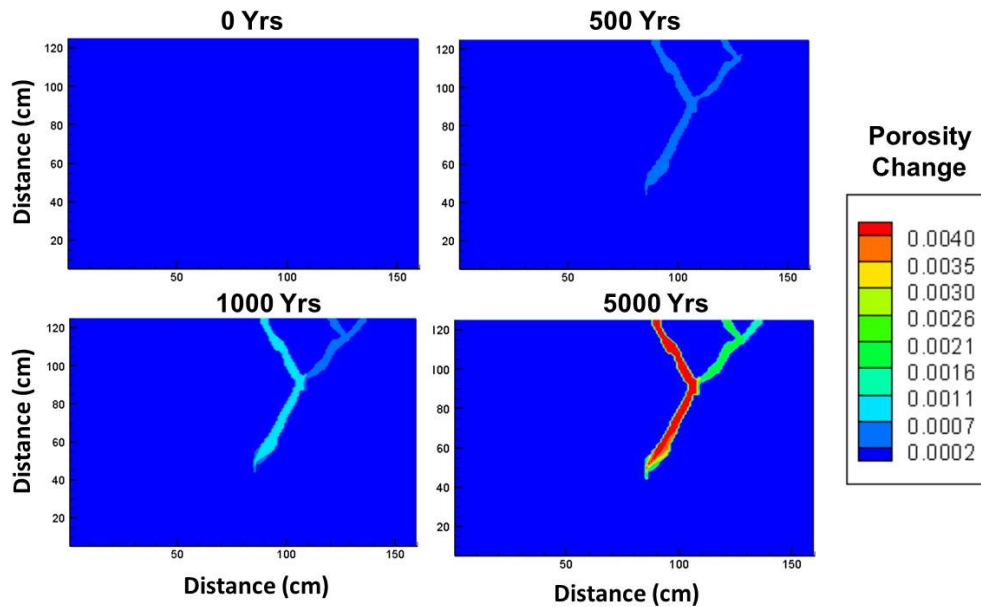


Figure 6-9. Absolute change in porosity due to magnesite precipitation.

Since the resulting porosity change in the fracture zone is relatively small, the effects on permeability are similarly minor (Figure 6-10), although clearly detectable between 1,000 and 5,000 years.

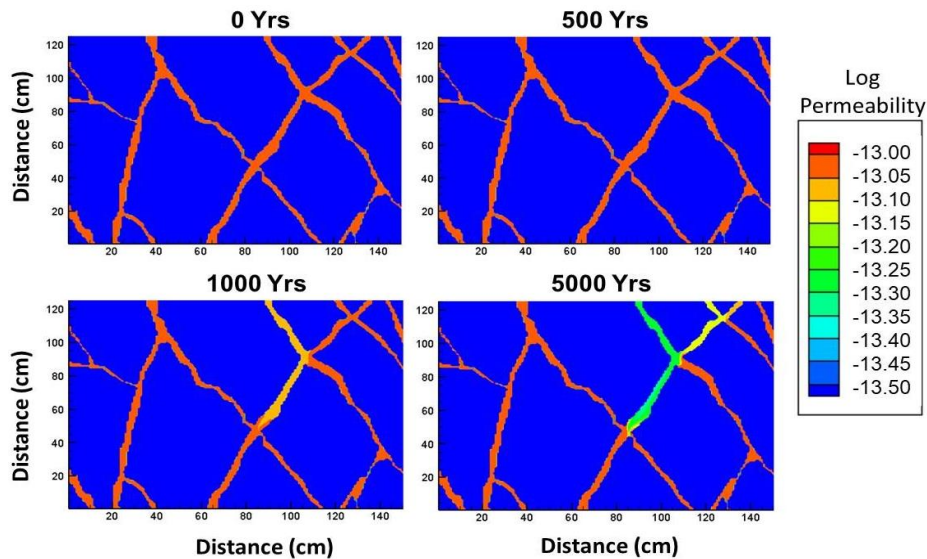
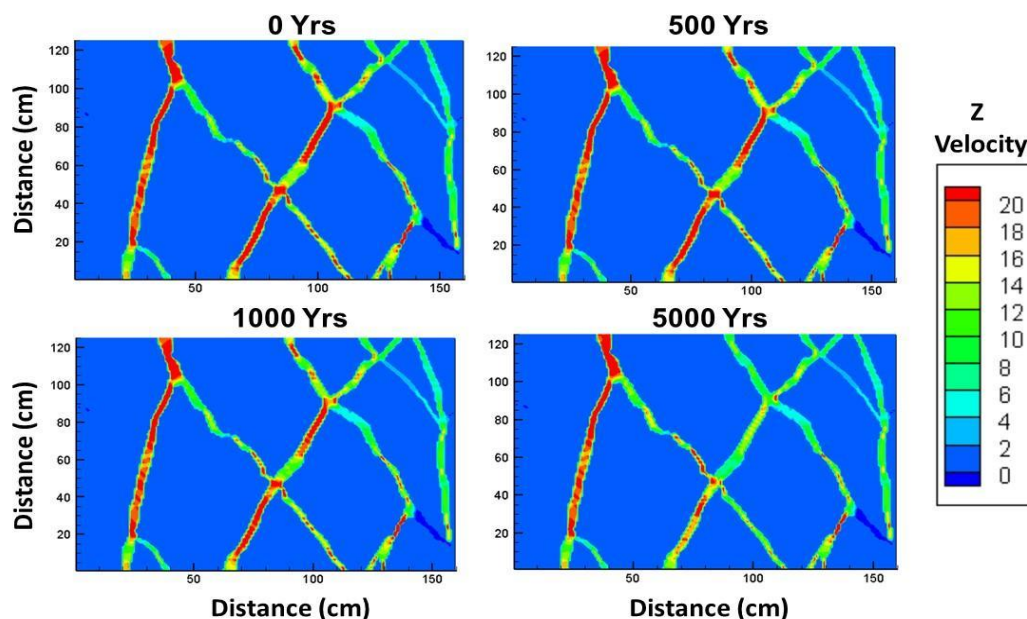


Figure 6-10. Evolution of the fracture permeability (m<sup>2</sup>) to 5,000 years. The precipitation of magnesite in the right-hand fracture segment above the intersection at Y = 50 cm causes the permeability decrease.

As expected from the gradual decrease in permeability in the fracture segment above and to the right of the intersection at approximately  $X=80$  cm and  $Y=50$  cm, the flow velocity is gradually reduced selectively within the fracture segment where the magnesite precipitation occurs (Figure 6-11).



**Figure 6-11.** Evolution of the fracture flow Z velocities ( $\text{m}^3 \text{m}^{-2} \text{yr}^{-1}$ ) for mixing case.

As discussed above, magnesite precipitation only occurs selectively in the right-hand segment of the fracture close to the intersection at 50 cm from the lower boundary. With the geochemical boundary conditions, summarized in Table 6-3, and the calculated flow velocities in the fractures, it is not possible to produce supersaturation and precipitation of magnesite on the left-hand side of the modeling domain. To produce supersaturation and magnesite precipitation, it requires that the left-hand boundary be slightly supersaturated with respect to magnesite (Table 6-3). However, this boundary condition then only results in magnesite precipitation on the left side of the domain (Figure 6-12), and in this case mixing plays little role.

**Table 6-3.** Geochemical boundary conditions for Mixing Case 2 used on lower boundary. Units for the magnesium, sodium, and chloride ions are in molarity (M).

	Left Boundary	Right Boundary	Initial
pH	7.8	8.0	7.5
pCO <sub>2</sub> (bars)	0.003	0.00075	0.0003
Mg <sup>++</sup> (M)	0.001	0.001	0.00001
Na <sup>+</sup> (M)	0.1	0.1	0.1
Cl <sup>-</sup> (M)	0.1	0.1	0.1
Magnesite Saturation	0.004	-0.584	-3.980

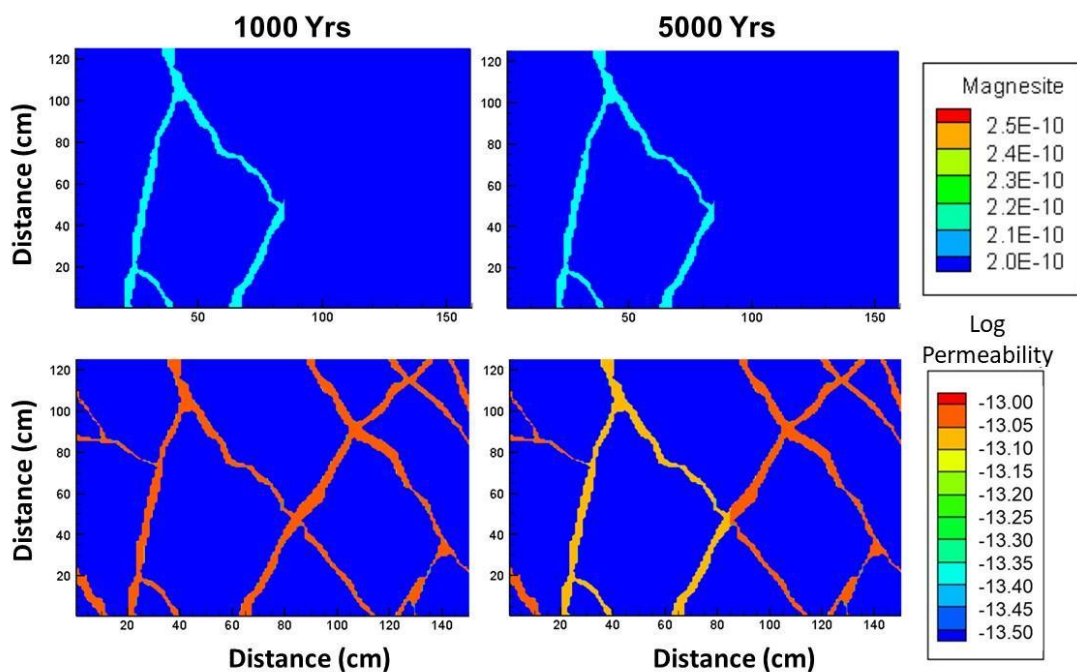


**Figure 6-12.** Simulations using geochemical conditions in Table 6-3, with the left-hand side of the lower boundary slightly supersaturated with respect to magnesite. Mixing on the right-hand side only serves to dilute the solution coming from the left side, thus preventing magnesite precipitation in this part of the domain altogether. Upper panel gives the magnesite rate in units of mol m<sup>-3</sup> s<sup>-1</sup>. Lower panel gives the value of the log permeability in m<sup>2</sup>.

### 6.3.5 Discussion

In this study we have considered several possible scenarios and environments associated with reactive flow in intersecting fracture networks. Nonetheless, several important generalizations emerge from these simulations. The most important of them is that the time evolution of physical and chemical properties in the case of an intersecting fracture network is likely very different from what is realized in natural fractured porous media. This is chiefly because the reaction processes in intersecting fractures can dramatically impact the connectivity of the flow system. This may be particularly the case where mixing, considered in the first set of simulations above, leads to mineral precipitation and/or dissolution in specific fracture segments, while leaving other segments nearly unaffected. This kind of behavior is evident in Figures 6-9 and 6-10, indicating that the porosity and permeability change will ultimately block the entire portion of the fracture flow system above and to the right of the intersection point 50 cm above the lower flow boundary.

The time scales for this to occur depend on the geochemical system considered, the flow rates, and the porosity and permeability of the fracture zones. In the case of a fracture network with numerous intersections, there is the possibility of extensive reorganization of the flow system because the reaction processes can affect specific segments and relatively small volumes, which are critical to the connectivity of the flow system. In this regard, the behavior is akin to what one might find at the pore scale, with local flow and geochemical gradients generating different geochemical conditions in individual pore bodies and pore throats. However, the effect is expected to be more dramatic in fracture networks, since there is very limited diffusive (as opposed to flow) mixing between fractures, in contrast to what is normally expected at the pore scale (Li et al, 2008; Molins et al., 2012; Molins et al., 2014). Thus, the local heterogeneous conditions in the fracture network, often separated by discrete intersections, may be effectively preserved compared to the pore scale where length scales are sufficiently small that diffusive mixing can occur. In fracture networks, the simulations presented here suggest that the time and space evolution of the flow connectivity due to local reactive flow and transport processes may be more important than the effects of the bulk or volume-averaged changes in physical and chemical properties.

## 6.4 Conclusions

We have investigated the effect of multi-scale heterogeneities on flow and transport properties in fracture networks. We have modeled flow and transport in fracture networks with varying degrees of fracture-to-fracture aperture heterogeneity and network density to show how changes in these properties can cause the emergence of anomalous flow and transport behavior. If fracture-to-fracture aperture heterogeneity is increased in sparse networks, velocity fluctuations inhibit high flow rates and solute transport can be delayed. Surprisingly, transport can be slowed even in cases where hydraulic aperture is monotonically increased. As the density of the networks is increased, more connected pathways allow for particles to bypass these effects. There exists transition behavior where with relatively few connected pathways in a network, first arrival times of particles are not heavily affected by fracture-to-fracture aperture heterogeneity, but the scaling behavior of the tails is strongly influenced. These results reinforce the importance of considering multi-scale effects in fractured systems and can inform flow and transport processes in both natural and engineered fracture systems and in particular, crystalline rocks.

We have also investigated the interplay between the geometric features of fracture networks (asperities and intersections) and mineral precipitation and its effect on porosity and permeability changes. Fracture intersections can significantly affect reaction-induced changes in fracture properties and therefore the connectivity of the fractures. This impact likely exceeds the effect(s) of changes of the geometry, and bulk physical and chemical properties. The time scales in an intersecting fracture network are likely to be shorter than would be the case for nearly homogeneous porous media, since local reaction-induced changes in the fracture can have an outsized impact on the flow and transport regime through modifications of the connectivity associated with mineral precipitation and dissolution at or close to fracture intersections.

## **7.0 BENTONITE EROSION, COAGULATION/FLOCCULATION, AND CLOGGING IN A FRACTURED CRYSTALLINE ROCK**

### **7.1 Introduction**

In FY23, experiments at LANL were designed to study bentonite clay erosion, coagulation/flocculation, and simulate fracture clogging behaviors under controlled conditions. Much of FY23 was spent assembling experimental apparatus, developing measurement techniques, and optimizing experimental conditions. As presented, these experiments consist of two parts: a bentonite erosion cell and a bentonite coagulation cell. Future experiments will work towards the integration of these two experimental approaches, so that erosion and coagulation can be studied and described from a single experimental system. All experiments described herein were performed using unwashed Wyo-Ben Big Horn 325 bentonite, a non-treated sodium bentonite in either an uncompacted, compacted, or colloidal form. Future experiments will use washed and homoionic forms of bentonite as well as hydrothermally aged/altered bentonite to better understand the parameters which significantly impact bentonite erosion and coagulation in geochemical conditions relevant to spent nuclear waste repositories.

### **7.2 Bentonite Erosion Cell**

A bentonite erosion cell was developed and fabricated that allows bentonite colloids to be eroded from a bentonite surface under specific and reproducible conditions. A diagram of the cell is shown in Figure 7-1. A plug of bentonite is emplaced in the erosion cell separated from the flow field by a porous titanium frit. The titanium frit is sized such that bentonite colloids can pass through the frit, but the bulk bentonite plug is retained. The distance between the upper (A) and lower (C) plates in Figure 7-1 is fixed by the 6 retaining bolts while the middle plate is free to move downwards as the bentonite plug swells. That swelling pressure is measured on a load cell, which is placed between the middle (B) and lower (C) plates and recorded by a computer. All components of the erosion cell are fabricated from titanium, Viton rubber, or PEEK plastic to prevent any contributions from iron corrosion. Iron oxides were observed in previous diffusion experiments utilizing a similar design, but with stainless steel components (Pope, 2017). Iron oxides are best avoided as they can clog filters and have high adsorption capacities for many radionuclides. The erosion cell was designed with an eye towards future experiments, which will involve influent flows of different chemistries, elevated temperatures, different bentonites and bentonite emplacement conditions, and radionuclide transport experiments. Plate B has also been designed with flow ports, so that future experiments can consider the effects of influent flows of different chemistries, temperatures, or solute transport across the bentonite plug.

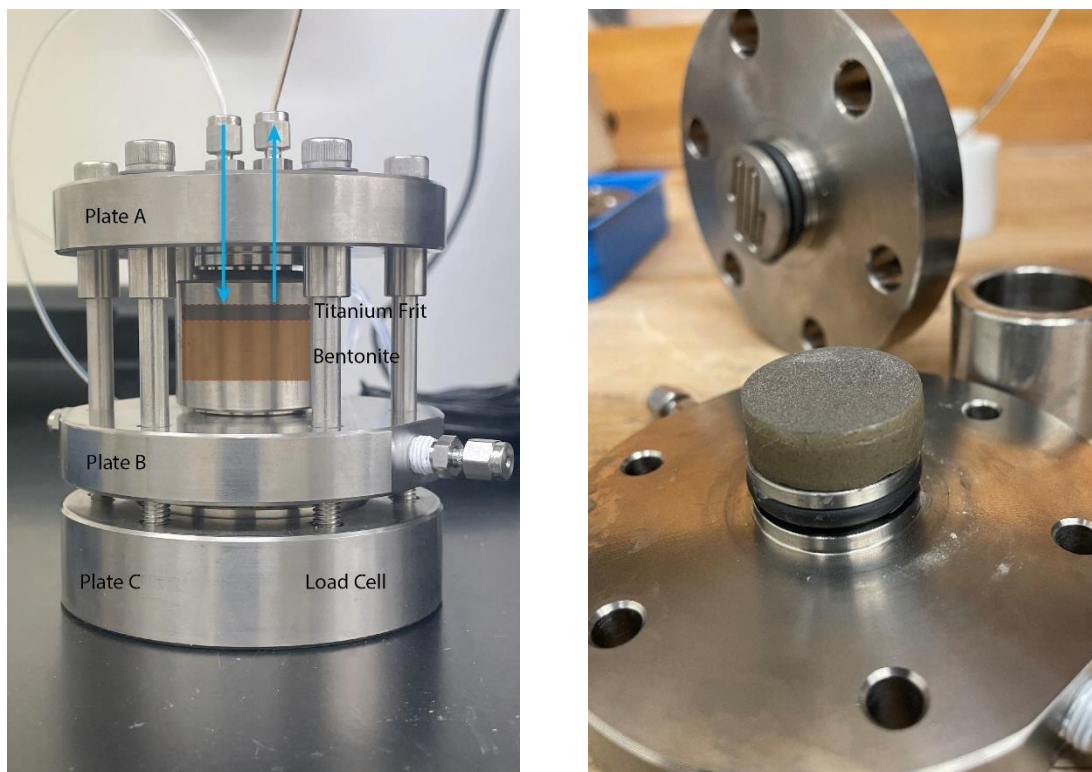


**Figure 7-1.** The bentonite erosion cell. A plug of bentonite is emplaced in the titanium cell and separated from the flow field by a titanium frit. The frit allows bentonite colloids to pass through while the bulk bentonite is retained.

### 7.3 Colloid Concentration Measurement Method Development

A method needed to be developed that would be capable of reliably quantifying bentonite colloids at low concentrations. A method was adapted from EPA Method 180.1 (*Determination of Turbidity by Nephelometry*) using a filter from a Hach turbidimeter and a UV-Vis spectrometer. Through experimentation it was found that an absorbance measurement taken at 425 nm and baseline corrected to an absorbance taken at 725 nm provided a highly linear response from the limit of detection to 300 mg·L<sup>-1</sup>. The limit of detection by this method was statistically determined to be 3.3 mg·L<sup>-1</sup>, whilst the limit of quantification was approximately 4 mg·L<sup>-1</sup>.

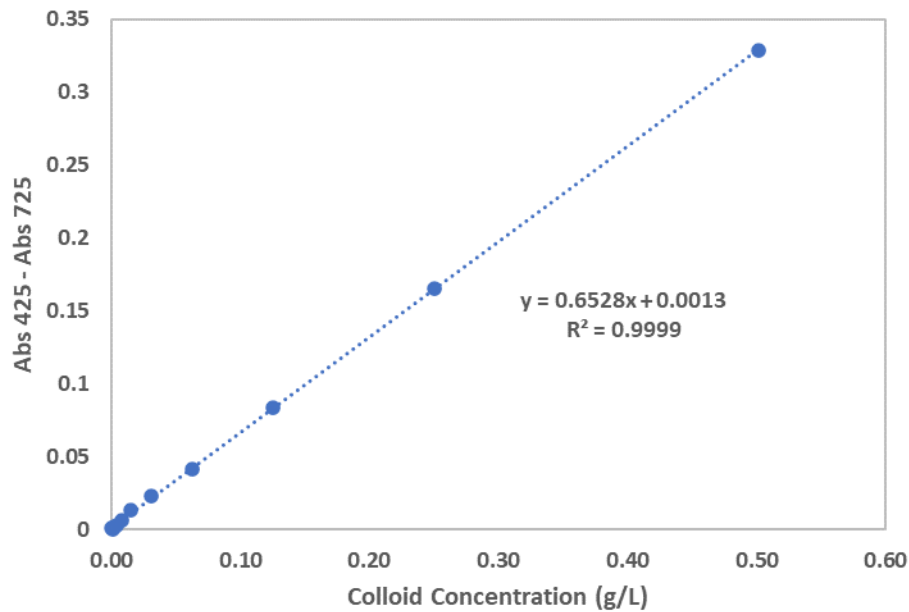


Figure 7-2. Linear range of bentonite colloid quantification methodology.

## 7.4 Selection of the Titanium Frit

An essential component of the experimental cell is the titanium frit. Without a frit, bulk bentonite can extrude directly out of the erosion cell as a gel, rather than as colloidal material. The inclusion of a frit ensures that only eroded bentonite colloids are transported out of the cell, making it possible to study bentonite colloid transport to a downfield fracture not in proximate contact with the bentonite buffer material. Titanium was selected as a frit material due to its inertness and commercial availability, and the possibility of stainless-steel frits to corrode and introduce iron precipitates to the experimental cell. Cylindrical frits manufactured from ASTM Grade 1 titanium were procured with the following parameters:

**Table 7-1.** Physical parameters of titanium frit filters, as provided by the manufacturer.

Diameter	25 ± 0.1 mm
Thickness	2 ± 0.1 mm
Porosity	30 – 40 %
Filter Size	1 µm & 10 µm

10 µm and 1 µm filter sizes were selected for preliminary tests based on previous filtering study by Birgersson et al (2009). Birgersson et al. (2009) undertook a systematic study to determine what sintered stainless steel frit sizes were capable of filtering bentonite colloids. Their work concluded that stainless-steel frits with filter sizes greater than 2 µm allowed colloids from a homoionic sodium bentonite to pass through, while frits with filter sizes of 0.5 µm or smaller effectively filtered the colloids (Figure 7-3). Birgersson et al. (2009) used stainless steel frits however, and it was not immediately apparent if stainless steel and titanium frits would behave identically. Therefore, some preliminary colloid generation experiments were performed using 10 µm and 1 µm filter sizes. Compacted bentonite plugs were loaded

into the erosion cell and a  $5 \text{ mL} \cdot \text{hr}^{-1}$  flow of deionized water was flowed through the cell and into a fraction collector which binned the eluent on a 1-hour (5 mL) basis. The experimental setup is shown in Figure 7-4 with the fraction collector to the right, out of frame. The swelling pressure was logged every minute and is plotted in Figure 7-5.

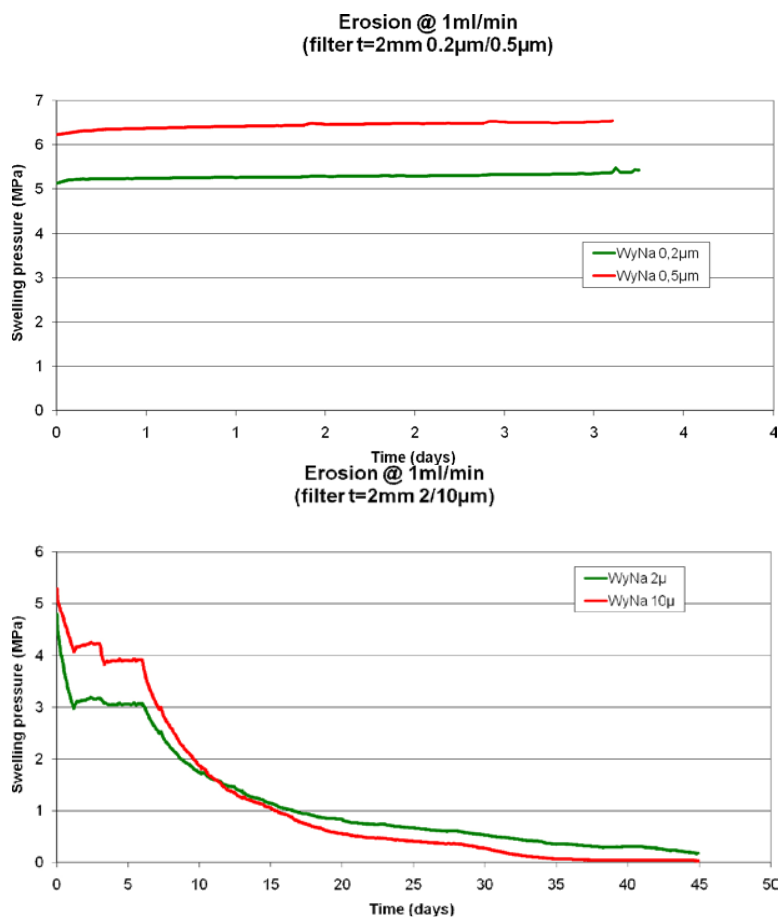


**Figure 7-3.** Top: Swelling pressure of homoionic purified sodium-montmorillonite as a function of time with  $0.2 \mu\text{m}$  (green) and  $0.5 \mu\text{m}$  (red) stainless steel porous frits installed. Bottom: Swelling pressure of homoionic purified sodium-montmorillonite as a function of time with  $2 \mu\text{m}$  (green) and  $10 \mu\text{m}$  (red) stainless steel porous frits installed. From Birgersson et al (2009).

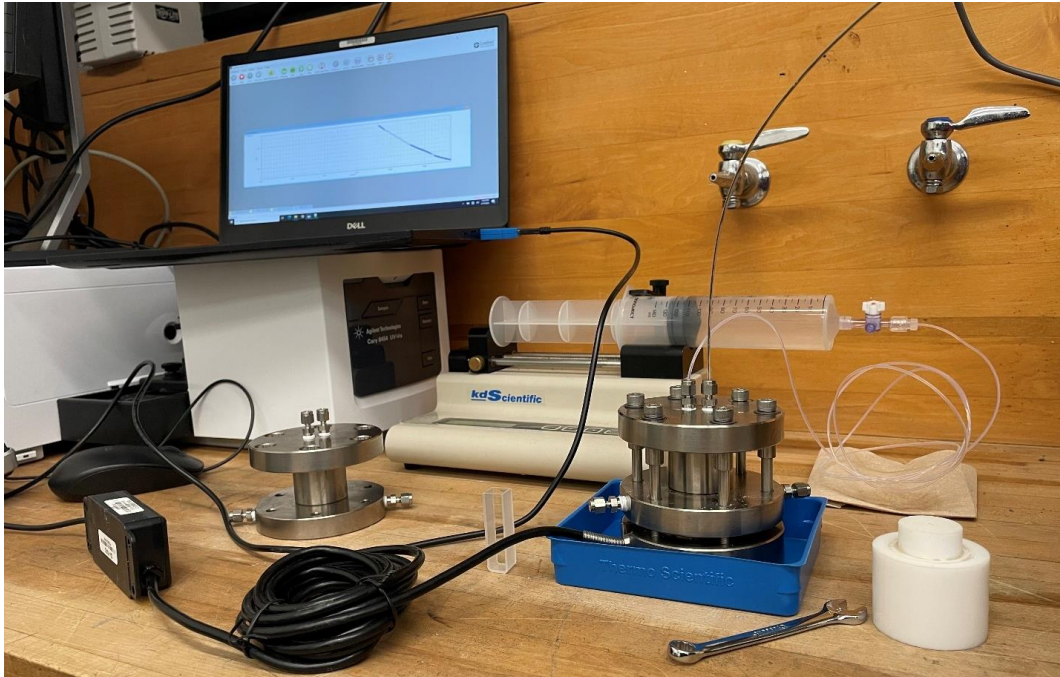


**Figure 7-4.** Bentonite erosion experiment. A  $5 \text{ mL}\cdot\text{hr}^{-1}$  flow of deionized water was provided by the syringe pump to the bentonite erosion cell and flowed to a fraction collector located to the right, just out of frame. The load cell measured a swelling pressure logged data to the computer.

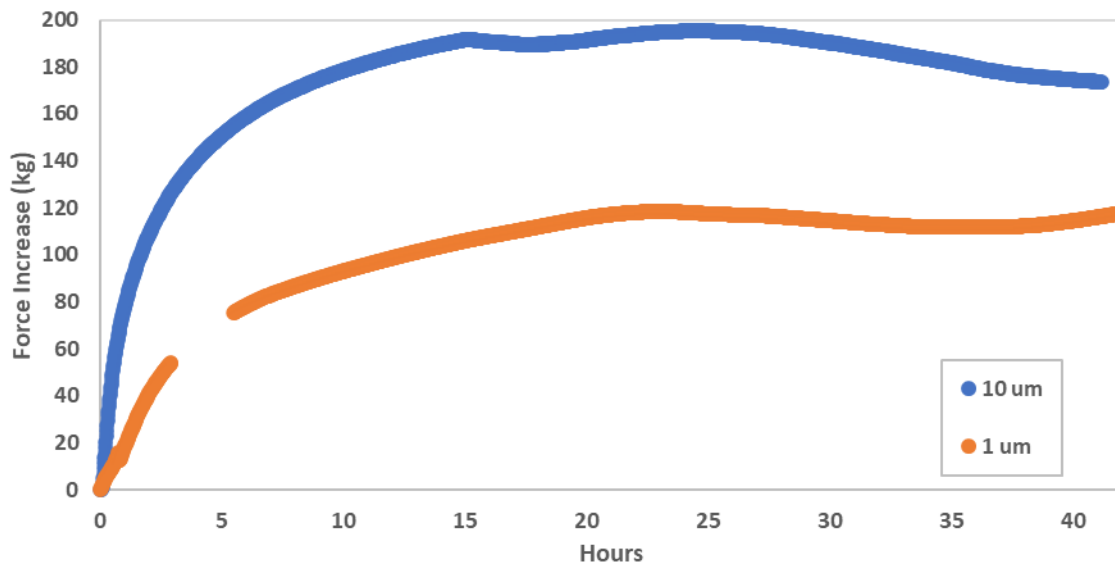


**Figure 7-5.** Swelling pressure of bentonite plugs wetted by a  $5 \text{ mL}\cdot\text{hr}^{-1}$  flow of deionized water confined in the erosion cell by  $1 \mu\text{m}$  (orange) or  $10 \mu\text{m}$  (blue) titanium frits.

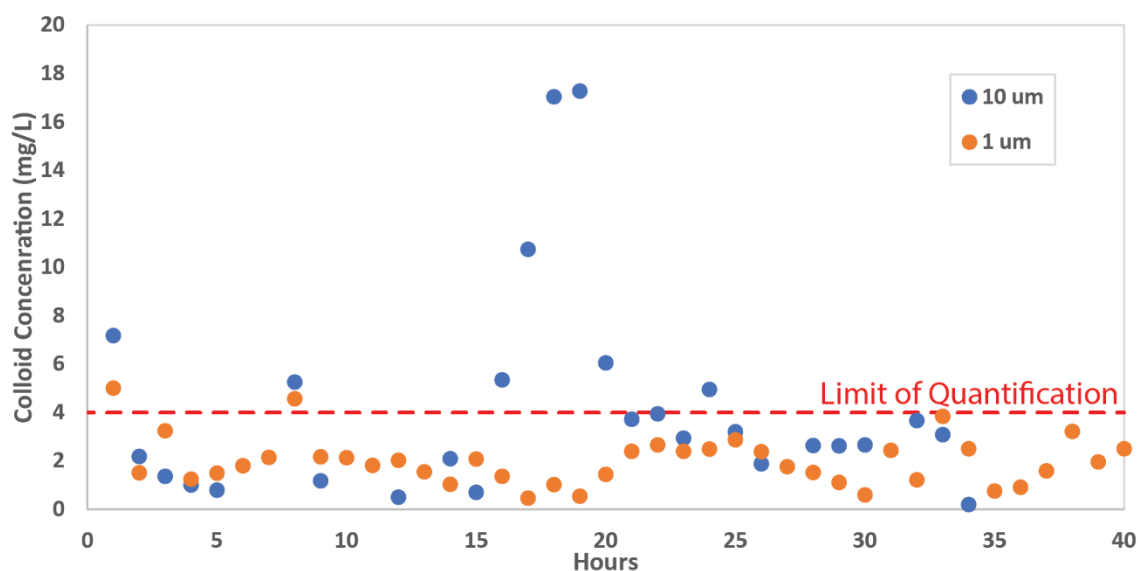


**Figure 7-6.** Colloid concentration of bentonite erosion experiment eluent. Bentonite plugs were wetted by a  $5 \text{ mL}\cdot\text{hr}^{-1}$  flow of deionized water confined in the erosion cell by  $1 \mu\text{m}$  (orange) or  $10 \mu\text{m}$  (blue) titanium frits. The colloid counting method limit of quantification is shown as a dashed red line.

The  $10 \mu\text{m}$  filter size resulted in a greater increase in cell pressure (Figure 7-5), despite being the larger filter size with greater colloid loss (Figure 7-6). This came as a surprise, as experiments with minimally compacted bentonite using  $10 \mu\text{m}$  filters resulted in an immediate decrease in pressure (Figure 7-8). Bentonite compaction may have been more effective at preventing erosion than expected. A more systematic study of the role of compaction will be conducted in the near future. Colloid concentrations were also measured from the eluent collected at the fraction collector. Colloid concentrations from the  $1 \mu\text{m}$  filter were generally below the limit of detection, but some values suggested that some trace colloids did pass through the  $1 \mu\text{m}$ . Therefore, future experiments will examine the use of larger and smaller filters for improved pass/no pass colloid filtration, as well as, different emplacement conditions, for example, various levels of initial bentonite compaction and initial emplacement pressure.

## 7.5 Compacted versus Non-Compacted Bentonite

To investigate the impact of compaction on bentonite swelling behavior, a simple free-swelling (i.e. unconfined) experiment was conducted.  $\sim 10 \text{ g}$  of bentonite, either compacted or non-compacted was placed in glass bottles, which were gently filled with solutions of deionized water,  $1 \text{ M NaCl}$ , or  $1 \text{ M CaCl}_2$ . A photo of the free-swelling experiments is shown in Figure 7-7 after 30 minutes. In this free-swelling (unconfined) experiment, compacted versus non-compacted bentonite behaved very similarly. The compacted bentonite demonstrated little additional resistance to free-swelling compared to the non-compacted bentonite and within  $\sim 1 \text{ hour}$  the compacted and non-compacted bentonites looked nearly identical.

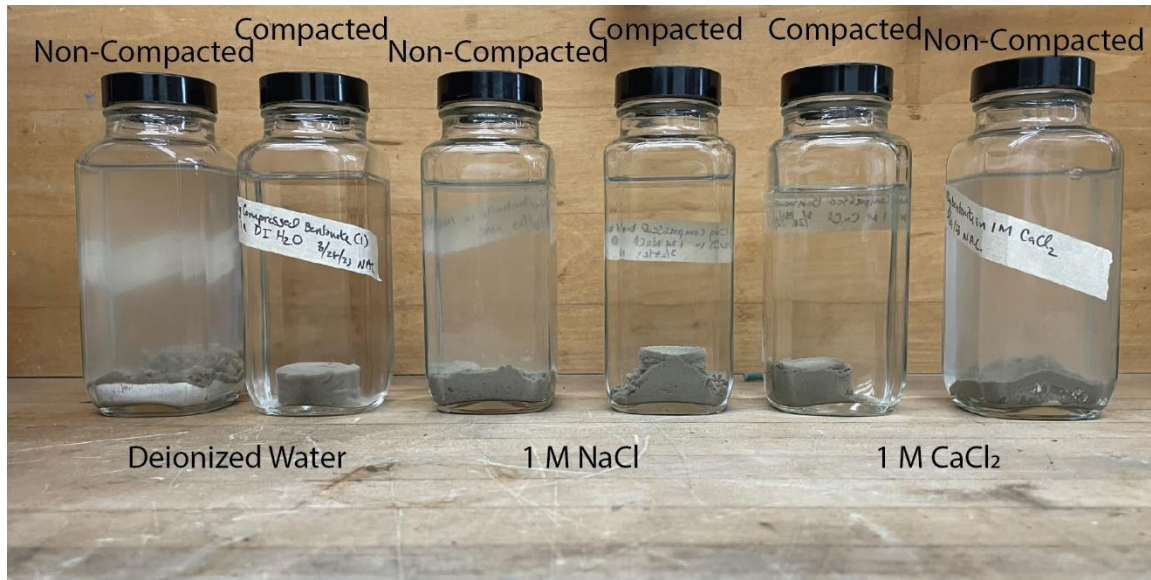


**Figure 7-7.** Bentonite free-swelling experiment after 30 minutes. Compacted and non-compacted forms of bentonite are shown in deionized water, 1 M NaCl, and 1 M CaCl<sub>2</sub>. All bottles contain 10 g of bentonite.

Within the erosion cell, compacted versus non-compacted bentonite behaved differently (Figure 7-8). In both experiments, a 10 $\mu$ m titanium frit was used. In the uncompacted experiment the density of the bentonite plug was  $1.4 \times 10^3 \text{ kg} \cdot \text{m}^{-3}$  (it should be noted that some incidental compaction occurred, as the reported bulk density of the dry bentonite material is  $0.7 \times 10^3 \text{ kg} \cdot \text{m}^{-3}$  -  $0.8 \times 10^3 \text{ kg} \cdot \text{m}^{-3}$ ). In the compacted experiment, a bentonite plug was prepared by compressing ~10 g of bentonite in a 25.4 mm press die to a height of 7 mm, resulting in a cylindrical plug with a density of  $\sim 2.8 \times 10^3 \text{ kg} \cdot \text{m}^{-3}$ , roughly twice that of the uncompacted material. From these results, it is not yet immediately apparent if the differences are the result of erosion or relaxation (i.e. density changes) of the uncompacted plug. Further optimizations, looking at emplacement pressure versus swelling pressure are planned for the near future.

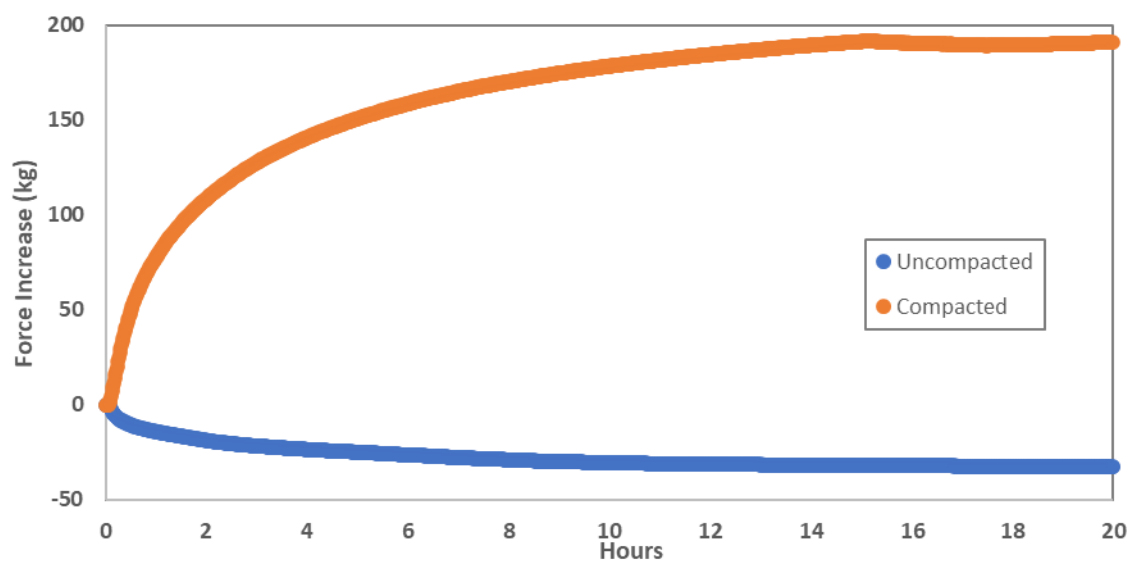


**Figure 7-8.** Swelling pressure of uncompact ( $1.4 \times 10^3 \text{ kg} \cdot \text{m}^{-3}$ ; blue) and compacted ( $2.8 \times 10^3 \text{ kg} \cdot \text{m}^{-3}$ ; orange) bentonite plugs subjected to  $5 \text{ mL} \cdot \text{hr}^{-1}$  flow of deionized water and confined in the erosion cell by a  $10 \mu\text{m}$  frit.

## 7.6 Bentonite Colloid Flocculation/Coagulation Experiments

Bentonite colloid flocculation and coagulation experiments were designed using microfluidic models, similar to those described by Bate et al. (2022). The models (Figure 7-9) were fabricated to our specifications by Ufluidix Toronto using molded PDMS bonded to glass slides.

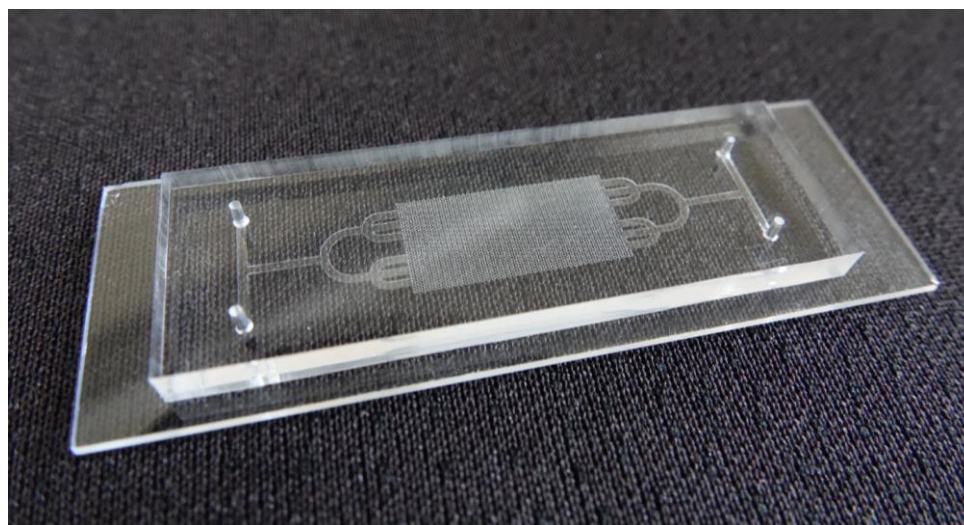


**Figure 7-9.** An image of the finished PDMS microfluidic model. Two ports were included in this design to allow connection to a differential pressure transducer.

Within the center flow chamber of the model, micropillars 50  $\mu\text{m}$  high with diameters of 250 $\mu\text{m}$  are arranged in a centrosymmetric pattern with the width of the pore throats between the pillars measuring 25 $\mu\text{m}$  (Figure 7-10). Two ports on the inlet and outlet of the models to allow for the connection of a differential pressure transducer (DPT). The measurements taken using this transducer help to better determine and quantify the degree of clogging occurring within the model, with a higher-pressure differential indicating more substantial blockage of flow and thus, increased clogging.

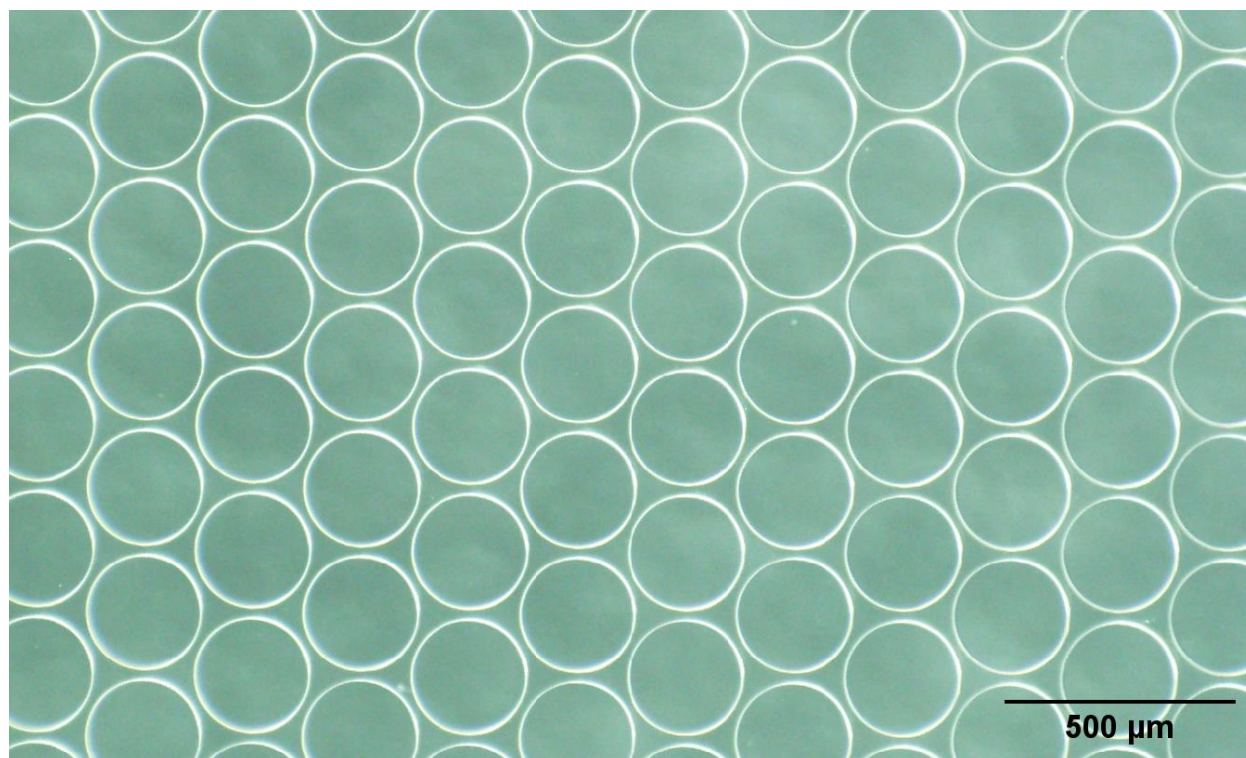


**Figure 7-10.** A magnified view of the micropillars within an empty microfluidic model.

Two  $1.0 \text{ g}\cdot\text{L}^{-1}$  colloidal bentonite suspensions, one in 1 M NaCl and one in deionized water were compared in flow-through microfluidic experiments. The experimental system consisted of a syringe pump (Chemyx Fusion 200) connected directly to the micromodel, with the differential pressure transducer (Validyne, Range  $\pm 5$  PSI) tied into the inlet and outlet side of the model to measure the pressure drop across the model over time (Figure 7-11). Before beginning the flow of either bentonite suspension, deionized water was injected into the models at  $400 \mu\text{L}\cdot\text{min}^{-1}$  to remove air within the pore space. Once the pore space was saturated, the rinse syringe was swapped out for a syringe containing one of the bentonite suspensions. The flow rate was reduced to  $200 \mu\text{L}\cdot\text{min}^{-1}$  and the bentonite suspensions were injected for a minimal of an hour. During this time, differential pressure measurements from the Validyne transducer were recorded every 5 seconds. Magnified photos of the central section of the model were taken every 10 minutes to visualize the accumulation of the bentonite clogging over time. The models were cleaned between experiments by submerging in an ultrasonic deionized water bath for 30 minutes while simultaneously using a syringe to pull a vacuum on one end of the model. This method of cleaning allowed for a high rate of flow

through the model to readily carry dislodged bentonite out without having to be concerned about damage resulting from too much pressure building within the model.

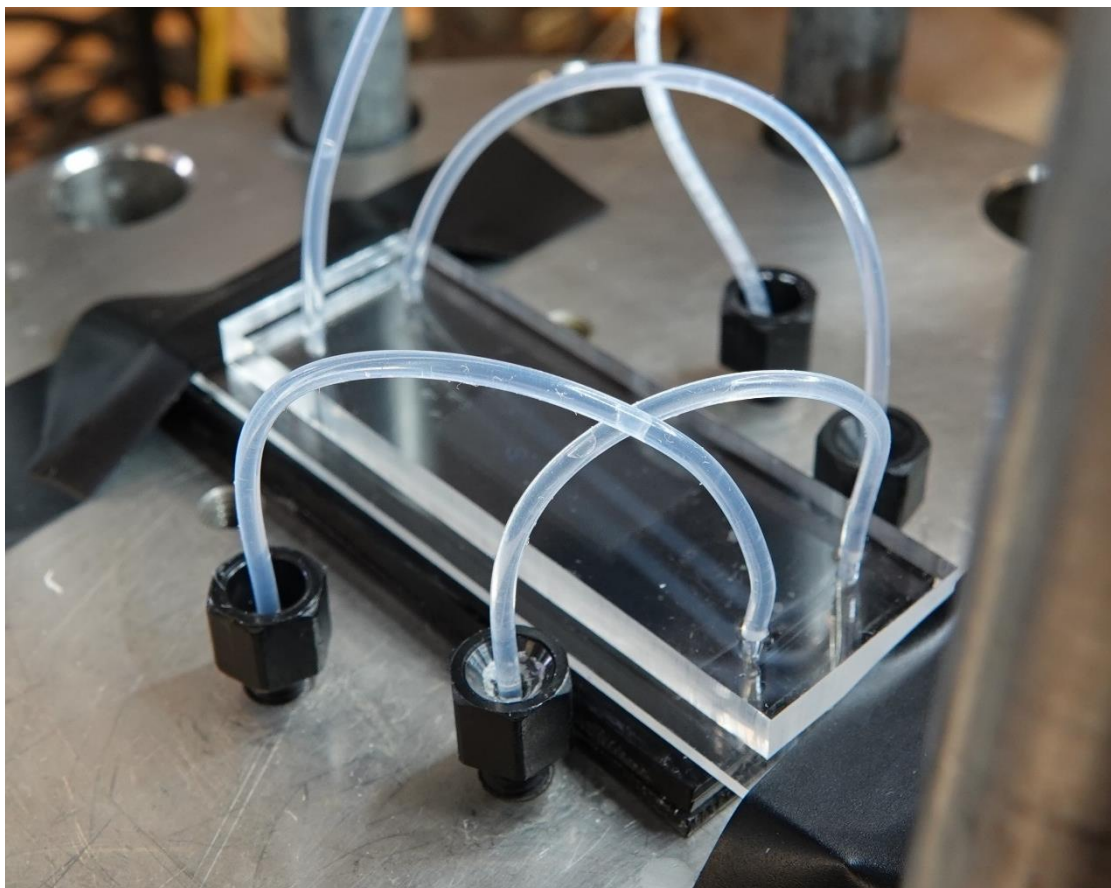


**Figure7-11.** A microfluidic model connected to the lines leading from the syringe pump and the differential pressure transducer, with the microscope objective lowered from above.

The addition of sodium chloride to the bentonite suspension significantly altered the pattern of accumulation of the bentonite against the micropillars. Triangular structures built up against the left sides of the micropillars, on the upgradient side of the flow (Figure 7-12, left). In contrast, flow of the bentonite suspension containing no sodium chloride resulted in no discernable accumulation of bentonite against the micropillars (Figure 7-12, right).

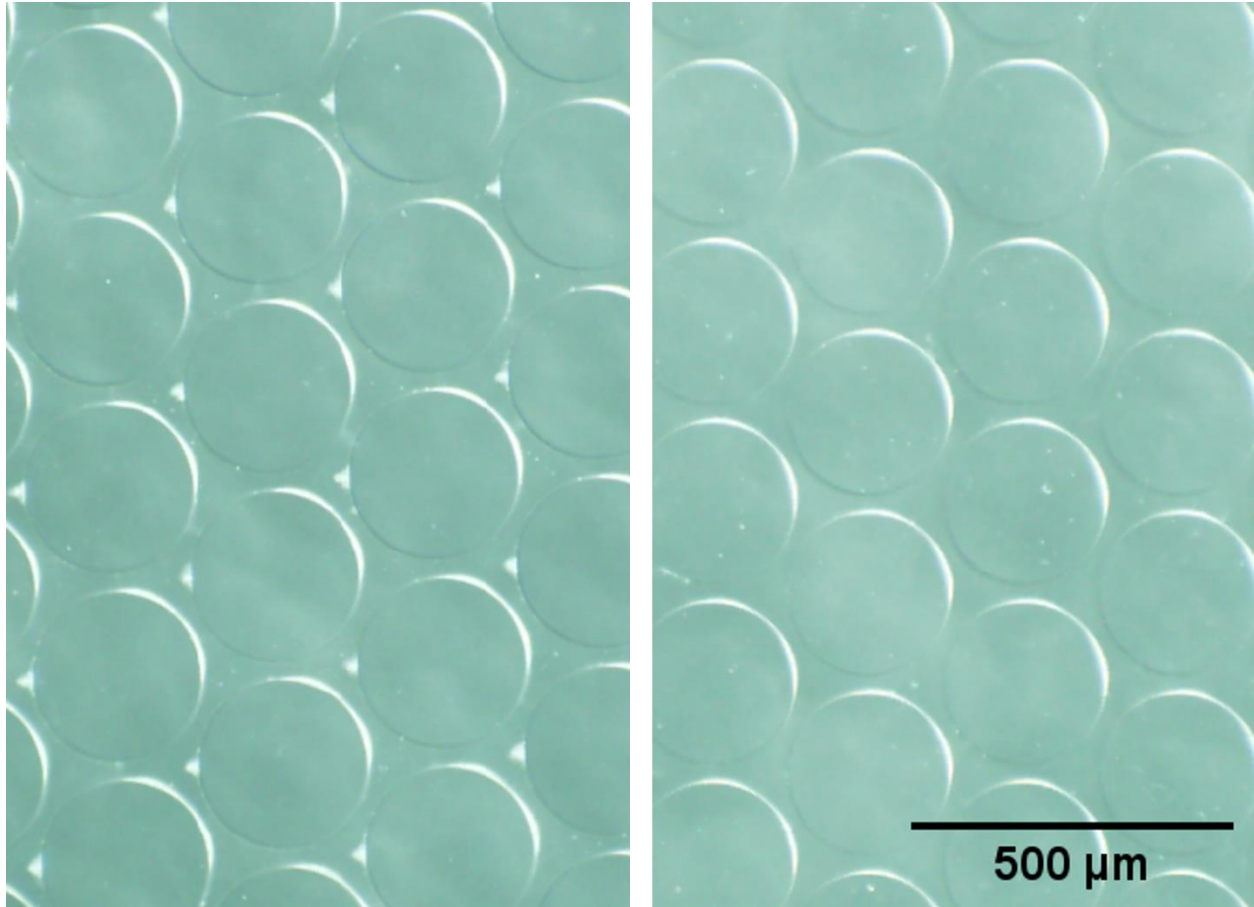


**Figure 7-12.** A comparison of the amount of bentonite accumulation occurring after 30 minutes of elapsed flow of both bentonite solutions. Left: The solution containing bentonite with NaCl. Right: The solution of only bentonite.

Clogging of pore throats near the inlet side of the model occurred for both bentonite suspensions and the clogs became more infrequent towards the outlet. Many smaller blockages and several large clogs along the face of the micropillar matrix (Figure 7-13) occurred while flowing the bentonite suspensions in 1 M NaCl. The bentonite suspension in deionized water did result in a few small clogs in the pore throats near the inlet of the model, but these clogs were both sparse and smaller in size when compared to the clogs that occurred after flowing the salt-saturated solution. The beginnings of colloidal flocculation were apparent after less than 10 minutes of flow of the sodium chloride-saturated bentonite solution (Figure 7-14).

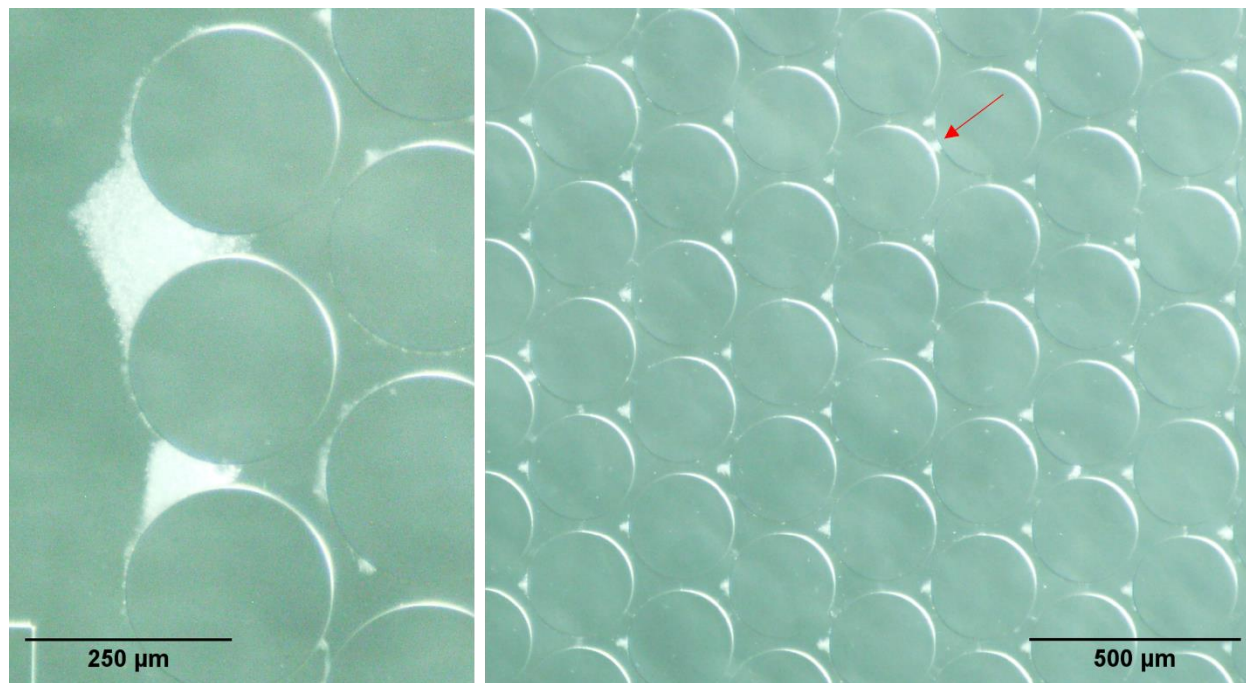


**Figure 7-13.** Left: A magnified view of the large bentonite clogs in the inlet of a model after flowing the bentonite in 1 M NaCl suspension. Right: Smaller clogs occurring further away from the inlet after 30 minutes of flowing the bentonite-salt solution.

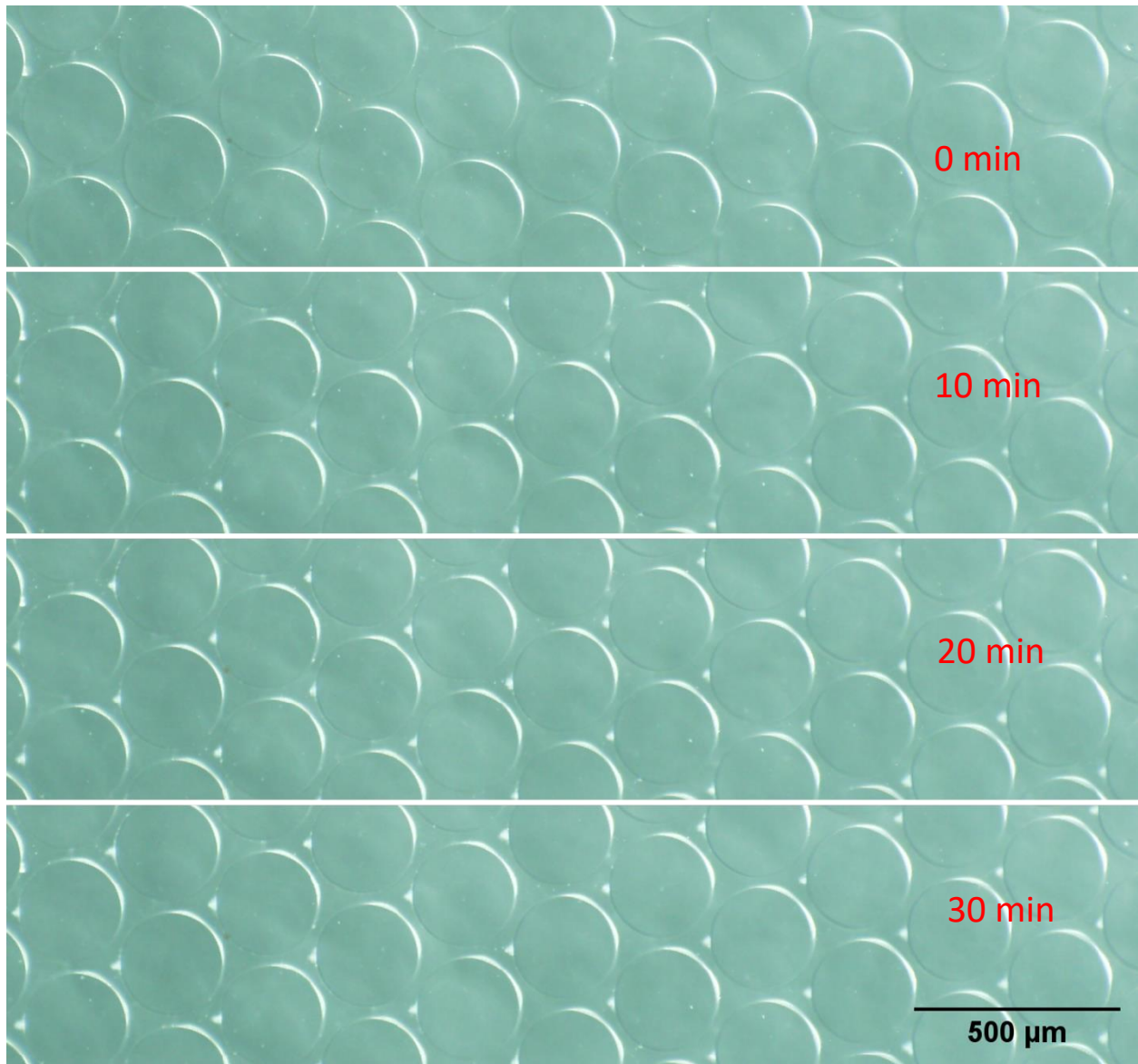


**Figure 7-14.** A timelapse of the accumulation of bentonite against the micropillars. From top to bottom: Immediately after beginning flow at 200  $\mu\text{L}/\text{min}$ , 10 minutes, 20 minutes, and 30 minutes after starting flow.

Minimal growth of the accumulated bentonite structures occurred after 30 minutes of flow. As such, there were no major discernible differences between timelapse photos taken beyond 30 minutes. In this amount of time, the buildup of bentonite within the models seemed to reach a maximum, as evidenced by the lack of change in the size and shape of the accumulated bentonite structures, as well as the relatively stable pressure differential readings throughout the entirety of each flow-through experiment (Figure 7-15).

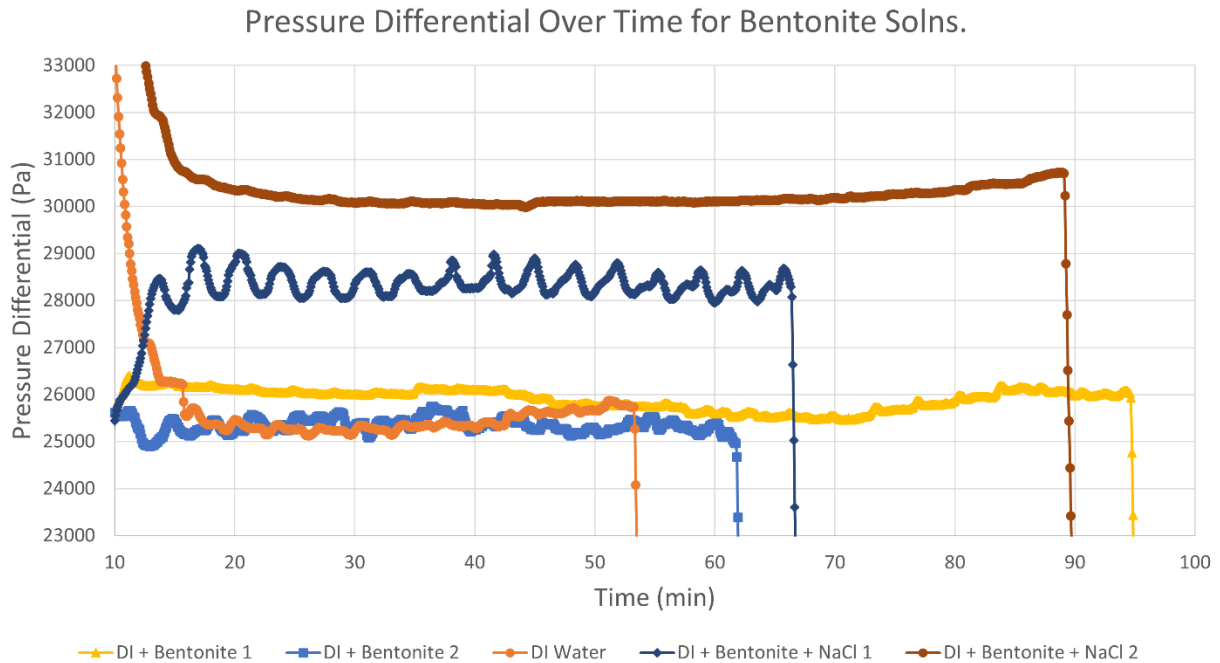


**Figure 7-15.** A plot showing the pressure difference between the inlet and outlet of the microfluidic model over time for the two bentonite solutions and DI water. Flow at  $200 \mu\text{L}/\text{min}$  was initiated 10 minutes after starting the DPT logging.

A baseline measurement was taken by flowing only deionized water through the model to get a sense of the pressure drop induced solely by the restriction of the pore space within the model. While the pressure measurements remained relatively stable for each experiment, there were noticeable differences in the pressures that each solution maintained over time. The bentonite solution containing salt stabilized at pressure readings that were consistently higher than the readings of the bentonite solution without salt (Figure 7-15). The first run of the bentonite salt solution (DI + Bentonite + NaCl 1) hovered around 27,000 Pa, while the second run (DI + Bentonite + NaCl 2) stabilized around 30,000 Pa for much of the length of the experiment before climbing slightly before flow was stopped. The undulations seen in the line representing the first bentonite salt solution run are likely due to bentonite blockage, which continuously built up and dislodged from the increase in pressure. The bentonite-deionized water suspension maintained pressure differentials between 25,000 and 26,000 Pa for both runs. The bentonite-deionized water suspension also maintained pressure measurements that were close to the measurements taken while flowing only deionized water. The higher-pressure differential readings resulting from the flow of the bentonite in 1 M NaCl suggest a higher degree of clogging and reduction of flow within the model compared to the bentonite in deionized water experiment. Similarly, the pressure differential measurements for both experiments using the bentonite-deionized water suspension are very similar to those taken for deionized water, suggesting very little clogging or impediment of flow during that experiment. It should be noted that

the clogging that occurred during the bentonite in 1 M NaCl experiments was not sufficient to completely stop the flow.

In addition to microfluidic experiments using cells fabricated from PDMS bonded to glass slides, we are actively working on developing a capability to allow similar experiments to be conducted using geologic materials as the microfluidic cell, simulating natural fractures while allowing us to have control over variables such as aperture size and fracture branching. To begin developing this technique, preliminary etching tests were conducted on acrylic chips using a Gravograph LS100 CO<sub>2</sub> laser system. A similarly patterned cell was fabricated in acrylic with larger pore throat widths to test the size limitations of our laser etching system (Figure 7-16). While the resulting etched pattern looks relatively uniform, closer inspection of the topographic image obtained from a laser scanning microscope (Keyence VKX-100) revealed some roughness resulting from melt and striations resulting from the mode of rasterization. The power and speed of the laser can be adjusted based on the hardness of the material being etched to minimize raster artifacts and melt. It is expected that these effects will be dampened by etching on a harder geologic sample. Further prototyping will be necessary to achieve the optimal etching settings. These efforts are to be continued next year.

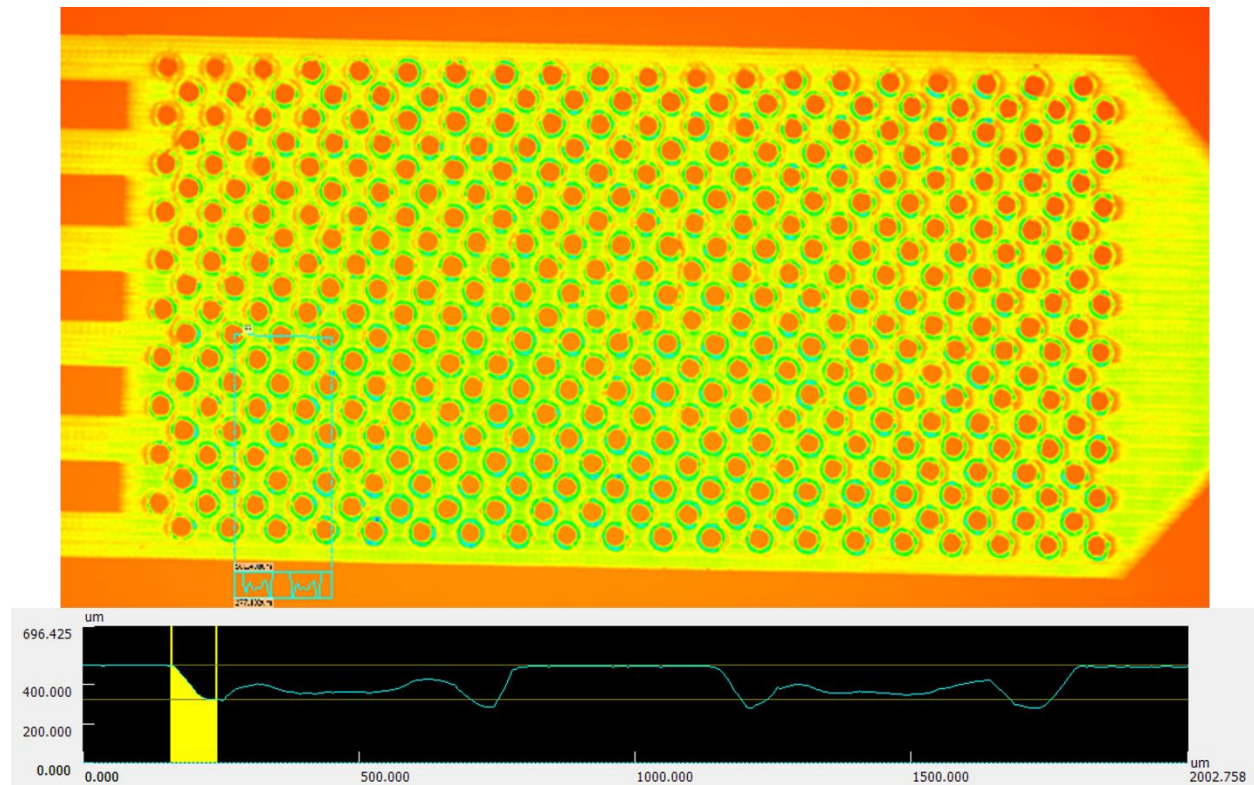


**Figure 7-16.** A topographic image and profile of the prototype laser-etched acrylic model. From the profile, the space between the pillars is not uniform and flat.

## 7.7 Conclusions

Compacted bentonite clay is the backfill material of choice for most countries spent nuclear fuel and high-level nuclear waste deep geological repository designs. The natural swelling behavior of the material contributes to its low hydraulic conductivity and self-healing abilities. However, the underlying hydration mechanisms that result in bentonite's swelling behavior also make it more likely to erode by both extrusion and free swelling. As such, bentonite free-expansion (i.e. the transition from compacted bentonite to gel/sol structures) and bentonite erosion (i.e. expansion into a flow field) have been studied extensively for decades. Although it has been recognized that the processes are geochemically reversible, bentonite coagulation/flocculation and its potential impact on fracture clogging has been studied relatively little. Our experimental work has been designed to investigate bentonite erosion, coagulation, and clogging behavior in a fractured crystalline rock under varying temperature, rock materials, rock fracture aperture properties, and bentonite colloid properties. Much of FY23 work was spent assembling experimental apparatus, developing measurement techniques, and optimizing experimental conditions. Preliminary tests on bentonite colloid flocculation, coagulation and clogging were performed using a microfluidic cell. The results show a significant effect of solution chemistry on bentonite flocculation, coagulation and clogging in microchannels of the cell.

## 8.0 GAS CHANNELING AND MIGRATION IN WATER-SATURATED COMPACTED BENTONITE THROUGH INTERFACE INSTABILITY (DECOVALEX 2023 TASK B)

### 8.1 Introduction

Gas breakthrough and migration across a low-permeability clay layer or a shale formation is an important process to be considered in the performance assessment of nuclear waste repositories or other subsurface systems such as those for CO<sub>2</sub>, H<sub>2</sub> or natural gas storage. In a nuclear waste repository, hydrogen gas (H<sub>2</sub>) generated from metal corrosion may build up around a waste package and eventually break through the surrounding bentonite buffer layer, thus directly impacting the performance of the engineered barrier system (EBS) designed for waste isolation. Existing gas injection experiments reveal complex dynamic behaviours of gas breakthrough and migration across a water saturated compacted bentonite layer, characterized by rapid breakthrough, periodic/chaotic gas flux, fast percolation, and low gas saturation (e.g., Cuss et al., 2022) (Figure 8-1), which suggest the likely development of discrete gas flow channels in the low-permeability bentonite layer upon gas injection.

In our previous work, we have shown that the complexity of gas migration processes can be explained using a phenomenological concept of nonlinear dynamics and deterministic chaos theory (Faybishenko et al., 2021). We have analyzed gas pressure and gas influx and outflux recorded in the gas injection experiment in a water-saturated compacted Mx80-D bentonite sample and have calculated a set of the diagnostic parameters of nonlinear dynamics and chaos, such a global embedding dimension, a correlation dimension, an information dimension, and a spectrum of Lyapunov exponents. The results suggest that the observed complex fluid flow behaviors could emerge from low-dimension deterministic chaos with a typical dimensionality ranging from 3-5. The actual mechanism for the emergence of the observed complex behavior of gas migration in water saturated compacted bentonite yet needs to be clarified.

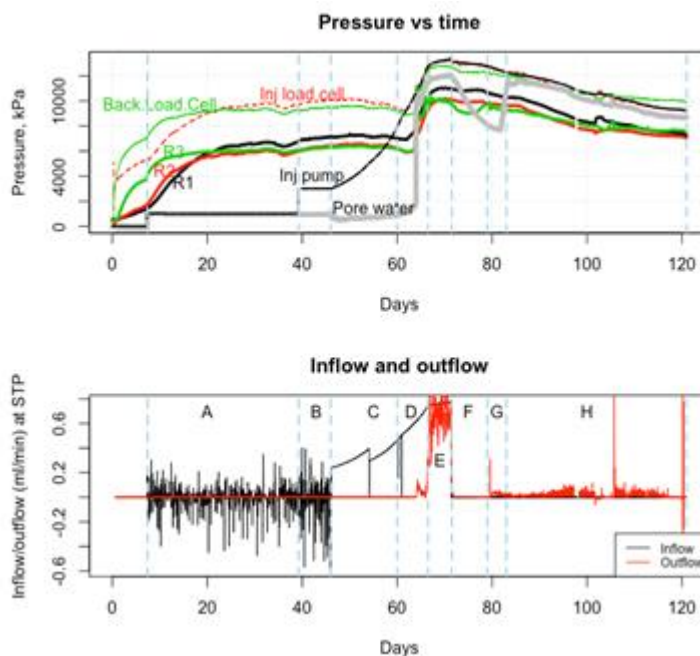


**Figure 8-1.** Time series of gas pressures and fluxes recorded during the Mx80 gas injection experiment conducted by the British Geological Survey.

### 8.2 Compaction, Positive Feedbacks, and Channeling

Gas migration in a porous geologic medium is generally treated as an immiscible displacement process within a rigid solid framework. This is likely to be the case in highly permeable geologic media such as sandstone, where an external hydraulic gradient imposed may be high enough to overcome the capillary pressure induced at the gas-water interface such that the gas phase can snap through the pores, displacing

the water phase. However, this may not be the case for compact bentonite, in which the pore size is generally extremely small, on a scale of nanometers. The capillary pressure  $P_c$  in such a medium can be estimated by:

$$P_c = \frac{2\gamma\cos(\theta)}{r} \quad (8-1)$$

where  $\gamma$  is the surface tension between gas and water;  $\theta$  is the contact angle water on the solid; and  $r$  is the radius of the pore neck. Given the typical values of these parameters ( $\sigma = \sim 70$  mN/m,  $\theta = \sim 40^\circ$ ,  $r = 1 - 10$  nm) (Wang et al., 2013; Wang, 2014),  $P_c$  is estimated to  $\sim 10 - 100$  MPa, which is significantly higher than a gas pressure generally used in an experiment (see Figure 8-1). Therefore, the entry of gas into the pores of a compacted bentonite to displace the porewater is unlikely. Instead, the gas injected would tend to compress the bentonite matrix as a whole by expelling the pre-existing pore water on the other. Then, the only possible way for gas to move through such media is by channeling.

As shown below, this channelling can emerge autonomously from the morphological instability of a gas-bentonite interface. This instability can be attributed to two positive feedbacks (Figure 8-2): (1) As a channel protrudes into the bentonite matrix, the hydraulic gradient becomes steeper at the tip of the channel, causing more water expulsion from the other side of the bentonite layer and therefore further enhancing channel growth; and (2) as a channel grows, the more tensile stress is created at the tip of the channel, causing local pore dilation and even fracturing at the tip and therefore in turn promoting channel opening.

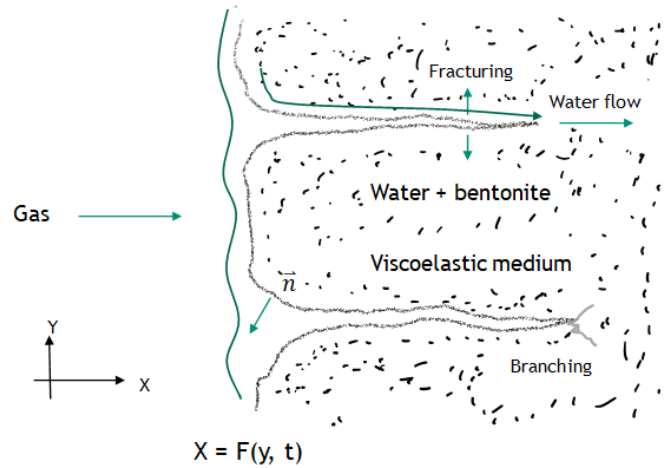


Figure 8-2. Illustration of gas flow channel development

### 8.3 Hydrological Instability of Gas-Bentonite Interface

Let's consider a 2-D system in which a water saturated bentonite matrix is compressed by the pressurized gas on the left side with porewater expelled from the right side (Figure 8-2). Due to a low-permeability bentonite matrix, we assume that the compaction of bentonite is limited by porewater flow. For simplicity, we assume that the permeability of the bentonite matrix ( $k$ ) remains roughly constant during compaction. The compaction process can then be described by the following equations:

$$\nabla^2 P = 0 \quad (8-2)$$

at  $X = F(Y, t)$  (gas-bentonite interface):

$$P \approx P_g + \gamma_e \frac{\partial^2 F}{\partial Y^2} \quad (8-3)$$

$$\frac{\partial F}{\partial t} = -k \frac{\partial P}{\partial X} + k \frac{\partial P}{\partial Y} \frac{\partial F}{\partial Y} \quad (8-4)$$

at  $X = L$  (right side):

$$P = P_L \quad (8-5)$$

where  $P$  is the porewater pressure;  $P_g$  is the gas injection pressure;  $\gamma_e$  is the effective surface tension of the interface between the injected gas and the bentonite matrix;  $k$  is the permeability of the bentonite matrix;  $t$  is the time; and  $P_L$  is the porewater pressure at the exit of water flow.

We performed a linear stability analysis of Equations (8-2) through (8-5) for an initially planar gas-bentonite interface. By imposing infinitely small perturbations on the planar interface:

$$\delta P = \hat{P}(X)e^{imY+\zeta t} \quad (8-6a)$$

$$\delta F = \hat{F}e^{imY+\zeta t} \quad (8-6b)$$

we obtain the following dispersion equation that relates the growth rate of perturbation ( $\zeta$ ) to the wave number of the perturbation ( $m$ ):

$$\zeta = -k \left( \frac{\partial \bar{P}}{\partial X} + \gamma_e m^2 \right) m \quad (8-7)$$

In Equations (8-6),  $\hat{P}$  and  $\hat{F}$  are the perturbation amplitudes of  $P$  and  $F$ , respectively. Since the porewater pressure gradient away from the interface ( $\partial \bar{P} / \partial X$ )  $< 0$ , the growth rate  $\zeta$  can become positive for  $m < \sqrt{-\frac{\partial \bar{P}}{\partial X} / \gamma_e}$ , implying that the gas-bentonite interface could become morphologically unstable and therefore fingered, leading to the development of gas flow channeling into the bentonite matrix. Especially, if the effect of surface tension is ignored, the interface would become unstable with respect to all wave numbers. In this case, the channel patterns formed would be fractal (Nittmann et al., 1985).

## 8.4 Mechanical instability of Gas-Bentonite Interface

During bentonite compaction by gas injection, another interface instability mechanism can potentially come into play: At the tip of an interface perturbation, the more tensile stress could be created at the tip, resulting in local pore dilation and even fracturing at the tip and therefore interface fingering. This tensile stress is partly driven by the swelling pressure of the bentonite matrix ( $P_s$ ). Initially, after hydrologic compaction, the system is critically stressed, that is, the swelling pressure is exactly balanced by the confining stress on a planar interface along the  $Y$ -axis:  $P_s = (P_g - \sigma_{YY}^\infty) / 2$ , where  $\sigma_{YY}^\infty$  is the confining stress imposed at  $Y = \pm\infty$ . However, at a perturbation tip of a perturbed interface,  $P_s > (P_g - \sigma_{YY}) / 2$ , leading to a tensile stress, where  $\sigma_{YY}$  is the local normal stress along the  $Y$  direction.

Assuming a viscoelastic behaviour for the bentonite matrix, we obtain the following governing equations:

$$\nabla^4 \psi = 0 \quad (8-8)$$

at  $X = F(Y, t)$ :

$$-\left(P_g - \gamma_e \frac{\partial^2 F}{\partial Y^2}\right) = \frac{\partial^2 \psi}{\partial Y^2} + \frac{\partial F}{\partial Y} \frac{\partial^2 \psi}{\partial X \partial Y} \quad (8-9)$$

$$-\frac{\partial F}{\partial Y} \frac{\partial^2 \psi}{\partial Y^2} + \frac{\partial^2 \psi}{\partial X \partial Y} + \frac{\partial F}{\partial Y} \frac{\partial^2 \psi}{\partial X^2} = 0 \quad (8-10)$$

$$\sigma_t = -\frac{\partial F}{\partial Y} \frac{\partial^2 \psi}{\partial X \partial Y} + \frac{\partial^2 \psi}{\partial X^2} \quad (8-11)$$

$$\frac{\partial F}{\partial t} = \alpha(\sigma_t - \bar{\sigma}_t) \quad (8-12)$$

at  $X = L$

$$\frac{\partial^2 \psi}{\partial X^2} = \sigma_{YY}^\infty \quad (8-13)$$

$$\frac{\partial^2 \psi}{\partial Y^2} = -P_g \quad (8-14)$$

where  $\psi$  is the Airy stress function;  $\sigma_t$  is the normal stress along the tangential direction of the interface;  $\alpha$  is the growth rate constant; and  $\bar{\sigma}_t$  is the  $\sigma_t$  evaluated at the planar interface. Equation (8-9) represents the force balance along the normal direction of the interface. Equation (8-10) assumes that the shear stress along the interface vanishes [Equation (8-10)].

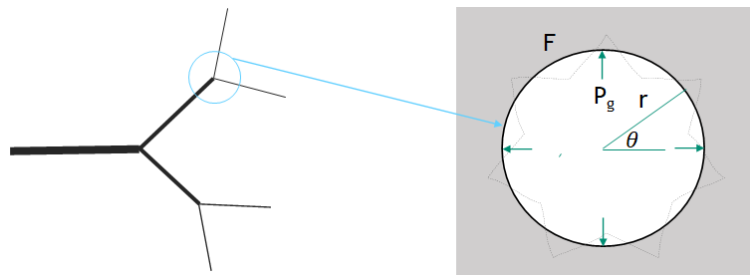


**Figure 8- 3.** Channel branching through mechanical instability of gas-bentonite interface.

A linear stability analysis was performed for Equations (8-8) through (8-14) for an initially planar gas-bentonite interface. By introducing infinitely small perturbations on the planar interface:

$$\delta P = \hat{\psi}(X)e^{imY+\zeta t} \quad (8-15a)$$

$$\delta F = \hat{f}e^{imY+\zeta t} \quad (8-15b)$$

where  $\hat{\psi}$  is the perturbation amplitude of  $\psi$ , we obtain the following dispersion equation that relates the growth rate of the perturbation ( $\zeta$ ) to the wave number of the perturbation ( $m$ ):

$$\zeta = \alpha m [2(P_g + \sigma_{YY}^{\infty}) - \gamma_e m] \quad (8-16)$$

Thus, the growth rate  $\zeta$  becomes positive for  $m < 2(P_g + \sigma_{YY}^{\infty})/\gamma_e$ , implying that the gas-bentonite interface would become morphologically unstable, leading to the development of gas flow channeling into the bentonite matrix. Again, if the effect of surface tension is negligible, the interface would become unstable with respect to all wave numbers. The channel patterns formed as such would be fractal (Nittmann et al., 1985).

## 8.5 Channel Branching

Mechanical instability of a gas-bentonite interface can be extended to understand channel branching. In a 2-D system, the tip of a channel can be viewed as circular hole internally pressurized by the injected gas (Figure 8-3). To simplify the mathematical treatment, we cast Equations (8-8) through (8-14) into a radial coordinate system  $(r, \theta)$ :

$$\nabla^2 \nabla^2 \psi = 0 \quad (8-17)$$

with

$$\nabla^2 = \frac{\partial^2}{\partial r^2} + \frac{1}{r} \frac{\partial}{\partial r} + \frac{1}{r^2} \frac{\partial^2}{\partial \theta^2}$$

$$\sigma_{rr} = \frac{1}{r} \frac{\partial \psi}{\partial r} + \frac{1}{r^2} \frac{\partial^2 \psi}{\partial \theta^2} \quad (8-18)$$

$$\sigma_{\theta\theta} = \frac{\partial^2 \psi}{\partial r^2} \quad (8-19)$$

$$\sigma_{r\theta} = -\frac{\partial}{\partial r} \left( \frac{1}{r} \frac{\partial \psi}{\partial \theta} \right) \quad (8-20)$$

at  $r = F(\theta, t)$ :

$$\kappa = \frac{2 \left( \frac{\partial F}{\partial \theta} \right)^2 - F \frac{\partial^2 \psi}{\partial \theta^2} + F^2}{\left[ F^2 + \left( \frac{\partial F}{\partial \theta} \right)^2 \right]^{3/2}} \quad (8-21)$$

$$-(P_g - \gamma_e \kappa) \left[ F^2 + \left( \frac{\partial F}{\partial \theta} \right)^2 \right] = \left( \frac{\partial F}{\partial \theta} \right)^2 \sigma_{\theta\theta} - 2F \frac{\partial F}{\partial \theta} \sigma_{r\theta} + F^2 \sigma_{rr} \quad (8-22)$$

$$F \frac{\partial F}{\partial \theta} \sigma_{\theta\theta} + \left[ \left( \frac{\partial F}{\partial \theta} \right)^2 - F^2 \right] \sigma_{r\theta} - F \frac{\partial F}{\partial \theta} \sigma_{rr} = 0 \quad (8-23)$$

$$F \frac{\partial F}{\partial \theta} \sigma_{\theta\theta} + \left[ \left( \frac{\partial F}{\partial \theta} \right)^2 - F^2 \right] \sigma_{r\theta} - F \frac{\partial F}{\partial \theta} \sigma_{rr} = 0 \quad (8-24)$$

$$\sigma_t = \frac{F^2 \sigma_{\theta\theta} + 2F \frac{\partial F}{\partial \theta} \sigma_{r\theta} + \left( \frac{\partial F}{\partial \theta} \right)^2 \sigma_{rr}}{F^2 + \left( \frac{\partial F}{\partial \theta} \right)^2} \quad (8-25)$$

$$\frac{\partial F}{\partial t} = \alpha(\sigma_t - \bar{\sigma}_t) \left[ \left( \frac{\partial F}{\partial \theta} \right)^2 + F \right] / \left[ F^2 + \left( \frac{\partial F}{\partial \theta} \right)^2 \right] \quad (8-26)$$

at  $r = +\infty$ :

$$\sigma_{rr} = \sigma_{rr}^{\infty} \quad (8-27)$$

$$\sigma_{r\theta} = 0 \quad (8-28)$$

where  $\sigma_{ij}$  is the component of a stress tensor;  $\kappa$  is the curvature of the interface; and  $\bar{\sigma}_t$  is the normal tangential stress evaluated at the unperturbed circular interface.

Similarly, a linear stability analysis was performed for Equations (8-17) through (8-28) by imposing the following infinitely small perturbations on an initially circular water-bentonite interface:

$$\delta P = \hat{\psi}(X) e^{im\theta + \zeta t} \quad (8-29a)$$

$$\delta F = \hat{f} e^{im\theta + \zeta t} \quad (8-29b)$$

A dispersion equation was then obtained to relate the growth rate of perturbation to the wave number of the perturbation:

$$\zeta = \frac{2\alpha \left( P_g + \sigma_{rr}^\infty - \frac{\gamma_e}{R} \right) m^2 (m-1) - \frac{2\alpha\gamma_e}{R} (m^2 - 1)^2}{2(m+1)(m-1)} \quad (8-30)$$

where  $R$  is the radius of the unperturbed interface. To match the boundary conditions around a circle,  $m$  must be a positive integer. Again, the growth rate of perturbation can be positive, implying that the interface could become unstable and thus channel branching could take place. Interestingly, the analysis shows that, to have a proper solution to the perturbed equations, wave number  $m$  must be larger than 2, that is, a channel can only branch into three or more channels. However, the stabilizing term  $\frac{2\alpha\gamma_e}{R} (m^2 - 1)^2$  in Equation (30) increases rapidly with  $\sim m^4$ . We thus expect that the most likely branching number would be close to three. By ignoring the surface effect ( $\gamma_e = 0$ ), Equation (8-30) is reduced to the early result obtained by Herrmann and Kertész (1991).

## 8.6. Gas Flow in a Deformable Channel

We now want to show that, once a percolating channel is established, the percolation of gas in the channel is also affected by the instability of gas-bentonite interface. For simplicity, we consider a 2-D system in which a flow channel is embedded in a viscoelastic bentonite matrix (Figure 8-4). Due to the Bernoulli effect, a positive feedback may exist between flow velocity and channel deformation: A local dilation of the channel reduces the flow velocity and therefore increases the fluid pressure, which in turn causes the local channel expansion, leading to the instability of the channel wall. On the other hand, this instability can be countered by the surface tension of the interface. This process can be described by the following dynamic equations:

$$\frac{\partial H}{\partial t} = \frac{\partial}{\partial X} \left( kH^3 \frac{\partial P}{\partial X} \right) \quad (8-31)$$

$$\frac{\partial H}{\partial t} = \lambda \left( \omega H^2 + (P - P_e) - (H - H_e)E + \gamma_e \frac{\partial^2 H}{\partial X^2} \right) \quad (8-32)$$

where  $H$  is the width of the channel;  $k$  is the conductivity of the channel;  $E$  is the Young's modulus of bentonite matrix;  $P_e$  and  $H_e$  are the gas pressure and channel width for an unperturbed case, respectively; and  $\lambda$  and  $\omega$  are adjustable parameters. Terms  $\omega H^2$  and  $\gamma_e \frac{\partial^2 H}{\partial X^2}$  capture the Bernoulli effect and the surface tension effect, respectively.

By introducing the following perturbations:

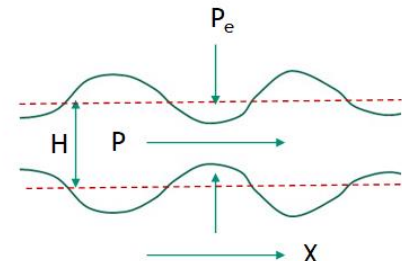


**Figure 8-4.** Gas percolation in a deformable channel.

$$\delta P = \hat{p} e^{imX + \zeta t} \quad (8-33a)$$

$$\delta H = \hat{H} e^{imX + \zeta t} \quad (8-33b)$$

a linear stability analysis was performed on Equations (8-31) and (8-32) and a dispersion equation was obtained:

$$\zeta = \frac{\lambda k \bar{H}^3 m^2 (2\omega \bar{H} - E - \gamma_e m^2) + 3\lambda k \bar{H}^2 \frac{\partial \bar{P}}{\partial X} m i}{\lambda + k \bar{H}^3 m^2} \quad (8-34)$$

Equation (8-34) indicates that a positive  $\text{Re}(\zeta)$  can attain for a large positive  $2\omega \bar{H} - E$  value, implying a possible morphological instability of the matrix wall and leading to gas bubble formation within the channel. The nonzero  $\text{Im}(\zeta)$  implies that the chain of bubbles formed would continuously move downstream (Wang and Budd, 2012). This postulated behavior seems confirmed by the observed periodic or chaotic variations in gas flow rate in gas injection tests (Fig. 8-5). In this case, each individual spike of flow rate may represent the arrival of a single gas bubble. As shown in Equation (8-34), as  $\beta \rightarrow 0$ , i.e., as the effect of surface tension vanishes,  $\text{Re}(\zeta)$  becomes positive for all wave numbers. In this case, the size distribution of bubbles within a channel would become more random, and as a result the gas flow would appear more chaotic. On the other hand, if the surface tension term is on the same magnitude as the instability term, the size distribution of gas bubble would then become more regular, resulting in a periodic gas flow rate.

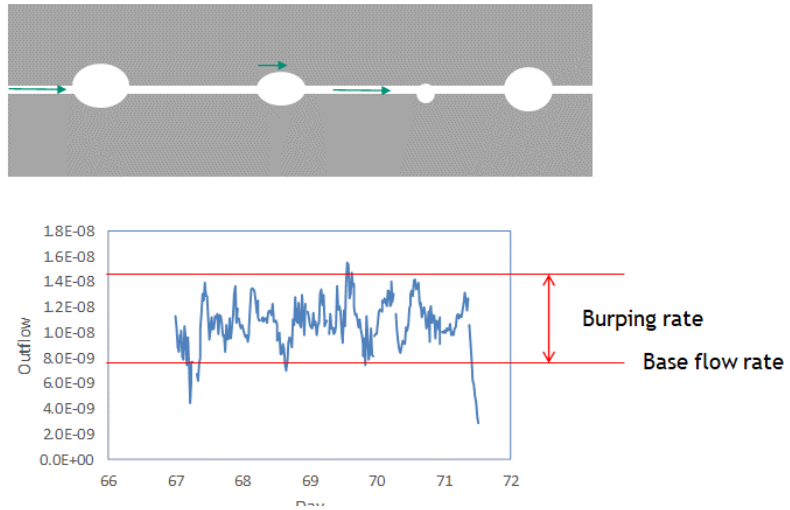


**Figure 8-5.** Periodic or chaotic gas flow rate induced by channel wall instability

## 8.7. Discussion

As shown in Equations (8-7), (8-16) and (8-30), without consideration of the surface tension effect, a simple relationship can be found between the growth rate ( $\zeta$ ) of an infinitely small perturbation around an unperturbed percolation front and the wave number of the perturbation ( $m$ ):

$$\text{Re}(\zeta) \propto P_g m \quad (8-35)$$

This relationship indicates that the growth rate  $\text{Re}(\zeta)$  attains positive values for all wave numbers and increases with both the gas injection pressure and the wave number of the perturbation. The pattern of

channels formed as such would have a fractal geometry (Nittmann et al., 1985). This fractal nature poses a challenge for numerical simulations of the process since the existing numerical algorithms and tools may not be able to directly handle the evolution of fractal structures.

The fractal nature of the system may provide a new perspective for property and process upscaling. Due to the scale invariance, some features observed in a small-scale experiment can be directly upscaled to a large scale. For example, we may expect that the same features such as fast gas breakthrough and periodic/chaotic variations in gas flow rate can be observed in both small and large-scale experiments, which seems consistent with experimental observations (Harrington et al., 2017; Cuss et al., 2022). Some other properties may need to be scaled using a power law. For example, the effective surface tension of a gas-bentonite interface ( $\gamma_e$ ) can be scaled according to (Wang et al., 2013):

$$\gamma_e = \gamma b d^{2-D} \quad (8-36)$$

where  $b$  is the proportional constant;  $D$  is the fractal dimension; and  $d$  is the measurement scale. With this effective surface tension estimated, we can calculate the spacing of gas channels on the “observed” scale. Let’s consider the mechanical instability of the interface. From Equation (8-16), by setting  $\frac{d\zeta}{dm} = 0$ , we obtain the preferred wave number for channel pattern development ( $m_p$ ):

$$m_p = \frac{P_g + \sigma_{YY}^\infty}{\gamma_e} \quad (8-37)$$

Accordingly, the channel spacing ( $L_p$ ) can be calculated by:

$$L_p = \frac{2\pi}{m_p} \quad (8-38)$$

We want to caution that the channels and the channel spacing discussed here can be viewed only as “equivalent” channels on the “observed” scale. As shown in Equations (8-37) and (8-38), the spacing (also roughly the channel size) is inversely proportional to the gas injection pressure. In a finite system, to match a boundary condition, the wave number and the spacing are not continuous and instead they are discrete (in other words, “quantized”). Thus, as the gas injection pressure decreases, we would expect to see stepwise decreases in gas flow rate as the channels collapse, which yet needs to be confirmed experimentally.

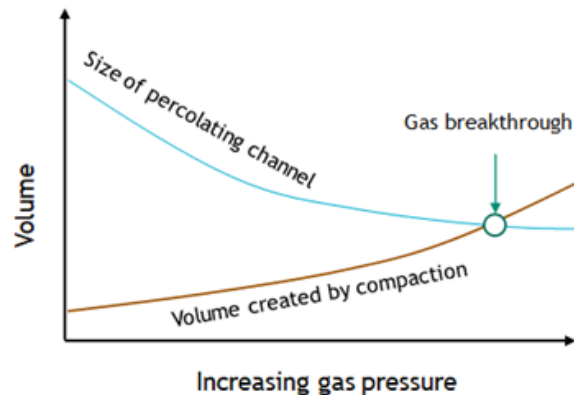


**Figure 8-6.** Conditions for gas breakthrough

Based on the concept developed above, for gas breakthrough, enough room must be made via the compaction of bentonite matrix to accommodate at least one percolating channel. As the gas pressure increases, the room made by compaction increases while the size of a channel decreases. At a certain pressure, the condition for breakthrough is met and gas breakthrough takes place (Figure 8-6). The breakthrough pressure is then on the same magnitude as the clay swelling pressure for a given dry density (Figures 8-1 and 8-7). Like fracturing, the whole channelling process is a self-accelerating process and thus the breakthrough period should be relatively short, as observed (Figure 8-1). Furthermore, since the total volume of channels is limited by the swelling pressure, the gas saturation degree in the system is always small, likely less than 10% (Figure 8-7).

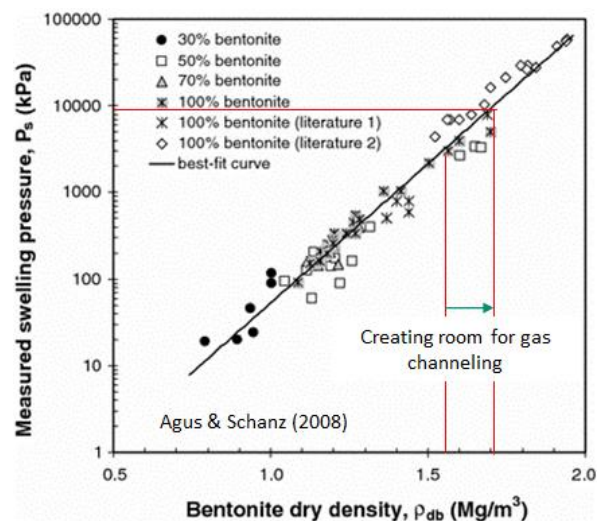


**Figure 8-7.** Making room for gas breakthrough through compaction

## 8.8 Conclusions

Gas breakthrough and migration across a low-permeability deformable clay layer is of great importance to subsurface systems for nuclear waste disposal and gas (e.g.,  $CO_2$ ,  $H_2$  or natural gas) storage, as well as for the development of natural gas/oil reservoirs in the geologic history. Experimental observations on gas injection into water saturated compacted bentonite have revealed rich distinct dynamic behaviours of such processes characterized by a short breakthrough period, a low gas saturation degree and a periodic/chaotic variation in gas flow rate, all indicating a channelling nature of the process. Using linear stability analyses, we here show that such channelling can autonomously emerge from the morphological instability of the interface between the injected gas and the compacted bentonite due to local stress concentration, pore dilation, and hydrologic gradient variation. We show that channel patterns formed as such would possess a fractal geometry, thus providing a new perspective for upscaling the process from small scale laboratory observations to a field scale. We further show that, once a percolating channel is established, the gas injected would percolate through the channel in a chain of gas bubbles, also due to the interface instability, resulting in periodic/chaotic variations in gas flow rate. Thus, the concept and the model developed in this work are able to predict the key features observed in gas injection experiments and portray a quite different picture for gas percolation in low-permeability deformable media than that traditionally conceived from permeable porous media.

## **9.0 UNDERSTANDING RADIONUCLIDE INTERACTIONS WITH ENGINEERED AND NATURAL MATERIALS**

### **9.1 Introduction**

This section documents the work performed at Lawrence Livermore National Laboratory (LLNL) on radionuclide interactions with repository-relevant engineered and natural materials. We have initiated experiments to identify radionuclide interaction with hydrothermally altered buffer materials. Recent research performed at Los Alamos National Laboratory (LANL) and Sandia National Laboratories (SNL) has provided key insights regarding the hydrothermal alteration behavior of bentonite backfill in the presence of repository materials (steel, concrete, etc.). We are now examining how mineral alteration affects retardation behavior of plutonium and a suite of other radionuclides. These experiments allow us to test the predictive ability of our component additivity approach to surface complexation and ion exchange. Our guiding hypothesis is that a robust surface complexation/ion exchange model and associated database, developed using our L-SCIE approach, can effectively predict changes in radionuclide sorption behavior resulting from the hydrothermal alteration of mineralogy in a repository near field. A manuscript is in preparation describing a self-consistent model and approach to simulating Se(IV) and Se(VI) sorption to 5 iron oxide phases based on our L-SCIE community database. This will be the first implementation of a multi-mineral and multi-oxidation state sorption model using our new L-SCIE database and workflow. A short summary of these results is presented below.

### **9.2 Effects of Bentonite Heating on Radionuclide Adsorption**

One of the more accepted ideas for high-level nuclear waste disposal is to emplace steel waste canisters in a geological repository with a bentonite/clay barrier between the canister and host rock (Meunier et al., 1998; Pusch, 1979). Bentonite is used to provide 1) a physical barrier to prevent fluid seeping in from natural surroundings and interacting with the waste package and 2) a chemical barrier by attenuating actinide migration if a release occurs.

High temperatures (100–200 °C) near waste canisters resulting from radioactive decay may alter the bentonite clay's ability to adsorb contaminants. Temperature effects on the bentonite/clay barrier may include changes to the clay's hydrological and mechanical properties, changes to pore water chemical compositions, and changes to the clay and accessory mineral composition (Cuadros and Linares, 1996; Wersin et al., 2007; Zheng et al., 2017). For these reasons the effects of elevated temperature on the engineered barrier must be taken into account when designing a nuclear waste repository

In this study, we examine the capacity of hydrothermally altered clay samples (Table 9-1) to adsorb radionuclides (Table 9-2) in batch sorption experiments. The hydrothermally altered samples were subjected to short-term (days to months)- high temperature (200-300 °C) heating in the laboratory.

**Table 9-1.** List of samples used for sorption experiments. Samples (unheated and hydrothermally altered) were provided by collaborators at Los Alamos National Laboratory (LANL) and Sandia National Laboratory (SNL). Cation exchange of selected unheated samples was performed at SNL (K, Na) and Lawrence Livermore National Laboratory (LLNL).

Mineralogical composition	Sample origin		Sample Name	Cation Exchange Solution		
<b>Unheated samples</b>						
Wyoming Bentonite	LANL		<b>WY</b>			
Opalinus Clay	LANL		<b>OPC</b>			
Grimsel Granodiorite	LANL		<b>GG</b>			
Illite	SNL		<b>IMt-1</b>			
Illite/Smectite (70:30) mixed layers	SNL		<b>ISCz-1</b>			
<b>Cation exchanged unheated samples</b>						
Na-exchanged Wyoming Bentonite	LANL/ LLNL		<b>Na-WY</b>	1M NaC <sub>2</sub> H <sub>3</sub> O <sub>2</sub>		
Na-exchanged Opalinus Clay	LANL/ LLNL		<b>Na-OPC</b>	1M NaC <sub>2</sub> H <sub>3</sub> O <sub>2</sub>		
K-exchanged Smectite	SNL		<b>K-Swy-2-SNL</b>	1M KCl		
Na-exchanged Wyoming bentonite	SNL		<b>Na-SWy-2-SNL</b>	1M NaCl		
<b>Hydrothermally altered samples</b>						
				<b>Hydrothermal Alteration Conditions</b>		
				<b>Synthetic Ground Water Type</b>	<b>Temperature (C)</b>	<b>Duration of Hydrothermal Experiment</b>
Wyoming Bentonite and 304 SS	LANL		<b>EBS-5</b>	Stripa V2.1	300	6 weeks
Wyoming Bentonite and Quartz Sand	LANL		<b>EBS-9</b>	Stripa V2.2	25/100/200/300/25	5 weeks
Wyoming Bentonite and 316 SS	LANL		<b>EBS-10</b>	Stripa V2.3	300	6 weeks
Wyoming Bentonite	LANL		<b>EBS-12</b>	Stripa V2.3	300	7 weeks
Wyoming Bentonite, Opalinus Clay, and 316 SS	LANL		<b>EBS-15</b>	Synthetic Opalinus GW	300	6 weeks
Wyoming Bentonite, Opalinus Clay, and 304 SS	LANL		<b>EBS-19</b>	Synthetic Opalinus GW	300	6 weeks
Wyoming Bentonite, Opalinus Clay, and 316 SS	LANL		<b>EBS-20</b>	Synthetic Opalinus GW	300	6 months
Wyoming Bentonite, Opalinus Clay, and Portland Cement	LANL		<b>EBS-28</b>	Synthetic Opalinus GW	300	8 weeks
Wyoming Bentonite, Grimsel Granodiorite, and 316 SS	LANL		<b>IEBS-5</b>	Synthetic Grimsel GW	250	8 weeks
Wyoming Bentonite, Grimsel Granodiorite, and Portland Cement	LANL		<b>IEBS-6</b>	Synthetic Grimsel GW	250	8 weeks
K exchanged Wyoming bentonite	SNL		<b>K-1000</b>	1M KCl	200	28 days

### 9.2.1 Materials and Methods

The hydrothermally altered samples used in this study were provided by collaborators from LANL and SNL (Table 9-1). All the samples received at LLNL were prepared for surface area analysis using BET, but no further characterization was performed at LLNL as complete chemical and mineralogical characterization of the selected samples was presented in previous publications (Caporuscio, 2014, 2015; Caporuscio, 2018; Caporuscio, 2019; Caporuscio, 2020; Cheshire et al., 2014; Mills et al., 2023).

In this work, batch sorption experiments with hydrothermally altered clays (Table 9-1) and different radionuclides (Table 9-2) are performed at a pH range of 7-8 using either a low (NaCl 0.01M, NaHCO<sub>3</sub> 0.01M) or high (NaCl 1M, NaHCO<sub>3</sub> 0.01M) ionic strength buffer solution as background electrolyte. In both low and high ionic strength solutions, a 0.01M HEPES buffer is used to maintain the pH in the desired range. Each sorption experiment is performed in triplicate using a solid to solution ratio of 5 g/L. To monitor the effects of heating on the adsorption properties of bentonite, batch sorption experiments are also performed using control (unheated) bentonite samples (Table 9-1). A list of all the radionuclides and the materials used for sorption experiments is reported in Tables 9-1 and 9-2.

**Table 9-2.** List of radionuclides chosen for adsorption studies with hydrothermally altered samples. The column labeled FY indicates the status of the work and/or when it will be completed.

Radionuclide	Oxidation state	FY
<sup>137</sup> Cs	(I)	2023 (complete, data analysis in progress)
<sup>90</sup> Sr	(II)	2023 (start)
<sup>243</sup> Am	(III)	2023 (complete)
<sup>238</sup> Pu	(IV)	2024
<sup>237</sup> Np	(V)	2024
<sup>233</sup> U	(VI)	2024
<sup>99</sup> Tc	(VII)	2024

### 9.2.2 Results

In FY23, we completed and analyzed data for the <sup>137</sup>Cs sorption experiments using samples provided by LANL. Batch sorption experiments using the hydrothermally altered samples provided by SNL are currently underway and will be completed by the end of FY23.

Figure 9-1 reports the <sup>137</sup>Cs partition coefficient (Kd, mL/g) calculated for unheated samples (OPC, Wy, GG, Na-Wy, Bent, Na-OPC) and hydrothermally altered samples (EBS 5, EBS9, EBS 10, EBS 12, EBS 15, EBS 19, EBS20, EBS28, IEBS5 and IEBS 6) in low ionic strength buffer solutions. For the unheated samples, the calculated Kd values range between 250-440 mL/g, with the Na- exchanged forms of OC and WY displaying slightly higher Kd values compared to their non-exchanged forms. As expected, the Grimsel granodiorite sample (GG) has the lowest measured Kd value (~10 mL/g). The Kd values calculated for the majority of the hydrothermally altered samples are within expected Kd ranges of unheated Opalinus clay and Wyoming bentonite (Wy, Na-Wy, OPC, Na-OPC), however samples EBS 12 and EBS 28 display lower Kd values (< 250 mL/g) (Figure 9-1, red line, red arrows).

In experiments conducted using a high ionic strength background electrolyte, the Kd values for the unheated samples range between 40-170 mL/g, with the Na- exchanged forms of OC and WY displaying lower Kd values compared to their non-exchanged forms. All of the Kd values calculated for sorption experiments conducted at high ionic strength are lower than Kd values calculated for experiments conducted at low ionic

strength (Figure 9-2), consistent with a Cs sorption behavior that is dominated by an ion exchange mechanism. Samples EBS 12 and EBS 28 display lower  $K_d$  values compared to unheated samples, consistent with the low ionic strength experiments. Additionally, samples EBS 9, IEBS 5 and IEBS 6 also display decreased sorption capacity in high ionic strength background electrolyte ( $K_d < 40$  mL/g) (Figure 9-2, red line, red arrows). All batch sorption experiments were performed in triplicate and results display good reproducibility (Figures 9-1 and 9-2).

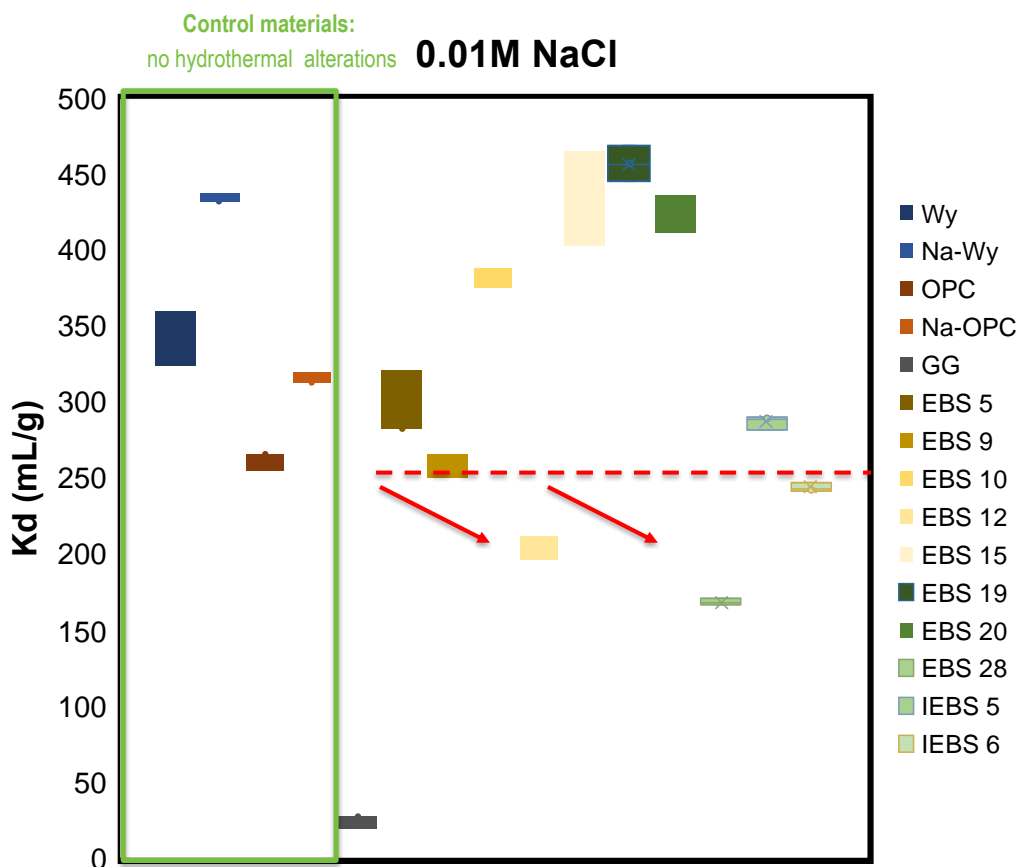


**Figure 9-1.** Values of  $K_d$  (mL/g) calculated for  $^{137}\text{Cs}$  batch sorption experiments using hydrothermally altered samples (EBS5, EBS9, EBS10, EBS12, EBS15, EBS19, EBS20, EBS28, IEBS5 and IEBS6) and unheated samples (green box: Wy, Na-Wy, OPC, Na-OPC, GG) in low ionic strength background electrolyte (0.011M NaCl, 0.01M  $\text{NaHCO}_3$ , 0.01M HEPES). Each experiment was performed in triplicates. Dash line indicates the lower limit of the  $K_d$  values for unheated samples. Red arrows indicate the decreases in  $K_d$  for thermally altered samples EBS-12 and EBS-28 relative to the unheated samples.

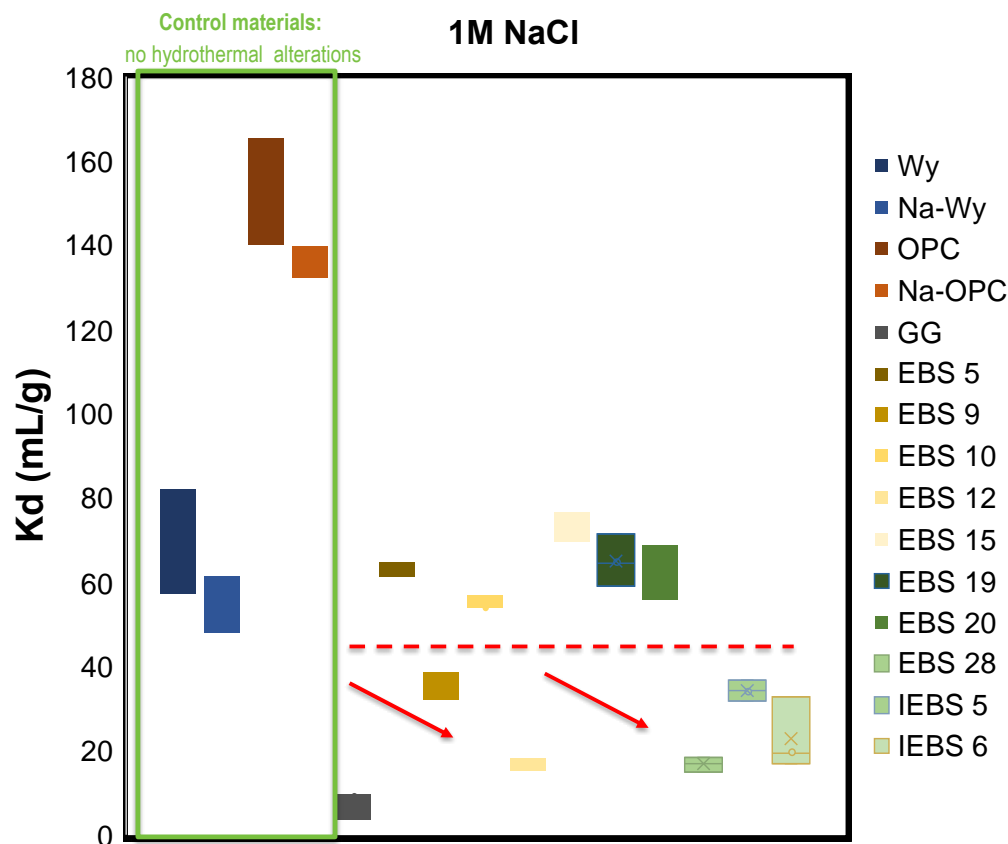


**Figure 9-2.** Values of Kd (mL/g) calculated for  $^{137}\text{Cs}$  batch sorption experiments using hydrothermally altered samples (EBS5, EBS9, EBS10, EBS12, EBS15, EBS19, EBS20, EBS28, IEBS5 and IEBS6) and unheated samples (green box: Wy, Na-Wy, OPC, Na-OPC, GG) in high ionic strength background electrolyte (1M NaCl, 0.01M  $\text{NaHCO}_3$ , 0.01M HEPES). Each experiment was performed in triplicates.

## 9.3 Comprehensive Surface Complexation Reaction Analysis Workflow: Surface Complexation of Se(IV) And Se(VI) on Iron Oxide Phases

### 9.3.1 Development of Radionuclide Surface Complexation Modeling Framework

Surface complexation models (SCM), which address the quantification of sorption processes, play a key role in Geological Disposal Safety Assessment (GDSA). Although enormous amounts of efforts have been made to develop reliable SCMs, obtaining global consensus among reported SCMs is still challenging since each SCM had been constructed with different foundations. In light of the limitation, this task aims at developing a more comprehensive SCM framework by compiling raw sorption data and the relevant surface complexation reactions reported from various literature sources. This effort is a follow-on to the earlier study supported by the crystalline work package that examined the sorption and coprecipitation of Se with iron(II) and iron(III) oxide mineral phases and reported in the FY22 milestone report.

Figure 9-3 describes the framework for SCM database development. The framework consists of a sorption database, i.e., L-SCIE (LLNL Surface Complexation/Ion Exchange) (Zavarin et al., 2022), a surface titration model, and a surface complexation model. L-SCIE database provides input data for surface titration/complexation models, and data processing and fitting routine have been done within each model.

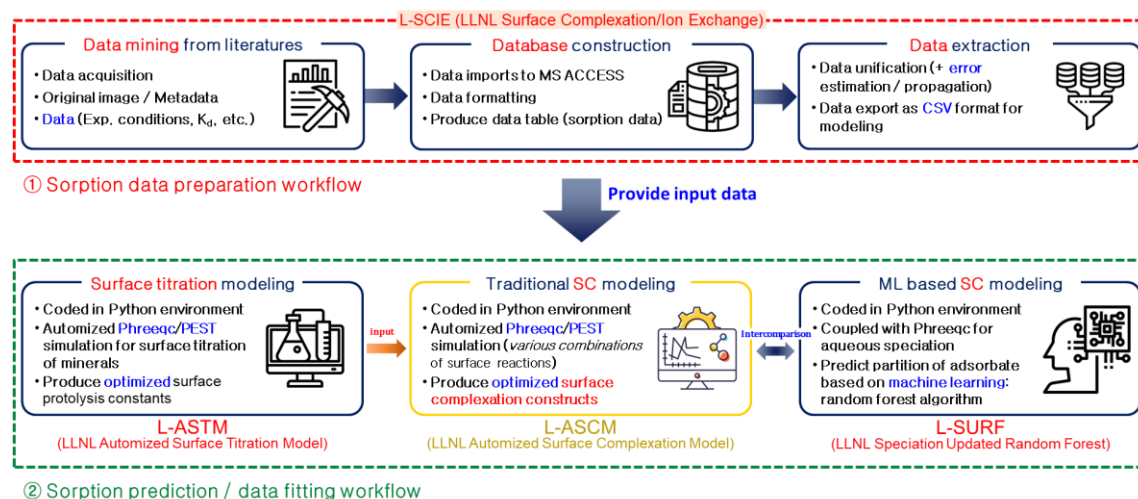
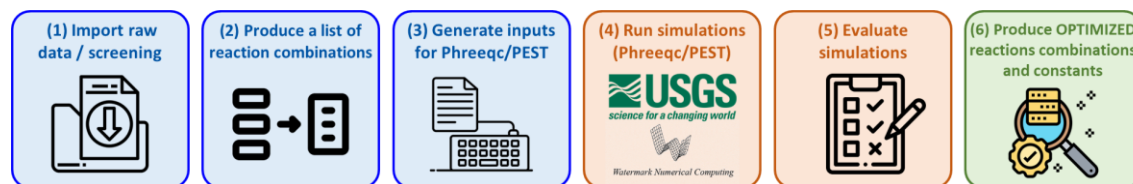


Figure 9-3. Workflow of community data driven surface complexation modeling framework

The newly developed SCM, LLNL Automated Surface Complexation Model (L-ASCM), was written in Python and the code was integrated with PhreeqC (Parkhurst and Appelo, 2013) and PEST (Doherty, 2018) for data fitting. One of the key features of the current model is that the model enables automation of the entire modeling process, for example, pre data analysis, input file generation, execution of data fitting routine, post simulation analysis, and visualization of simulation results. Furthermore, the model automatically examines the fitting for all possible SCM structural configurations (e.g., types of SCM and surface reactions) without any user interference.

The details of the workflow of L-ASTM are shown in Figure 9-4. First, the code imports sorption data extracted from the L-SCIE database. Like an example of Se(IV)-ferrihydrite sorption system given in Table 9-3, there could be a number of surface complexation reactions for given mineral and adsorbate pair from different literature references. The L-ASCM makes a list of all possible surface complexation reaction combinations and produces the relevant SCM constructs for all combinations. Then the code generates the PHREEQC/PEST input files for each SCM construct and runs simulations for all possible SCM constructs. Once the simulations are done, the code automatically evaluates the quality of each SCM construct and finally, the optimized SCM constructs with the relevant surface complexation reactions and the corresponding reaction constants are produced.



**Figure 9-4.** Surface complexation modeling workflow (L-ASCM code) for adsorption data.

**Table 9-3.** Surface complexation reactions of selenium sorption to ferrihydrite as reported in the RES<sup>3</sup>T database (Brendler et al., 2003; Dresden-Rossendorf, 2013).

	Surface complexation reactions	Initial log <sub>10</sub> K	Reference
1	$\gg\text{Fe-OH} + \text{SeO}_3^{2-} \leftrightarrow \gg\text{Fe-OH-SeO}_3^{2-}$	5.17	(Dzombak and Morel, 1990)
2	$\gg\text{Fe-OH} + \text{SeO}_3^{2-} + \text{H}^+ \leftrightarrow \gg\text{Fe-OH}_2\text{-SeO}_3^-$	12.90	(Benjamin and Bloom, 1981)
3	$\gg\text{Fe-OH} + \text{SeO}_3^{2-} + 2\text{H}^+ \leftrightarrow \gg\text{Fe-OH}_2\text{-HSeO}_3$	22.00	(Benjamin and Bloom, 1981)
4	$\gg\text{Fe-OH} + \text{SeO}_3^{2-} + 3\text{H}^+ \leftrightarrow \gg\text{Fe-OH}_2\text{-SeO}_3\text{H}_2^+$	29.00 <sup>a</sup>	-*
5	$2\gg\text{Fe-OH} + \text{SeO}_3^{2-} \leftrightarrow (\gg\text{Fe-O})_2\text{-SeO}_3^{4-} + 2\text{H}^+$	-6.96	(Wang et al., 2001)
6	$2\gg\text{Fe-OH} + \text{SeO}_3^{2-} + 2\text{H}^+ \leftrightarrow (\gg\text{Fe-OH}_2)_2\text{-SeO}_3$	26.06	(Wang et al., 2001)

<sup>a</sup>Presumed value. \*Newly added in this work

### 9.3.2 Case Study of Selenium Sorption to Ferrihydrite

Sorption characteristics of selenium to ferrihydrite were examined using L-ASCM and community selenium sorption data. For Se(IV) – ferrihydrite sorption system, six surface complexation reactions (Table 9-3) and the diffuse double layer model (DDLDM) were employed. Since six surface complexation reactions were used, a total of 63 reaction combinations were obtained (Table 9-4). In other words, 63 different SCM constructs had been tested to find appropriate surface complexation reactions which can model Se(IV) sorption to ferrihydrite. The quality of each SCM construct was evaluated based on weighted Pearson correlation coefficient (R value) and standard deviation (SD) of surface complexation reaction constant calculated from the model. If the R value is higher than 0.9 and SDs of all reaction constants are lower than 1.0, it was presumed that the model has a good quality.

**Table 9-4.** List of surface complexation reaction combinations: Se(IV) – ferrihydrite sorption system.

SCM construct	Surface species	SCM construct	Surface species
	<b>One species reaction</b>	<b>33</b>	$\gg\text{Fe-OH}_2\text{-SeO}_3^-$ , $\gg\text{Fe-OH}_2\text{-HSeO}_3$ , $(\gg\text{Fe-O})_2\text{-SeO}_3^{4-}$
<b>1</b>	$\gg\text{Fe-OH-SeO}_3^{2-}$	<b>34</b>	$\gg\text{Fe-OH}_2\text{-SeO}_3^-$ , $\gg\text{Fe-OH}_2\text{-HSeO}_3$ , $(\gg\text{Fe-OH}_2)_2\text{-SeO}_3$
<b>2</b>	$\gg\text{Fe-OH}_2\text{-SeO}_3^-$	<b>35</b>	$\gg\text{Fe-OH}_2\text{-SeO}_3^-$ , $\gg\text{Fe-OH}_2\text{-SeO}_3\text{H}_2^+$ , $(\gg\text{Fe-O})_2\text{-SeO}_3^{4-}$
<b>3</b>	$\gg\text{Fe-OH}_2\text{-HSeO}_3$	<b>36</b>	$\gg\text{Fe-OH}_2\text{-SeO}_3^-$ , $\gg\text{Fe-OH}_2\text{-SeO}_3\text{H}_2^+$ , $(\gg\text{Fe-OH}_2)_2\text{-SeO}_3$
<b>4</b>	$\gg\text{Fe-OH}_2\text{-SeO}_3\text{H}_2^+$	<b>37</b>	$\gg\text{Fe-OH}_2\text{-SeO}_3^-$ , $(\gg\text{Fe-O})_2\text{-SeO}_3^{4-}$ , $(\gg\text{Fe-OH}_2)_2\text{-SeO}_3$
<b>5</b>	$(\gg\text{Fe-O})_2\text{-SeO}_3^{4-}$	<b>38</b>	$\gg\text{Fe-OH}_2\text{-HSeO}_3$ , $\gg\text{Fe-OH}_2\text{-SeO}_3\text{H}_2^+$ , $(\gg\text{Fe-O})_2\text{-SeO}_3^{4-}$
<b>6</b>	$(\gg\text{Fe-OH}_2)_2\text{-SeO}_3$	<b>39</b>	$\gg\text{Fe-OH}_2\text{-HSeO}_3$ , $\gg\text{Fe-OH}_2\text{-SeO}_3\text{H}_2^+$ , $(\gg\text{Fe-OH}_2)_2\text{-SeO}_3$
	<b>Two species reaction</b>	<b>40</b>	$\gg\text{Fe-OH}_2\text{-HSeO}_3$ , $(\gg\text{Fe-O})_2\text{-SeO}_3^{4-}$ , $(\gg\text{Fe-OH}_2)_2\text{-SeO}_3$
<b>7</b>	$\gg\text{Fe-OH-SeO}_3^{2-}$ , $\gg\text{Fe-OH}_2\text{-SeO}_3^-$	<b>41</b>	$\gg\text{Fe-OH}_2\text{-SeO}_3\text{H}_2^+$ , $(\gg\text{Fe-O})_2\text{-SeO}_3^{4-}$ , $(\gg\text{Fe-OH}_2)_2\text{-SeO}_3$
<b>8</b>	$\gg\text{Fe-OH-SeO}_3^{2-}$ , $\gg\text{Fe-OH}_2\text{-HSeO}_3$		<b>Four species reaction</b>
<b>9</b>	$\gg\text{Fe-OH-SeO}_3^{2-}$ , $\gg\text{Fe-OH}_2\text{-SeO}_3\text{H}_2^+$	<b>42</b>	$\gg\text{Fe-OH-SeO}_3^{2-}$ , $\gg\text{Fe-OH}_2\text{-SeO}_3^-$ , $\gg\text{Fe-OH}_2\text{-HSeO}_3$ , $\gg\text{Fe-OH}_2\text{-SeO}_3\text{H}_2^+$
<b>10</b>	$\gg\text{Fe-OH-SeO}_3^{2-}$ , $(\gg\text{Fe-O})_2\text{-SeO}_3^{4-}$	<b>43</b>	$\gg\text{Fe-OH-SeO}_3^{2-}$ , $\gg\text{Fe-OH}_2\text{-SeO}_3^-$ , $\gg\text{Fe-OH}_2\text{-HSeO}_3$ , $(\gg\text{Fe-O})_2\text{-SeO}_3^{4-}$
<b>11</b>	$\gg\text{Fe-OH-SeO}_3^{2-}$ , $(\gg\text{Fe-OH}_2)_2\text{-SeO}_3$	<b>44</b>	$\gg\text{Fe-OH-SeO}_3^{2-}$ , $\gg\text{Fe-OH}_2\text{-SeO}_3^-$ , $\gg\text{Fe-OH}_2\text{-HSeO}_3$ , $(\gg\text{Fe-OH}_2)_2\text{-SeO}_3$
<b>12</b>	$\gg\text{Fe-OH}_2\text{-SeO}_3^-$ , $\gg\text{Fe-OH}_2\text{-HSeO}_3$	<b>45</b>	$\gg\text{Fe-OH-SeO}_3^{2-}$ , $\gg\text{Fe-OH}_2\text{-SeO}_3^-$ , $\gg\text{Fe-OH}_2\text{-SeO}_3\text{H}_2^+$ , $(\gg\text{Fe-O})_2\text{-SeO}_3^{4-}$
<b>13</b>	$\gg\text{Fe-OH}_2\text{-SeO}_3^-$ , $\gg\text{Fe-OH}_2\text{-SeO}_3\text{H}_2^+$	<b>46</b>	$\gg\text{Fe-OH-SeO}_3^{2-}$ , $\gg\text{Fe-OH}_2\text{-SeO}_3^-$ , $\gg\text{Fe-OH}_2\text{-SeO}_3\text{H}_2^+$ , $(\gg\text{Fe-OH}_2)_2\text{-SeO}_3$
<b>14</b>	$\gg\text{Fe-OH}_2\text{-SeO}_3^-$ , $(\gg\text{Fe-O})_2\text{-SeO}_3^{4-}$	<b>47</b>	$\gg\text{Fe-OH-SeO}_3^{2-}$ , $\gg\text{Fe-OH}_2\text{-SeO}_3^-$ , $(\gg\text{Fe-O})_2\text{-SeO}_3^{4-}$ , $(\gg\text{Fe-OH}_2)_2\text{-SeO}_3$
<b>15</b>	$\gg\text{Fe-OH}_2\text{-SeO}_3^-$ , $(\gg\text{Fe-OH}_2)_2\text{-SeO}_3$	<b>48</b>	$\gg\text{Fe-OH-SeO}_3^{2-}$ , $\gg\text{Fe-OH}_2\text{-HSeO}_3$ , $\gg\text{Fe-OH}_2\text{-SeO}_3\text{H}_2^+$ , $(\gg\text{Fe-O})_2\text{-SeO}_3^{4-}$
<b>16</b>	$\gg\text{Fe-OH}_2\text{-HSeO}_3$ , $\gg\text{Fe-OH}_2\text{-SeO}_3\text{H}_2^+$	<b>49</b>	$\gg\text{Fe-OH-SeO}_3^{2-}$ , $\gg\text{Fe-OH}_2\text{-HSeO}_3$ , $\gg\text{Fe-OH}_2\text{-SeO}_3\text{H}_2^+$ , $(\gg\text{Fe-OH}_2)_2\text{-SeO}_3$
<b>17</b>	$\gg\text{Fe-OH}_2\text{-HSeO}_3$ , $(\gg\text{Fe-O})_2\text{-SeO}_3^{4-}$	<b>50</b>	$\gg\text{Fe-OH-SeO}_3^{2-}$ , $\gg\text{Fe-OH}_2\text{-HSeO}_3$ , $(\gg\text{Fe-O})_2\text{-SeO}_3^{4-}$ , $(\gg\text{Fe-OH}_2)_2\text{-SeO}_3$
<b>18</b>	$\gg\text{Fe-OH}_2\text{-HSeO}_3$ , $(\gg\text{Fe-OH}_2)_2\text{-SeO}_3$	<b>51</b>	$\gg\text{Fe-OH-SeO}_3^{2-}$ , $\gg\text{Fe-OH}_2\text{-SeO}_3\text{H}_2^+$ , $(\gg\text{Fe-O})_2\text{-SeO}_3^{4-}$ , $(\gg\text{Fe-OH}_2)_2\text{-SeO}_3$
<b>19</b>	$\gg\text{Fe-OH}_2\text{-SeO}_3\text{H}_2^+$ , $(\gg\text{Fe-O})_2\text{-SeO}_3^{4-}$	<b>52</b>	$\gg\text{Fe-OH}_2\text{-SeO}_3^-$ , $\gg\text{Fe-OH}_2\text{-HSeO}_3$ , $\gg\text{Fe-OH}_2\text{-SeO}_3\text{H}_2^+$ , $(\gg\text{Fe-O})_2\text{-SeO}_3^{4-}$
<b>20</b>	$\gg\text{Fe-OH}_2\text{-SeO}_3\text{H}_2^+$ , $(\gg\text{Fe-OH}_2)_2\text{-SeO}_3$	<b>53</b>	$\gg\text{Fe-OH}_2\text{-SeO}_3^-$ , $\gg\text{Fe-OH}_2\text{-HSeO}_3$ , $\gg\text{Fe-OH}_2\text{-SeO}_3\text{H}_2^+$ , $(\gg\text{Fe-OH}_2)_2\text{-SeO}_3$
<b>21</b>	$(\gg\text{Fe-O})_2\text{-SeO}_3^{4-}$ , $(\gg\text{Fe-OH}_2)_2\text{-SeO}_3$	<b>54</b>	$\gg\text{Fe-OH}_2\text{-SeO}_3^-$ , $\gg\text{Fe-OH}_2\text{-HSeO}_3$ , $(\gg\text{Fe-O})_2\text{-SeO}_3^{4-}$ , $(\gg\text{Fe-OH}_2)_2\text{-SeO}_3$
	<b>Three species reaction</b>	<b>55</b>	$\gg\text{Fe-OH}_2\text{-SeO}_3^-$ , $\gg\text{Fe-OH}_2\text{-SeO}_3\text{H}_2^+$ , $(\gg\text{Fe-O})_2\text{-SeO}_3^{4-}$ , $(\gg\text{Fe-OH}_2)_2\text{-SeO}_3$
<b>22</b>	$\gg\text{Fe-OH-SeO}_3^{2-}$ , $\gg\text{Fe-OH}_2\text{-SeO}_3^-$ , $\gg\text{Fe-OH}_2\text{-HSeO}_3$		$\gg\text{Fe-OH}_2\text{-HSeO}_3$ , $\gg\text{Fe-OH}_2\text{-SeO}_3\text{H}_2^+$ , $(\gg\text{Fe-O})_2\text{-SeO}_3^{4-}$ , $(\gg\text{Fe-OH}_2)_2\text{-SeO}_3$
<b>23</b>	$\gg\text{Fe-OH-SeO}_3^{2-}$ , $\gg\text{Fe-OH}_2\text{-SeO}_3^-$ , $\gg\text{Fe-OH}_2\text{-SeO}_3\text{H}_2^+$	<b>56</b>	<b>Five species reaction</b>
<b>24</b>	$\gg\text{Fe-OH-SeO}_3^{2-}$ , $\gg\text{Fe-OH}_2\text{-SeO}_3^-$	<b>57</b>	$\gg\text{Fe-OH-SeO}_3^{2-}$ , $\gg\text{Fe-OH}_2\text{-SeO}_3^-$ ,

SCM construct	Surface species	SCM construct	Surface species
	$(\gg\text{Fe-O})_2\text{-SeO}_3^{4-}$		$\gg\text{Fe-OH}_2\text{-HSeO}_3$ , $\gg\text{Fe-OH}_2\text{-SeO}_3\text{H}_2^+$ , $(\gg\text{Fe-O})_2\text{-SeO}_3^{4-}$
25	$\gg\text{Fe-OH-SeO}_3^{2-}$ , $\gg\text{Fe-OH}_2\text{-SeO}_3^-$ , $(\gg\text{Fe-OH}_2)_2\text{-SeO}_3$	58	$\gg\text{Fe-OH-SeO}_3^{2-}$ , $\gg\text{Fe-OH}_2\text{-SeO}_3^-$ , $\gg\text{Fe-OH}_2\text{-HSeO}_3$ , $\gg\text{Fe-OH}_2\text{-SeO}_3\text{H}_2^+$ , $(\gg\text{Fe-OH}_2)_2\text{-SeO}_3$
26	$\gg\text{Fe-OH-SeO}_3^{2-}$ , $\gg\text{Fe-OH}_2\text{-HSeO}_3$ , $\gg\text{Fe-OH}_2\text{-SeO}_3\text{H}_2^+$	59	$\gg\text{Fe-OH-SeO}_3^{2-}$ , $\gg\text{Fe-OH}_2\text{-SeO}_3^-$ , $\gg\text{Fe-OH}_2\text{-HSeO}_3$ , $(\gg\text{Fe-O})_2\text{-SeO}_3^{4-}$ , $(\gg\text{Fe-OH}_2)_2\text{-SeO}_3$
27	$\gg\text{Fe-OH-SeO}_3^{2-}$ , $\gg\text{Fe-OH}_2\text{-HSeO}_3$ , $(\gg\text{Fe-O})_2\text{-SeO}_3^{4-}$	60	$\gg\text{Fe-OH-SeO}_3^{2-}$ , $\gg\text{Fe-OH}_2\text{-SeO}_3^-$ , $\gg\text{Fe-OH}_2\text{-SeO}_3\text{H}_2^+$ , $(\gg\text{Fe-O})_2\text{-SeO}_3^{4-}$ , $(\gg\text{Fe-OH}_2)_2\text{-SeO}_3$
28	$\gg\text{Fe-OH-SeO}_3^{2-}$ , $\gg\text{Fe-OH}_2\text{-HSeO}_3$ , $(\gg\text{Fe-OH}_2)_2\text{-SeO}_3$	61	$\gg\text{Fe-OH-SeO}_3^{2-}$ , $\gg\text{Fe-OH}_2\text{-HSeO}_3$ , $\gg\text{Fe-OH}_2\text{-SeO}_3\text{H}_2^+$ , $(\gg\text{Fe-O})_2\text{-SeO}_3^{4-}$ , $(\gg\text{Fe-OH}_2)_2\text{-SeO}_3$
29	$\gg\text{Fe-OH-SeO}_3^{2-}$ , $\gg\text{Fe-OH}_2\text{-SeO}_3\text{H}_2^+$ , $(\gg\text{Fe-O})_2\text{-SeO}_3^{4-}$	62	$\gg\text{Fe-OH}_2\text{-SeO}_3^-$ , $\gg\text{Fe-OH}_2\text{-HSeO}_3$ , $\gg\text{Fe-OH}_2\text{-SeO}_3\text{H}_2^+$ , $(\gg\text{Fe-O})_2\text{-SeO}_3^{4-}$ , $(\gg\text{Fe-OH}_2)_2\text{-SeO}_3$
30	$\gg\text{Fe-OH-SeO}_3^{2-}$ , $\gg\text{Fe-OH}_2\text{-SeO}_3\text{H}_2^+$ , $(\gg\text{Fe-OH}_2)_2\text{-SeO}_3$		<b>Six species reaction</b>
31	$\gg\text{Fe-OH-SeO}_3^{2-}$ , $(\gg\text{Fe-O})_2\text{-SeO}_3^{4-}$ , $(\gg\text{Fe-OH}_2)_2\text{-SeO}_3$	63	$\gg\text{Fe-OH-SeO}_3^{2-}$ , $\gg\text{Fe-OH}_2\text{-SeO}_3^-$ , $\gg\text{Fe-OH}_2\text{-HSeO}_3$ , $\gg\text{Fe-OH}_2\text{-SeO}_3\text{H}_2^+$ , $(\gg\text{Fe-O})_2\text{-SeO}_3^{4-}$ , $(\gg\text{Fe-OH}_2)_2\text{-SeO}_3$
32	$\gg\text{Fe-OH}_2\text{-SeO}_3^-$ , $\gg\text{Fe-OH}_2\text{-HSeO}_3$ , $\gg\text{Fe-OH}_2\text{-SeO}_3\text{H}_2^+$		

**Table 9-5.** Surface complexation models with good quality fit

Number of reactions	Surface species	R value
1	$\gg\text{Fe-OH-SeO}_3^{2-}$	0.9131
2	$\gg\text{Fe-OH-SeO}_3^{2-}$ , $\gg\text{Fe-OH}_2\text{-SeO}_3^-$	0.9192
2	$\gg\text{Fe-OH-SeO}_3^{2-}$ , $\gg\text{Fe-OH}_2\text{-HSeO}_3$	0.9202
2	$\gg\text{Fe-OH-SeO}_3^{2-}$ , $\gg\text{Fe-OH}_2\text{-SeO}_3\text{H}_2^+$	0.9198
2	$\gg\text{Fe-OH-SeO}_3^{2-}$ , $(\gg\text{Fe-O})_2\text{-SeO}_3^{4-}$	0.9002
2	$\gg\text{Fe-OH-SeO}_3^{2-}$ , $(\gg\text{Fe-OH}_2)_2\text{-SeO}_3$	0.9204
3	$\gg\text{Fe-OH-SeO}_3^{2-}$ , $\gg\text{Fe-OH}_2\text{-SeO}_3^-$ , $(\gg\text{Fe-O})_2\text{-SeO}_3^{4-}$	0.9083
3	$\gg\text{Fe-OH-SeO}_3^{2-}$ , $\gg\text{Fe-OH}_2\text{-HSeO}_3$ , $(\gg\text{Fe-O})_2\text{-SeO}_3^{4-}$	0.9085
3	$\gg\text{Fe-OH-SeO}_3^{2-}$ , $\gg\text{Fe-OH}_2\text{-SeO}_3\text{H}_2^+$ , $(\gg\text{Fe-O})_2\text{-SeO}_3^{4-}$	0.9111
3	$\gg\text{Fe-OH-SeO}_3^{2-}$ , $\gg\text{Fe-OH}_2\text{-SeO}_3\text{H}_2^+$ , $(\gg\text{Fe-OH}_2)_2\text{-SeO}_3$	0.9206

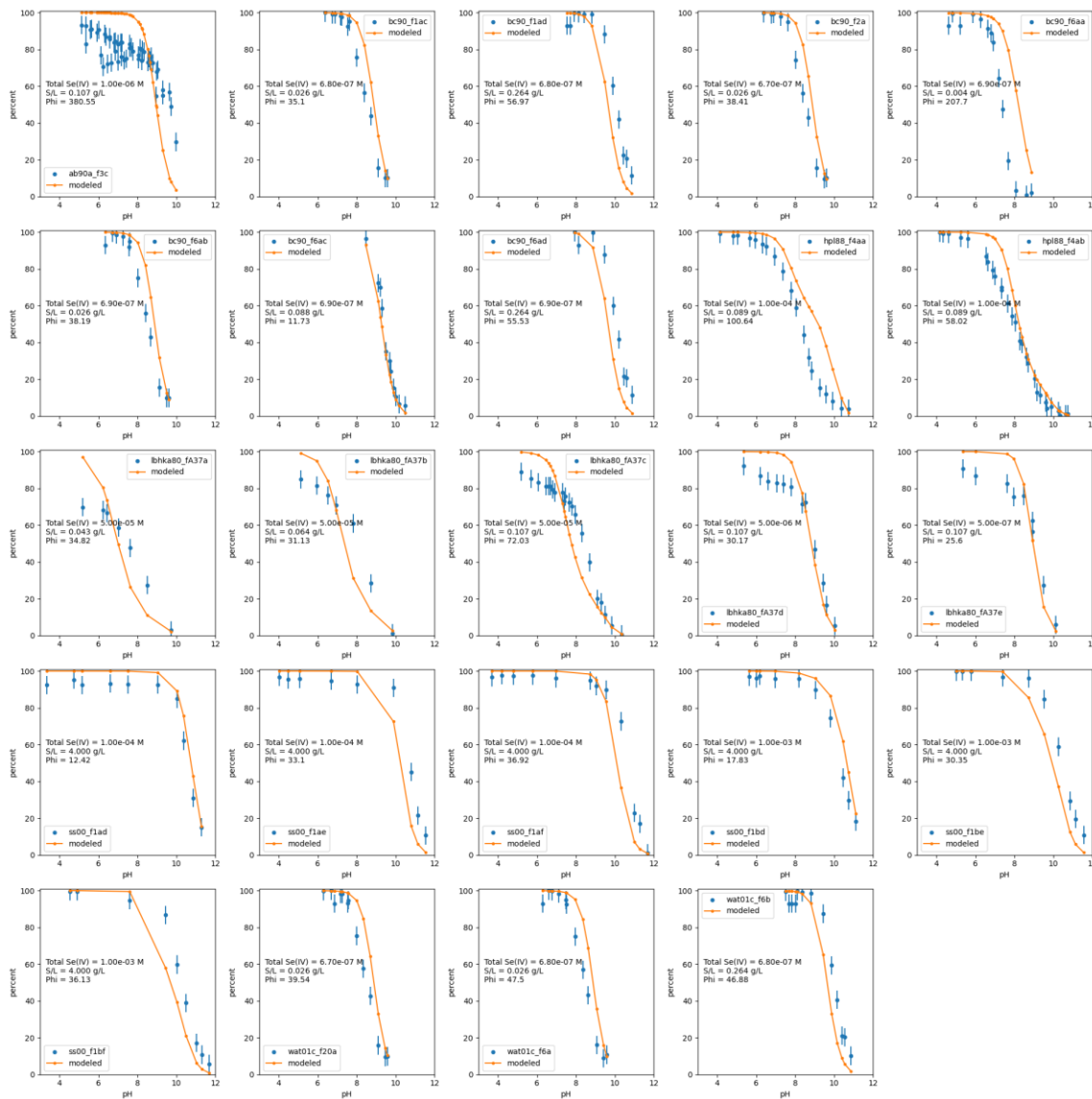


**Figure 9-5.** Simulation results for Se(IV) sorption to ferrihydrite obtained from the best SCM construct. Datapoints colored in blue represent experimental data and orange solid lines represent modeled data from L-ASCM.

The simulation results showed that only ten combinations, out of 63, can effectively simulate the Se(IV) sorption data (Table 9-5). A good quality model had not been obtained when four, five, and six surface complexation reactions were used. In addition, the contribution of surface species to model quality was observed: »Fe-OH-SeO<sub>3</sub><sup>2-</sup> species are always included in the good quality models and despite the introduction of additional species other than »Fe-OH-SeO<sub>3</sub><sup>2-</sup> species, the R value was only slightly improved. In other words, even though a number of surface complexation reactions had been reported in the literature, full community sorption data can be effectively fitted using only one species, i.e. »Fe-OH-SeO<sub>3</sub><sup>2-</sup>, and only nominal increases in R are achieved with the addition of multiple surface species. Figure 9-5 describes the simulation results obtained from the best quality SCM construct. As shown in the graphs, surface complexation reaction constants produced by the community data-driven workflow can reproduce most of the experimental data effectively.

Simulation results showed that community data-driven surface complexation modeling approach also can describe sorption features across multiple oxidation states that are internally consistent. For example, it is widely known that sorption affinity of Se(IV) is higher than that of Se(VI). Using our approach and as shown in Table 9-6, surface complexation reaction constant obtained for Se(IV) are greater than Se(VI) when the reactions have the same reaction stoichiometry.

**Table 9-6.** One species surface complexation model for Se(IV) and Se(VI) sorption to ferrihydrite

Surface Complexation Reaction	Se(IV)	Se(VI)	
»Fe-OH + SeO <sub>3(4)</sub> <sup>2-</sup> ↔ »Fe-OH-SeO <sub>3(4)</sub> <sup>2-</sup>	6.33 ± 0.04	1.08	0.04

## 9.4 Conclusions

Our preliminary analysis indicates a possible impact of material heating on radionuclide uptake by bentonite. Observed changes in radionuclide adsorption after bentonite heating have implications for radionuclide diffusive transport through engineered barriers and must be considered when designing waste disposal repositories. Results from this comprehensive analysis will inform performance assessment models on how much reduction of K<sub>d</sub> values can be expected for the original clay material as a result of heating under different ionic strengths.

The model developed through this work showed its ability for automation of simulation workflow for modeling sorption phenomena. Therefore, it was made possible to examine a lot of SCM constructs for obtaining the best quality model which can reproduce experimental data. Follow up studies have been conducted to analyze the sorption phenomena of selenium to various iron oxides. Since the developed framework is readily expandable (as community data increase) and extensible (as the number of minerals increase), the framework can be easily applied to other sorption system of interest.



## 10.0 SAPONITE AS A NEW ENGINEERED BUFFER MATERIAL FOR HIGH LEVEL NUCLEAR WASTE DISPOSAL: ITS CHEMICAL AND THERMAL STABILITY AND SORPTION CAPABILITY

### 10.1 Introduction

The barrier/buffer material is an important component of a multi-component engineered barrier system (EBS) in a high-level nuclear waste (HLW) deep geological repository. The key functions of the buffer material are to prevent the percolation of groundwater into waste packages, and to retard the movement of radionuclides from a waste package to the surrounding environment, should the waste package become breached.

Montmorillonite with an empirical formula of  $(\text{Na}, \text{Ca})_{0.33}(\text{Mg}, \text{Al})_2\text{Si}_4\text{O}_{10}(\text{OH})_2(\text{H}_2\text{O})_n$  has a di-octahedral smectite structure. Montmorillonite-rich bentonite has been favorably considered as a barrier/buffer material for HLW owing to its high swelling, high sorption properties and extremely low permeability. To ensure the stability of the mineral phase, the application of montmorillonite as a buffer material is suggested to be limited to mild environmental conditions, including: (1) temperatures  $\leq 90^\circ\text{C}$  (e.g., Pusch, 2001; Kaufhold and Dohrmann, 2011); (2) low ionic strength solutions (Pusch and Kasbohm, 2002), and (3) pH close to neutral (e.g., Kaufhold and Dohrmann, 2011). However, in many disposal concepts, the actual repository conditions may be outside the above mild environments. In addition, the presence of potassium in solution promotes the transformation of montmorillonite to illite. Potassium is present in groundwaters and can also be released from rocks and disposed waste forms. In a harsh environment, the performance of montmorillonite-rich bentonite is deteriorated because of collapse of swelling particles as a result of phase transformation to illite/chlorite or zeolites (Pusch, 2001). Therefore, a new generation of buffer materials that are relatively stable under potentially harsh repository conditions is needed to provide the flexibility for repository design, for example, for thermal management.

It has been known that tri-octahedral smectites such as saponite, with an ideal formula of  $\text{Mg}_3(\text{Si}, \text{Al})_4\text{O}_{10}(\text{OH})_2 \cdot 4\text{H}_2\text{O}$  for an Mg-end member (saponite-15Å), are less susceptible to alteration under harsh conditions (e.g., high pH and high temperatures) (Eberl et al. 1978; Guven, 1990; Elert et al., 2015). Recently, Mg-bearing saponite has been favorably considered as a preferable engineered buffer material for the Swedish very deep holes (VDH) disposal concept in crystalline rock formations (Yang et al., 2014). Liu et al. (2011) and Kasbohm et al. (2013) have demonstrated that saponite has the desirable physical properties such as high swelling pressures and very low hydraulic conductivities comparable to montmorillonite. For instance, at the same density of  $1,800 \text{ kg/m}^3$  (dry density  $1,175 \text{ kg/m}^3$  for saponite; dry density  $1,310 \text{ kg/m}^3$  for MX-80), saponite has hydraulic conductivity and swelling pressure of  $4 \times 10^{-12} \text{ m/s}$  and  $1,300 \text{ kPa}$ , respectively, in comparison with  $1 \times 10^{-10} \text{ m/s}$  and  $200 \text{ kPa}$ , respectively, for MX-80 (Liu et al., 2011; Kasbohm et al., 2013). Notice that they did not compare the values at the optimal dry densities for MX-80, which is usually about  $1780 \text{ kg/m}^3$ , and for saponite, which is yet to be established. Villar and Rivas (1994) did the similar tests for the Spanish montmorillonite and saponite. The hydraulic conductivity and swelling pressure for the saponite at  $1,600 \text{ kg/m}^3$  dry density are  $5 \times 10^{-13} \text{ m/s}$  and  $11,500 \text{ kPa}$ , respectively, in comparison with the hydraulic conductivity and swelling pressure of  $2 \times 10^{-13} \text{ m/s}$  and  $5,000 \text{ kPa}$ , respectively, for the montmorillonite at  $1,650 \text{ kg/m}^3$  dry density (Villar and Rivas, 1994).

In the VDH design concept, HLW is disposed in deep holes at depth between 2,000 m and 4,000 m. At such emplacement depths, the temperatures are expected to be between  $100^\circ\text{C}$  and  $150^\circ\text{C}$ , and the groundwater is of high ionic strength (Yang et al., 2014). In addition, high ionic strength environments also need to be considered in nuclear waste disposal in salt formations and sedimentary basins. For instance, the two brines associated with the salt formations at the Waste Isolation Pilot Plant (WIPP) in the U.S.A.

have ionic strengths of  $5.82 \text{ mol}\cdot\text{kg}^{-1}$  (ERDA-6) and  $8.26 \text{ mol}\cdot\text{kg}^{-1}$  (GWB) (Xiong and Lord, 2008). At the Asse site proposed for a geological repository in salt formations in Germany, the Q-brine has an ionic strength of  $\sim 13 \text{ mol}\cdot\text{kg}^{-1}$  (Schuessler et al., 2010).

Besides the afore mentioned harsh conditions of high temperature and high ionic strength, the harsh chemical conditions of high pH can be induced in a disposal environment due to the possible use of concretes and cementitious materials in plugs, liners, and seals (Becerro et al., 2009; Wieland et al., 2014). In this work, we investigate the stability of saponite under hydrothermal conditions at temperatures up to  $150^\circ\text{C}$  in high pH environments controlled by portlandite. The pore fluids in equilibrium with portlandite could last a long period in the temporal evolution of a geological repository (e.g., Becerro et al., 2009).

One of major functions of a buffer material is to absorb radionuclides and therefore provide an additional barrier for preventing or retarding the migration of radionuclides from breached waste containers. Actinides are among the major source-term elements having the most environmental concerns, because of their long decay half-lives and high radiotoxicity. In our previous study, we have demonstrated that Pr(III) is an excellent analog to trivalent actinides, especially to Pu(III) (Xiong and Wang, 2021). In this work, using Pr(III) as an analog to Pu(III), we study the sorption of Pr(III) onto saponite as a function of pH, ionic strength, and temperature.

## 10.2 Experimental

### 10.2.1 Materials

In our experimental study, we use both synthetic and well-characterized research-grade natural saponite to investigate their interactions with portlandite-saturated solutions. The synthetic saponite used in this work has a stoichiometry of  $\text{Na}_{0.95}\text{Mg}_{5.90}\text{Al}_{0.06}[(\text{Si}_{7.07}\text{Al}_{0.93})\text{O}_{20}](\text{OH})_4$  (see Xiong, 2022). The use of the synthetic and research-grade natural saponite is to avoid the side reactions that could be caused by the impurities present in the industrial grade materials, as the potential side reactions could complicate the interpretation of the results. The synthetic saponite was synthesized according to the procedure described in Xiong (2022). The natural, research-grade saponite was purchased from the Excalibur Mineral Corporation (Charlottesville, Virginia, USA). The locality for the natural saponite was King Island, Tasmania, Australia. We analyzed the chemical compositions of the natural saponite by using X-ray Fluorescence Spectroscopy (XRF). The chemical compositions are listed in Table 10.1, and the calculated saponite stoichiometry is  $(\text{Na}_{0.42}\text{K}_{0.03}\text{Ca}_{0.58})(\text{Mg}_{3.43}\text{Fe}^{\text{II}}_{1.46}\text{Mn}^{\text{II}}_{0.12}\text{Fe}^{\text{III}}_{0.30}\text{Ti}_{0.05}\text{Al}_{0.13})[(\text{Si}_{7.03}\text{Ti}_{0.05}\text{Al}_{0.92})\text{O}_{20}](\text{OH})_4$  based on  $\text{O}_{20}(\text{OH})_4$  per formula unit. Notice that total iron was speciated as Fe(II) and Fe(III) based on the charge balance constraint in the calculation.

**Table 10.1.** Chemical compositions determined by this study for the natural saponite from King Island, Tasmania, Australia.

Oxide	Natural Saponite from King Island, Tasmania, Australia, wt% <sup>A</sup>
SiO <sub>2</sub>	51.26
TiO <sub>2</sub>	0.48
Al <sub>2</sub> O <sub>3</sub>	6.50
Fe <sub>2</sub> O <sub>3</sub> <sup>B</sup>	2.88
FeO <sup>B</sup>	12.71
MnO	1.00
MgO	16.75
CaO	3.95
Na <sub>2</sub> O	1.58
K <sub>2</sub> O	0.18
H <sub>2</sub> O (LOI) <sup>C</sup>	15.89

<sup>A</sup> With a stoichiometry of (Na<sub>0.42</sub>K<sub>0.03</sub>Ca<sub>0.58</sub>)(Mg<sub>3.43</sub>Fe<sup>II</sup><sub>1.46</sub>Mn<sup>II</sup><sub>0.12</sub>Fe<sup>III</sup><sub>0.30</sub>Al<sub>0.13</sub>)(Si<sub>7.03</sub>Ti<sub>0.05</sub>Al<sub>0.92</sub>)O<sub>20</sub>(OH)<sub>4</sub>. The stoichiometry is calculated in this work on the basis of O<sub>20</sub>(OH)<sub>4</sub> per formula unit.

<sup>B</sup> The total iron concentrations were determined as 15.59 wt%. They are speciated as Fe<sub>2</sub>O<sub>3</sub> and FeO based on the charge balance constraint in our calculations.

<sup>C</sup> Based on the TGA analysis up to 900°C using a Netzsch STA 409 thermal gravimetric analyzer (TGA).

The USP/FCC grade (i.e., United States Pharmacopeia grade/Food Chemical Codex grade) portlandite [Ca(OH)<sub>2</sub>(cr)] (CAS # 1305-6201, LOT # 041246) used for preparing the portlandite-saturated solution at 22°C was obtained from Fisher Scientific. The portlandite was analyzed by using the XRD, confirming that it is pure Ca(OH)<sub>2</sub>. The saturated portlandite solution was prepared by dissolving 0.7085 grams of Ca(OH)<sub>2</sub> into 500.04 grams of de-ionized (DI) water. Notice that the required amounts of Ca(OH)<sub>2</sub> for a saturated portlandite solution at room temperature are 0.6296 grams (0.017 mol•kg<sup>-1</sup>). Therefore, the amounts of Ca(OH)<sub>2</sub> used are slightly in excess. Indeed, small amounts of Ca(OH)<sub>2</sub> are observed to be present at the bottom of the plastic container. DI water was degassed with ultrahigh purity N<sub>2</sub> gas before making the solution. The prepared portlandite saturated solution has a pH of 12.56.

In the parallel experiments investigating the interactions of montmorillonite with the portlandite-saturated solutions, both natural Wyoming montmorillonite (Swy-2) as received from the Source Clays Repository (Clay Minerals Society), and purified SWy-2 (i.e., the fraction < 2 μm) montmorillonite were used.

### 10.2.2 Procedures

In our experiments, we used a 0.017 mol•kg<sup>-1</sup> portlandite [Ca(OH)<sub>2</sub>(cr)]-saturated solution prepared at room temperature. As portlandite has a retrograde solubility with increasing temperature, the usage of this solution ensures that the solution is in equilibrium with portlandite at high temperatures.

In the presence of cementitious materials in a geological repository, alkaline solutions can be present in at least two stages. During the initial, short stage of cement hardening, the fresh or “young” ordinary Portland cement (OPC) pore fluids are mainly composed of Na<sup>+</sup>, K<sup>+</sup>, and OH<sup>-</sup> with minor amounts of Ca<sup>2+</sup> reaching pH values above 13.5 (e.g., Becerro et al., 2009; Kaufhold and Dohrmann, 2011; Fernandez et al., 2014; Chen et al., 2019; Sun et al., 2020). Then, the pore fluids in the second stage are buffered by portlandite with Ca<sup>2+</sup> and OH<sup>-</sup> being the dominant ions (Becerro et al., 2009; Kaufhold and Dohrmann, 2011; Sun et

al., 2020). This stage is expected to last very long, up to 200,000 years (e.g., Sun et al., 2020). Therefore, the experimental objective of this work is to investigate the stability of saponite in this stage.

In our experiments investigating the interactions of saponite with portlandite-saturated solutions, both the natural saponite and synthetic saponite were used. In the comparison experiments, we also investigate the interactions of natural montmorillonite (Swy-2) with portlandite-saturated solutions.

Various solid-to-solution mass ratios were employed in our experiments. The solid-to-solution mass ratio was 1:5 in experiments with natural saponite, while it was 1:17 in experiments using synthetic saponite. The parallel experiments investigating the stability of the natural montmorillonite in the presence of a portlandite-saturated solution also used a solid-to-solution ratio of 1:5.

The experiments were performed using Parr® vessels. First, the desired amounts of the starting solid material (0.5-2 grams) were weighed using a balance with a precision of up to four decimal places prior to loading into the vessel. Then, the desired amounts of the portlandite-saturated solution (~10 grams) were weighed and loaded into the vessel. After that, the vessel was sealed and placed into an oven at the temperature of interest. After the desired experimental duration, the vessel was taken out from the oven and quenched to room temperature. Subsequently, the vessel was opened, aqueous solutions for some experiments were sampled if there were enough solutions, filtered with 0.2 µm syringe filters, and weighed. Then, the solution was acidified with concentrated HNO<sub>3</sub> and diluted to 10 mL for ICP-AES analyses. Meanwhile, reaction products were carefully retrieved. The reaction products were washed with deionized (DI) water and dried at a room temperature. For the sampling procedure and analysis for aqueous samples, please refer to one of our recent publications (Xiong and Wang, 2021).

Chemical analyses of solution samples were conducted by using a Perkin Elmer dual-view inductively coupled plasma-atomic emission spectrometer (ICP-AES) (Perkin Elmer DV 8300). Calibration blanks and standards were precisely matched with experimental matrices. The instrument was warmed-up for at least one and half hours before the calibration and analysis were performed. The instrument was calibrated with at least five standards (e.g., blank, 0.1 ppm to 100 ppm for elements of interest) with 1 ppm Sc as the internal standard. Immediately after the calibration, samples were analyzed. In the analysis, the calibration standards were also analyzed as samples to check if there were significant shifts. At least one calibration standard and one blank were analyzed as samples after usually every eight samples were analyzed. If significant drifts (e.g., higher than 5%) from the known concentrations of the standards were observed, the instrument was re-calibrated. The linear correlation coefficients of calibration curves in all measurements were better than 0.9995. The analytical precision for ICP-AES is better than 1.00% in terms of the relative standard deviation (RSD) based on replicate analyses.

The XRD patterns of reaction products were analyzed by using a Bruker AXS D2 Phaser to scan for a 2θ range from 5° to 70°, before and after the experiments. The chemical compositions of the natural saponite were determined by using an ARL Quant'x ED-XRF Analyzer from the Thermo Electron Corporation. Scanning electron microscopy (SEM) analyses were also performed for the reaction products by using a Tescan VEGA 3 scanning electron microscope.

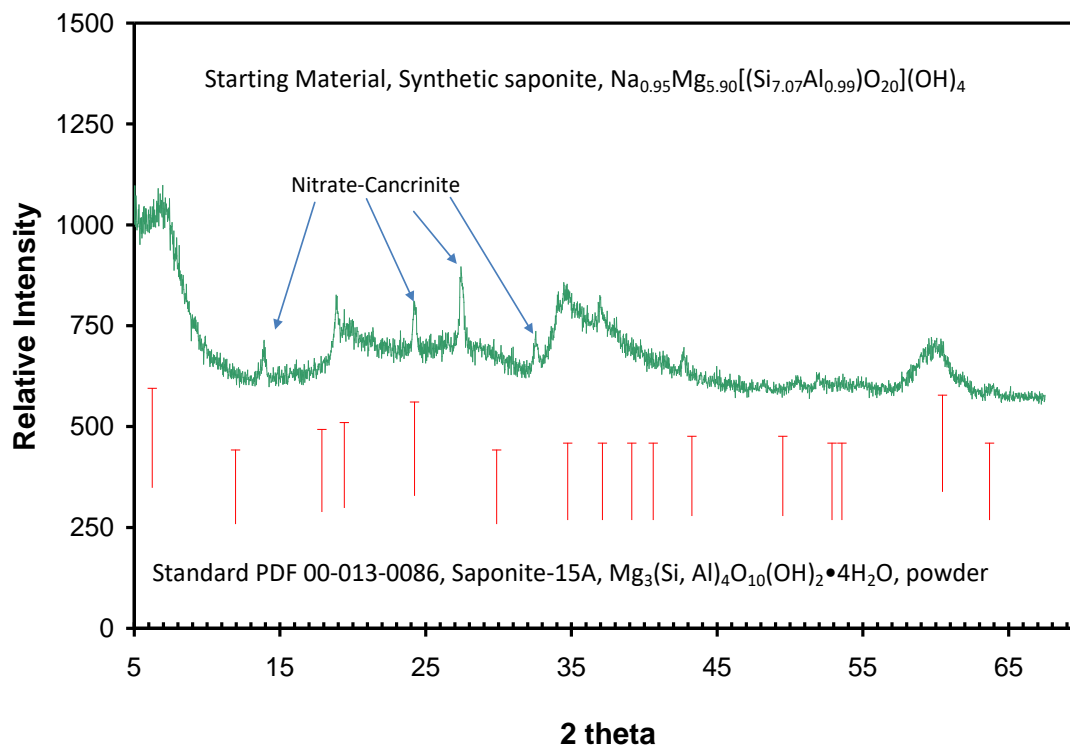


**Figure 10.1.** XRD pattern for the synthetic saponite used as a starting material in this study. The standard XRD pattern for a Mg-end member of saponite, saponite-15Å, is included as a reference.

In our sorption experiments, the amounts of saponite are ~50 mg (~0.05 g). The natural saponite is from King Island, Tasmania, Australia. The volume of a constant ionic strength supporting solution for each experiment is 100 mL. Each experiment is initially spiked with 8.5 ppm ( $6 \times 10^{-5} \text{ mol} \cdot \text{kg}^{-1}$ ) PrCl<sub>3</sub>. We use NaCl solutions as ionic strength supporting media. The ionic strengths in our experiments range from 0.001 mol·kg<sup>-1</sup> to 0.1 mol·kg<sup>-1</sup>. At each ionic strength, we have two sets of experiments. In one set of experiments, we first adjust pH of a supporting solution to acidic pH by titrating trace amounts of 1.0 mol·dm<sup>-3</sup> HCl. Then, we gradually adjust pH conditions to alkaline pH with 1.0 mol·dm<sup>-3</sup> NaOH. In another set of experiments, we first adjust pH of a supporting solution to alkaline pH by titrating trace amounts of 1.0 mol·dm<sup>-3</sup> NaOH. Then, we gradually adjust pH conditions to acidic pH with 1.0 mol·dm<sup>-3</sup> HCl. As it has been demonstrated by similar studies that sorption equilibrium for La(III) onto bentonite usually takes 24 hours (Chen et al., 2012), we take solution samples from our experiments to ensure that the duration between two samples should be longer than 24 hours.

Before taking solution samples from experiments, pH values were first measured. Then, about 3 mL solution was withdrawn from each experiment. The solution sample was filtered with a 0.2 μm syringe filter, and the mass of the filtered solution was determined with a balance precise to the fourth decimal place. After that, the solution was acidified with 0.5 mL concentrated HNO<sub>3</sub>, and was diluted to 10 mL for chemical analyses. Pr(III) concentrations are determined using a Perkin Elmer 8300 Dual View inductively coupled plasma-atomic emission spectrometer (ICP-AES). The details of the ICP-AES analyses are similar to those described in our previous study (Xiong and Wang, 2021).

### 10.3. Results and Discussion

In Figure 10.1, the XRD pattern of the synthetic saponite with a stoichiometry of  $\text{Na}_{0.95}\text{Mg}_{5.90}\text{Al}_{0.06}[(\text{Si}_{7.07}\text{Al}_{0.93})\text{O}_{20}](\text{OH})_4$ , similar to saponite-15Å, is presented. Notice that there are small amounts of nitrate-cancrinite present in the starting material. This is expected, because the synthetic saponite was produced by using the procedure of Shao and Pinnavaia (2010), in which nitrate-cancrinite was generally observed.

In Figure 10.2, the XRD pattern of the natural saponite from King Island, Tasmania, Australia, is shown. According to our XRF analysis, the chemical compositions for this natural saponite is presented in Table 10.1. The stoichiometry of the natural saponite is  $(\text{Na}_{0.42}\text{K}_{0.03}\text{Ca}_{0.58})(\text{Mg}_{3.43}\text{Fe}^{\text{II}}_{1.46}\text{Mn}^{\text{II}}_{0.12}\text{Fe}^{\text{III}}_{0.30}\text{Al}_{0.13})[(\text{Si}_{7.03}\text{Ti}_{0.05}\text{Al}_{0.92})\text{O}_{20}](\text{OH})_4$ , which is also a Mg-rich saponite, similar to saponite-15Å, but with more complex chemistry.

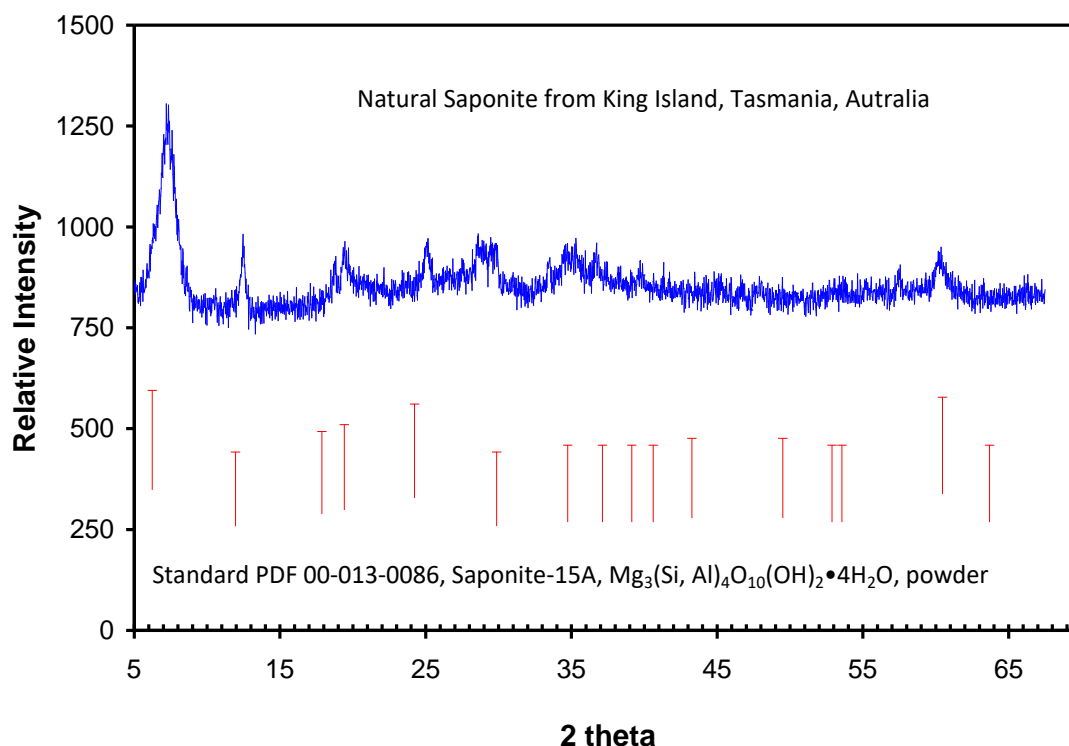


**Figure 10.2.** XRD pattern for the natural saponite from King Island, Tasmania, Australia, used as a starting material in this study. The standard XRD pattern for a Mg-end member of saponite, saponite-15Å, is included as a reference.

In Figure 10.3, the results regarding the interactions of the synthetic saponite with saturated portlandite solutions are shown. The results at 60°C, 125°C and 150°C indicate that the XRD peaks associated with nitrate-cancrinite disappear in comparison with the starting material as shown by Figure 10.1. Notice that all XRD peaks associated with saponite are retained according to the analyses. Also of note, the peaks associated with portlandite did not appear in the XRD pattern, and that is expected because of washing the run products after the experiments.

Notice the low solid-to-solution mass ratio used in the experiments with the synthetic saponite. Low solid-to-solution mass ratios (in the order of 1:5) would favor a phase transformation, should the phase become unstable. Therefore, the experiments with a low solid to solution mass ratio (i.e., 1:17) for the synthetic

saponite demonstrates that the synthetic saponite is more stable in high pH solutions at elevated temperatures. Notice that while the synthetic saponite was synthesized in a high pH solution (pH ~12), the natural saponite was not formed in such a high pH solution. The fact that both the synthetic and natural saponite is stable in high pH solutions demonstrates their chemical stability under hyperalkaline conditions.

Figure 10.4 shows the results regarding the interactions of the natural saponite with portlandite-saturated solutions. Similar to the synthetic saponite, the results at 60°C, 125°C and 150°C indicate that all peaks associated with saponite are retained after the natural saponite interacts with the saturated portlandite solutions, indicating the stability of saponite in the presence of a portlandite-saturated solution.

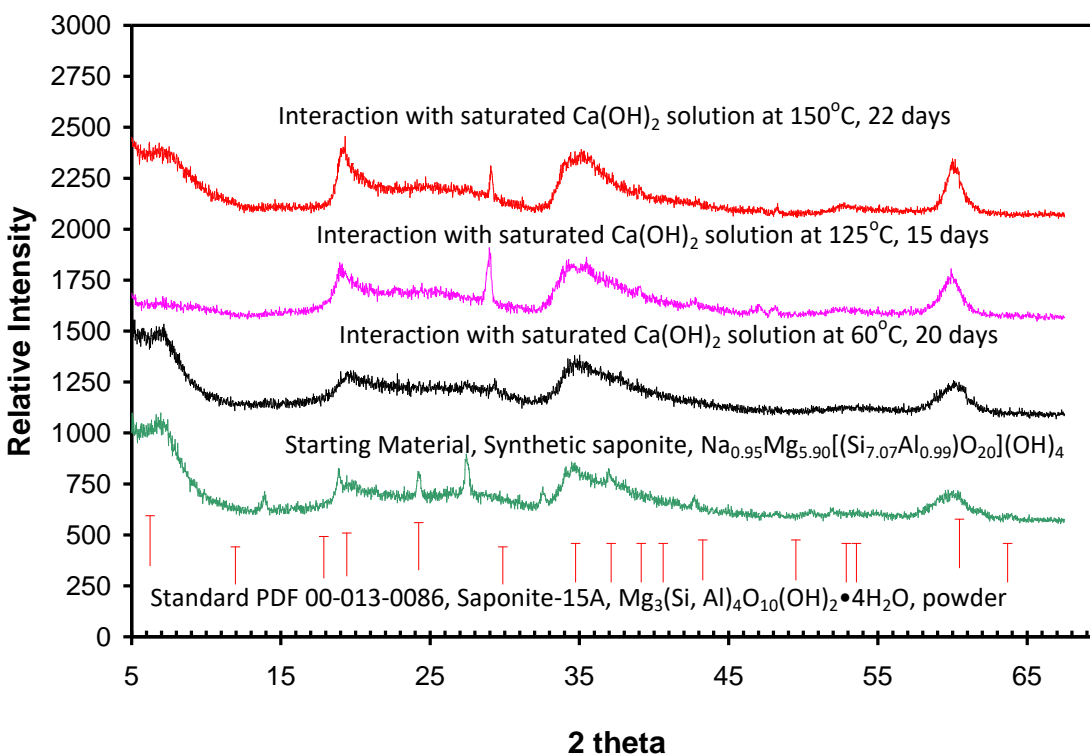
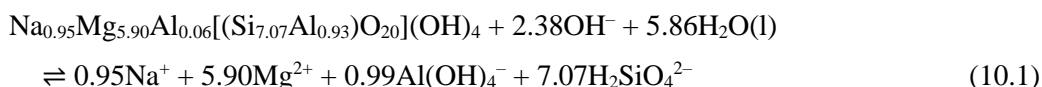


**Figure 10.3.** XRD patterns for the experiments of the synthetic saponite interacting the portlandite-saturated solutions at 60°C, 125°C and 150°C. The standard XRD pattern for a Mg-end member of saponite, saponite-15A, is included as a reference.

The above results demonstrate that both the synthetic and natural saponites are stable in the high pH environments buffered by portlandite. We attribute their stability to their low solubility, as indicated by the absence of brucite [Mg(OH)<sub>2</sub>(cr)]. Should the synthetic or natural saponite be dissolved appreciably, brucite would be precipitated, as brucite is a stable phase in high pH environments when certain concentrations of dissolved Mg are present. This can be elucidated as follows.

The dissolution of Mg-dominated saponite, represented by the synthetic saponite, in an alkaline solution, can be expressed as,



If the concentrations of dissolved  $\text{Mg}^{2+}$  reach the saturation level of brucite, we have the following precipitation reaction for brucite,



The equilibrium constant ( $\log_{10}K$ ) for the dissolution of brucite in the following form,



has been determined to be  $15.63 \pm 0.11$  at  $60^\circ\text{C}$  (Kirkes and Xiong, 2018). Based on Xiong (2006), the equilibrium constant for Reaction (10.3) at  $150^\circ\text{C}$  is 11.63.

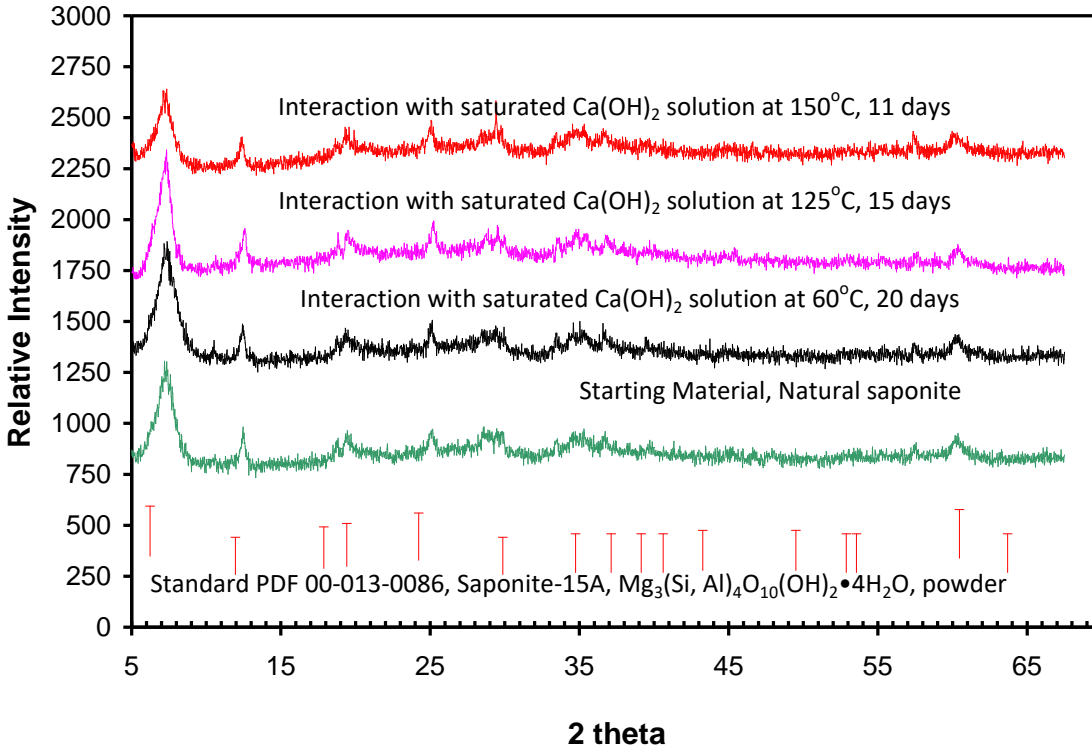


**Figure 10.4.** XRD patterns for the experiments of the natural saponite from King Island, Tasmania, Australia, interacting the portlandite-saturated solutions at  $60^\circ\text{C}$ ,  $125^\circ\text{C}$  and  $150^\circ\text{C}$ . The standard XRD pattern for a Mg-end member of saponite, saponite-15Å, is included as a reference.

The equilibrium constants for Reaction (10.2) at  $60^\circ\text{C}$  and  $150^\circ\text{C}$  can be obtained by combination of Reaction (10.3) with the ionization constants of water cast below at the same temperatures,

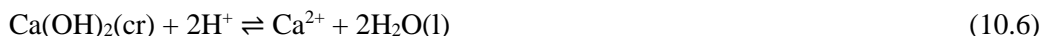


The equilibrium constants for Reaction (10.4) at  $60^\circ\text{C}$  and  $150^\circ\text{C}$  are -13.03 and -11.63, respectively, from the database DATA0.YMP.R2 (Wolery and Sutton, 2011). Therefore, based on the equilibrium constants for Reactions (10.3) and (10.4), the equilibrium constants for Reaction (2) at  $60^\circ\text{C}$  and  $150^\circ\text{C}$  are computed to be 10.43 and 11.63, respectively.

The concentrations of hydroxyl ion in our experiments are controlled by portlandite,



The equilibrium constants for the dissolution of portlandite in the following form,



at 60°C and 150°C are 20.18 and 15.95, respectively, according to database DATA0.YMP.R2 (Wolery and Sutton, 2011). Therefore, the equilibrium constants for Reaction (10.5) at 60°C and 150°C are -5.88 and -7.31, respectively, when Reaction (10.6) is combined with Reaction (10.4).

As the ionic strength of the portlandite-saturated solutions is low ( $I \leq 0.051 \text{ mol}\cdot\text{kg}^{-1}$ ), the activity coefficient corrections for deviation from unity are insignificant and can be ignored. Accordingly, the hydroxyl ion concentrations can be calculated from the equilibrium constants for Reaction (10.5). The hydroxyl ion concentrations are calculated to be  $1.10 \times 10^{-2} \text{ mol}\cdot\text{kg}^{-1}$  and  $3.63 \times 10^{-3} \text{ mol}\cdot\text{kg}^{-1}$  at 60°C and 150°C, respectively.

Based on the above hydroxyl ion concentrations, the minimum magnesium concentrations required forming brucite at 60°C and 150°C can be calculated from Reaction (2). The required minimum magnesium concentrations are at least  $3.07 \times 10^{-7} \text{ mol}\cdot\text{kg}^{-1}$  and  $1.78 \times 10^{-7} \text{ mol}\cdot\text{kg}^{-1}$  at 60°C and 150°C, respectively, for the precipitation of brucite. The absence of brucite in those experiments indicate that the magnesium concentrations are below those levels, which is consistent with the analytical results indicating the magnesium concentrations are below the detection limit of ICP-AES (see below), suggesting the low solubility of the synthetic saponite in the presence of the saturated portlandite solutions.

The solution chemistry for the experiments with the synthetic saponite supports the above conclusion. First, the magnesium concentrations are low, and below the detection limit of ICP-AES (Table 10.2). Second, the apparent solubility products in terms of  $m_{\Sigma\text{Al}} \times m_{\Sigma\text{Si}}$  are also orders of magnitude lower than those for zeolites and hydroxyl sodalite in alkaline solutions (e.g., Xiong, 2013, 2016). For instance, the apparent solubility product for hydroxyl sodalite in  $\sim 0.01 \text{ mol}\cdot\text{kg}^{-1}$  NaOH at 90°C is about  $10^{-6} (\text{mol}\cdot\text{kg}^{-1})^2$ , which is about two orders of magnitude higher than those for saponite.

**Table 10.2.** Aqueous chemistry of interactions of saponite with initially saturated  $\text{Ca(OH)}_2$  solutions\*

Experiment	T, °C	Na,	Mg	Al	Si	Al×Si
SAP-1 <sup>A</sup>	150	$1.15 \times 10^{-3}$	BDL	$1.51 \times 10^{-4}$	$6.13 \times 10^{-4}$	$9.29 \times 10^{-8}$
SAP-2 <sup>B</sup>	60	$1.03 \times 10^{-3}$	BDL	$7.54 \times 10^{-5}$	$4.09 \times 10^{-4}$	$3.09 \times 10^{-8}$

\*The aqueous chemistry was determined for the quenched solution samples by using ICP-AES, and concentration units are on a molal scale ( $\text{mol}\cdot\text{kg}^{-1}$ ). All samples were filtered with 0.2  $\mu\text{m}$  syringe filters.

<sup>A</sup>: Experimental duration: 22 days

<sup>B</sup>: Experimental duration: 20 days

BDL: Below detection limit of ICP-AES

Interestingly, the magnesium concentrations in the experiments performed by Kaufhold and Dohrmann (2011) with Mg-containing montmorillonite in a portlandite-saturated solution at 90°C are generally below  $2.08 \times 10^{-6} \text{ mol}\cdot\text{kg}^{-1}$ , and brucite was also absent. The Mg-containing montmorillonite was stable at this temperature after interactions with the portlandite-saturated solution (Kaufhold and Dohrmann, 2011).

In summary, with regard to the experiments with saponite, we attribute the stability of saponite, in the presence of the portlandite-saturated solutions, to its low solubility, as indicated by the lack of brucite in the reaction products.

Figure 10.5 shows the results in parallel experiments with the natural montmorillonite in the presence of a portlandite solution-saturated at 150°C. The results indicate that montmorillonite undergoes the phase transformation under such conditions, as zeolite (phillipsite) started to form and some of the peaks

characteristic of montmorillonite disappeared. The formation of zeolite is consistent with other studies (de la Villa et al., 2001; Ramirez et al., 2002; Cuevas, 2004). Notice that the peaks for zeolite become stronger when the experimental durations increased from 9 days to 72 days for the purified montmorillonite (see the top XRD pattern in Figure 10.5). Also of note, the new peak at  $2\theta \sim 62.9^\circ$  may represent the  $d(060)$  reflection that may indicate a phase transformation (Lippmann, 1968; Kauhold et al., 2013).

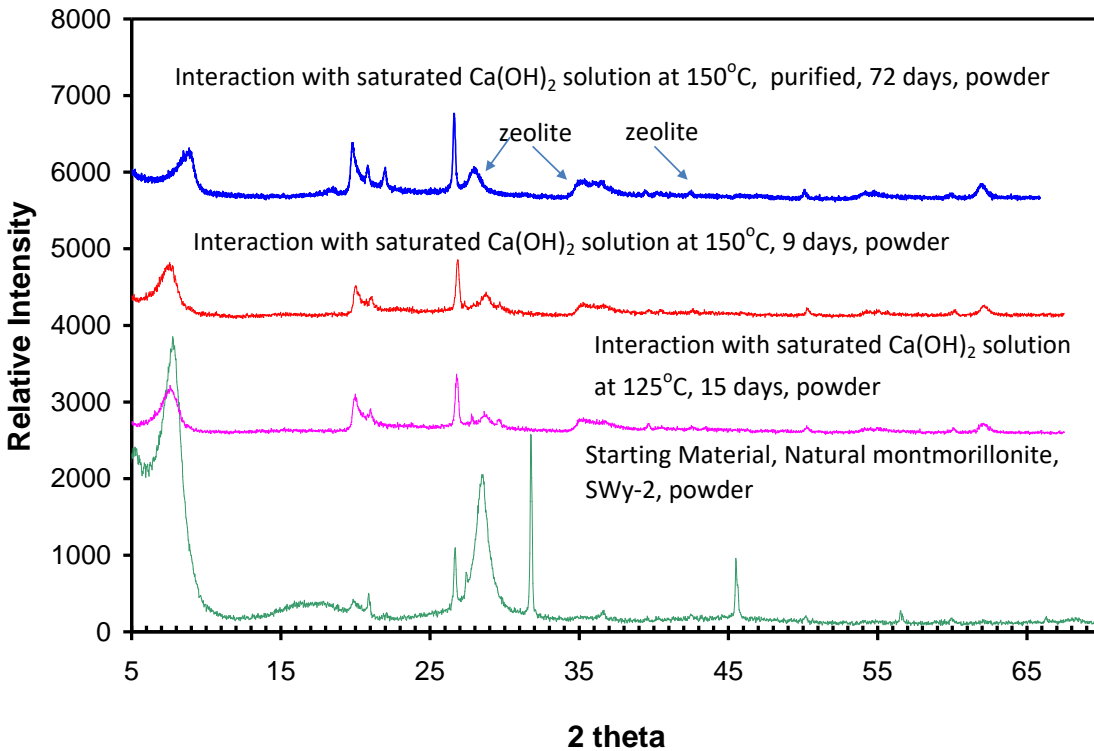


**Figure 10.5.** XRD patterns for the experiments of the natural montmorillonite (SWy-2) from Wyoming, USA, interacting the portlandite-saturated solution up to  $150^\circ\text{C}$ . The pattern for the starting material is included as a reference. Both the as-received SW-2 (the middle XRD pattern) and purified SWy-2 ( $< 2 \mu\text{m}$  fraction) (the top XRD pattern) were used.

The results from the scanning electron microscopy (SEM) analyses are supportive of the above evaluations. Figure 10.6 shows the SEM analyses for the run products in the experiment investigating the interactions of the synthetic saponite with portlandite saturated solutions at  $150^\circ\text{C}$ . Figure 6 indicates that the synthetic saponite does not show alterations. Figure 10.7 presents the SEM analyses for the run products in the experiment investigating the interactions of montmorillonite with portlandite saturated solutions at  $150^\circ\text{C}$ . The images in Figure 10.7 show that montmorillonite may have been subject to alteration. The SEM analyses for the interaction of the natural saponite with the saturated portlandite solution at  $150^\circ\text{C}$  are shown in Figure 10.8. Similar to the results for the synthetic saponite in Figure 10.6, there is no evidence of alterations for the natural saponite (Figure 10.8).

There have been a number of studies investigating the interactions of montmorillonite with high pH solutions at various temperatures up to  $90^\circ\text{C}$  since 2000. Claret et al. (2002) investigated its interactions with the fresh cement pore water at  $60^\circ\text{C}$ . The fresh cement pore water has the following compositions:  $0.0625 \text{ mol}\cdot\text{dm}^{-3} \text{ NaOH} + 0.161 \text{ mol}\cdot\text{dm}^{-3} \text{ KOH} + 2.24 \times 10^{-3} \text{ mol}\cdot\text{dm}^{-3} \text{ Ca(OH)}_2$ . They found that montmorillonite was partially transformed to illite. Ramirez et al. (2003) studied the interactions of montmorillonite with a series of alkaline solutions at  $90^\circ\text{C}$ . The alkaline solutions used by Ramirez et al.

(2003) include  $1 \times 10^{-4} \text{ mol} \cdot \text{dm}^{-3}$  NaOH, the portlandite-saturated solution ( $22.3 \times 10^{-3} \text{ mol} \cdot \text{dm}^{-3}$  Ca(OH)<sub>2</sub> at room temperature), the mixtures of sodium, potassium and calcium hydroxides.. Their experimental results suggested that montmorillonite was stable in  $1 \times 10^{-4} \text{ mol} \cdot \text{dm}^{-3}$  NaOH and the portlandite-saturated solution, whereas it was unstable in all of other solutions with potassium. Cuevas et al. (2007) did similar experiments at 60°C by using the mixture of NaOH + KOH and the portlandite-saturated solution, and they reached a conclusion similar to that of Ramirez et al. (2003), i.e., montmorillonite was unstable in the mixture of NaOH and KOH, but stable in the portlandite-saturated solution at 60°C, though their experimental temperature (60°C) was lower than that of Ramirez et al. (2003) (90°C).

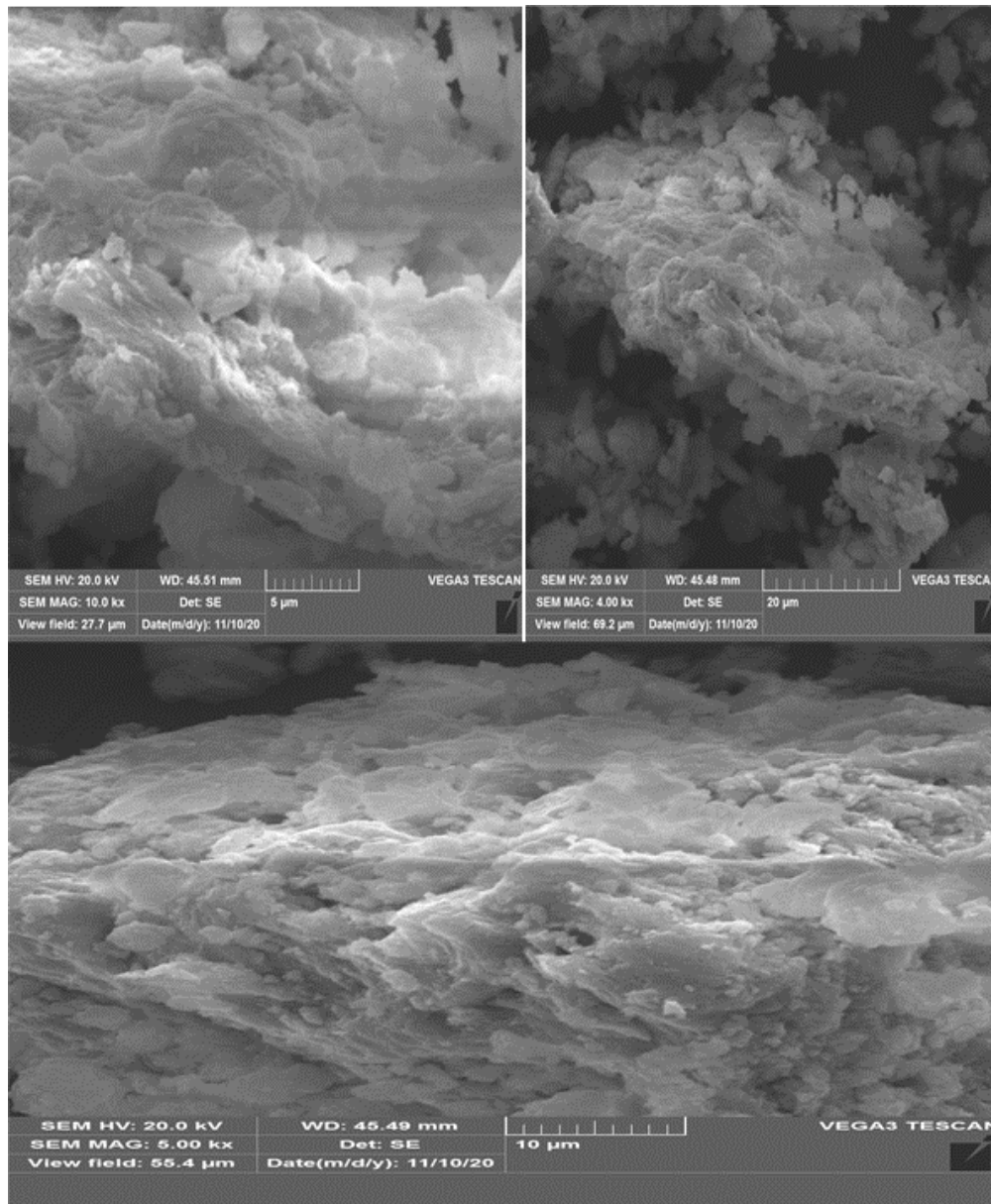


**Figure 10.6.** SEM images from the run products in the experiment of the synthetic saponite interacting the portlandite-saturated solutions at 150°C.

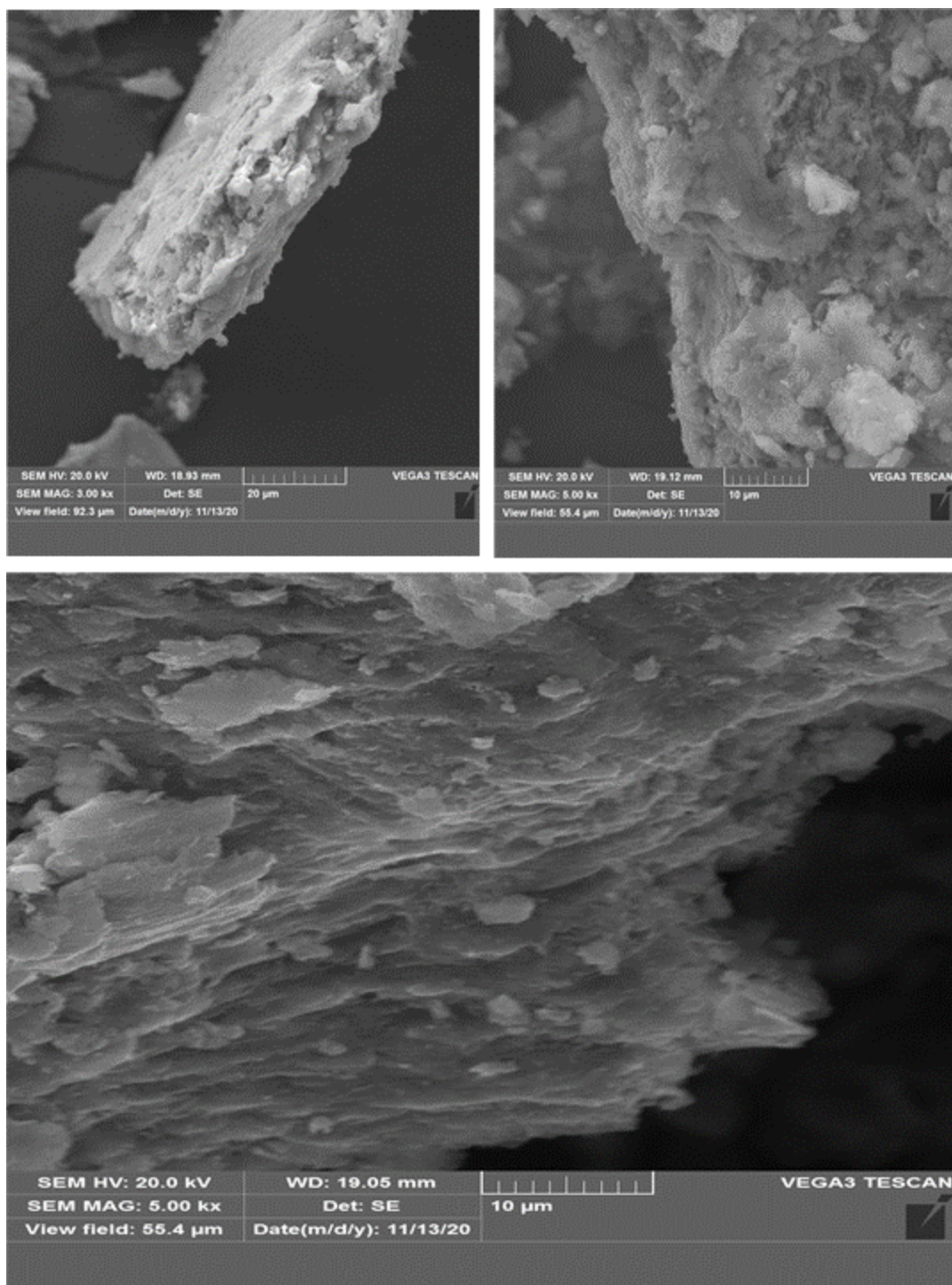


**Figure 10.7.** SEM images from the run products in the experiment of montmorillonite in the Wyoming bentonite (SWy-2) interacting the portlandite-saturated solutions at 150°C.

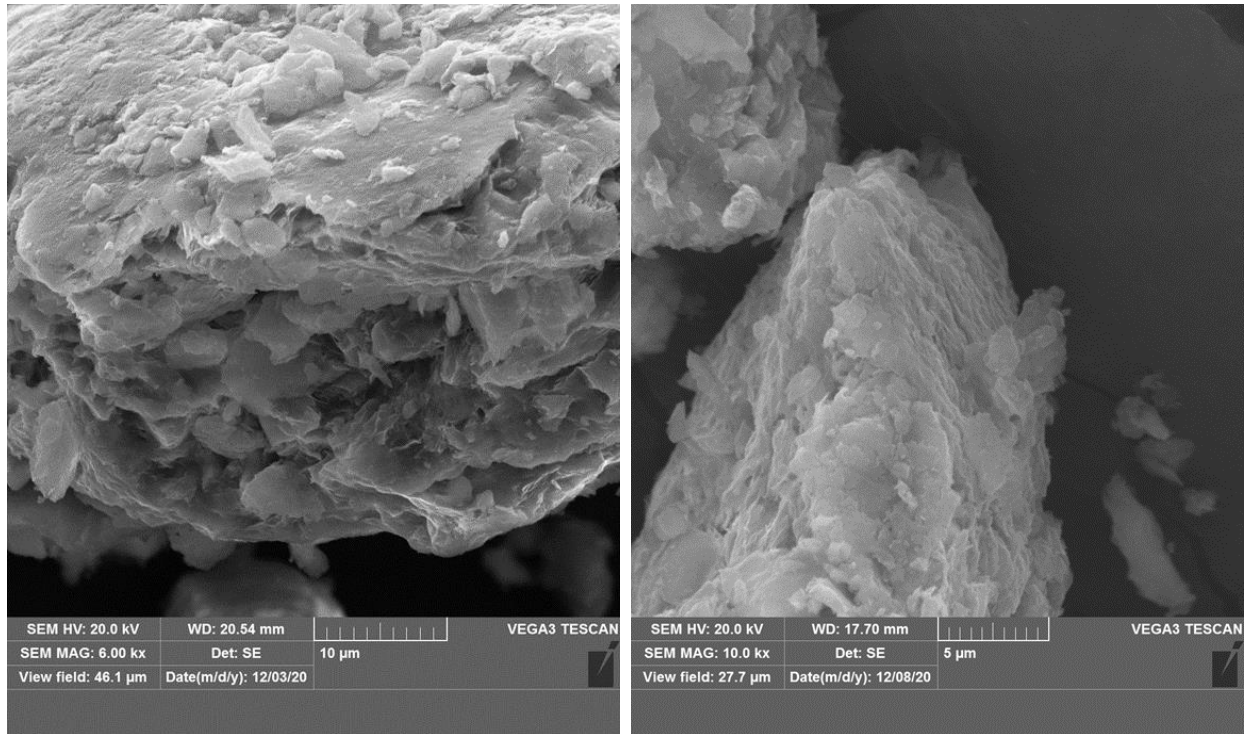


**Figure 10.8.** SEM images from the run products in the experiment of the natural saponite from King Island, Tasmania, interacting the portlandite-saturated solutions at 150°C.

More recently, Kaufhold and Dohrmann (2011) experimentally investigated the interactions of bentonites with portlandite solutions at 60°C and 90°C. They concluded that bentonite is stable in portlandite solutions up to 90°C, and therefore recommended that the temperature for a repository should be kept below 90°C for the sake of the chemical stability of bentonite buffers. Their results are supported by the studies on the Chinese candidate Gaomiaozi (GMZ) bentonite (Sun et al., 2018; 2020). This temperature limit is consistent with the design concept for a clay repository in the countries such as Belgium, France, and Switzerland (e.g., Grambow, 2016). It is also consistent with the temperature used for the long-term (up to 18 years) heating tests on the bentonite buffer material performed in Spain (Villar et al., 2020)

Therefore, regarding the experiments with montmorillonite, our experiments demonstrate that montmorillonite undergoes the phase transformation at 150°C in saturated portlandite solution, which, thermodynamically speaking, becomes unstable. Previous studies indicate that montmorillonite is stable up to 90°C in the presence of the saturated portlandite solutions, which sets a fundamental boundary condition (i.e.,  $T \leq 90^\circ\text{C}$ ) for a geological repository when montmorillonite is used as a buffer material. Therefore, if a geological repository design concept requires a higher temperature boundary, thermodynamically speaking, montmorillonite buffer materials seem subject to phase transformation under those combined harsh conditions of both high temperature and high pH, as indicated by this study. Notice that this temperature of 150°C was not reached in the previous studies. As the interaction between hyperalkaline solutions and montmorillonite is an important subject, more systematic investigations may be desirable.

The results of our sorption experiments are presented in Figures 10-9 through 10-11. Figure 10-9 shows the sorption of Pr(III) onto the natural saponite as a function of pH in  $0.001 \text{ mol}\cdot\text{kg}^{-1}$  NaCl at  $25^\circ\text{C}$ . The two sets of experiments agree well with each other. The results indicate that saponite has excellent sorption capabilities above pH 6.5 with 100% sorption. In the acidic pH at pH  $\sim 4$ , the sorption percentage is between  $\sim 55\%$  and  $75\%$ . The results in  $0.01 \text{ mol}\cdot\text{kg}^{-1}$  NaCl (Figure 10-2) are similar to those in  $0.001 \text{ mol}\cdot\text{kg}^{-1}$  NaCl. Again, saponite has excellent sorption capabilities above pH 6.5 with 100% sorption. In the acidic pH at pH  $\sim 4$ , the sorption percentage is  $\sim 75\%$ . The results in  $0.1 \text{ mol}\cdot\text{kg}^{-1}$  NaCl (Figure 10-3) are similar to those in  $0.001$  and  $0.01 \text{ mol}\cdot\text{kg}^{-1}$  NaCl. Again, saponite has excellent sorption capabilities above pH 6.5 with 100% sorption. However, in the acidic pH at pH  $\sim 4$ , the sorption percentage is lower, between  $\sim 30\%$  and  $\sim 50\%$ . Currently, we are extending our experiments to other temperatures. When those experiments are completed, we will perform the detailed thermodynamic analyses for the sorption equilibrium.

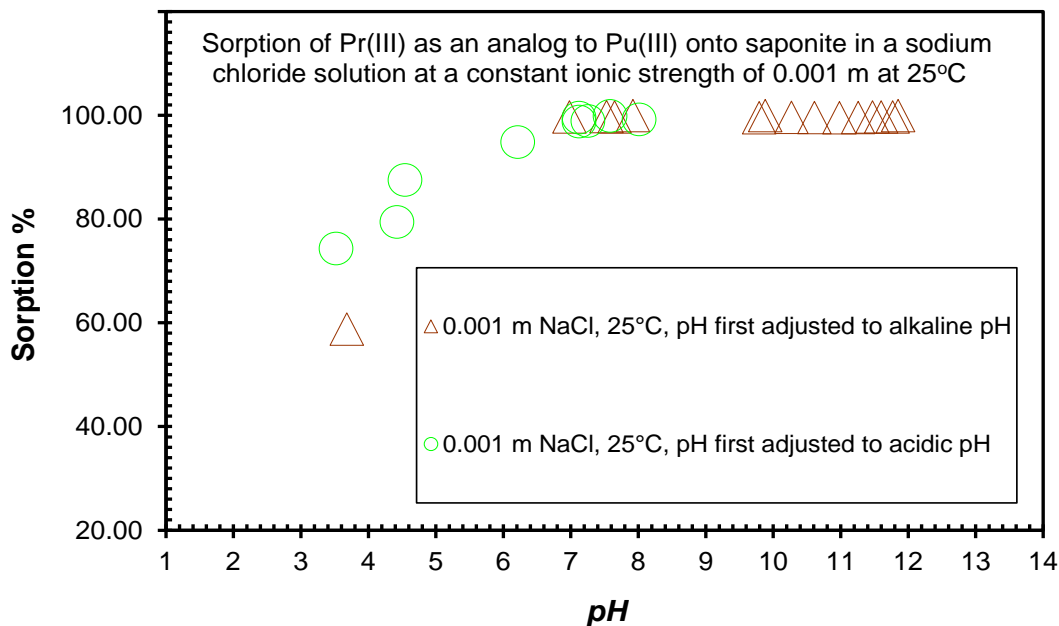


**Figure 10-9.** Sorption of Pr(III) onto the natural saponite as a function of pH in  $0.001 \text{ mol}\cdot\text{kg}^{-1}$  NaCl at  $25^\circ\text{C}$ .

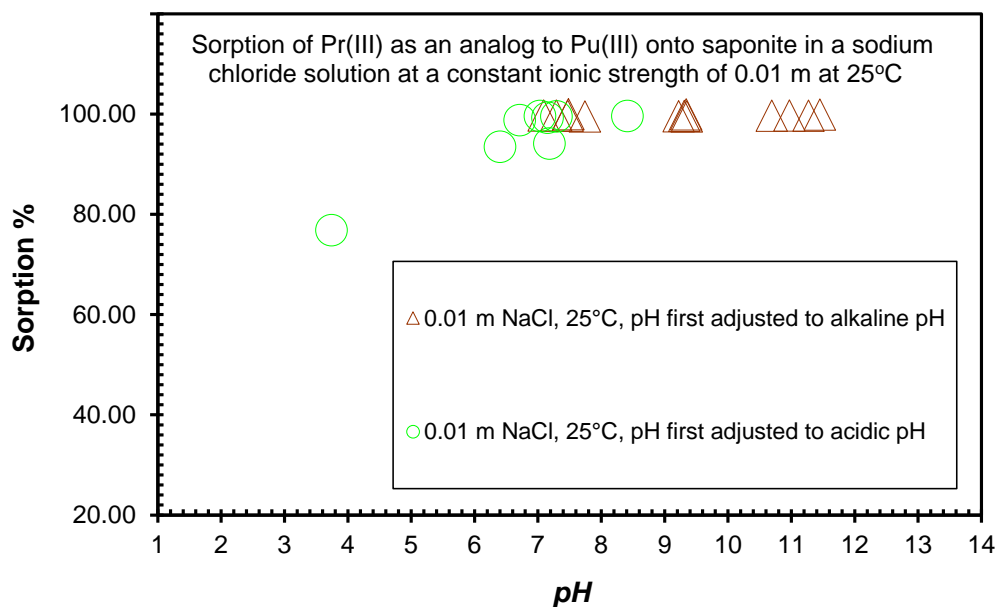


**Figure 10-10.** Sorption of Pr(III) onto the natural saponite as a function of pH in 0.01 mol•kg<sup>-1</sup> NaCl at 25°C.

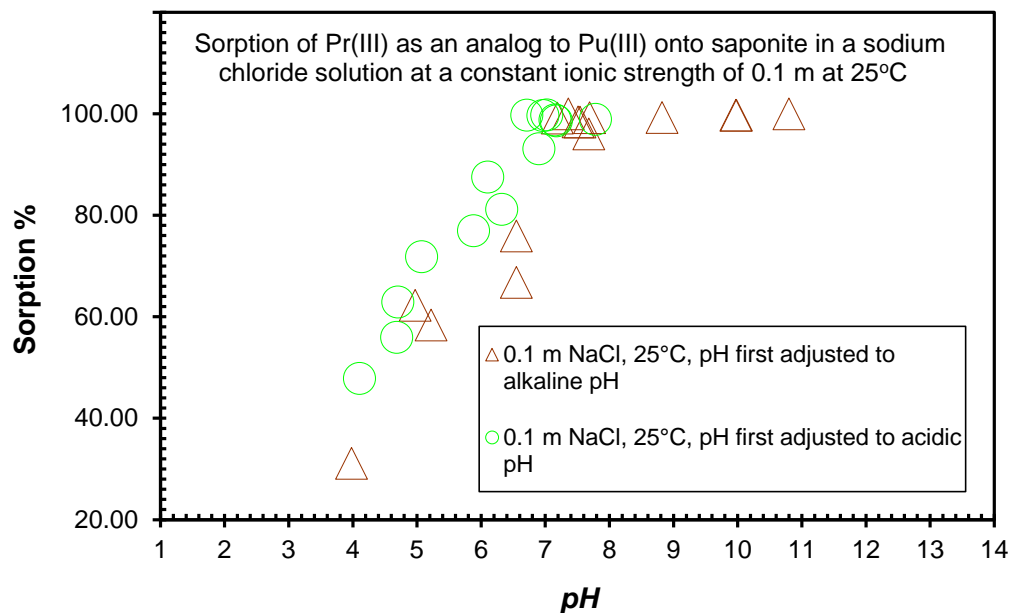


**Figure 10-11.** Sorption of Pr(III) onto the natural saponite as a function of pH in 0.1 mol•kg<sup>-1</sup> NaCl at 25°C.

## 10.4 Conclusions

In this study, we have investigated the stability of Mg-rich saponite in alkaline solutions saturated with portlandite at 60°C and 150°C. In the temporal evolution of a geological repository, the stage in which the porewater is in equilibrium with portlandite is expected to last very long, up to 200,000 years (e.g., Sun et al., 2020). Hence, the experimental objective of this work is to investigate the stability of saponite at this stage. Our results suggest that Mg-rich saponite is stable in alkaline solutions at these temperatures. In contrast, montmorillonite is not stable in interactions with the alkaline solutions saturated with portlandite at 150°C, as indicated by the appearance of zeolite when the experimental duration was 9 days. Therefore, it is expected that saponite will be stable under two of the harsh chemical conditions—high temperatures and high pH's introduced by concrete and cement buffers, seals, liners, and plugs. Consequently, saponite offers a strong candidate for buffer materials under harsh conditions. In addition, our sorption experiments with Pr(III) shows that saponite can also be an excellent adsorbent for cationic radionuclides, especially trivalent actinides. We are going to investigate the stability and sorption capability of saponite under other harsh geochemical conditions such as high ionic strength brines which may not be as harsh as high pH conditions.

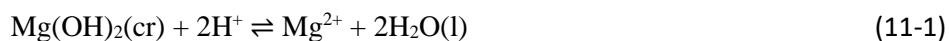
## 11.0 USING MACHINE LEARNING TO PREDICT BRØNSTED-GUGGENHEIM-SCATCHARD SPECIFIC ION INTERACTION THEORY (SIT) COEFFICIENTS

### 11.1 Introduction

The behaviors of high ionic strength solutions are of interest in many fields, including geological nuclear waste disposal. For instance, at the Waste Isolation Pilot Plant (WIPP), an operational geologic repository for defense-related transuranic waste, the two representative brines important for the performance assessment (PA), Energy Research and Development Administration Well 6 (ERDA-6) and Generic Weep Brine (GWB), have ionic strengths of 5.82 and 8.26 mol•kg<sup>-1</sup> (Xiong and Lord, 2008), respectively. In the field of hydrochemistry, in salt lakes such as those in the Qinghai-Xizang Plateau (Zheng and Liu, 2009), the brines have ionic strengths up to ~6 mol•kg<sup>-1</sup> (Xiong and Cetiner, 2017). In general, for solutions with ionic strength above ~0.7, the extended Debye-Huckel equation may no longer be valid for estimating the activity coefficients of aqueous species, and other electrolyte theories may need to be used.

Brønsted-Guggenheim-Scatchard specific interaction theory (SIT) is a model for the calculation of activity coefficients of aqueous species in moderate to high ionic strength solutions (e.g., Xiong, 2006), similar to the Pitzer model (e.g., Li and Duan, 2007). SIT is useful in geochemical applications, and several examples are provided in Xiong (2006). In the Nuclear Energy Agency (NEA) review series for chemical elements relevant to nuclear energy (e.g., Gamsjager et al., 2005; Hummel et al., 2005), the SIT model is adopted for extrapolation of thermodynamic parameters at certain ionic strengths to an infinite dilution reference state. Although the SIT model is useful in numerous fields, the limited SIT interaction coefficient database restricts its more wide-spread usage. This is because SIT interaction parameters are empirical and derived from experimental data. Therefore, it is highly desirable to estimate SIT interaction parameters from the fundamental properties of chemical species.

The interaction coefficient between two ionic solute species,  $\epsilon$ , is a key parameter in SIT models. For instance, the specific interaction coefficients are needed to calculate equilibrium coefficients at certain ionic strengths or equilibrium constants at infinite dilution, as illustrated by the dissolution reaction of brucite in NaCl solutions shown below (taken from Xiong, 2006; Kirkes and Xiong, 2018),



$$Q_{s2} = \frac{m_{\text{Mg}^{2+}}}{(m_{\text{H}^+})^2} \quad (11-2)$$

$$\log_{10} K_{s2}^0 = \log_{10} Q_{s2} - 2D + \epsilon(\text{Mg}^{2+}, \text{Cl}^-)I_m - 2\epsilon(\text{H}^+, \text{Cl}^-)I_m + 2\log_{10} a_{\text{H}_2\text{O}} \quad (11-3)$$

where  $\log K_{s2}^0$  is an equilibrium coefficient constant at infinite dilution for Reaction (1) at infinite dilution;  $\log Q_{s2}$  an equilibrium coefficient for Reaction (1) at certain ionic strengths;  $D$  the Debye-Hückel term defined by the following equation;  $I_m$  ionic strength on a molal scale;  $a_{\text{H}_2\text{O}}$  activity of water,

$$D = \frac{A_\gamma \sqrt{I_m}}{1 + 1.5 \times \sqrt{I_m}} \quad (11-4)$$

where  $A_\gamma$  is the Debye-Hückel slope for activity coefficient.

SIT interaction parameters are often evaluated from mean activity coefficients of an electrolyte. For instance, the relation between mean activity coefficients of HCl and its SIT interaction coefficient  $\varepsilon(\text{H}^+, \text{Cl}^-)$  can be cast as follows (Xiong, 2006),

$$\text{Log } \gamma_{\pm, \text{HCl}} + D = \varepsilon(\text{H}^+, \text{Cl}^-) m_{\text{HCl}} \quad (11-5)$$

where  $\log \gamma_{\pm, \text{HCl}}$  is mean activity coefficient of HCl at a certain molality;  $D$  the Debye-Hückel term defined in Equation (4);  $m_{\text{HCl}}$  molality of HCl. Therefore, by plotting  $m_{\text{HCl}}$  versus  $\log \gamma_{\pm, \text{HCl}} + D$ , the slope is  $\varepsilon(\text{H}^+, \text{Cl}^-)$  (Xiong, 2006).

Though experimental data exists for  $\varepsilon$  for various pairs of species, there is intensive interest in developing models for  $\varepsilon$  for pairs of species where experimental data may prove more challenging, such as for elevated temperature and pressure conditions. Ideally, a model for  $\varepsilon$  would be able to predict/estimate the interaction parameters between any two species, based on the current understanding of these behaviors, and bypass the need for exhaustive experimental studies, though experimental investigations may be still needed for further calibrations and improvement of the model. Development of wider-ranging SIT parameter data will expand the applicability of SIT.

Artificial neural networks (ANNs) are considered to be a universal approximator to any continuous functions, either linear or nonlinear (Hornk et al., 1989) and therefore would be able to retrieve the underlying correlations between the output and the input of a system from experimental measurements (Hsieh, 2000; Jain et al. 1996). An extensive multidisciplinary review of available literature found over 500 applications for ANNs across 18 categories of research (Abiodun et al., 2018). In the field of environmental sciences, for example, an ANN has been implemented to improve modeling of regional particulate matter levels and found advantageous over the use of multiple linear regression (Zhong et al., 2021). In chemical applications, ANNs have been used to model  $\text{CO}_2$  solubility in salt solutions (Jeon and Lee, 2021), the thermal conductivity of electrolyte solutions (Eslamloueyan et al., 2011), and electrolyte/amino acid solution activity coefficients (Dehghani et al., 2006). Additionally, there are clear applications to reactive transport modeling (Prasianakis et al., 2020), and potential applications in radioactive waste disposal research (Ben-Haim and MacDonald, 1994). It would appear, therefore, that ANNs have the potential to provide insight into expected ion interaction behaviors.

The primary aim of this study is to model the SIT interaction parameter,  $\varepsilon$ , by developing ANNs based on literature data for chemical characteristics of pairs of species at various conditions. In so doing, we will provide a basis for further chemical and geochemical applications, particularly for use in geologic nuclear waste disposal research.

## 11.2 Methodology

### 11.2.1 Data Selection and Database Preparation

The database used for this study comprises electrochemical data and interaction parameters for numerous species, selected from the literature (Gamsjager et al., 2005; Xiong, 2006; Xiong, 2010; Xiong, 2009; Xiong et al., 2013; Xiong, 2014). Among them, the primary source for the SIT interaction coefficients is Xiong (2006), which is currently the only source that covers not only a wide range of species but also both temperature and pressure effects on the SIT interaction coefficients. The interaction coefficients at high

temperatures as well as those at 25°C in Xiong (2006) have been adopted by other researchers (e.g., Jordan et al., 2022). Selection was based on completeness of available data. A total of 229 unique entries without duplicates were chosen, which encompass a diverse selection of ion pairings and temperature/pressure conditions.

The species and variables considered for this study are listed in Table 11-1. All listed variables were used in all our models. Data collected from the literature includes temperature (in K), pressure (in bar),  $\epsilon$ , species charge, coordination number, crystal radius (Å), and effective ionic radius (EIR; in Å). For species for which literature did not include an EIR value, a value was estimated by taking the average of unique entries for the EIR from the unedited, larger collection of literature data (Shannon, 1976). The same procedure was used to fill in values for crystal radius and coordination number, as the literature that included  $\epsilon$  did not include measurements for either parameter. Crystal radii for  $\text{Ox}^{2-}$  and derivatives,  $\text{EDTA}^{4-}$  and derivatives,  $\text{NO}_3^-$ ,  $\text{SO}_4^{2-}$ ,  $\text{IO}_3^-$ ,  $\text{ClO}_4^-$ ,  $\text{Tl}^+$  ions and  $\text{Pb}^{2+}$  were approximated as being equal to the effective ionic radii of those species. The crystal radius and electronegativity of  $\text{PbNO}_3^+$  were approximated as being equal to those of  $\text{Pb}^{2+}$ . The radii of organic ligands were approximated as equal to those of acetate (online database from Wired Chemist, 2022). Additional data relevant to the interacting species (NCBI, 2021) included molar masses (AMU), and cation electronegativity (Pauling scale). A value for the electronegativity of europium was estimated by applying a linear fit to the available electronegativities of the lanthanide series (NCBI, 2021; linear fit  $R^2=0.994$ ).

**Table 11-1.** List of species and available variables included in the final database used for modeling.

Ionic Species			Variables
<i>Cations</i>			<i>Condition Variables</i>
<b>Ag<sup>+</sup></b>	<b>Eu<sup>3+</sup></b>	<b>Na<sup>+</sup></b>	$\epsilon$
<b>Al<sup>3+</sup></b>	<b>Fe<sup>3+</sup></b>	<b>Ni<sup>2+</sup></b>	
<b>Am<sup>3+</sup></b>	<b>Gd<sup>3+</sup></b>	<b>Pb<sup>2+</sup></b>	Temp (K)
<b>Ba<sup>2+</sup></b>	<b>H<sup>+</sup></b>	<b>PbNO<sub>3</sub><sup>+</sup></b>	
<b>Ca<sup>2+</sup></b>	<b>Hg<sup>2+</sup></b>	<b>Sm<sup>3+</sup></b>	Pressure (bar)
<b>Co<sup>2+</sup></b>	<b>K<sup>+</sup></b>	<b>Sr<sup>2+</sup></b>	
<b>Cr<sup>3+</sup></b>	<b>La<sup>3+</sup></b>	<b>Th<sup>4+</sup></b>	<i>Species Variables</i>
<b>Cs<sup>+</sup></b>	<b>Li<sup>+</sup></b>	<b>Tl<sup>+</sup></b>	Charge
<b>Cu<sup>2+</sup></b>	<b>Mg<sup>2+</sup></b>	<b>Tl<sup>3+</sup></b>	
<b>Cu<sup>+</sup></b>	<b>Mn<sup>2+</sup></b>	<b>Zn<sup>2+</sup></b>	Effective Ionic Radius (Å)
<i>Anions</i>			
<b>Br<sup>-</sup></b>	<b>H<sub>3</sub>EDTA<sup>-</sup></b>	<b>OH<sup>-</sup></b>	Coordination Number
<b>Cl<sup>-</sup></b>	<b>HEDTA<sup>3-</sup></b>	<b>Ox<sup>2-</sup></b>	
<b>ClO<sub>4</sub><sup>-</sup></b>	<b>HOx<sup>-</sup></b>	<b>Pb(Ox)<sub>2</sub><sup>2-</sup></b>	Molar Mass (AMU)
<b>EDTA<sup>4-</sup></b>	<b>I<sup>-</sup></b>	<b>SO<sub>4</sub><sup>2-</sup></b>	
<b>F<sup>-</sup></b>	<b>IO<sub>3</sub><sup>-</sup></b>		Crystal Radius (Å)
<b>H<sub>2</sub>EDTA<sup>2-</sup></b>	<b>NO<sub>3</sub><sup>-</sup></b>		
			Electronegativity (Pauling scale) [cations only]

## 11.2.2 Software

Preliminary database preparation required to compile the database was done using Microsoft Excel and the R statistical analysis code (R Core Team, 2021). Machine learning simulations were done using the Python scripting language, version 3.9 (Python Software Foundation, 2021; Chollet, 2017). Key Python libraries used for this work included sklearn, seaborn, nnv, and tensorflow.

## 11.2.3 Machine Learning Methodology

The unsupervised and supervised machine learning methods of choice were K-means clustering and neural networks, respectively. Prior to use in modeling, all parameters in the database were normalized to avoid specific parameter magnitudes from a biased influence on the results.

The K-means algorithm can group data into K number of clusters. The utility of cluster designation is that, based on a set of parameters for any given point, that an input can be used to identify a range of possible  $\epsilon$  that is bounded by points with similar characteristics. Pre-processing for K-means clustering includes principal component analysis (PCA). User judgement determines an adequate or representative number of clusters K, ideally where clusters are distinct and have little to no overlap. Clusters are assigned from the PCA, based on the Euclidean distances between points and distances from the centroids. The number of clusters selected for this work was 5; that is, the K-means algorithm was used to assign each entry in the database a class value from 0 to 4.

We developed neural network models that could easily be modified (by adding layers, adding/subtracting nodes, and/or changing functions and optimization methods), evaluated, and reused. Two networks were used. Model I was used to validate neural network against K-means clustering by comparing class assignments produced by the two. Model II was used to predict  $\epsilon$  outright. In both models, the dataset was split into training and testing datasets to validate the networks. The Model I network used 80% of the data for testing and 20% for validation. In Model II, 20% of the overall data was kept to model with after the network was built. The remaining 80% of the data was split 80/20 for testing/validation by the algorithm, respectively (Chollet 2017). Each run of each model includes reinitialization of the network and redistribution of the data between testing and validation datasets.

Figure 11-1 is a visualization of the neural network that was used for Model I. The input layer takes data with 14 dimensions and distributes it to ten neurons and has the activation function Relu. The second layer has eight neurons and the Relu activation function. The output layer has the activation function Softmax

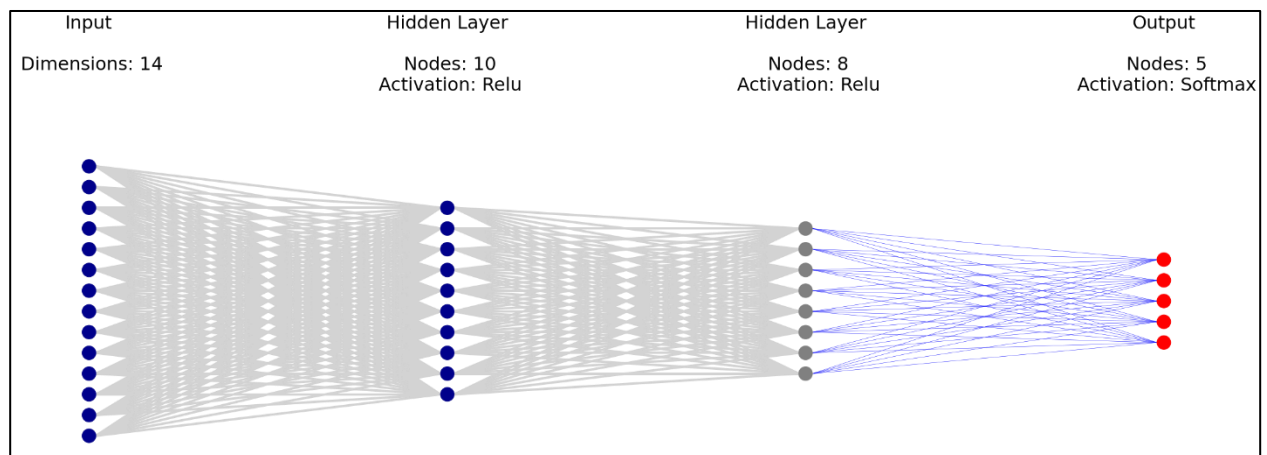


**Figure 11-1.** Visualization of the neural network used for

and has five neurons (one for each possible cluster). The optimization function in the model was Adam, and the loss function was Categorical Crossentropy. As before, the model was trained for 100 epochs.

Figure 11-2 is a visualization of the primary neural network structure that was used for Model II. The input layer has 14 neurons. There are two hidden layers; the first hidden layer has 64 neurons, and the second has 32 neurons. The activation function of choice was Relu (Rectified Linear Unit). The output has one neuron. The model was trained for 100 epochs. The optimization and loss functions were Adam and Mean Absolute Error, respectively.

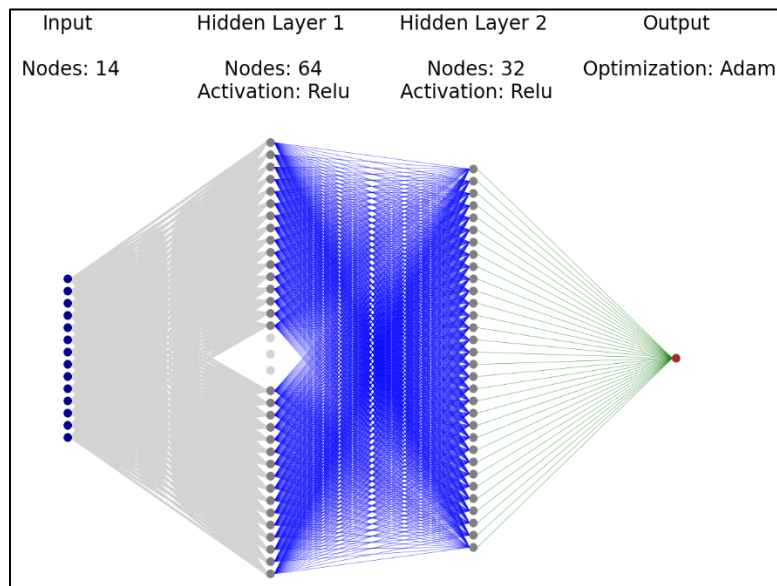


Figure 11-2. Visualization of the neural network used for Model II.

## 11.3 Results and Discussion

### 11.3.1 Unsupervised Machine Learning via K-Means Clustering

The K-means clustering algorithm successfully clustered the input data into five distinct groups (Classes). The clusters formed are shown in Figure 11-3, and the range of  $\epsilon$  included in each cluster are listed in Table 11-2. Apparent distinctions among the clusters are observed with very little overlap, indicating similarity between the points in an individual cluster. The ranges of  $\epsilon$  are most narrow in in classes 1-3. Some ion pairings appear in more than one cluster, owing to different principal components derived from different experimental condition data.

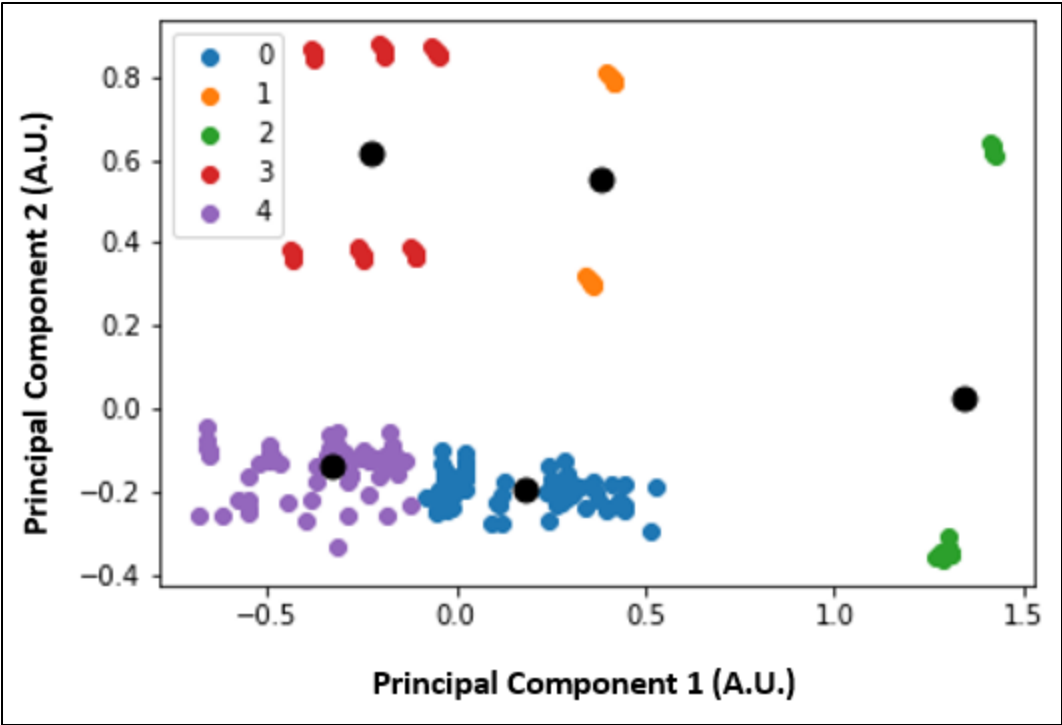


Figure 11-3. Data clusters formed via K-means algorithm, based on principal components derived with sklearn.

**Table 11-2.** Ranges of  $\epsilon$  and included ion pairings for each of the classes clustered with the K-means algorithm.

	<b>Class 0</b>	<b>Class 1</b>	<b>Class 2</b>	<b>Class 3</b>	<b>Class 4</b>	
Lowest $\epsilon$	-0.28	0.078	0.0444	0.0299	-0.77	
Highest $\epsilon$	0.56	0.235	0.14	0.175	0.4950	
<b>Ion Pairings</b>	(Ag <sup>+</sup> , Cl) (Ag <sup>+</sup> , ClO <sub>4</sub> ) (Ag <sup>+</sup> , NO <sub>3</sub> ) (Al <sup>3+</sup> , Cl) (Co <sup>2+</sup> , Cl) (Co <sup>2+</sup> , ClO <sub>4</sub> ) (Cr <sup>3+</sup> , Cl) (Cr <sup>3+</sup> , NO <sub>3</sub> ) (Cu <sup>2+</sup> , Cl) (Cu <sup>+</sup> /Cu <sup>2+</sup> , ClO <sub>4</sub> ) (Cu <sup>2+</sup> , NO <sub>3</sub> ) (Fe <sup>3+</sup> , ClO <sub>4</sub> ) (Fe <sup>3+</sup> , NO <sub>3</sub> ) (Hg <sup>2+</sup> , Cl) (Li <sup>+</sup> , Br) (Li <sup>+</sup> , Cl) (Li <sup>+</sup> , ClO <sub>4</sub> ) (Li <sup>+</sup> , I) (Li <sup>+</sup> , OH) (Li <sup>+</sup> , SO <sub>4</sub> <sup>2-</sup> ) (Mg <sup>2+</sup> , Br) (Mg <sup>2+</sup> , Cl) (Mg <sup>2+</sup> , ClO <sub>4</sub> )	(Mg <sup>2+</sup> , I) (Mg <sup>2+</sup> , IO <sub>3</sub> ) (Mg <sup>2+</sup> , NO <sub>3</sub> ) (Mn <sup>2+</sup> , Cl) (Na <sup>+</sup> , Br) (Na <sup>+</sup> , Cl) (Na <sup>+</sup> , ClO <sub>4</sub> ) (Na <sup>+</sup> , EDTA <sup>4-</sup> ) (Na <sup>+</sup> , F) (Na <sup>+</sup> , H <sub>2</sub> EDTA <sup>2-</sup> ) (Na <sup>+</sup> , H <sub>3</sub> EDTA) (Na <sup>+</sup> , HEDTA <sup>3-</sup> ) (Na <sup>+</sup> , Hox) (Na <sup>+</sup> , I) (Na <sup>+</sup> , IO <sub>3</sub> ) (Na <sup>+</sup> , OH) (Na <sup>+</sup> , Ox <sup>2-</sup> ) (Na <sup>+</sup> , SO <sub>4</sub> <sup>2-</sup> ) (Ni <sup>2+</sup> , Cl) (Ni <sup>2+</sup> , NO <sub>3</sub> ) (Zn <sup>2+</sup> , Cl) (Zn <sup>2+</sup> , ClO <sub>4</sub> ) (Zn <sup>2+</sup> , NO <sub>3</sub> )	(Mg <sup>2+</sup> , Cl)	(H <sup>+</sup> , Cl) (H <sup>+</sup> , ClO <sub>4</sub> ) (H <sup>+</sup> , NO <sub>3</sub> )	(Ba <sup>2+</sup> , Cl) (Ca <sup>2+</sup> , Cl) (Sr <sup>2+</sup> , Cl)	(Am <sup>3+</sup> , Cl) (Am <sup>3+</sup> , ClO <sub>4</sub> ) (Ba <sup>2+</sup> , Cl) (Ba <sup>2+</sup> , ClO <sub>4</sub> ) (Ba <sup>2+</sup> , NO <sub>3</sub> ) (Ba <sup>2+</sup> , OH) (Ca <sup>2+</sup> , Cl) (Ca <sup>2+</sup> , ClO <sub>4</sub> ) (Ca <sup>2+</sup> , NO <sub>3</sub> ) (Cs <sup>+</sup> , OH) (Eu <sup>3+</sup> , Cl) (Eu <sup>3+</sup> , ClO <sub>4</sub> ) (Gd <sup>3+</sup> , Cl) (Gd <sup>3+</sup> , ClO <sub>4</sub> ) (K <sup>+</sup> , Br) (K <sup>+</sup> , Cl) (K <sup>+</sup> , F) (K <sup>+</sup> , I) (K <sup>+</sup> , IO <sub>3</sub> ) (K <sup>+</sup> , OH) (K <sup>+</sup> , Ox <sup>2-</sup> ) (K <sup>+</sup> , Pb(Ox) <sub>2</sub> <sup>2-</sup> ) (K <sup>+</sup> , SO <sub>4</sub> <sup>2-</sup> ) (La <sup>3+</sup> , Cl) (La <sup>3+</sup> , ClO <sub>4</sub> ) (La <sup>3+</sup> , Ox <sup>2-</sup> ) (Pb <sup>2+</sup> , Cl) (Pb <sup>2+</sup> , ClO <sub>4</sub> ) (Pb <sup>2+</sup> , NO <sub>3</sub> ) (PbNO <sub>3</sub> , NO <sub>3</sub> ) (Sm <sup>3+</sup> , Cl) (Sm <sup>3+</sup> , ClO <sub>4</sub> ) (Sr <sup>2+</sup> , Cl) (Sr <sup>2+</sup> , OH) (Th <sup>4+</sup> , Cl) (Th <sup>4+</sup> , NO <sub>3</sub> ) (Tl <sup>+</sup> , Cl) (Tl <sup>+</sup> , ClO <sub>4</sub> ) (Tl <sup>+</sup> , I) (Tl <sup>+</sup> , NO <sub>3</sub> ) (Tl <sup>+</sup> , SO <sub>4</sub> <sup>2-</sup> )

### 11.3.2 Supervised Machine Learning via Neural Network

#### Model I

The neural network algorithm was successful in assigning a Class to each entry in the test dataset of 46 data points. The model was run 100 times to assess the variability that occurs when data is split differently across the training and test datasets at random. Figure 11-4 shows the distribution of accuracies achieved in these iterations (runs) when validated against the K-means algorithm. An accuracy of 100% indicates that the neural network assigned all 46 points into the same Classes as the K-means algorithm did. The model accurately categorized over 80% of the test data, in 90 out of 100 runs. Accuracy never fell below 70%. An accuracy of 100% was achieved in two of the 100 runs.

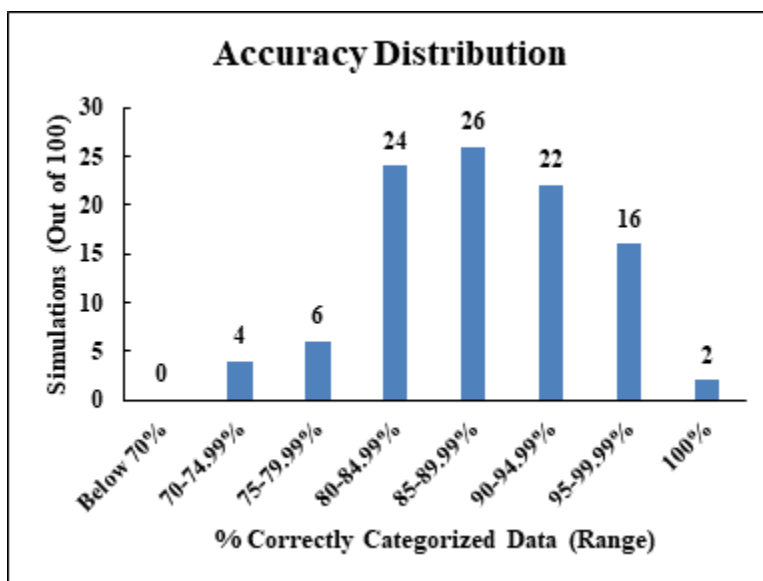


**Figure 11-4.** Distribution of accuracy ranges achieved by the Model I neural network when attempting to categorize test data identically to the K-means algorithm in 100 iterations.

The sensitivity of Model I to the network structure was assessed by varying the number of nodes in each of the hidden layers. The base model has 10 and 8 nodes in each layer, respectively (Network 1). Two alternate models were tested: one with 9 and 7 nodes, respectively (Network 2), and another with 11 and 9 nodes, respectively (Network 3). As before, the neural network was run 100 times for each of these alternate structures.

Figure 11-5 shows the distribution of accuracies achieved in these runs. T-tests comparing the means of these structures (type 2, two-tailed, 95% significance) indicate that the mean MAEs of Networks 1 and 3 are not significantly statistically different. Network 2 introduces a higher incidence of outliers and a lower mean accuracy than the other two structures. These results could indicate that the sensitivity of the problem to the sizes of the hidden layers has a limit. That is, additional complexity appears to increase mean accuracy, but only to a certain extent.

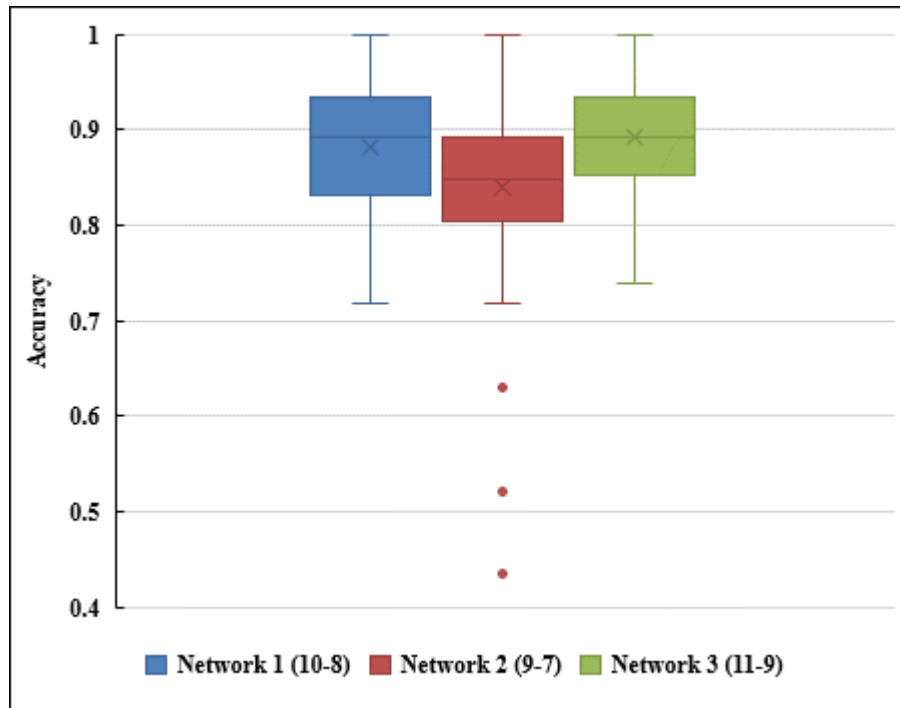


**Figure 11-5.** Box-and-whisker plot of accuracy achieved by three Model I neural network structures with different numbers of neurons in the hidden over 100 iterations.

## Model II

The neural network algorithm successfully developed a model for the SIT interaction parameter,  $\varepsilon$  from the training dataset based on the normalized database. Results for the mean absolute error in the model vary from run to run, and, as such, the results of predictions of the testing data vary as well.

Model II was run 100 times for each of three network structures. The base model (Network 1) has 64 and 32 nodes in each hidden layer, respectively. Network 2 has 32 and 16 nodes, and Network 3 has 16 and 8 nodes, respectively. The mean absolute error (MAE) of each run was treated as an analogue for accuracy; the lower the MAE, the more accurate the predictions made by that model are overall.

The results of these runs are summarized in Figure 11-6. T-tests comparing the means of these structures (type 2, two-tailed, 95% significance) indicate that the mean MAEs of the three networks are likely to be statistically different. There is an observable increase in the possible values and broader range of MAE if the network is simplified. The more robust structure provides a smaller range of, and smaller values for, MAE. The model appears to be highly sensitive to the number of nodes in the hidden layers.

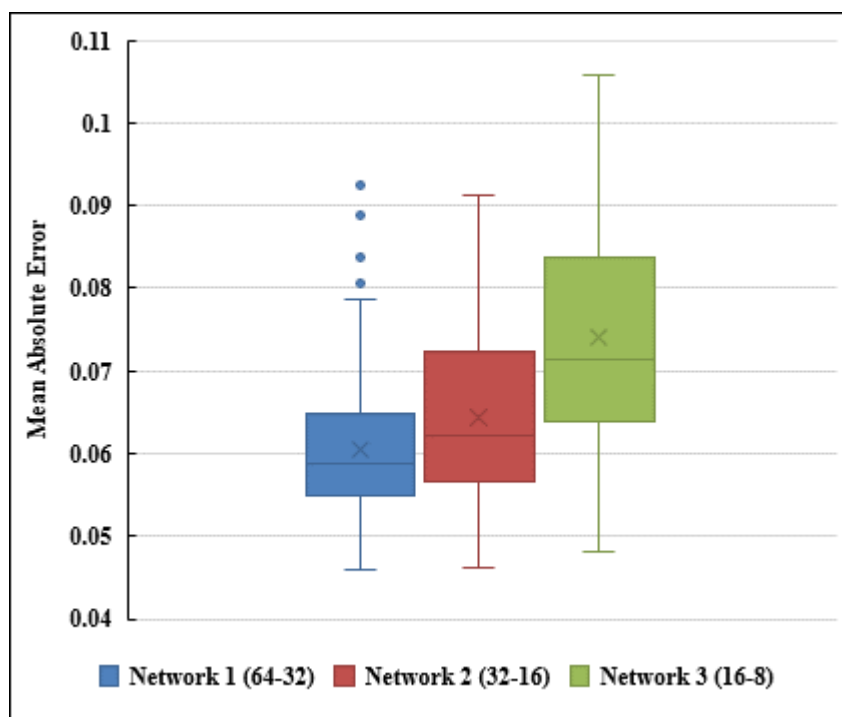


**Figure 11-6.** Box-and-whisker plot of MAE (normalized  $\epsilon$  scale) achieved by three neural network structures of Model II with different numbers of neurons in the hidden layers over 100 iterations.

### Model II Parameter Sensitivity: Electrostatic Field

An additional parameter of interest in this work is the electrostatic field (ESF) of the solute ions. This parameter is not measured directly but is rather derived from other measured quantities. ESF (in units of charge/Å) is computed by dividing the absolute value of the charge by the absolute value of the effective ionic radius, for each species. While mathematically related to these quantities, the physical significance of the ESF is distinct, and thus may affect the ability of the neural networks to predict  $\epsilon$ .

The ESF was computed for each cation and anion in each entry of the database, then included in the overall parameters fed to Network 1 of Model II to predict values of  $\epsilon$ . The model was run 100 times as described previously. As before, the mean absolute error was used as an analogous metric to accuracy. MAE values resulting from the model containing ESF entries were compared against the previously shown results for Model II Network 1.

The results of these runs are summarized in Figure 11-7. The inclusion of the ESF for solute ions produces a higher average MAE, which means accuracy has been lost. A type 2, two-tailed T-test comparing the means of the two models at 95% significance produces a p-value of 6.82E-20. This indicates that the mean MAEs of the two models are likely to be statistically significantly different. Thus, the accuracy of the Model II approach appears to be sensitive to the input parameters of choice.

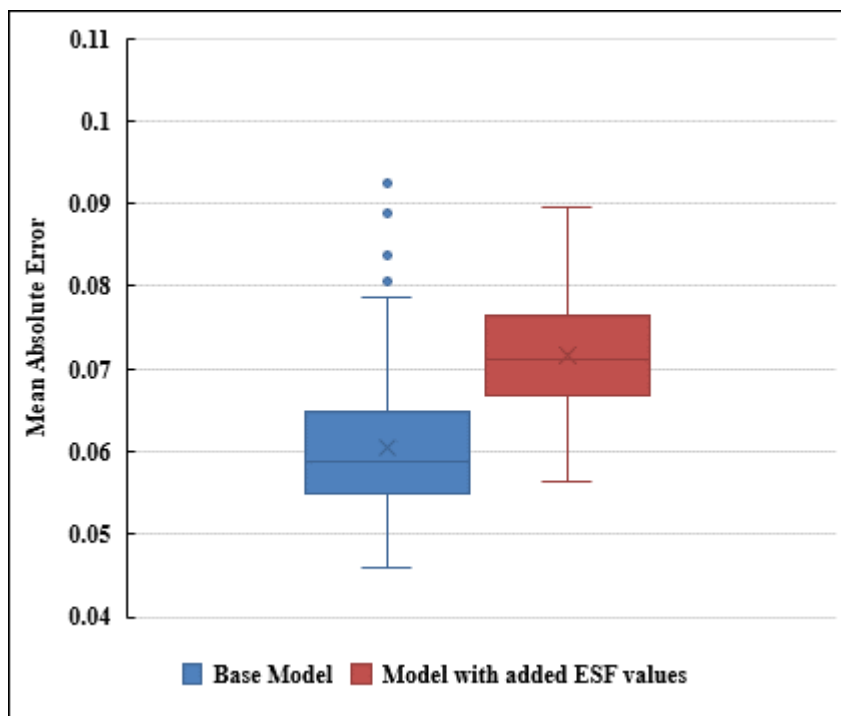


**Figure 11-7.** Box-and-whisker plot of MAE (normalized  $\varepsilon$  scale) achieved by Model II networks with and without electrostatic field values, over 100 iterations.

### Model II Verification and Application

The predictions made by Model II were verified against a subset of the literature data. The model was run 50 times to predict the interaction between  $\text{Na}^+$  and  $\text{Cl}^-$  at eight temperature/pressure conditions (starting at 275.15 K at 1 bar, up to 475.15 K at 15.55 bar). The base, two-layer network with 64 and 32 nodes, respectively, was used. The mean absolute error for the 50 networks produced averaged to  $0.059 \pm 0.005$ , which is within the expected range shown in Figure 11-6. The results of this test are shown in Figure 11-8A. Actual values of  $\varepsilon$  are within one standard deviation of the prediction for seven of the eight conditions, and within two standard deviations for the remaining point at 298.15 K. This reaffirms the validity of the predictions that can be made with Model II.

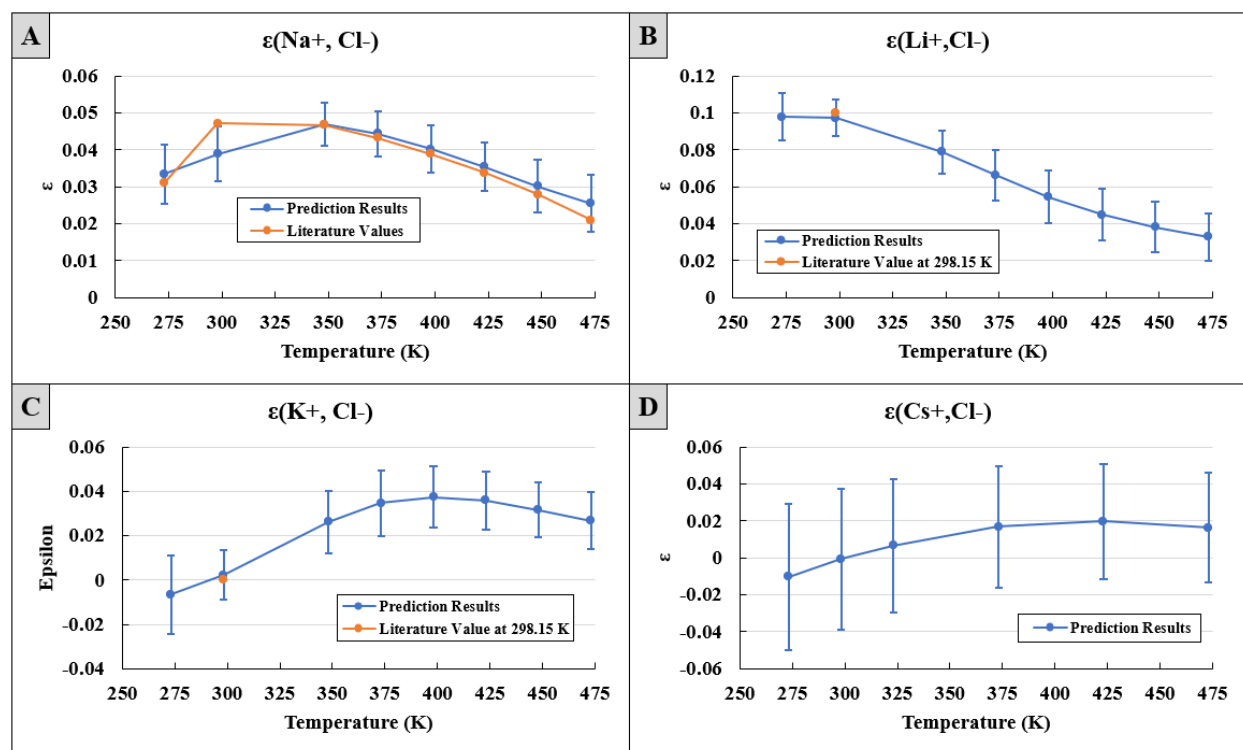


**Figure 11-8.** Predictions of  $\epsilon$  for four pairings of ions as a function of temperature. Predictions were made with 50 iterations of Model II. A)  $\text{Na}^+$  and  $\text{Cl}^-$ . B)  $\text{Li}^+$  and  $\text{Cl}^-$ . C)  $\text{K}^+$  and  $\text{Cl}^-$ . D)  $\text{Cs}^+$  and  $\text{Cl}^-$ .

Model II was then applied to estimate the interaction parameter between  $\text{Cl}^-$  and each of three cations:  $\text{Li}^+$ ,  $\text{K}^+$  and  $\text{Cs}^+$  (Figures 11-8B, 11-8C, 11-8D, respectively). Among them, there are interaction parameters for  $(\text{Li}^+, \text{Cl}^-)$  and  $(\text{K}^+, \text{Cl}^-)$  at 25°C. However, these interactions at high temperatures are not available and so are used to test the ability of the neural network to extrapolate. The  $\text{Cs}^+$  and  $\text{Cl}^-$  interaction is important for nuclear waste disposal, considering the facts of degradation of Cs-waste forms (e.g., Grote et al., 2019; Fang et al., 2022; Wang et al., 2022) but is not currently characterized.

The model was run 50 times for each pairing to predict the interaction at the same eight temperature/pressure conditions (starting at 275.15 K at 1 bar, up to 475.15 K at 15.55 bar). The same network setup as was used for verification was used here. Parameters for each ion were taken from the existing dataset. The mean absolute error for the networks produced averaged to  $0.059 \pm 0.007$ ,  $0.058 \pm 0.007$  and  $0.060 \pm 0.008$ , which were used for  $(\text{Li}^+, \text{Cl}^-)$ ,  $(\text{K}^+, \text{Cl}^-)$ , and  $(\text{Cs}^+, \text{Cl}^-)$  modeling, respectively. These are within the expected range shown in Figure 11-6. The results constrain expected  $\epsilon$  values for  $\text{Cs}^+$  and  $\text{Cl}^-$ , however they do not reflect an expected downtrend with increasing temperature for  $(\text{Na}^+, \text{Cl}^-)$  (Xiong, 2006). In contrast, the interaction parameters for  $(\text{Li}^+, \text{Cl}^-)$  as a function of temperature follow the temperature function trend defined by that for  $(\text{Na}^+, \text{Cl}^-)$ . Therefore, the above predicted results may provide the opportunity for further experimental studies to find out whether there is a cascade effect in terms of temperature functions for the interactions of alkali metal ions with chloride.

Another example of applications is to estimate solubilities of portlandite  $[\text{Ca}(\text{OH})_2(\text{s})]$  in  $\text{LiCl}$  solutions in comparison with experimental data. The solubility of portlandite in  $\text{LiCl}$  solutions is of interest in nuclear waste management, because portlandite is used in engineered barrier systems in geological repositories, and

LiCl waste is generated in electrochemical reprocessing of spent nuclear fuel (e.g., Xiong, 2016; Herrmann et al., 2022). The dissolution of portlandite can be cast as follows,



The equilibrium quotient for Reaction (11-6) in LiCl solutions is expressed as

$$\log_{10} Q_{sp} = \log_{10} K_{sp}^0 + 6D - \varepsilon(\text{Ca}^{2+}, \text{Cl}^-)I_m - 2\varepsilon(\text{Li}^+, \text{OH}^-)I_m \quad (11-7)$$

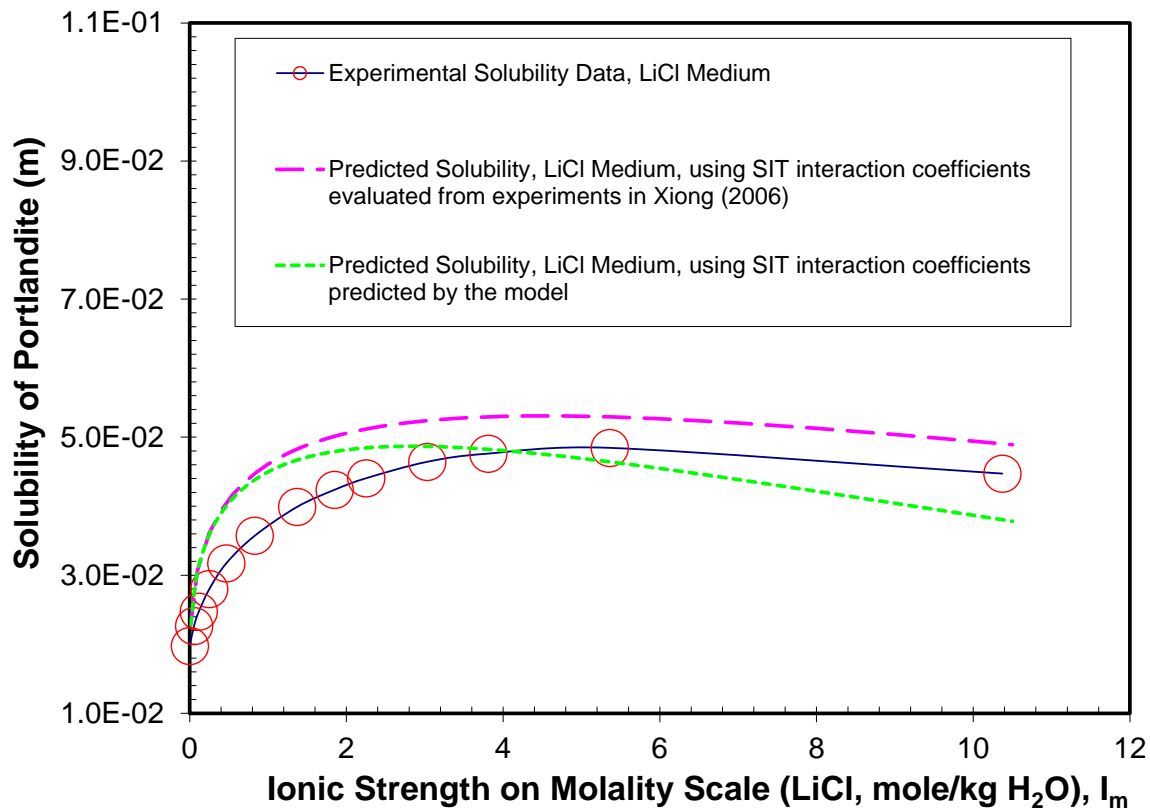


**Figure 11-9.** Predicted solubilities of portlandite in LiCl solutions at 25°C in comparison with the experimental solubilities at the same temperature. The experimental solubility data in LiCl solutions at 25°C are from Johnson and Grove (1931).

In Figure 11-9, the predicted solubilities of portlandite in LiCl solutions at 25°C are compared with the experimental data at the same temperature from Johnson and Grove (1931). The experimental data are represented by open circles with a connecting solid line. The values predicted using the SIT parameters evaluated from experimental data from Xiong (2006) are shown by the long-dashed line. The values predicted by the SIT interaction coefficients generated by the model in this study are illustrated by the short-dashed line. The SIT interaction parameters for  $\text{Ca}^{2+}\text{---Cl}^-$  and  $\text{Li}^+\text{---OH}^-$  generated by the model are listed in Tables B-3 and B-4 in Supplementary Materials. The values predicted by both sets of the SIT coefficients are close to the experimental values. The solubility curve predicted by the set of the SIT coefficients evaluated from experimental data in Xiong (2006) follows the curvature of the solubility curve defined by the experimental data over the entire ionic strength range. However, the curvature of the solubility curve predicted by the set of the SIT parameters generated by the model follows that defined by experimental data below  $I = \sim 1.5$  molal but deviates above  $I = \sim 1.5$  molal.

## 11.4 Conclusions

This proof-of-concept study highlights the applicability of machine learning methods to the modeling of the SIT parameter  $\epsilon$ . Neural networks were able to successfully model  $\epsilon$  as desired, via both clustering and direct predictions. This will allow for further prediction of behaviors of high ionic strength solutions where empirical data is limited and potentially difficult to obtain.

There is additional capability to model other geochemical parameters via these methods. The applicability of other supervised and unsupervised machine learning methods remains to be assessed but may easily be implemented within the framework presented here. Further work should emphasize collection of additional database entries with complete information for the dimensions of interest, where possible. Entries representative of a greater breadth of ion pairs will expand the ability of these networks to understand chemical phenomena. Additionally, complete data on alternate parameters could allow for further parameter optimization.

## 12.0 SUMMARY

Major accomplishments for FY2023 are summarized below and the evaluation of the current status of each task identified in the SFWST R&D roadmap is provided in Table A-1.

- *Excavation disturbed zone (EDZ) characterization:* The twin-cell triaxial loading system was modified for bentonite sample characterization and bentonite-rock interaction studies. Two sets of experiments were completed on bentonite stacked with a granitic core with a tight and rough fracture embedded under room and elevated temperatures. Water infiltration rate was monitored for permeability evolution. Under the room temperature, the fracture permeability was found to be reduced by 5 orders of magnitude. Images of the fracture surface showed that bentonite hydration caused considerable bentonite particle migration and fracture clogging due to clay swelling. It was shown that the calculated permeability of stacked bentonite-fracture system was close to measured bentonite permeability, indicating that bentonite could maintain good sealing characteristics in the presence of tight (1.3  $\mu\text{m}$  aperture) and rough fractures. After the heating of the system to 90°C, a 65% increase in stacked column permeability was observed, indicating that the bentonite sealing capability was compromised to a certain degree.
- *Downhole characterization of stress and fractures:* Direct downhole measurements were performed for flow, pressure, and displacement evolution during a water injection cycle. The data analyses were also performed using both inversion methods and fully coupled hydromechanical forward numerical models. The experimental results highlighted the activation sequence of fractures in crystalline rocks at ~500 m depth in the COSC-1 borehole. It was detected that mainly flat-lying fractures subparallel to foliation opened under variations of the normal effective stress in a slightly reversed stress regime. Fractures first opened at an injection pressure in a range of the sub-vertical minimum principal stress. This opening preceded a reactivation of reverse shear that occurred at higher injection pressure and after several water injection cycles. All tests showed this evolution of fracture activation from mode 1 to a mixed mode as the stimulated water volume increased. Adding a borehole displacement measurement to a standard hydrofracturing or hydraulic tests on pre-existing fractures (HTPF) test allowed for defining an early test period where fracturing mainly depended on the minimum principal stress, and a later test period where the fracture hydromechanical response was more dependent on the triaxial far-field stress tensor. Using the slip vector triggered on fracture plane during this latter period, we estimated for the present case the three principal stresses orientations and magnitudes with a 10-to-20° and a 2-to-14 MPa variation between tests. These are typical ranges of uncertainties in stress magnitude and orientation given by classical HTPF method, likely because of a limited number of tests. The estimated maximum horizontal stress orientation is consistent with the N120° trend deduced from breakouts mapped in the same COSC-1 borehole at greater depths. Displacement measurements also show the strong influence of borehole wall deformation on the onset of fracture activation, and until breakdown pressure. After several fracture reopening cycles, this influence vanishes, and displacements are mainly driven by hydromechanical movements of the fractures. It is found that the borehole wall displacement before the fracturing pressure can be used to estimate intact rock and fracture properties such as the bulk and shear moduli and the fracture normal and shear stiffness. They can also be used to quantify the evolution of these properties during a hydraulic fracturing (HF) test.
- *Understanding thermal-hydrological-mechanical couplings in a single fracture:* Using the numerical manifold method (NMM) model and FLAC3D, we conducted numerical simulations to analyze shearing of intersecting fractures and thermal slip of single fractures for DECOVALEX Task G step 3. It was found that the intersections of fractures did not fundamentally change the shearing of two intersecting fractures if the intersecting angles satisfy certain conditions. A new simplified discrete fracture network (DFN) model was developed to simplify modeling of the slip of fracture networks by

using major path(s). The model was verified based on several examples involving different numbers of major path(s). This new simplified DFN model is promising to serve as a new conceptual model which is complementary to the existing models to characterize DFNs. A parameter sensitivity study was also conducted for thermal slip of fractures. The results suggest that a more refined intrinsic friction angle may affect the shearing behavior of a rough fracture. In addition, the damage of asperities may explain the increased shearing of single rough fractures as observed in the KICT experiment for for DECOVALEX Task G. In addition, using COMSOL Multiphysics™ software, we conducted simulations for DECOVALEX 2023 Task G Step 1a, mechanical case, with solid body deformation only and Step 2a, hydro-mechanical case, with fluid flow in a fracture surrounded by impermeable matrix. For the mechanical only case (Step 1a) an intact uniform resin sample was subjected to axisymmetric and triaxial loading conditions. Stress, strain, and displacement results were obtained for different loading conditions. Comparison of circumferential strain, model results closely match laboratory experimental data for the axisymmetric loading case. For the hydro-mechanical modeling case (Step 2a), a cylindrical uniform resin sample with a single vertical fracture was subjected to triaxial external loading and fluid flow. The fluid flow was introduced to the fracture using a central hole. A COMSOL model was developed to include coupled solid mechanics and Darcy flow. For the current work a selected loading position with respect to the fracture axis was selected. Stress, strain, and displacement results were obtained for the coupled problem. Pressure changes in the fracture between the fluid inlet and outlet were recorded. The results were used to estimate hydraulic aperture and fracture permeability using the Cubic law.

- *Understanding flow, transport, and chemical reactions in fracture networks:* We investigated the effect of multi-scale heterogeneities on flow and transport properties in fracture networks. We modeled flow and transport in fracture networks with varying degrees of fracture-to-fracture aperture heterogeneity and network density to show how changes in these properties could cause the emergence of anomalous flow and transport behavior. If the fracture-to-fracture aperture heterogeneity is increased in sparse networks, velocity fluctuations inhibit high flow rates and therefore solute transport can be delayed. Surprisingly, transport can be slowed even in cases where hydraulic aperture is monotonically increased. As the density of the networks is increased, more connected pathways allow for particles to bypass these effects. There exists a transition behavior where, with relatively few connected pathways in a network, first arrival times of particles are not heavily affected by fracture-to-fracture aperture heterogeneity, but the scaling behavior of the tails is strongly influenced. These results reinforce the importance of considering multi-scale effects in fractured systems and can inform flow and transport processes in both natural and engineered fracture systems and in particular, crystalline rocks. We also investigated the interplay between the geometric features of fracture networks (asperities and intersections) and mineral precipitation and its effect on porosity and permeability changes. Fracture intersections can significantly affect reaction-induced changes in fracture properties and therefore the connectivity of the fractures. This impact likely exceeds the effect(s) of changes of the geometry, and bulk physical and chemical properties. The time scales in an intersecting fracture network are likely to be shorter than would be the case for nearly homogeneous porous media, since local reaction-induced changes in the fracture can have an outsized impact on the flow and transport regime through modifications of the connectivity associated with mineral precipitation and dissolution at or close to fracture intersections.
- *Understanding bentonite erosion, coagulation/flocculation, and clogging in a fractured crystalline rock:* Compacted bentonite clay is a backfill material of choice for deep geological disposal of spent nuclear fuel and high-level nuclear waste in many countries. The natural swelling behavior of the material contributes to its low hydraulic conductivity and self-healing ability. However, the underlying hydration mechanisms that result in bentonite's swelling behavior also make it more likely to erode by both extrusion and free swelling. As such, bentonite free-expansion (i.e. the transition from compacted bentonite to gel/sol structures) and bentonite erosion (i.e. expansion into a flow field) have been studied extensively for decades. Although it has been recognized that the processes are geochemically

reversible, bentonite coagulation/flocculation and its potential impact on fracture clogging has been studied relatively little. Our experimental work has been designed to investigate bentonite erosion, coagulation, and clogging behavior in a fractured crystalline rock under varying temperature, rock materials, rock fracture aperture properties, and bentonite colloid properties. Much of FY23 work was spent assembling experimental apparatus, developing measurement techniques, and optimizing experimental conditions. Preliminary tests on bentonite colloid flocculation, coagulation and clogging were performed using a microfluidic cell. The results show a significant effect of solution chemistry on bentonite flocculation, coagulation and clogging in microchannels of the cell.

- *Understanding gas migration in low-permeability deformable media:* Gas breakthrough and migration across a low-permeability deformable clay layer is of great importance to subsurface systems for nuclear waste disposal and gas (e.g., CO<sub>2</sub>, H<sub>2</sub> or natural gas) storage, as well as for the development of natural gas/oil reservoirs in the geologic history. Experimental observations on gas injection into water saturated compacted bentonite have revealed rich distinct dynamic behaviours of such processes characterized by a short breakthrough period, a low gas saturation degree and a periodic/chaotic variation in gas flow rate, all indicating a channelling nature of the process. Using linear stability analyses, we showed that such channelling could autonomously emerge from the morphological instability of the interface between the injected gas and the compacted bentonite due to local stress concentration, pore dilation, and hydrologic gradient variation. We showed that channel patterns formed as such would possess a fractal geometry, thus providing a new perspective for upscaling the process from small scale laboratory observations to a field scale. We further showed that, once a percolating channel was established, the gas injected would percolate through the channel in a chain of gas bubbles, also due to the interface instability, resulting in periodic/chaotic variations in gas flow rate. Thus, the concept and the model developed in this work predict the key features observed in gas injection experiments and portray a quite different picture for gas percolation in low-permeability deformable media than that traditionally conceived from permeable porous media.
- *Understanding radionuclide interactions with engineered and natural materials:* We initiated experiments to identify radionuclide interactions with hydrothermally altered buffer materials. Recent research performed at LANL and SNL has provided key insights regarding the hydrothermal alteration behavior of bentonite backfill in the presence of repository materials (steel, concrete, etc.). We are now examining how mineral alteration affects retardation behavior of plutonium and a suite of other radionuclides. These experiments will allow us to test the predictive ability of our component additivity approach to surface complexation and ion exchange. Our preliminary experimental result indicates a possible impact of material heating on radionuclide uptake by bentonite. Observed changes in radionuclide adsorption after bentonite heating have implications for radionuclide diffusive transport through engineered barriers and must be considered when designing waste disposal repositories. We showed that the model developed in this work was able to automate a simulation workflow for modeling sorption phenomena. Therefore, it is made possible to examine a large number of surface complexation (SCM) constructs for obtaining the best quality model which can reproduce experimental data. Follow up studies were conducted to analyze the sorption phenomena of selenium to various iron oxides. Since the developed framework is readily expandable (as community data increase) and extensible (as the number of minerals increase), the framework can be easily applied to other sorption system of interest.
- *Development of new generation buffer materials for high temperature and high pH environments:* Saponite, a tri-octahedral smectite with an ideal formula of Mg<sub>3</sub>(Si, Al)<sub>4</sub>O<sub>10</sub>(OH)<sub>2</sub>•4H<sub>2</sub>O for an Mg-end member (saponite-15Å), has similar swelling properties as montmorillonite. In FY22, we investigated the stability of Mg-rich saponite in alkaline solutions saturated with portlandite at 60°C and 150°C. Our results suggest that Mg-rich saponite is stable in alkaline solutions at these temperatures. In contrast, montmorillonite is not stable in interactions with the alkaline solutions saturated with

portlandite at 150°C, as indicated by the appearance of zeolite when the experimental duration was 9 days. Therefore, saponite offers a strong candidate for buffer materials under harsh conditions. In FY23, we further showed that saponite could also be an excellent adsorbent for cationic radionuclides, especially trivalent actinides. Our sorption experiments with Pr(III) as a chemical analog to Pu(III) showed that saponite had a sorption capability of 100% above pH 6.5 and between ~55% and 75% at pH ~4.

- *Application of machine learning in the prediction of thermodynamic properties of complex fluids:* The behavior of high ionic strength solutions is of interest in many fields, including geological nuclear waste disposal. Similar to the Pitzer model, Brønsted-Guggenheim-Scatchard specific interaction theory (SIT) is a model for the calculation of activity coefficients of aqueous species in moderate to high ionic strength solutions. Though experimental data exist for the interaction coefficient ( $\epsilon$ ) for various pairs of species, it is still highly desirable to develop a model to predict interaction coefficients for pairs of species that are hard to obtain experimentally, for example, for those at elevated temperatures and pressures. In FY23, we attempted to use deep learning neural networks to correlate the SIT coefficient of a species pair in a concentrated electrolyte solution to a basic set of known or easily estimated properties of individual species. We showed that such correlations did exist and could be extracted using both unsupervised and supervised machine learning. We further showed that such correlations were able to provide a reasonable prediction of the SIT coefficients for various species pairs under certain chemical conditions. This work thus opens a new avenue for modeling thermodynamic properties of complex fluids relevant to nuclear waste disposal.

The crystalline disposal R&D work packages will continue to focus the key thrust topics formulated in the SFWST roadmap:

*Near-Term Thrust Topics (Next 1- to 2-year period)*

- Improved representation of coupled THM processes affecting fracture transmissivity,
- Improved statistical sampling and representation of fracture networks,
- New generation EBS materials including new buffer and waste package materials.

A primary thrust is advanced capability development for generating discrete fracture networks (Hyman et al. 2015) in high performance-computing systems for use in the GDSA Framework. In the near-term, model capability development will support assessment of coupled THM processes affecting fracture transmissivity and use multi-fidelity approaches to evaluate the uncertainty introduced by the stochastic nature of fracture networks. This area will continue to focus on model capability demonstrations using actual field data obtained from international collaborations. Systematic investigations of the potential effects of fracture geometry and distribution on fracture connectivity and field-scale permeability will continue. Such work may feed long-term studies delineating site characterization and siting characteristics.

*Longer-Term Thrust Topics (Next 3- to 5-year period)*

a) Performance of candidate buffer materials under a range of disposal conditions

The interaction between the crystalline host rock and the EBS has been an important research thrust in the crystalline area and will continue to be because of fast transport in the natural fracture systems. Engineered buffer materials in the EBS are an important component for waste isolation in a crystalline repository. This area is pursuing development of a new generation of buffer materials that can be tailored to disposal environments for effective waste isolation. This effort includes molecular modeling and experiments to constrain and parameterize radionuclide interactions with newly developed buffer materials or corrosion products of EBS components. The goal of this modeling effort is the development of a continuum model used to simulate fluid flow and transport in the EBS materials as they degrade. Such a model will be used to evaluate the efficacy of new buffer materials and EBS design options. International collaborations have been, and will continue to be, a significant aspect of the crystalline research area. These activities include continued participation in DECOVALEX (for validation models), as well as collating and analyzing data from international URL.

## 13.0 REFERENCES

- [Database] National Library of Medicine – National Center for Biotechnology Information (NCBI), 2021. Periodic table of elements. PubChem. Accessed 19-October-2021 via <https://pubchem.ncbi.nlm.nih.gov/periodic-table/>.
- Abiodun, O.I., Jantan, A., Omolara, A.E., Dada, K.V., Mohamed, N.A., Arshad, H., 2018. State-of-the-art in artificial neural network applications: A survey. *Heliyon* 4. DOI: 10.1016/j.heliyon.2018.e00938
- Ajo-Franklin, J., Marco, V., Molins, S., Yang, L., 2018. Coupled Processes in a Fractured Reactive System: A Dolomite Dissolution Study with Relevance to GCS Caprock Integrity. In *Caprock Integrity in Geological Storage: Hydrogeochemical and Hydrogeomechanical Processes and their Impact on Storage Security*; Wiley Publishing.
- Ameli, P., Elkhoury, J.E., Morris, J.P. and Detwiler, R.L., 2014. Fracture permeability alteration due to chemical and mechanical processes: a coupled high-resolution model. *Rock mechanics and rock engineering*, 47(5), 1563-1573.
- Andrade, J. S., Costa, U. M. S., Almeida, M. P., Makse, H. A., Stanley, H. E., 1999. Inertial effects on fluid flow through disordered porous media. *Phys. Rev. Lett.*, 82, 5249–5252.
- Arcosa, D., Bruno, J., Karnland, O., 2003. Geochemical model of the granite–bentonite–ground water interaction at ASPO HRL (LOT experiment), *Applied Clay Science* 23, 219–228.
- Bate, B., Chen, C., Liu, P., Zhou, C., Chen, X., Nie, S., Chen, K., Chen, Y., Zhang, S., 2022. The Migration and Deposition Behaviors of Montmorillonite and Kaolinite Particles in a Two-Dimensional Micromodel. *Materials* 15 (3): 855. <https://doi.org/10.3390/ma15030855>.
- Becerro, A., Mantovani, M., Escudero, A., 2009. Mineralogical stability of phyllosilicates in hyperalkaline fluids: Influence of layer nature, octahedral occupation and presence of tetrahedral Al. *American Mineralogist* 94, 1187-1197.
- Bell, R., Dean, P., Hibbins-Butler, D., 1970. Localization of normal modes in vitreous silica, germania and beryllium fluoride. *J. Phys C Solid State*, 3 (10), 2111.
- Ben-Haim, M., MacDonald, D.D., 1994. Modeling geological brines in salt-dome high level nuclear waste isolation repositories by artificial neural networks. *Corrosion Science* 36(2), 385-393. DOI: 10.1016/0010-938X(94)90164-3
- Benjamin, M.M., Bloom, N.S., 1981. Effects of Strong Binding of Anionic Adsorbates on Adsorption of Trace Metals on Amorphous Iron Oxyhydroxide, in: Tewari, P.H. (Ed.) *Adsorption From Aqueous Solutions*. Springer US, Boston, MA, pp. 41-60. [doi.org/10.1007/978-1-4613-3264-0\\_3](https://doi.org/10.1007/978-1-4613-3264-0_3).
- Berkowitz, B., Scher, H., 1997. Anomalous transport in random fracture networks. *Phys. Rev. Lett.*, 79, 4038–4041.
- Bian, X., Cui Y., Zeng, Ling, Li, X., 2019. Swelling behavior of compacted bentonite with the presence of rock. *Engineering Geology* 254, 25–33.
- Birgersson, M., Börgesson, L., Hedström, M., Karnland, O., Nilsson, U., 2009. Bentonite Erosion- Final Report. TR-09-34. Swedish Nuclear Fuel and Waste Management Co.
- Birkholzer, J., Rutqvist, J., Sonnenthal, E. Barr, D., 2007. DECOVALEX-THMC Project. Task D. Long-Term Permeability/Porosity Changes in the EDZ and Near Field due to THM and THC Processes in Volcanic and Crystalline-Bentonite Systems, Phase 1 Report.

- Birkholzer, J.T., Tsang, C.T., Bond, A.E., Hudson, J.A., Jing, L., Stephansson, O., 2019. 25 years of DECOVALEX - Scientific advances and lessons learned from an international research collaboration in coupled subsurface processes. *Int J Rock Mech Min Sci* 122, 103995.
- Bond, A.E., I. Brusky, T. Cao, N. Chittenden et al. 2017. A synthesis of approaches for modelling coupled thermal–hydraulic–mechanical–chemical processes in a single novaculite fracture experiment. *Environ. Earth. Sci.* 76, 12.
- Bonnet, E., Bour, O., Odling, N. E., Davy, P., Main, I., Cowie, P., Berkowitz, B., 2001. Scaling of fracture systems in geological media. *Reviews of geophysics*, 39 (3), 347–383.
- Bourg, I.C., Bourg, A. C. M., Sposito, G., 2003. Modeling diffusion and adsorption in compacted bentonite: a critical review. *J. Contam. Hydrol.* 61 (1–4), 293–302.
- Brendler, V., Vahle, A., Arnold, T., Bernhard, G., Fanghänel, T., 2003. RES3T-Rosendorf expert system for surface and sorption thermodynamics. *J Contam Hydrol* 61(1-4), 281-291. doi.org/10.1016/s0169-7722(02)00129-8.
- Brown, P. E. (1989). FLINCOR; a microcomputer program for the reduction and investigation of fluid-inclusion data. *American Mineralogist*, 74(11-12), 1390-1393.
- Cao, X., Hu, L., Wang, J., and Wang, J., (2017). Regional Groundwater Flow Assessment in a Prospective High-Level Radioactive Waste Repository of China. *Water*. 9, 551.
- Caporuscio, F.A., Cheshire, M. C., Palaich, S., Norskog, K., Jove Colon, C. , 2015. Argillite Disposal R&D-LANL 2015. Summary of baseline experiments for generic repository engineered barriers. (FY 2015). (FCRD-UFD-2015-000356, LA-UR-15-26110). Los Alamos National Lab. (LANL), Los Alamos, NM (United States).
- Caporuscio, F.A., Cheshire, M. C., Rearick, M. S., Jove Colon, C. , 2014. LANL argilliteEBS experimental program 2014. (FCRD-USED-2014-000491). Los Alamos National Lab. (LANL), Los Alamos, NM (United States).
- Caporuscio, F.A., Migdisov, A., Rock, M. J., Sauer, K. B., van Hartesveldt, N. F. , 2019. Engineered Barrier System R&D and International Collaborations–LANL (FY19) (No. LA-UR-19-24222). Los Alamos National Lab. (LANL), Los Alamos, NM (United States).
- Caporuscio, F.A., Sauer, K.B., Rock, M.J., Houser, L.M., 2018. Engineered System R&D and International Collaborations – Los Alamos National Laboratory SF&WD R&D Work package # SF18LA01030801/SF-18LA01030805, LA-UR-18- 27601.
- Caporuscio, F.A., Sauer, K.B., Rock, M.J., 2020. Engineered System R&D and International Collaborations – Los Alamos National Laboratory (FY18). SF&WD R&D Work package # SF-02LA01030801 Rev2/SF-20LA01030805, LA-UR-20-25330.
- Cardenas, M. B., Slotke, D. T., Ketcham, R. A., Sharp, J. M., 2007. Navier- Stokes flow and transport simulations using real fractures shows heavy tailing due to eddies. *Geophys. Res. Lett.*, 34 (14).
- Chen, Y. F., Ye, Y., Hu, R., Yang, Z., & Zhou, C. B. (2022). Modeling unsaturated flow in fractured rocks with scaling relationships between hydraulic parameters. *Journal of Rock Mechanics and Geotechnical Engineering* <https://doi.org/10.1016/j.jrmge.2022.02.008>
- Chen, Y., Zhu, C., Sun, Y., Duan, H., Ye, W. and Wu, D., 2012. Adsorption of La (III) onto GMZ bentonite: effect of contact time, bentonite content, pH value and ionic strength. *Journal of Radioanalytical and Nuclear Chemistry*, 292(3), pp.1339-1347.
- Chen, Y.G., Sun, Z., Cui, Y.J., Ye, W.M., Liu, Q.H., 2019. Effect of cement solutions on the swelling pressure of compacted GMZ bentonite at different temperatures. *Construction and Building Materials* 229, 116872.

- Cheng, Y., Wong, L.N.Y., 2018. Microscopic Characterization of Tensile and Shear Fracturing in Progressive Failure in Marble. *Journal of Geophysical Research: Solid Earth* 123: 204–225.
- Cheshire, M.C., Caporuscio, F.A., Rearick, M.S., Jove-Colon, C., McCarney, M.K., 2014. Bentonite evolution at elevated pressures and temperatures: An experimental study for generic nuclear repository designs. *American Mineralogist* 99(8-9), 1662-1675.
- Chollet, F., 2017. *Deep Learning with Python* (1<sup>st</sup> ed.). Manning; 384pp. ISBN-10 9781617294433.
- Claret, F., Bauer, A., Schäfer, T., Griffault, L. and Lanson, B., 2002. Experimental investigation of the interaction of clays with high-pH solutions: A case study from the Callovo-Oxfordian formation, Meuse-Haute Marne underground laboratory (France). *Clays and Clay Minerals* 50(5), pp.633-646.
- COMSOL Multiphysics™ v. 5.6. [www.comsol.com](http://www.comsol.com). COMSOL AB, Stockholm, Sweden.
- Council, N. R., et al., 1996. *Rock fractures and fluid flow: contemporary understanding and applications*. National Academies Press.
- Crandall, D., Hajirezaie, S., Peters, C., Swift, A., Sheets, J., Stack, A., Anovitz, L., Cheshire, M., Cole, D., 2017. *Mineral Precipitation in Fractures: Multiscale Imaging and Geochemical Modeling* (No. NETL-PUB-21613). National Energy Technology Laboratory (NETL), Pittsburgh, PA, Morgantown, WV (United States).
- Cuadros, J., Linares, J., 1996. Experimental kinetic study of the smectite-to-illite transformation. *Geochimica Et Cosmochimica Acta* 60(3), 439-453. doi.org/Doi 10.1016/0016-7037(95)00407-6.
- Cuevas, J., 2004. Geochemical reactions between the FEBEX bentonite and portlandite-type cement porewater. In *Ecoclays II: Effect of cement on clay barrier performance II*. Final Report. (ANDRA) European contract FIKW-CT-2000-0028. (ed. N. Michan).
- Cuevas, J., Fernández, R., Sánchez, L., Vigil de la Villa, R., Rodríguez, M. and Leguey, S., 2007. Reactive diffusion front driven by an alkaline plume in compacted Mg homoionic bentonite. In *Clays in natural & engineered barriers for radioactive waste confinement, international meeting, Lille 2007online* available at: [http://www.andra.fr/lille2007/abstract\\_lille2007/donnees/pdf/509\\_510\\_P\\_MTPM\\_44.pdf](http://www.andra.fr/lille2007/abstract_lille2007/donnees/pdf/509_510_P_MTPM_44.pdf).
- Cuss R.J., Harrington J.F., Tamayo-Mas, E., Noy, D.J., Birchall, D.J., Brüning T., Sellin, P., Nord., M., 2022. Large scale gas injection test (Lasgit) performed at the Äspö Hard Rock Laboratory. Final report SKB TR-22-06.
- Dang, W., Wu, W., Konietzky, H., Qian, J., 2019. Effect of shear-induced aperture evolution on fluid flow in rock fractures. *Computers and Geotechnics*, 114, 103152.
- Davy, P., Hansen, A., Bonnet, E., Zhang, S.-Z., 1995. Localization and fault growth in layered brittle ductile systems: Implications for deformations of the continental lithosphere. *J. Geophys. Res.-Sol. Ea.*, 100 (B4), 6281–6294.
- Davy, P., Le Goc, R., Darcel, C., Bour, O., De Dreuzy, J.-R., Munier, R., 2010. A likely universal model of fracture scaling and its consequence for crustal hydromechanics. *J. Geophys. Res.-Sol. Ea.*, 115 (B10).
- de Dreuzy, J.-R., Méheust, Y., Pichot, G., 2012. Influence of fracture scale heterogeneity on the flow properties of three-dimensional discrete fracture networks. *J. Geophys. Res.-Sol. Ea.*, 117 (B11).
- de la Villa, R.V., Cuevas, J., Ramírez, S., Leguey, S., 2001. Zeolite formation during the alkaline reaction of bentonite. *European Journal of Mineralogy* 13(3), pp.635-644.

- Dehghani, M.R., Modarress, H., Bakhshi, A., 2006. Modeling and prediction of activity coefficient ratio of electrolytes in aqueous electrolyte solution containing amino acids using artificial neural network. *Fluid Phase Equilibria* 244, 153-159. DOI: 10.1016/j.fluid.2006.04.003
- Detwiler, R.L., 2008. Experimental observations of deformation caused by mineral dissolution in variable-aperture fractures. *Journal of Geophysical Research: Solid Earth*, 113(B8).
- Dobson, P., Tsang, C.-F., Doughty, C., Ahonen, L., Kietäväinen, R., Juhlin, C., Rosberg, J.-E., Borglin, S., Kneafsey, T., Rutqvist, J., Zheng, L., Xu, H., Nakagawa, S., Nihei, K., 2017. Deep borehole field test activities at LBNL 2017. US DOE Spent Fuel and Waste Science and Technology, SFWD-SFWST-2017-000046, Rep. LBNL-2001043, Lawrence Berkeley National Lab., Berkeley, CA, 118 p..
- Dobson, P., Tsang, C.-F., Kneafsey, T., Borglin, S., Piceno, Y., Andersen, G., Nakagawa, S., Nihei, S., K., Rutqvist, J., Doughty, C., Reagan, M., 2016. Deep borehole field test research activities at LBNL. US DOE Spent Fuel and Waste Science and Technology, FCRD-UFD-2016-000438, Rep. LBNL-1006044, Lawrence Berkeley National Lab., Berkeley, CA, 124 p.
- Doherty, J., 2018. PEST: Model-Independent Parameter Estimation. Watermark Numerical Computing.
- Dresden-Rosendorf, H.-Z., 2013. RES<sup>3</sup>T - Rossendorf Expert System for Surface and Sorption Thermodynamics. <https://www.hzdr.de/db/RES3T disclaimer>. 2013).
- Dzombak, D.A., Morel, F.M.M., 1990. Surface complexation modeling: hydrous ferric oxide. John Wiley & Sons.
- Eberl, D.D., Whitney, G. Khoury, H., 1978. Hydrothermal reactivity of smectite. *American Mineralogist* 63, 401–409.
- Ederly, Y., Geiger, S., Berkowitz, B., 2016. Structural controls on anomalous transport in fractured porous rock. *Water Resour. Res.*, 52 (7), 5634–5643.
- Edwards, J., Thouless, D., 1972. Numerical studies of localization in disordered systems. *J. Phys C Solid State*, 5 (8), 807.
- Elert, K., Pardo, E.S., Rodriguez-Navarro, C., 2015. Mineralogical evolution of di- and trioctahedral smectites in highly alkaline environments. *Clays and Clay Minerals* 63(6), pp.414-431.
- Eslamloueyan, R., Khademi, M.H., Mazinani, S., 2011. Using a multilayer perceptron network for thermal conductivity prediction of aqueous electrolyte solutions. *Industrial & Engineering Chemistry Research* 50, 4050-4056. DOI: 10.1021/ie101513z
- Fang, Z., Xu, X., Yang, X., Xie, H., Zhao, X., Wang, B., Zhao, D., Yang, Y., 2022. Structural stability and aqueous durability of Cs incorporation into BaAl<sub>2</sub>Ti<sub>6</sub>O<sub>16</sub> hollandite. *Journal of Nuclear Materials*, 565, p.153716.
- Faybishenko, B., Wang, Y., Harrington, J. *et al.*, 2022. Phenomenological model of nonlinear dynamics and deterministic chaotic gas migration in bentonite: experimental evidence and diagnostic parameters. *Transp. Porous Med* 141, 585–606. <https://doi.org/10.1007/s11242-021-01733-9>.
- Feng, J., Zhang, X., Luo, P., Li, X., Du, H., 2019. Mineral filling pattern in complex fracture system of carbonate reservoirs: implications from geochemical modeling of water-rock interaction. *Geofluids*, 2019.
- Fernández, R., Ruiz, A.I., Cuevas, J., 2014. The role of smectite composition on the hyperalkaline alteration of bentonite. *Applied Clay Science* 95, pp.83-94.
- Follin, S., Hartley, L., Rhen, I., Jackson, P., Joyce, S., Roberts, D., Swift, B., 2014. A methodology to constrain the parameters of a hydrogeological discrete fracture network model for sparsely

- fractured crystalline rock, exemplified by data from the proposed high-level nuclear waste repository site at Forsmark, Sweden. *Hydrogeol. J.*, 22 (2), 313–331.
- Frampton, A., Hyman, J., Zou, L., 2019. Advective transport in discrete fracture networks with connected and disconnected textures representing internal aperture variability. *Water Resour. Res.*, 55 (7), 5487–5501.
- Fraser-Harris, A. P., McDermott, C. I., Couples, G. D., Edlmann, K., Lightbody, A., Cartwright-Taylor, A., et al., 2020. Experimental investigation of hydraulic fracturing and stress sensitivity of fracture permeability under changing polyaxial stress conditions. *Journal of Geophysical Research: Solid Earth*, 125, e2020JB020044. <https://doi.org/10.1029/2020JB020044>.
- Gamsjäger, H., Bugajski, J., Preis, W., 2005. *Chemical thermodynamics of nickel*. Amsterdam: Elsevier.
- Garipov, T., Karimi-Fard, M., Tchelepi, H., 2016. Discrete fracture model for coupled flow and geomechanics. *Computational Geosciences*, 20 (1), 149–160.
- Giammar, D.E., Bruant Jr, R.G., Peters, C.A., 2005. Forsterite dissolution and magnesite precipitation at conditions relevant for deep saline aquifer storage and sequestration of carbon dioxide. *Chemical Geology*, 217(3-4), 257-276.
- Goodman, R. E., 1989. *Introduction to Rock Mechanics (Second Edition)*. John Wiley & Sons Ltd.
- Grambow, B., 2016. Geological disposal of radioactive waste in clay. *Element* 12, 239-245.
- Grote, R., Hong, T., Shuller-Nickles, L., Amoroso, J., Tang, M. and Brinkman, K.S., 2019. Radiation tolerant ceramics for nuclear waste immobilization: Structure and stability of cesium containing hollandite of the form  $(\text{Ba}, \text{Cs})_{1.33}(\text{Zn}, \text{Ti})_8\text{O}_{16}$  and  $(\text{Ba}, \text{Cs})_{1.33}(\text{Ga}, \text{Ti})_8\text{O}_{16}$ . *Journal of Nuclear Materials*, 518, pp.166-176.
- Guglielmi, Y., C. Chang, P. Cook, P. Dobson, F. Soom, S. Nakagawa, A. Niemi, C. Juhlin, H. Lorenz, J.-E. Rosberg, B. Dessirier, C.-F. Tsang, A. Tatomir, F. Basirat, E. Lundberg, B. Almqvist, S. Borglin, C. Doughty, L. Zheng, 2020. Crystalline Disposal R&D at LBNL: FY20 Progress Report, Rep. LBNL-2001334, Lawrence Berkeley National Lab., Berkeley, CA.
- Güven, N., 1990. Longevity of bentonite as buffer material in a nuclear-waste repository. *Engineering Geology* 28, 233–247.
- Hadermann, J., Heer, W., 1996. The Grimsel (Switzerland) migration experiment: integrating field experiments, laboratory investigations and modelling. *Journal of Contaminant Hydrology*. 21, 87-100.
- Hadgu, T., Kalinina, E., Wang, Y., 2022: Investigations of the Effect of Underground Excavations Using Hydrologic and Tracer Transport Modeling, *Tunneling and Underground Space technology Incorporating Trenchless Technology Research Journal*, 127 (2022) 104577.
- Hadgu, T., Karra, S., Kalinina, E., Makedonska, N., Hyman, J. D., Klise, K., Viswanathan, H. S., Wang, Y., 2017. A comparative study of discrete fracture network and equivalent continuum models for simulating flow and transport in the far field of a hypothetical nuclear waste repository in crystalline host rock. *J. Hyd.*, 553, 59-70.
- Han, S.-C., Chang, E., Zechel, S., Bok, F., Zavarin, M., 2023. Application of community data to surface complexation modeling framework development: Iron oxide protolysis. *J Colloid Interf Sci* 648, 1015-1024. doi.org/<https://doi.org/10.1016/j.jcis.2023.06.054>.
- Hanna, R. B., Rajaram, H., 1998. Influence of aperture variability on dissolutional growth of fissures in karst formations. *Water Resources Research*, 34 (11), 2843-2853.

- Harrington, J. F., Graham, C. C., Cuss, R. J., Norris, S., 2017. Gas network development in a precompacted bentonite experiment: Evidence of generation and evolution, *Applied Clay Science*, 147, 80-89. <https://doi.org/10.1016/j.clay.2017.07.005>.
- Heidbach, O., Iaffaldano, G., Bunge, H. P., 2008. Topography growth drives stress rotations in the central Andes: observations and models. *Geophysical Research Letters*, 35(8).
- Herrmann, H.J., Kertész, J., 1991. Stability analysis of crack propagation, *Physica A: Statistical Mechanics and its Applications*, 178(2), 227-235. [https://doi.org/10.1016/0378-4371\(91\)90018-8](https://doi.org/10.1016/0378-4371(91)90018-8).
- Herrmann, S.D., Westphal, B.R., Li, S.X. Zhao, H., 2022. Parametric Study of Used Nuclear Oxide Fuel Constituent Dissolution in Molten LiCl-KCl-UCl<sub>3</sub>. *Nuclear Technology*, 208(5), pp.871-891.
- Hornk, K., Stinchcombe, M., White, H., 1989, Multilayer feedforward networks are universal approximator, *Neural Networks*, 2, 359-366
- Hsieh, W. W., 2000, Nonlinear canonical correlation analysis by neural networks, *Neural Networks*, 13, 1095-1105.
- Hu, M., Rutqvist, J., 2020b. Numerical Manifold Method Modeling of Coupled Processes in Fractured Geological Media at Multiple Scales. *Journal of Rock Mechanics and Geotechnical Engineering* 12(4): 667-681.
- Hu, M., Rutqvist, J., 2021. Multi-scale Coupled Processes Modeling of Fractures as Porous, Interfacial and Granular Systems from Rock Images with the Numerical Manifold Method. *Rock Mechanics and Rock Engineering*. <https://doi.org/10.1007/s00603-021-02455-6>
- Hu, M., Rutqvist, J., Wang, Y., 2016. A Practical Model for Flow in Discrete-Fracture Porous Media by Using the Numerical Manifold Method. *Advances in Water Resources* 97: 38–51.
- Hu, M., Rutqvist, J., Wang, Y., 2017. A numerical manifold method model for analyzing fully coupled hydro-mechanical processes in porous rock masses with discrete fractures. *Advances in Water Resources* 102:111–26.
- Hu, M., Rutqvist, J., 2020a. Microscale mechanical modeling of deformable geomaterials with dynamic contacts based on the numerical manifold method. *Computational Geosciences* 24: 1783–1797.
- Hu, M., Wang, Y., Rutqvist, J. 2017a. Fully coupled hydro-mechanical numerical manifold modeling of porous rock with dominant fractures. *Acta Geotechnica* 12(2): 231–252.
- Hummel, W., Anderegg, G., Puigdomenech, I., Rao, L., Tochiyama, O., 2005. *Chemical thermodynamics of compounds and complexes of U, Np, Pu, Am, Tc, Se, Ni and Zr with selected organic ligands* (Vol. 9, pp. 1-1130). F. J. Mompean, M. Illemassène, & J. Perrone (Eds.). Amsterdam: Elsevier.
- Hyman, J. D., Aldrich, G., Viswanathan, H., Makedonska, N., Karra, S., 2016 Fracture size and transmissivity correlations: Implications for transport simulations in sparse three-dimensional discrete fracture networks following a truncated power law distribution of fracture size. *Water Resource Res.*, 52 (8), 6472–6489.
- Hyman, J. D., Dentz, M., Hagberg, A., Kang, P., 2019. Linking structural and transport properties in three-dimensional fracture networks. *J. Geophys. Res. Sol. Ea*.
- Hyman, J. D., Jimenez-Martinez, J., 2017. Dispersion and mixing in threedimensional discrete fracture networks: Nonlinear interplay between structural and hydraulic heterogeneity. *Water Resour. Res.*, 54 (5), 3243-3258.
- Hyman, J. D., Jiménez-Martínez, J., 2018. Dispersion and mixing in three-dimensional discrete fracture networks: Nonlinear interplay between structural and hydraulic heterogeneity. *Water Resources Research*, 54(5), 3243-3258.

- Hyman, J. D., Jimenez-Martinez, J., Gable, C. W., Stauffer, P. H., & Pawar, R. J., 2020. Characterizing the impact of fractured caprock heterogeneity on super critical CO<sub>2</sub> injection. *Transp. Porous Media*, 131 (3), 935–955.
- Hyman, J. D., Karra, S., Makedonska, N., Gable, C. W., Painter, S. L., Viswanathan, H. S., 2015. dfnWorks: A discrete fracture network framework for modeling subsurface flow and transport. *Comput. Geosci.*, 84, 10–19.
- Hyman, J. D., Sweeney, M. R., Frash, L. P., Carey, J. W., Viswanathan, H. S., 2021. Scale-bridging in three-dimensional fracture networks: Characterizing the effects of variable fracture apertures on network-scale flow channelization. *Geophysical Research Letters*, 48 (19), e2021GL094400.
- Itasca Consulting Group, 2020. FLAC3D — Fast Lagrangian Analysis of Continua in Three-Dimensions, Ver. 7.0. <https://www.itascacg.com/software/FLAC3D>
- Iwatsuki, T., Ishibashi, M., Onoe, H., Ozaki, Y., Hadgu, T., Jove-Colon, C.F., Kalinina, E., Wang, Y., Balvin, A., Hokr, M., Landa, J., Šembera, J., Zeman, J., 2020: DECOVALEX-2019 Task C final report, LBNL-2001264.
- Jain, A.K., Mao, J., Mohiuddin, K.M., 1996. Artificial neural networks: A tutorial. *Computers* 29(3), 31-44. DOI: 10.1109/2.485891
- Jenkins, C., Chadwick, A., Hovorka, S. D., 2015. The state of the art in monitoring and verification ten years on. *Int. J. Greenh. Gas. Con.*, 40, 312–349.
- Jeon, P.R., Lee, C., 2021. Artificial neural network modelling for solubility of carbon dioxide in various aqueous solutions from pure water to brine. *Journal of CO<sub>2</sub> Utilization* 47. DOI: 10.1016/j.jcou.2021.101500.
- Johnston, J., Grove, C., 1931. The solubility of calcium hydroxide in aqueous salt solutions. *Journal of the American Chemical Society*, 53(11), pp.3976-3991.
- Jones, T. A., Detwiler, R. L., 2019. Mineral precipitation in fractures: Using the Level-Set method to quantify the role of mineral heterogeneity on transport properties. *Water Resources Research*, 55(5), 4186-4206.
- Jordan, N., Thoenen, T., Starke, S., Spahiu, K., Brendler, V., 2022. A critical review of the solution chemistry, solubility, and thermodynamics of europium: Recent advances on the Eu<sup>3+</sup> aqua ion and the Eu (III) aqueous complexes and solid phases with the sulphate, chloride, and phosphate inorganic ligands. *Coordination Chemistry Reviews*, p.214608.
- Kang, P. K., Brown, S., Juanes, R., 2016. Emergence of anomalous transport in stressed rough fractures. *Earth Planet. Sc. Lett.*, 454, 46–54.
- Kang, P. K., Dentz, M., Le Borgne, T., Juanes, R., 2015. Anomalous transport on regular fracture networks: Impact of conductivity heterogeneity and mixing at fracture intersections. *Phys. Rev. E*, 92 (2), 022148.
- Kang, P. K., Dentz, M., Le Borgne, T., Lee, S., Juanes, R., 2017. Anomalous transport in disordered fracture networks: spatial Markov model for dispersion with variable injection modes. *Adv. Water Resour.*, 106, 80–94.
- Kang, P. K., Hyman, J. D., Han, W. S., Dentz, M., 2020. Anomalous transport in three-dimensional discrete fracture networks: Interplay between aperture heterogeneity and injection modes. *Water Resources Research*, 56 (11), e2020WR027378.

- Kang, P. K., Lei, Q., Dentz, M., Juanes, R., 2019. Stress-induced anomalous transport in natural fracture networks. *Water Resources Research*, 55 (5), 4163-4185. doi: 10.1029/2019WR024944
- Kasbohm, J., Pusch, R., Nguyen-Thanh, L. Hoang-Minh, T., 2013. Lab-scale performance of selected expandable clays under HLW repository conditions. *Environmental Earth Sciences* 69(8), pp.2569-2579.
- Kaufhold, S., Dohrmann, R., 2011. Stability of bentonites in salt solutions III—calcium hydroxide. *Applied Clay Science* 51(3), pp.300-307.
- Kaufhold, S., Dohrmann, R., Sander, T., Sellin, P., Svensson, D., 2013. Mineralogical investigations of the first package of the alternative buffer material test---I. Alteration of bentonites. *Clay Minerals* 48, 199-213.
- Kirkes, L., Xiong, Y.-L., 2018. Experimental determination of brucite solubility in NaCl solutions at elevated temperatures. In Xiong, Y.-L., ed., *Solution Chemistry: Advances in Research and Applications*, pp.48-68, ISBN: 978-1-53613-101-7, Nova Science Publishers, Inc., New York.
- Komarneni, S., Roy, D.M., 1982. Hydrothermal interactions of cement or mortar with zeolites or montmorillonites. *MRS Proceedings*, 15:55.
- Lang, P., Paluszny, A., Zimmerman, R., 2014. Permeability tensor of three dimensional fractured porous rock and a comparison to trace map predictions. *J. Geophys. Res.-Sol. Ea.*, 119 (8), 6288–6307.
- Laubach, S. E., Lander, R. H., Criscenti, L. J. et al., 2019. The role of chemistry in fracture pattern development and opportunities to advance interpretations of geological materials. *Reviews of Geophysics*, 57(3), 1065-1111.
- Lei, Q., Latham, J.-P., Tsang, C.-F., 2017. The use of discrete fracture networks for modelling coupled geomechanical and hydrological behaviour of fractured rocks. *Computers and Geotechnics*, 85, 151–176.
- Levi, M., 2023. A pressure puzzle: More is less. *SIAM News*, 56 (2).
- Li, D., Duan, Z., 2007. The speciation equilibrium coupling with phase equilibrium in the H<sub>2</sub>O–CO<sub>2</sub>–NaCl system from 0 to 250 C, from 0 to 1000 bar, and from 0 to 5 molality of NaCl. *Chemical Geology*, 244(3-4), pp.730-751.
- Li, Z., Özgen-Xian, I. and Maina, F.Z., 2021. A mass-conservative predictor-corrector solution to the 1D Richards equation with adaptive time control. *Journal of Hydrology*, 592, 125809.
- Lichtner, P., Hammond, G., Lu, C., Karra, S. et al., 2015. PFLOTRAN user manual: A massively parallel reactive flow and transport model for describing surface and subsurface processes (Tech. Rep.). (Report No.: LA-UR-15-20403) Los Alamos National Laboratory.
- Lippmann, F., 1968. Enhancement of (0k0) reflections of clay minerals in a Guinier camera. *Contributions to Mineralogy and Petrology* 19, 260-270.
- Lisjak, A., Tatone, B.S.A., Mahabadi, O.K., Grasselli, G., Marschall, P., Lanyon, G.W., de la Vaissiere, R., Shao, H., Leung, H., Nussbaum, C., 2016. Hybrid Finite-Discrete Element Simulation of the EDZ Formation and Mechanical Sealing Process Around a Microtunnel in Opalinus Clay. *Rock Mech Rock Eng* 49:1849–1873.
- Liu, X.-D., Prikryl, R., Pusch, R., 2011. THMC-testing of three expandable clays of potential use in HLW repositories. *Applied Clay Science* 52(4), pp.419-427.
- Maillot, J., Davy, P., Le Goc, R., Darcel, C., De Dreuzy, J.-R., 2016. Connectivity, permeability, and channeling in randomly distributed and kinematically defined discrete fracture network models. *Water Resour. Res.*, 52 (11), 8526–8545.

- Makedonska, N., Hyman, J. D. D., Karra, S., Painter, S. L., Gable, C. W. W., Viswanathan, H. S., 2016. Evaluating the effect of internal aperture variability on transport in kilometer scale discrete fracture networks. *Adv. Water Resour.*, 94, 486–497.
- Makedonska, N., Painter, S. L., Bui, Q. M., Gable, C. W., Karra, S., 2015. Particle tracking approach for transport in three-dimensional discrete fracture networks. *Computat. Geosci.*, 1–15.
- Martin, C. and Christiansson, R., 2009. Estimating the potential for spalling around a deep nuclear waste repository in crystalline rock. *International Journal of Rock Mechanics and Mining Sciences*. 46, 219-228.
- McClure, M. W., Babazadeh, M., Shiozawa, S., Huang, J., 2016. Fully coupled hydromechanical simulation of hydraulic fracturing in 3d discrete-fracture networks. *Spe Journal*, 21 (04), 1302–1320.
- McDermott, C. I., Fraser-Harris, A. P., Sauter, M., Couples, G. D., Edlmann, K. P., Kolditz, O., et al., 2018. New experimental equipment recreating geo-reservoir conditions in large, fractured, porous samples to investigate coupled thermal, hydraulic and polyaxial stress processes. *Scientific Reports*, 8(1), 14549. <https://doi.org/10.1038/s41598-018-32753-z>.
- Meunier A., Velde, B., Griffault, L., 1998. The reactivity of bentonites, a review. An application to clay barrier stability for nuclear waste storage. *Clay Miner.* 33, 187–196.
- Mills, M.M., Sanchez, A.C., Boisvert, L., Payne, C.B., Ho, T.A., Wang, Y.F., 2023. Understanding smectite to illite transformation at elevated (>100 degrees C) temperature: Effects of liquid/solid ratio, interlayer cation, solution chemistry and reaction time. *Chemical Geology* 615. doi.org/ARTN 12121410.1016/j.chemgeo.2022.121214.
- Molins, S., Trebotich, D., Steefel, C. I., Shen, C., 2012. An investigation of the effect of pore scale flow on average geochemical reaction rates using direct numerical simulation. *Water Resources Research*, 48(3).
- Molins, S., Trebotich, D., Yang, L., Ajo-Franklin, J. B., Ligocki, T. J., Shen, C., & Steefel, C. I., 2014. Pore-scale controls on calcite dissolution rates from flow-through laboratory and numerical experiments. *Environmental science & technology*, 48(13), 7453-7460.
- National Academies of Sciences, E., Medicine, et al., 2020. Characterization, modeling, monitoring, and remediation of fractured rock. National Academies Press.
- Nittmann, J., Daccord, G. & Stanley, H., 1985. Fractal growth viscous fingers: quantitative characterization of a fluid instability phenomenon. *Nature* 314, 141–144. <https://doi.org/10.1038/314141a0>
- Noiriel, C., Seigneur, N., Le Guern, P., Lagneau, V., 2021. Geometry and mineral heterogeneity controls on precipitation in fractures: An X-ray micro-tomography and reactive transport modeling study. *Advances in Water Resources*, 152, 103916.
- Pandey, S., Chaudhuri, A., Rajaram, H., Kelkar, S., 2015. Fracture transmissivity evolution due to silica dissolution/precipitation during geothermal heat extraction. *Geothermics*, 57, 111-126.
- Parkhurst, D.L., Appelo, C.A.J., 2013. Description of input and examples for PHREEQC version 3—A computer program for speciation, batch-reaction, one-dimensional transport, and inverse geochemical calculations, US geological survey techniques and methods. p. 497.
- Pollard D., Segall P., 1987. Theoretical displacements and stresses near fractures in rock: with applications to faults, joints, veins, dikes, and solution surfaces. *Fracture mechanics of rock* 277-349, Academic Press, London, UK.

- Ponikvar-Svet, M., Thomas, A.T., Dodson, B.J., Henegar, B.M., Brewster M.W., Neerchal, N.K., Liebman, J.F., 2013. Linear model for estimating the entropy of formation of aqueous anions. *Structural Chemistry* 24, 2069-2082. DOI: 10.1007/s11224-013-0310-5
- Pope, R. N., 2017. Influence of Temperature on Diffusion and Sorption of  $^{237}\text{Np(V)}$  through Bentonite Engineered Barriers. Clemson University.
- Prasianakis, N.I., Haller, R., Mahrous, M., Poonosamy, J., Pflingsten, W., Churkov, S.V., 2020. Neural network based process coupling and parameter upscaling in reactive transport simulations. *Geochimica et Cosmochimica Acta* 291, 126-143. DOI: 10.1016/j.gca.2020.07.019
- Pusch, R., 1979. Highly Compacted Sodium Bentonite for Isolating Rock-Deposited Radioactive-Waste Products. *Nucl Technol* 45(2), 153-157. doi.org/Doi 10.13182/Nt79-A32305.
- Pusch, R., 2001. *The buffer and backfill handbook. Part 2: Materials and techniques* (No. SKB-TR--02-12). Swedish Nuclear Fuel and Waste Management Co.
- Pusch, R., Kasbohm, J., 2002. *Alteration of MX-80 by hydrothermal treatment under high salt content conditions* (No. SKB-TR--02-06). Swedish Nuclear Fuel and Waste Management Co.
- Python Software Foundation, 2021. Python. Version 3.8 initially released October 2019. Source code hosted on <https://www.python.org/>.
- R Core Team, 2021. R: A language and environment for statistical computing. R Foundation for Statistical Computing, Vienna, Austria. Accessed 27-September-2021 via <https://www.R-project.org>.
- Ramírez, S., Cuevas, J., Vigil, R., Leguey, S., 2002. Hydrothermal alteration of “La Serrata” bentonite (Almeria, Spain) by alkaline solutions. *Applied Clay Science*, 21(5-6), pp.257-269.
- Roubinet, D., De Dreuzy, J.-R., Tartakovsky, D. M., 2013. Particle-tracking simulations of anomalous transport in hierarchically fractured rocks. *Computers & geosciences*, 50, 52–58.
- Rutqvist, J., 2020. Thermal management associated with geologic disposal of large spent nuclear fuel canisters in tunnels with thermally engineered backfill. *Tunnelling and Underground Space Technology* 102: 103454.
- Rutqvist, J., Bäckström, A., Chijimatsu, M., Feng, X.-T., Pan, P.-Z., Hudson, J., Jing, L., Kobayashi, A., Koyama, T., Lee, H.-S., Huang, X.-H., Rinne, M., Shen, B., 2009. Multiple-code simulation study of the long-term EDZ evolution of geological nuclear waste repositories. *Environmental Geology* 57: 1313–1324.
- Sasaki, T., Hu, M., 2023. 3D modeling of thermal shearing of fractures at the asperity scale. *57th US Rock Mechanics/Geomechanics Symposium*. June 25-28, Atlanta, Georgia.
- Sasaki, T., Rutqvist, J., 2021. Estimation of stress and stress-induced permeability change in a geological nuclear waste repository in a thermo-hydrologically coupled simulation. *Computers and Geotechnics*, 129, 103866. <https://doi.org/10.1016/j.compgeo.2020.103866>
- Schuessler, W., Kienzler, B., Wilhelm, S., Neck, V., Kim, J.I., 2000. Modeling of near field actinide concentrations in radioactive waste repositories in salt formations: effect of buffer materials. *Mater. Res. Soc. Symp. Proc.* 663, pp.791-798.
- Sellin, P., Leupin, O.X., 2013. The use of clay as an engineered barrier in radioactive waste management—a review. *Clay Miner.* 61 (6), 477–498.
- Selroos, J.-O., Walker, D. D., Ström, A., Gylling, B., Follin, S., 2002. Comparison of alternative modelling approaches for groundwater flow in fractured rock. *J. Hydrol.*, 257 (1-4), 174–188.

- Sevougian, S.D., Mariner, P.E., Connolly, L.A., MacKinnon, R.J., Roger, R.D., Dobson, D.C., Prouty, J. L., 2019. DOE SFWST Campaign R&D Roadmap Update. M2SF-19SN010304042; SAND2019-5179R. Albuquerque, NM: Sandia National Laboratories.
- Shannon, R.D., 1976. Revised effective ionic radii and systematic studies of interatomic distances in halides and chalcogenides. *Acta Crystallographica*, A 32, 751.
- Shao, H., Pinnavaia, T.J., 2010. Synthesis and properties of nanoparticle forms saponite clay, cancrinite zeolite and phase mixtures thereof. *Microporous and Mesoporous Materials* 133, 10-17.
- Sherman, T., Engdahl, N. B., Porta, G., Bolster, D., 2021. A review of spatial markov models for predicting pre-asymptotic and anomalous transport in porous and fractured media. *Journal of Contaminant Hydrology*, 236, 103734.
- Shi, G. 1992. Manifold method of material analysis. Transaction of the 9th army conference on applied mathematics and computing. U.S. Army Research Office.
- Shi, G. 1996. Simplex integration for manifold method, FEM and DDA. *Discontinuous Deformation Analysis (DDA) and Simulations of Discontinuous Media*. TSI press. 205-262.
- Singurindy, O., Berkowitz, B., 2005. The role of fractures on coupled dissolution and precipitation patterns in carbonate rocks. *Advances in water resources*, 28(5), 507-521.
- Steeffel, C. I., Hu, M., 2022. Reactive transport modeling of mineral precipitation and carbon trapping in discrete fracture networks. *Water Resources Research*, 58(9), e2022WR032321.
- Steeffel, C.I., Appelo, C.A.J., Arora, B., Jacques, D., Kalbacher, T., Kolditz, O., Lagneau, V., Lichtner, P.C., Mayer, K.U., Meeussen, J.C.L., Molins, S., 2015. Reactive transport codes for subsurface environmental simulation. *Computational Geosciences*, 19(3), 445-478.
- Steeffel, C.I., Lasaga, A.C., 1994. A coupled model for transport of multiple chemical species and kinetic precipitation/dissolution reactions with application to reactive flow in single phase hydrothermal systems. *American Journal of Science*, 294, 529-592.
- Steeffel, C.I., Lichtner, P.C., 1994. Diffusion and reaction in rock matrix bordering a hyperalkaline fluid-filled fracture. *Geochimica et Cosmochimica Acta*, 58(17),3595-3612.
- Steeffel, C.I., Lichtner, P.C., 1998. Multicomponent reactive transport in discrete fractures: II: Infiltration of hyperalkaline groundwater at Maqarin, Jordan, a natural analogue site. *Journal of Hydrology*, 209(1-4), 200-224.
- Steeffel, C.I., Yang, L. (2021) Secondary magnesite formation from forsterite under CO<sub>2</sub> sequestration conditions via coupled heterogeneous nucleation and crystal growth. *Geochimica et Cosmochimica Acta*, 311, 29-42.
- Sun, C., Zhuang, L., Jung, S., Lee, J., Yoon, J. S., 2021. Thermally induced slip of a single sawcut granite fracture under biaxial loading. *Geomechanics and Geophysics for Geo-Energy and Geo-Resources*, 7(4), 1–13. <https://doi.org/10.1007/s40948-021-00293-y>
- Sun, C., Zhuang, L., Yoon, J. S., Min, K., 2023. Thermally induced shear reactivation of critically-stressed smooth and rough granite fractures. *IOP Conference Series: Earth and Environmental Science*, 1124(1). <https://doi.org/10.1088/1755-1315/1124/1/012119>
- Sun, Z., Chen, Y.G., Cui, Y.J., Xu, H.D., Ye, W.M., Wu, D.B., 2018. Effect of synthetic water and cement solutions on the swelling pressure of compacted Gaomiaozi (GMZ) bentonite: the Beishan site case, Gansu, China. *Engineering Geology* 244, pp.66-74.

- Sun, Z., Chen, Y.G., Ye, W.M., Cui, Y.J., Wang, Q., 2020. Swelling deformation of Gaomiaozi bentonite under alkaline chemical conditions in a repository. *Engineering Geology* 279, p.105891.
- Sweeney, M. R., Hyman, J., 2020. Stress effects on flow and transport in three-dimensional fracture networks. *Journal of Geophysical Research: Solid Earth*, 125 (8), e2020JB019754.
- Tran, M., Jha, B., 2021. Effect of poroelastic coupling and fracture dynamics on solute transport and geomechanical stability. *Water Resources Research*, 57 (10), e2021WR029584.
- Villar, M.V., Iglesias, R.J., García-Siñeriz, J.L., Lloret, A., Huertas, F., 2020. Physical evolution of a bentonite buffer during 18 years of heating and hydration. *Engineering Geology* 264, p.105408.
- Villar, M.V., Rivas, P., 1994. Hydraulic properties of montmorillonite-quartz and saponite-quartz mixtures. *Applied Clay Science*, 9(1), pp.1-9.
- Viswanathan, H. S., Ajo-Franklin, J., Birkholzer, J. T., Carey, J. W., Guglielmi, Y., Hyman, J., et al., 2022. From fluid flow to coupled processes in fractured rock: Recent advances and new frontiers. *Reviews of Geophysics*, 60 (1), e2021RG000744.
- Wang Y. et al., 2014. Used Fuel Disposal in Crystalline Rocks: Status and FY14 Progress, FCRD-UFD-2014-000060, SAND2014, Sandia National Laboratories, Albuquerque, NM.
- Wang Y., Budd D. A., 2012. Stress-induced chemical waves in sediment burial diagenesis, *Nature Communications*, 3:685. <https://doi.org/10.1038/ncomms1684>.
- Wang, J., Wei, Y., Wang, J., Zhang, X., Wang, Y., Li, N., 2022. Simultaneous immobilization of radionuclides Sr and Cs by sodium zirconium phosphate type ceramics and its chemical durability. *Ceramics International*, 48(9), pp.12772-12778.
- Wang, M., Chen, Y.-F., Ma, G.-W., Zhou, J.-Q., Zhou, C.-B., 2016. Influence of surface roughness on nonlinear flow behaviors in 3d self-affine rough fractures: Lattice boltzmann simulations. *Advances in Water Resources*, 96, 373-388.
- Wang, P., Anderko, A., Turner, D.R., 2001. Thermodynamic modeling of the adsorption of radionuclides on selected minerals. II: Anions. *Industrial and Engineering Chemistry Research* 40(20), 4444-4455. doi.org/10.1021/ie000992h.
- Wang, Y. (2017): On subsurface fracture opening and closure. *J. Petroleum Sci. Eng.*, 155, 46-53.
- Wang, Y., 2014. Nanogeochemistry: Nanostructures, emergent properties and their control on geochemical reactions and mass transfers. *Chem. Geol.* 378, 1–23.
- Wang, Y., Bryan, B., Dewers, T., Heath, J. E., Jove-Colon, C., 2013. Ganglion dynamics and its implications to geologic carbon dioxide storage. *Environ. Sci. Technol.* 47, 219–226.
- Wang, Y., Hu, M., Zhou, Q., Rutqvist, J., 2014. Energy-work-based numerical manifold seepage analysis with an efficient scheme to locate the phreatic surface. *International Journal for Numerical and Analytical Methods in Geomechanics* 38: 1633-1650.
- Wang, Y., Hu, M., Zhou, Q., Rutqvist, J., 2016. A new second-order numerical manifold method model with an efficient scheme for analyzing free surface flow with inner drains. *Applied Mathematical Modelling* 40: 1427-1445.
- Wang, Z., Zhou, C., Wang, F., Li, C., Xie, H., 2021. Channeling flow and anomalous transport due to the complex void structure of rock fractures. *Journal of Hydrology*, 601, 126624.
- Wenning, Q. C., Berthet, T., Ask, M., Zappone, A., Rosberg, J. E., Almqvist, B. S. G (2017). Image log analysis of in situ stress orientation, breakout growth, and natural geologic structures to 2.5 km depth in central Scandinavian Caledonides: Results from the COSC-1 borehole. *Journal of Geophysical Research: Solid Earth*, 122(5), 3999-4019.

- Wersin, P., Johnson, L.H., McKinley, I.G., 2007. Performance of the bentonite barrier at temperatures beyond 100 degrees C: A critical review. *Physics and Chemistry of the Earth* 32(8-14), 780-788. doi.org/10.1016/j.pce.2006.02.051.
- Whitney, G., 1983. Hydrothermal reactivity of saponite. *Clays and Clay Minerals* 31, 1-8.
- Wieland, W., Lothenbach, B., Glaus, M.A., Thoenen, T. Schwyn, B., 2014. Influence of superplasticizers on the long-term properties of cement pastes and possible impact on radionuclide uptake in a cement-based repository for radioactive waste. *Applied Geochemistry* 49, 126–142.
- Wired Chemist, <https://www.wiredchemist.com/chemistry/data/atomic-and-ionic-radii>, accessed on March 7, 2022.
- Witherspoon, P. A., Wang, J. S. Y., Iwai, K., Gale, J. E., 1980. Validity of cubic law for fluid flow in a deformable rock fracture. *Water Resources Research*, 16 (6), 1016-1024.
- Witherspoon, P. A., Wilson, C. R., Long, J. C. S., DuBois, A. O., Gale, J. E., McPherson, M., 1980. The role of large-scale permeability measurements in fractured rock and their application at stripa. In C. J. M. Northrup (Ed.), *Scientific basis for nuclear waste management* (pp. 519–526). Boston, MA: Springer US.
- Wolery, T.W., Sutton, M., 2011. *Generic Natural Systems Evaluation-Thermodynamic Database Development and Data Management* (No. LLNL-TR-500113). Lawrence Livermore National Lab. (LLNL), Livermore, CA (United States).
- Xiong, W. Giammar, D., 2014. Forsterite carbonation in zones with transport limited by diffusion. *Environmental Science & Technology Letters*, 1(8), 333-338.
- Xiong, Y., 2006. Estimation of medium effects on equilibrium constants in moderate and high ionic strength solutions at elevated temperatures by using specific interaction theory (SIT): Interaction coefficients involving  $\text{Cl}^-$ ,  $\text{OH}^-$  and  $\text{Ac}^-$  up to 200°C and 400 bars. *Geochemical Transactions* 7(4). DOI: 10.1186/1467-4866-7-4
- Xiong, Y., 2009. The aqueous geochemistry of thallium: speciation and solubility of thallium in low temperature systems. *Environmental Chemistry* 6, pp. 441-451. doi: 10.1071/EN08086.
- Xiong, Y., 2014. Speciation and solubility of thallium in low temperature systems: Additional aqueous and solid thallium species potentially important in soil environments. *Speciation Studies in Soil, Sediment and Environmental Samples*, Chapter 7, pp.325-340, CRC Press.
- Xiong, Y., 2016. Solubility constants of hydroxyl sodalite at elevated temperatures evaluated from hydrothermal experiments: Applications to nuclear waste isolation. *Applied Geochemistry*, 74, pp.138-143.
- Xiong, Y., Cetiner, Z., 2017. Comment on “The experimental determination of hydromagnesite precipitation rates at 22.5–75° C” by Berninger, U.-N., Jordan, G., Schott, J. and Oelkers, EH. *Mineralogical Magazine*, 81(3), 689-693.
- Xiong, Y., Kirkes, L., Westfall, T., Roselle, R., 2013. Experimental determination of solubilities of lead oxalate ( $\text{PbC}_2\text{O}_4(\text{cr})$ ) in a NaCl medium to high ionic strengths, and the importance of lead oxalate in low temperature environments. *Chemical Geology* 342, pp. 128-137. doi: 10.1016/j.chemgeo.2013.01.012
- Xiong, Y., Lord, A. S., 2008. Experimental investigations of the reaction path in the  $\text{MgO}-\text{CO}_2-\text{H}_2\text{O}$  system in solutions with various ionic strengths, and their applications to nuclear waste isolation. *Applied Geochemistry*, 23(6), 1634-1659.

- Xiong, Y.-L., 2008. Thermodynamic properties of brucite determined by solubility studies and their significance to nuclear waste isolation. *Aquatic Geochemistry* 14, 223–238.
- Xiong, Y.-L., 2011. Organic species of lanthanum in natural environments: implications to mobility of rare earth elements in low temperature environments. *Applied Geochemistry* 26, 1130–1137.
- Xiong, Y.-L., 2013. A Thermodynamic Model for Silica and Aluminum in Alkaline Solutions with High Ionic Strength at Elevated Temperatures up to 100 °C: Applications to Zeolites. *American Mineralogist* 98, 141–153.
- Xiong, Y.-L., 2016. Solubility constants of hydroxyl sodalite at elevated temperatures evaluated from hydrothermal experiments: Applications to nuclear waste isolation. *Applied Geochemistry* 74, 138–143.
- Xiong, Y.-L., 2022. Experimental determination of solubility constants of saponite at elevated temperatures in high ionic strength solutions. *American Mineralogist* 107, 1091–1099.
- Xiong, Y.-L., Lord, A.S., 2008. Experimental investigations of the reaction path in the MgO–CO<sub>2</sub>–H<sub>2</sub>O system in solutions with various ionic strengths, and their applications to nuclear waste isolation. *Applied Geochemistry* 23, 1634–1659.
- Xiong, Y.-L., Wang, Y.-F., 2021. Experimental and modeling studies of Pr and Nd oxalates to high ionic strengths: Insight into actinide(III) oxalates. *Chemical Geology* 573, p. 120200.
- Yang, T., Pusch, R., Knutsson, S., Liu, X.-D., 2014. The assessment of clay buffers for isolating highly radioactive waste. *WIT Transactions on Ecology and the Environment* 180, 403–413.
- Zavarin, M., Chang, E., Wainwright, H., Parham, N., Kaukuntla, R., Zouabe, J., Deinhart, A., Genetti, V., Shipman, S., Bok, F., Brendler, V., 2022. Community Data Mining Approach for Surface Complexation Database Development. *Environ Sci Technol* 56(4), 2827–2838. doi.org/10.1021/acs.est.1c07109.
- Zheng, L., Deng, H., Nakagawa, S., Kim, K., Kneafsey, T., Dobson, P., Borglin, S., Doughty, C., Voltolini, M., Tsang, C.-F., Dessirier, B., Wenning, Q., Juhlin, C., 2018. Crystalline Disposal R&D at LBNL: FY18 Progress Report., Rep. LBNL-2001177, Lawrence Berkeley National Lab., Berkeley, CA, 71 p.
- Zheng, L., Niemi, A., Juhlin, C., Lorenz, H., Rosberg, J.-E., Dessirier, B., Tsang, C.-F., Tatomir, A., Basirat, F., Lundberg, E., Almquist, B., Borglin, S., Doughty, C., 2019. Crystalline Disposal R&D at LBNL: FY19 Progress Report, Rep. LBNL-2001221, Lawrence Berkeley National Lab., Berkeley, CA.
- Zheng, L., Rutqvist, J., Xu, H., Birkholzer, J.T., 2017. Coupled THMC models for bentonite in an argillite repository for nuclear waste: Illitization and its effect on swelling stress under high temperature. *Eng Geol* 230, 118–129. doi.org/10.1016/j.enggeo.2017.10.002.
- Zheng, M., Liu, X., 2009. Hydrochemistry of salt lakes of the Qinghai-Tibet Plateau, China. *Aquatic Geochemistry*, 15(1), 293–320.
- Zhong, S., Zhang, K., Bagheri, M., Burken, J.G., Gu, A., Li, B., Ma, X., Marrone, B.L., Ren, Z.J., Schrier, J., Shi, W., Tan, H., Wang, T., Wang, X., Wong, B.M., Xiao, X., Yu, X., Zhu, J., Zhang, H., 2021. Machine learning: New ideas and tools in environmental science and engineering. *Environmental Science and Technology* 55, 12741–12754. DOI: 10.1021/acs.est.1c01339.
- Zhou, J.-Q., Wang, M., Wang, L., Chen, Y.-F., Zhou, C.-B., 2018. Emergence of nonlinear laminar flow in fractures during shear. *Rock Mechanics and Rock Engineering*, 51, 3635–3643.
- Zimmerman, R. W., Bodvarsson, G. S., 1996. Hydraulic conductivity of rock fractures. *Transport Porous Med.*, 23 (1), 1–30.

## APPENDIX A

Table A-1. Evaluation of the current status of tasks identified in SFWST R&amp;D roadmap

R&D Task #	R&D Task (or Activity) Name	Brief Task Description	Importance to Safety Case (ISC)	Generic R&D Needed	Accomplishments and status
C-1	<b>Discrete Fracture Network (DFN) Model</b>	<ul style="list-style-type: none"> <li>• Generation and representation of realistic fracture networks</li> <li>• Fluid flow &amp; transport in fracture networks</li> <li>• Mapping tools (dfnWorks to PFLOTRAN)</li> <li>• Dual continuum; matrix diffusion- transient flow particle tracker</li> </ul>	ISC = High	<ul style="list-style-type: none"> <li>• Continued improvement of models of RN F&amp;T in fractured media by simulation of field scale and laboratory testing programs, particularly in coordination with international programs in crystalline rock, will result in increased confidence and better validation of models.</li> <li>• Develop a reduced order model based DFN simulations for total system performance assessments.</li> <li>• High-resolution characterization of multiscale fracture distributions is technically changing.</li> <li>• Obtaining statistically representative fracture fields is an open question in total system performance assessments.</li> </ul>	<ul style="list-style-type: none"> <li>• Software package dfnWorks was developed.</li> <li>• Fracture continuum model (FCM) was adapted. A comparison with DFN model was performed.</li> <li>• DECOVALEX Japanese Mitsunami Site and South Korean KURT site data were obtained.</li> <li>• Workflow model for field data synthesis, tested with Mitsunami data was developed.</li> <li>• Parallelized the particle tracking code.</li> <li>• Development of reduced order models using machine learning is in progress.</li> <li>• Significant progress was made in understanding THMC couplings in a single fracture.</li> <li>• A simple model was developed to relate fracture aperture changes to far field stresses.</li> </ul>
C-2	<b>Flow and Transport in Fractures - modeling approaches</b>	<ul style="list-style-type: none"> <li>• Different modeling approaches - graphs, pruning, FCM, other ECPM, particle tracking v. reactive transport.</li> <li>• Validation of simpler models against more mechanistic models.</li> </ul>	ISC = High	<p>Future activities will focus on understanding the uncertainty in fluid flow and radionuclide transport associated with different modeling approaches. We will consider different modeling approaches - graphs, pruning, FCM, other ECPM, particle tracking v. reactive transport, as well as validation of simpler models against more complex, mechanistic ones. Further evaluate the statistical stability of multiple DFN realizations for PA.</p>	<ul style="list-style-type: none"> <li>• Comparison between DFN and fractured continuum models was completed.</li> <li>• FCM was tested against Mitsunami data.</li> <li>• Matrix diffusion was incorporated into DFN model.</li> <li>• Particle tracking vs. reactive transport was compared for uncertainty quantification.</li> <li>• A limited number of realizations for a given fracture distribution were performed and compared with Mitsunami data.</li> <li>• The effects of stress on fracture aperture and permeability have been investigated.</li> <li>• Fluid mixing and chemical reactions in fracture networks was explored.</li> </ul>
C-3	<b>Fracture-Matrix Diffusion</b>	Crystalline rock - see also SKB GWFTS Task (I-10) and consider relation to microstructure DFN	ISC = High	Continued participation in DECOVALEX and other modeling efforts will result in improved confidence and validation of coupled F&T models of repository performance, both in the EDZ and undamaged host rock. Additional column and field scale testing on matrix diffusion and upscaling modeling are needed. Incorporate modeling advances from International work in our methods.	<ul style="list-style-type: none"> <li>• Matrix diffusion was incorporated in DFN model and tested with data from SKB task 9.</li> <li>• Dual porosity model in PFLOTRAN can partly account for matrix diffusion.</li> <li>• FCM can also capture matrix diffusion.</li> </ul>

C-4	<b>Lab and modeling study of EDZ - Crystalline</b>	<ul style="list-style-type: none"> <li>Hydrologic properties of damage zone in crystalline rocks.</li> <li>Modeling and lab studies (LBL Seiji Nakagawa). Relevant to extent of EDZ/probability of connecting to transmissive feature.</li> <li>Thermal effects (DPC)</li> </ul>	ISC = Medium	Continue to improve confidence in models by improving characterization techniques (e.g., geophysical methods) . Testing rock samples from field laboratories, including samples from the Grimsel and Stripa mines will help validate models and the understanding of the hydro-mechanical-chemical interaction between the filling materials within the excavation and the EDZ. Concurrently, we plan to simulate the laboratory-observed EDZ development using the RBSN model and predict the development of an EDZ in the field and its hydro-mechanical properties. Develop methods to differentiate background fractures from excavation induced fractures on a tunnel surface. Have not yet demonstrated that the modeling can match the observations. Also need to address upscaling. How to observation at core scale relate	<ul style="list-style-type: none"> <li>A high pressure (up to 10,000 psi), high temperature (up to 200°C) triaxial loading system was developed and tested using granite samples from Grimsel site.</li> <li>Step-rate Injection Method for Fracture <i>In-situ</i> Properties (SIMFIP) was developed to measure real-time 3D mechanical deformation of rock in a borehole; and method was tested in the COSC-1 borehole.</li> <li>Significant progress was made in the development of multi-scale hydrologic and mechanical couplings, e.g., the development of the rigid body spring network (RBSN) model and the models based on the numerical manifold method in supporting the DECOVALEX tasks.</li> <li>Bentonite-fracture interaction has been experimentally studied, which shows that clay particle plugging can significantly reduce fracture permeability.</li> </ul>
C-5	<b>Development and demonstration of geophysical techniques for site characterization</b>	Existing non-invasive geophysical techniques are adequate for characterizing large-scale subsurface features and physical properties, but continued advances could help achieve high-resolution images of time-varying properties and structural changes that may be important during the site selection or characterization stages. This task will focus on the development of new geophysical techniques that can provide unprecedented high spatial resolutions. Develop invasive (downhole) hydrological characterization techniques to resolve flowing fractures in a borehole. Understand issues of scale (and direction). Which techniques give the most/best information? Understand which features (e.g. stress state, fracture orientation..) have greatest	ISC = High	Continue development and demonstration of geophysical techniques for site characterization. One particular area to look into is a possibility of using acoustic wave to characterize fractures in a DRZ. Use boreholes as analog for characterizing DRZ. Develop methodology for transferring field observations to better DFN model. DFN distributions include only flowing probability distributions. DFN is directly calibrated to include observed flowing fractures.  High-resolution characterization of multiscale fracture distributions is technically changing.	<ul style="list-style-type: none"> <li>The SIMFIP technique was tested in the COSC-1 borehole. This technique allows us to infer downhole in-situ stresses based on displacement measurements.</li> <li>Downhole Robotic Stress Analyzer (DORSA) was developed.</li> </ul>

		influence on which fractures are flowing and which are not? Develop novel techniques for characterizing groundwater chemistry. The emphasis will be given to the techniques that can provide fast, accurate, in-situ, and high spatial resolution measurements (in boreholes) with minimum human perturbations. The techniques that can characterize flow localization and the associated chemical			
<b>C-6</b>	<b>Buffer Erosion</b>	In crystalline rock, low ionic strength fluids erode engineered barrier (e. g glaciation) relevant to sites where future glaciation is expected or other process causes big change in infiltration. This process is also directly linked to colloid generation and transport.	ISC = High	If the repository program considers potential sites in glaciated areas, site specific studies to assess the potential changes in infiltration flux associated with climate change would be necessary. Development of mechanistic model for buffer erosion for inclusion in PA?	<ul style="list-style-type: none"> <li>• Buffer material erosion experiment was initiated. Surface potential measurements of bentonite suspension were performed.</li> <li>• Possibilities for stabilizing buffer materials, e.g., using chemical additives, were explored.</li> <li>• Work on bentonite-fracture interaction indicates that particle clogging can be an important mechanism for fracture permeability reduction.</li> <li>• Microfluidic cell for clay particle transport and clogging was developed.</li> </ul>
<b>C-7</b>	<b>Colloids in Fractures</b>	This task will focus on two key aspects of the CFT: (1) colloid particle formation and transport in porous geologic media and (2) radionuclide partitioning among pore water, colloid particles, and stationary substrates. Particle size dependent colloid transport and radionuclide uptake.	ISC = Medium	Continue to improve models to simulate colloid transport and improve techniques for in-situ characterization and quantification of colloids. Leverage info from NAGRA working group on colloids. Need to better understand colloid formation from clay materials, and address uncertainties related to sorption/desorption (attachment/detachment) and colloid instability in high ionic strength environments. Need to reduce uncertainty in infiltration, improve representation of heterogeneous behavior of colloids, colloid transport behavior in unsaturated environments, multiple rate kinetics and irreversibility of radionuclide sorption onto colloids, and better understand size dependence.	<ul style="list-style-type: none"> <li>• Multiple site colloid transport model was developed and tested against multiple column experiments.</li> <li>• Pu interaction and colloid formation at clay and Fe oxide surfaces were investigated.</li> <li>• Experiments on buffer erosion and colloid formation were initiated.</li> <li>• Colloid-facilitated transport model and the data supporting the model are ready for GDSA implementation.</li> </ul>
<b>C-8</b>	<b>Interaction of Buffer w/ Crystalline Rock</b>	• Chemical interactions, effect on buffer stability, related to buffer erosion, colloid generation and	ISC =High	DOE's continued participation in multinational programs analyzing potential repositories in crystalline rocks are an excellent and very cost-effective way to developed improved, validated	<ul style="list-style-type: none"> <li>• Participated in the HotBENT program.</li> <li>• Some understanding was obtained from the FEBEX program.</li> </ul>

		transport, buffer materials by design		THMC models that could be directly applicable to the US program. As an example, HotBENT could provide highly relevant experimental validation of important repository processes at high temperature. Substantial cost savings would be achieved in the design of a repository if HotBENT demonstrates that the maximum temperature of bentonite backfill can be raised without drastic performance implications.	<ul style="list-style-type: none"> <li>The triaxial rock mechanical testing system can be used for studying buffer-crystalline rock interaction.</li> </ul>
<b>C-9</b>	<b>Development of Centralized Technical Database for Crystalline Disposal System Evaluation</b>	The data to be collected will include thermodynamic data for radionuclide speciation and sorption, groundwater chemistry, hydraulic and mechanical property data, mineralogical and compositional data of representative host and far-field media, spatial distributions of potential host formations, etc. To support site screening and selection, there is a need to develop tools for spatial data analysis and visualization (e.g., a geographic information system). O-2, O-4 cross-cut to GFM and to thermodynamic database	ISC = Medium	A data management plan was developed but not implemented. Actual implementation of the central database is needed.	<ul style="list-style-type: none"> <li>Continued engagement with the NEA-thermodynamic database program.</li> <li>Collaborated with JAEA on sorption data compilation.</li> <li>Developed codes for data management and synthesis (e.g., using machine learning).</li> <li>Developed a geographic information system for geological data management and representation.</li> <li>Developed a model approach to using machine learning to predict thermodynamic properties of complex fluids.</li> </ul>
<b>C-10</b>	<b>Collate Data from International URL's</b>	Identify and collate potential data sets from URL's that support/inform the crystalline reference case and/or development of process models, including groundwater chemistry, rock mineralogy, associated radionuclide retardation parameters, fracture distribution, flow in fractures, groundwater residence times (pores, fractures) site testing data (e.g., tracer tests) for model validation. Formulate a strategy for domestic URL development; crosscut to O-2, O-4, and tie-in to C-9.	ISC = Medium	Continue site characterization data collection through international collaborations and make full use of the data for model development and validation.	Data have been collected from DECOVALEX, SKB, Japanese Mitsunami, South Korean KURT, and Czech URL.

C-11	<b>Investigation of Fluid Flow and Transport in Low Permeability Media (clay materials)</b>	Understanding water movement in such media is crucial for the performance assessment of a waste isolation system. It was recently discovered that fluid flow and chemical diffusion in low-permeability media may not follow traditional linear laws such as Darcy's law and Fick's law. This task will systematically study water flow regimes and their transport behaviors in clay formations as a function of clay formation texture and pore geometry.	ISC = High	Refine the existing model to better match experimental data. Understand a potential thermal effect on Non-Darcian flow.	<ul style="list-style-type: none"> <li>• Significant understanding has been obtained for gas migration in water-saturated compacted bentonite from the DECOVALEX program.</li> <li>• Demonstrated the existence of a fast advective water flow in clay interlayers.</li> <li>• Better understanding of non-Darcian fluid flow and its temperature dependence in clay materials was obtained.</li> <li>• Demonstrated the impacts of nanopore confinement on fluid flow and radionuclide transport.</li> <li>• Demonstrated a possibility for the existence of porosity wave in fluid flow in low-permeability media.</li> <li>• Significant understanding of gas migration in water saturated bentonite was obtained, which is based on interface instability and nonlinear dynamics.</li> </ul>
C-12	<b>Model Validation: Evolution of groundwater chemistry and radionuclide transport in fractured rock</b>	Coupling of radionuclide transport with evolving water chemistry along a transport pathway (e.g. alkaline plumes). This is a modeling project for which the tools already exist. Developing flexible modeling tools for simulating radionuclide sorption/desorption behavior for GDSA. Robustness of numerical algorithms for coupling chemical reactions with solute transport - Gibbs free energy minimization may be more robust than equilibrium constants. C-2 Explicit consideration of structural complexity of the media in the solute transport	ISC = Medium	Future work may include additional chemical processes other than a simple Kd-based sorption-desorption process. A future model should also consider the of multiple scale heterogeneities and more robust uncertainty quantification.	<ul style="list-style-type: none"> <li>• A smart Kd approach combined with machine learning is being explored.</li> <li>• Irreversible processes such as radionuclide coprecipitation with secondary mineral phases is being investigated.</li> <li>• PFLOTRAN is able to simulate evolving water chemistry in both the near and the field.</li> </ul>
C-13	<b>Evaluation and upscaling of the effects of spatial heterogeneity on radionuclide transport</b>	This task will develop modeling capabilities to capture the effects of the spatial heterogeneity (e.g., Kd values) on radionuclide transport in natural	ISC = High	Future DFN simulations need to be performed on more realistic fracture networks. Incorporate the effect of spatial heterogeneity in Kd into the GDSA model.	<ul style="list-style-type: none"> <li>• Simulations of radionuclide transport with spatially distributed Kd values were performed, demonstrating the necessity to account for the spatial heterogeneity of Kd to appropriately capture the uncertainties of radionuclide transport and retention.</li> </ul>

		<p>systems. The work will include two parts: the modeling capabilities for realistic representation of spatial heterogeneity and the experimental technique for quantification of this heterogeneity. The work will significantly reduce both the predicted total radionuclide release from a repository and the associated uncertainty through improved performance prediction of the natural barrier system. Improved representation of spatial heterogeneity of chemical and transport properties. Development of spatial correlation fields for things like <math>K_d</math> or for spatial heterogeneity in water chemistry and mineralogy and its relationship to <math>K_d</math> variability (via surface complexation/ion exchange). This task will systematically evaluate the existing techniques for upscaling key hydrologic and geochemical parameters, identify the gaps in upscaling, and develop new methodologies for bridging the identified gaps. The parameters of interest include matrix diffusion coefficients, sorption coefficient, chemical reaction kinetics, etc. The laboratory and field experiments of various scales will be explored for conceptual model development and validation.</p>			<ul style="list-style-type: none"><li>• A bimolecular chemical reaction in a fracture network was investigated.</li><li>• Demonstrated a potential effect of heterogeneity in aperture distribution on fluid flow and transport in fracture networks.</li></ul>
--	--	---	--	--	---

<p><b>C-14</b></p>	<p><b>Radionuclide sorption and incorporation by natural and engineered materials: Beyond a simple Kd approach</b></p>	<p>As they move through the engineered barrier system and the natural system, radionuclides released from the engineered barrier will experience a complex set of physical and chemical interactions with the materials. Existing models generally assume that radionuclide retention in the natural system could be described with a linear, equilibrium Kd approach. The reality may be much more complex. Incorporation of interfacial reactions would be a much more flexible approach for GDSA as it allows for rational variation of retardation parameters based on a range of potential geochemical</p>	<p>ISC = High</p>	<p>Further mechanistically understand a potential effect of heating on radionuclide adsorption on bentonite materials. Better understand radionuclide interaction with clays and metal corrosion products, especially irreversible sorption and desorption processes. Radionuclide interaction with evolving engineered barrier system components (e.g. secondary mineral formation and EBS mineral alteration) will be exacerbated in thermal conditions associated with direct disposal of DPCs. Test the model for other radionuclides. Incorporation of interfacial reactions would be a much more flexible approach for GDSA as it allows for rational variation of retardation parameters based on a range of potential geochemical conditions that iodide can potentially interact with interlayer sites of a clay material</p>	<ul style="list-style-type: none"> <li>• Iodine uptake by negatively charged clay materials has been studied. The study shows that this uptake proceeds in clay interlayers through ion pairing.</li> <li>• A column experiment is being performed on U transport through compacted bentonite under influence of various chemical conditions.</li> <li>• Coprecipitation of radionuclides such as Pu with corrosion products and other secondary minerals is being studied.</li> <li>• Long-term vs. short term sorption experiments indicate that the experimental duration affects the Kd values determined.</li> <li>• A relationship between sorption and coprecipitation has been explored.</li> <li>• Smart Kd approach using machine learning is being explored.</li> <li>• Sorption behavior of trivalent cations on saponite was investigated.</li> </ul>
<p><b>C-15</b></p>	<p><b>Design improved backfill and seal materials</b></p>	<p>This effort will focus on designing new buffer/backfill and seal materials for effective isolation of waste in a repository. The new design will fully take into account the capabilities of the materials as a hydrologic barrier (low permeability to a fluid flow) and a reactive barrier (high radionuclide sorption capacity). It will also consider the availability of the materials and their compatibility with repository environments. DPCs may require buffer materials engineered for high thermal conductivity. Relax thermal limit for buffer materials. This task</p>	<p>ISC = High</p>	<p>Continuing progress in materials science and technology opens new opportunities for buffer material design and improvement. Development a subsystem model that can be used to evaluate the effectiveness of new buffer materials for waste isolation.</p>	<ul style="list-style-type: none"> <li>• New additive materials to bentonite have been explored for enhanced radionuclide uptake and thermal conductivity of bentonite materials.</li> <li>• The transformation of smectite to illite has been studied, which demonstrates the dependence of this transformation on water/rock ratio, K concentration, and silica concentration.</li> <li>• Thermal effects on bentonite performance were investigated and results indicate that the thermal limit can potentially be raised from the existing assumption.</li> <li>• Participating in drift-scale HotBENT testing on thermal effects on bentonite performance.</li> <li>• Possibilities for using chemical additives to minimize buffer erosion was explored.</li> <li>• A capability of modeling coupled THMC processes in buffer materials was developed.</li> <li>• Copper meshes were proposed as a means for enhancing the thermal conductivity of bentonite materials.</li> </ul>

		will systematically examine the technical basis for the thermal limits of various disposal media (i.e., the maximum wall temperature allowed). Minimize erosion and colloid generation. Ensure self-sealing properties.			<ul style="list-style-type: none"> <li>• A new statistical mechanics model was developed for clay particle size distribution and layer stacking.</li> <li>• New buffer materials such as saponite for high temperature and pH has been proposed. The concept has been tested.</li> </ul>
<b>C-16</b>	<b>Development of new waste package concepts and models for evaluation of waste package performance for long-term disposal.</b>	Waste packages are an important layer of an engineered system for waste isolation, especially for a repository in fractured crystalline rocks. This effort will include two parts: (1) new materials (e.g. coatings) and new concepts for waste package design and (2) improved models for predicting the long-term performance of waste packages in a crystalline repository. One aspect to be examined is the potential interactions of waste packages with buffer materials in the EBS. Cross cut to EBS (E-4).	ISC = High	Continue development of a waste package degradation model. Incorporate the model into a GDSA model.	<ul style="list-style-type: none"> <li>• Lead or lead alloys as outer layer packaging materials were studied.</li> <li>• Chemical reactions at metal-bentonite interface will be investigated as a part of HotBENT tests.</li> <li>• High entropy alloys have been explored for waste packaging materials.</li> </ul>
<b>C-17</b>	<b>Model DFN evolution due to changes in stress field</b>	Fracture apertures and therefore the permeability of a fracture network change due to changes in stress field, which can be caused by excavation, waste emplacement, or glaciation/deglaciation.	ISC = High	Incorporate the stress effect into the existing DFN model and study the effect on DRZ evolution and the impact of glaciation. Increased heating from DPC could also impact the local stress regime.	<ul style="list-style-type: none"> <li>• In DECOVALEX 2023 Task G, the effects of stress on a single fracture or a fracture network is being studied.</li> <li>• A simple model relating far-field stress to fracture aperture was developed.</li> </ul>